University of California
Santa Barbara

Coherent dynamics of a hybrid quantum spin-mechanical oscillator system

A dissertation submitted in partial satisfaction
of the requirements for the degree

Doctor of Philosophy
in
Physics

by

Kenneth William Lee III

Committee in charge:

Professor Ania C. Bleszynski Jayich, Chair
Professor David M. Weld
Professor Andreas Ludwig

September 2017

The Dissertation of Kenneth William Lee III is approved.

Professor David M. Weld

Professor Andreas Ludwig

Professor Ania C. Bleszynski Jayich, Committee Chair

September 2017

Coherent dynamics of a hybrid quantum spin-mechanical oscillator system

by

Kenneth William Lee III

For Pia and my family

Acknowledgements

Graduate school was a very difficult journey for me. There were many times when I thought about quitting, but the incredible support from my friends, family, mentors, and coworkers propelled me to the end. I would like to take the time to thank all of the people who have gotten me to this point, for none of this would have been possible without them.

I would like to start off by thanking a few teachers from highschool that really whooped my butt and taught me the value of hard work and determination in math and science: Mr. Coe, Mr. Siegert, and Mr. Eisenstein. I still remember my very first tests in your classes, which were my very first failing grades ever in school. From that point on, I was never afraid to ask questions. Your belief in my abilities and determination to keep me from slipping through the cracks are a big reason for my successes today

Next, I would like to thank my undergraduate research advisor, Chris Monroe. Chris is an amazing physicist, and an even more amazing advisor. There were many times when it would be better for me to go think about a problem on my own or make a few mistakes to learn an important lesson about research. Chris always knew when that time was, and was always there to point me in the right direction when I started to get in over my head. Chris continues to give me guidance and encouragement to this day, and is a big reason that I am choosing to continue down the physics rabbit hole.

In Chris' lab, I had the privilege of working directly under a number of extraordinary physicists, including my good friend and graduate student Dave Hayes. Dave was an amazing mentor and taught me an immense amount of theoretical and experimental physics. It is safe to say that many of my laboratory habits have been adopted from him. Thank you for all of the opportunities you have given me throughout the years.

In graduate school, I have been fortunate to work in the group of professor Ania Jayich, who was the person who actually convinced me to come to UCSB. As one of Ania's first graduate students, I had the privilege of building a brand new experiment from the ground up. Ania's enthusiasm and determination have been instrumental to my growth as a scientist. Ania gave me a lot of freedom in determining the future of the spin-phonon project, and was always willing to discuss new and exciting ideas that either of us had. Apart from science, one of Ania's greatest strengths is her ability to build a cohesive group. Throughout my time at UCSB, the Jayich group has proven to be one of the nicest, most collaborative, and supportive groups I could ever imagine working with. Working in her group has taught me a lot about experimental research and for that I am very thankful.

The work presented here would not have been possible without the incredible effort from the spin-phonon team: Preeti Ovartchaiyapong, Donghun Lee, and Jeff Cady. I would especially like to acknowledge Preeti, who designed and fabricated all of the beautiful devices presented in this thesis (although Preeti would probably say they are "just ok"). Without his patience, determination, legendary tweezer hands, and prodigious skill, none of this would have been possible. Preeti taught me a lot about the lab and experiment during my early years in grad school, and was a great partner. I wish him the best of luck as he begins his career as a professor, and hope that the Bulls and Bears turn it around for him so he can enjoy watching them again. In my third year in the lab, the spin-phonon team grew to three members with the addition of postdoc Donghun Lee. Donghun's vast knowledge of optomechanics and experimental physics gave an immediate boost to the team, and his attention to detail and patience were critical to the low temperature experiments. Donghun always supported my ideas and was an overwhelmingly positive influence on the entire group. I am so grateful that I met him and thankful for all that he has done for me and the spin-phonon team. I wish him the best of luck

as a professor at Korea University. Toward the end of graduate school, the spin-phonon team was joined by graduate student Jeff Cady. Despite his unwavering allegiance to LeBron James, Jeff has already made many valuable contributions to the spin-phonon project. As you will see in the final chapter of this thesis, Jeff has already become a pro at making diamond nanostructures. I think it is very safe to say that the future of the spin-phonon project could not be in better hands, and I look forward to the 25 Nature papers that will be published from this experiment in the next few years.

In addition to the spin-phonon team, I had the privilege of working with several talented people in the Jayich lab who were critical to the success of my Ph.D. I need to first acknowledge the enormous contributions made by graduate student Bryan Myers. Bryan is an incredibly polished scientist and has an unmatched attention to detail. Bryan singlehandedly set up all of the software infrastructure for the lab, and was the group expert on all things NV center, especially dynamical decoupling and quantum sensing. I enjoyed our many conversations throughout grad school and it was always fun to share half-baked ideas with you (note that Bryan's were always well thought out – mine were the half-baked ideas). Next, I would like to acknowledge Matt Pelliccione, who joined the group as a postdoc on the scanning magnetometry experiment during my third year. Matt's impact on the group has been immeasurable. He is easily one of the most talented and skilled scientists I have ever met. Matt taught me everything I know about electronics and cryogenics, and without his help, the low-temperature experiments would not have gotten off the ground. Matt quickly became one of my closest friends here, and I am very grateful for all of his support. Thanks for also reading this dissertation and giving me valuable feedback. I also need to acknowledge graduate student Claire McLellan, who joined the group just before I did. Claire is the official materials guru for the lab. She is an excellent teacher and was extremely patient as she taught me how to do diamond fabrication. Her positivity and enthusiasm are infectious. I look forward to seeing her

fully functional diamond magnetometer capable of imaging an entire brain in real time, and seeing where the future takes her. Finally, I would like to acknowledge the rest of the Jayich group. Although we did not work together directly, I learned something from each one of you and enjoyed being your coworker. Thank you to postdocs Laetitia Pascal, Tim Eichhorn, Amila Ariyaratne, Suzanne Baumann, graduate students Alec Jenkins, Bo Dwyer, and Sasha Zibrov, master's students Jens Boss, Danijela Markovic, Thomas Chalopin, Chris Vazquez, and undergraduates Gino Graziano, Ilan Rosen, Anand Das, Dolev Bluvstein, and Chris Reetz. I'd like to make a special shoutout to Suzanne who graciously allowed me to crash at her apartment in my last and homeless month at UCSB.

I have had the immense privilege of collaborating with several people during graduate school, including Marcus Doherty, Jero Maze, Joaquin Minguzzi, John Morton, and Amir Safavi-Naeini. I would like to especially thank Marcus and Jero, who never lost their patience after I screwed up my derivation of the strain interaction for the millionth time and were always happy to answer questions I had. Amir has been absolutely essential to our latest experiments on diamond optomechanical crystals, and I look forward to seeing what the future holds for our collaboration. John Morton was a pleasure to work with, and taught me a lot about bismuth donors in silicon and spin physics in the short time that he was at UCSB.

I would also like to acknowledge the many UCSB staff members that have made my life as easy as possible during graduate school. Thank you to graduate advisor Jennifer Farrar for all that you have done for me and my fellow graduate students over the last 5 years. Thank you to building manager Mike Deal who was always there when things went wrong no matter what time of night it was. Thank you to cleanroom engineers Mike Day and Aidan Hopkins for helping me fish out diamond samples that I had dropped into the various wet benches in the cleanroom. Thank you to CNSI staff Sonya Perez, Daniel Daniels, Lynne Leininger, Paul Weakliem, and Fuzzy Rogers for helping keep the

lab running smoothly. Thank you to Dr. Amanda Strom who graciously allowed me to use the gold wirebonder in MRL. Finally, thank you to machine shop supervisor Guy Patterson, who taught me how to do everything I know in the machine shop and stopped me before I was about to do something stupid or inefficient.

At times, graduate school drove me absolutely insane. Without all of my friends, old and new, I would not have been able to make it through. Thanks to the CHS guys: Diddy, TC, Trevor, Joel, Rossberg, BYoo, Zach, Neubs, Pearse, Anderson, and Huy. Thanks to the citizens of Za City: Nick, Andrew, Scott, Kurt, Jason, and Sarah (I guess Clyde, too). I would also like to thank Sarah and James, who made the last year of graduate school especially fun.

Fitness is without a doubt a major part of my life. Exercise is crucial to my mental well being and is my primary outlet for relieving stress. Coming into graduate school, I had a shoulder injury that had prevented me from weightlifting for more than a year. In my third year, I sustained a partial hamstring tear that sidelined me for a few months as well. The expertise and care of Dr. Jennifer Stafford, Dr. Omar Flores, and Dr. Dave Dallmeyer helped me overcome my injuries and come out even stronger than before. After returning to the gym, I became friends with Jose Navarrete, aka the Fatman. Despite his small calves, Jose has been a source of constant support and a great friend. Jose and I established the "Swole Patrole" at the rec center (lifters who showed up at 6:30 am), which became my main group of friends at UCSB. Thanks to the homies Edward (The Dog), Ra'am, Andy (Slayer), Christian (Ze Doktor), Naveen (Beta), Barnes, and the rest of the crew.

Finally, I would like to thank my family, present and future. Thank you, Mom, for your unconditional support. You have given me so much throughout my life and I will always be proud to be your son. Dad, thank you for your love and guidance. Thank you, Kevin, for being an incredible parent and embracing me as your own son. My brother

Ethan has been a source of inspiration to me and I thank him for always being thoughtful of me. My sister Madeline, aka fatso, has grown up so much during my time in grad school. Thanks for being a great friend and for keeping me from getting too old too quickly. Finally, I would like to thank my girlfriend Pia. Pia has been my rock for the past 2+ years. Thank you for your immense love, encouragement, and patience. You have made so many sacrifices for me, especially in the last few months, and I am forever grateful. I cannot imagine life without you, and I am excited for our next journey in Colorado.

Curriculum Vitæ

Kenneth William Lee III

Education

2017	Ph.D. in Physics, University of California, Santa Barbara.
2016	M.A. in Physics, University of California, Santa Barbara.
2011	B.S. in Physics (High Honors), University of Maryland, College Park

Publications

8. D. Lee*, **K. W. Lee***, and A. C. Bleszynski Jayich, "Hybrid mechanical systems based on negatively charged D_{3d} defect centers in diamond," *in preparation* (2017).

7. **K. W. Lee**, J. V. Cady, D. Lee, and A. C. Bleszynski Jayich, "Enhanced spin coherence in a hybrid spin-mechanical oscillator system," *in preparation* (2017).

6. D. Lee*, **K. W. Lee***, J. V. Cady, P. Ovartchaiyapong, and A. C. Bleszynski Jayich, "Topical Review: Spins and mechanics in diamond," *Journal of Optics* **19** 033010 (2016).

5. C. W. Pester, B. Narupai, K. M. Mattson, D. P. Bothman, D. Klinger, **K. W. Lee**, E. H. Discekici, and C. J. Hawker, "Engineering Surfaces through Sequential Stop-Flow Photopatterning," *Advanced Materials* **28** 9292-9300 (2016).

4. **K. W. Lee***, D. Lee*, P. Ovartchaiyapong, J. Minguzzi, J. R. Maze, and A. C. Bleszynski Jayich, "Strain Coupling of a Mechanical Resonator to a Single Quantum Emitter in Diamond," *Physical Review Applied* **6** 034005 (2016).

3. P. Ovartchaiyapong*, **K. W. Lee***, B. A. Myers, and A. C. Bleszynski Jayich, "Dynamic strain-mediated coupling of a single diamond spin to a mechanical resonator," *Nature Communications* **5** 4429 (2014).

2. R. Islam, W. C. Campbell, T. Choi, S. M. Clark, S. Debnath, E. E. Edwards, B. Fields, D. Hayes, D. Hucul, I. V. Inlek, K. G. Johnson, S. Korenblit, A. Lee, **K. W. Lee**, T. A. Manning, D. N. Matsukevich, J. Mizrahi, Q. Quraishi, C. Senko, J. Smith, and C. Monroe, "Beat note stabilization of mode-locked lasers for quantum information processing," *Optics Letters* **39** (2012) 3238-3241 (2014).

1. D. Hayes, S. M. Clark, S. Debnath, D. Hucul, I. V. Inlek, **K. W. Lee**, Q. Quraishi, and C. Monroe, "Coherent error suppression in multi-qubit entangling gates," *Physical Review Letters* **109** 020503 (2012).

Abstract

Coherent dynamics of a hybrid quantum spin-mechanical oscillator system

by

Kenneth William Lee III

A fully functional quantum computer must contain at least two important components: a quantum memory for storing and manipulating quantum information and a quantum data bus to securely transfer information between quantum memories. Typically, a quantum memory is composed of a matter system, such as an atom or an electron spin, due to their prolonged quantum coherence. Alternatively, a quantum data bus is typically composed of some propagating degree of freedom, such as a photon, which can retain quantum information over long distances. Therefore, a quantum computer will likely be a hybrid quantum device, consisting of two or more disparate quantum systems. However, there must be a reliable and controllable quantum interface between the memory and bus in order to faithfully interconvert quantum information. The current engineering challenge for quantum computers is scaling the device to large numbers of controllable quantum systems, which will ultimately depend on the choice of the quantum elements and interfaces utilized in the device. In this thesis, we present and characterize a hybrid quantum device comprised of single nitrogen-vacancy (NV) centers embedded in a high quality factor diamond mechanical oscillator. The electron spin of the NV center is a leading candidate for the realization of a quantum memory due to its exceptional quantum coherence times. On the other hand, mechanical oscillators are highly sensitive to a wide variety of external forces, and have the potential to serve as a long-range quantum bus between quantum systems of disparate energy scales. These two elements are interfaced through crystal strain generated by vibrations of the mechanical oscillator.

Importantly, a strain interface allows for a scalable architecture, and furthermore, opens the door to integration into a larger quantum network through coupling to an optical interface.

There are a few important engineering challenges associated with this device. First, there have been no previous demonstrations of a strain-mediated spin-mechanical interface and hence the system is largely uncharacterized. Second, fabricating high quality diamond mechanical oscillators is difficult due to the robust and chemically inert nature of diamond. Finally, engineering highly coherent NV centers with a coherent optical interface in nanostructured diamond remains an outstanding challenge. In this thesis, we theoretically and experimentally address each of these challenges, and show that with future improvements, this device is suitable for future quantum-enabled applications. First, we theoretically and experimentally demonstrate a dynamic, strain-mediated coupling between the spin and orbital degrees of freedom of the NV center and the driven mechanical motion of a single-crystal diamond cantilever. We employ Ramsey interferometry to demonstrate coherent, mechanical driving of the NV spin evolution. Using this interferometry technique, we present the first demonstration of nanoscale strain imaging, and quantitatively characterize the previously unknown spin-strain coupling constants. Next, we use the driven motion of the cantilever to perform deterministic control of the frequency and polarization dependence of the optical transitions of the NV center. Importantly, this experiment constitutes the first demonstration of on-chip control of both the frequency and polarization state of a single photon produced by a quantum emitter. In the final experiment, we use mechanical driving to engineer a series of spin "clock" states and demonstrate a significant increase in the spin coherence time of the NV center. We conclude this thesis with a theoretical discussion of prospective applications for this device, including generation of non-classical mechanical states and spin-spin entanglement, as well as an evaluation of the current limitations of our devices, including a

possible avenues for improvement to reach the regime of strong spin-phonon coupling.

Contents

List of Figures

Chapter 1

Introduction

> "Welcome to a new year at Hogwarts! Before we begin our banquet, I would like to say a few words. And here they are: Nitwit! Blubber! Oddment! Tweak!" - Albus Dumbledore

Quantum information science has largely driven the remarkable developments in the control of individual quantum systems for the past 3 decades. Quantum information science uses the strange and unique features of quantum mechanics, such as superposition and entanglement, to perform tasks that are infeasible or impossible to accomplish with any known classical algorithm. Within the past few years, researchers have been able to develop highly complex quantum systems while retaining high levels of coherence and control. There are now experimental demonstrations of small, programmable quantum computers [4, 5] operating with fault tolerance [6], as well as quantum simulators probing many-body quantum phase transitions with more than 50 qubits [7, 8]. As the quest for a universal quantum computer progresses, the choice of hardware platform and architecture will become more significant, both in terms of cost and efficiency. Therefore, it is useful to breakdown the necessary components of a quantum computer and evaluate current technologies and how they might be improved.

The fundamental building block of a quantum computer is the quantum bit, or qubit. Like its classical analog, the qubit consists of two logical states, $|0\rangle$ or $|1\rangle$. Physically, these logical states correspond to two, well-isolated energy levels of a quantum system, such as the spin states of an electron. However, unlike its classical counterpart, the qubit can be in an arbitrary superposition of its two logical states

$$|\psi\rangle = \alpha\,|0\rangle + \beta\,|1\rangle \tag{1.1}$$

provided that $|\alpha|^2 + |\beta|^2 = 1$. In short, a classical bit is always 0 OR 1, whereas a qubit can be both 0 AND 1 at the same time. In general, if we have N qubits, there are 2^N possible states that can be assumed simultaneously. At first glance it appears that by using qubits, we have already gained a lot of processing power. However, when we perform a measurement of the qubits, we project the system into a single logical state and the superposition is destroyed. For instance, if we measure a qubit prepared in the state given by equation 1, then we will recover the state $|0\rangle$ with probability $|\alpha|^2$ or the state $|1\rangle$ with probability $|\beta|^2$. Now it appears that quantum computers do not afford us any more processing power, so how do quantum computers achieve parallel processing? The answer lies in quantum interference. By designing a quantum logic gate appropriately, superpositions can interfere with each other and generate a single output state that depends on all possible input states. Even more importantly, quantum gates can be designed so that their results are deterministic instead of probabilistic.

The potential power of a quantum computer can be seen by considering a 300 qubit quantum computer. A 300 qubit system can simultaneously assume 2^{300} states through quantum superposition. As it turns out, 2^{300} is larger than the number of particles in the universe. Therefore, a computer using every particle in the universe would be unable to match the potential power of a 300 qubit device. However, a real device will require

much more than 300 qubits, in order to account for errors induced by decoherence and relaxation. It is generally accepted that more than one thousand logical qubits will be required to achieve anything truly useful with a quantum computer. However, with only 50 logical qubits, a quantum computer may surpass the processing power of any classical computer. This limit has been dubbed quantum supremacy [9].

Another central resource for quantum information science is entanglement. Entanglement quantifies the correlations between quantum systems that collectively have a well-defined state, but individually do not have well-defined states. Another way to say this is that the total wavefunction of the system is not separable – it cannot be factored into a product state. To see this, consider the following two qubit unentangled state:

$$|\psi\rangle = \frac{1}{\sqrt{2}}(|0\rangle\,|0\rangle + |0\rangle\,|1\rangle) \tag{1.2}$$

Clearly, this $|\psi\rangle$ can be written as the product state

$$\begin{aligned} |\psi\rangle &= \frac{1}{\sqrt{2}}\,|0\rangle \otimes (|0\rangle + |1\rangle) \\ &= |\psi\rangle_1 \otimes |\psi\rangle_2 \end{aligned} \tag{1.3}$$

In this case, the dynamics of each qubit can be separated from each other and the state does not exhibit any quantum correlations. Now, consider the two qubit entangled state

$$|\Phi^+\rangle = \frac{1}{\sqrt{2}}(|0\rangle\,|0\rangle + |1\rangle\,|1\rangle) \tag{1.4}$$

Note that it is impossible to factor the total wavefunction, and hence it is inappropriate to discuss the state of the individual qubits. Although the states of the individual

qubits are unknown, they will exhibit correlations that have no classical analog. To see where these correlations arise, consider the result of a measurement of one of the qubits. For instance, if a measurement of the first qubit results in $|0\rangle$, then the second qubit is projected into the state $|0\rangle$ as well. Likewise, a measurement of the first qubit that results in $|1\rangle$ will project the second qubit into the state $|1\rangle$. If we prepare the entangled state and measure it many times, we find that the states of the two qubits will always be correlated. However, if you look at the measurement statistics of only one of the qubits, the results are random. This is the defining feature of quantum mechanics.

The immense parallel processing afforded by a quantum information processor offers several important applications relevant to the fields of cryptography, communication, simulation, and optimization. For instance, a quantum computer can efficiently find the prime factorization of large numbers using Shor's algorithm [10]. The RSA encryption scheme, which is commonly used in modern technology relies on the inefficiency of a classical computer to factor large numbers, and therefore could be potentially cracked by a quantum computer. In addition, a quantum information processor integrated into a quantum network could be use for secure communication, as guaranteed by the no-cloning theorem [11]. Perhaps the most appealing application that has emerged is quantum simulation [12], in which a small set of controllable quantum systems is used to simulate complicated, many-body dynamics, such as frustrated magnetism in an antiferromagnetic Ising model [13], many-body localization [14, 8, 15, 16, 17], or entanglement propagation in long-range interacting systems [18]. In current state of the art technologies, the number of qubits that can be reliably controlled is limited to about 50. As these systems scale to larger numbers of qubits, the choice of qubit platform will become highly relevant.

1.1 Qubit platforms

Although there are many physical systems that exhibit quantum effects, few actually make good qubit systems. The criteria for a good qubit were established by David DiVincenzo [19], and are listed below in a modified form

- State initialization of the qubit
- Long qubit coherence times
- Arbitrary manipulation of qubit
- Readout of the qubit states
- Entanglement with stationary and flying qubits
- Scalability to large numbers of qubits

In order for a qubit to be useful, it must be able to be initialized to any arbitrary state with high fidelity. Moreover, the qubit must exhibit long quantum coherence times. The coherence time of the qubit determines how long quantum information can be preserved. Consequently, the coherence time sets the upper bound on the number of quantum logic operations that can be performed before the qubit loses its memory. Additionally, in order to extract quantum information from the system, the qubit must have a mechanism that allows for high fidelity readout of the qubit states. In addition, the qubit must be able to entangle with "stationary" and "flying" qubits. A stationary qubit is used for storage and manipulation of quantum information, whereas a flying qubit propagates quantum information between nodes of the quantum information processor. In most cases, a stationary qubit is encoded in a matter system, such as an atom, and a flying qubit is encoded in a propagating degree of freedom, such as a photon. The final requirement

for a good qubit is that it can be scaled to large numbers within a system without compromising the other criteria.

The physical platforms that have emerged as good qubit candidates include trapped atomic ions [4], neutral atoms [20], superconducting circuits [5], quantum dots [21], and spins in the solid state [22]. Although all in principle can meet these requirements, there is no platform that excels in all aspects. In general, there is an inherent tradeoff between qubit coherence and the ability to rapidly manipulate the qubits. For instance, trapped ions and neutral atoms are hosted inside of a ultrahigh vacuum chamber and are thus very isolated from the environment, allowing for coherence times exceeding minutes. However, this isolation comes at a cost. It is very difficult to bring control fields in proximity to the atoms to manipulate the qubit states. On the other end of the spectrum, solid-state systems such as superconducting qubits or quantum dots can be rapidly manipulated (typically on ps timescales), but exhibit limited coherence times. The ideal qubit would combine long-lived quantum coherence with rapid manipulation. Currently, no single quantum system has emerged as the ideal qubit to address this issue.

1.2 Hybrid quantum devices

To address this paradoxical requirement, the quantum information community began developing hybrid quantum systems [23]. Indeed, a practical quantum device of the future will likely integrate multiple physical systems in a synergistic way, allowing the combined merits of the system to mitigate the weaknesses of its constituent components. For example, a quantum information processor may leverage the long coherence times of solid-state spins to store quantum information and the fast manipulation times of superconducting qubits to manipulate quantum information in a hybrid quantum memory. In order to construct a hybrid device, it is necessary to develop a universal quantum

data bus, which serves as an interface between differing components [24]. A universal quantum data bus is represented by a shared, external degree of freedom between the individual components. Quite often, the quantum bus corresponds to a flying qubit, such as photon or phonon. In such cases, the quantum bus can also be used to coherently shuttle quantum information over long distances.

The figure of merit for a good quantum bus and thus a good hybrid device is the so-called cooperativity [25], which compares the strength of the interaction between the qubits and the quantum bus to the dissipative interactions with the environment. Explicitly, the cooperativity is defined to be

$$C = \frac{g^2}{\Gamma_2 \gamma} \tag{1.5}$$

where g is the interaction strength between the qubit and quantum bus, Γ_2 is the qubit decoherence rate, and γ is the bus decoherence rate. In the high cooperativity regime, $C > 1$ and the qubit and quantum bus can coherently exchange energy with each other. In order to reach this regime, one needs to sufficiently isolate the qubit and quantum bus from the environment while allowing strong mutual coupling. Again, it appears that these requirements are at odds with each other. Nonetheless, there have already been demonstrations of hybrid devices operating in the high cooperativity regime, validating the hybrid approach [23, 26, 27, 28].

1.3 Hybrid mechanical devices

Traditionally, single photons have served as the primary interconnect between remote quantum systems [29]. Photons are natural carriers of quantum information, and can propagate over large distances without significant losses. Several experiments have now

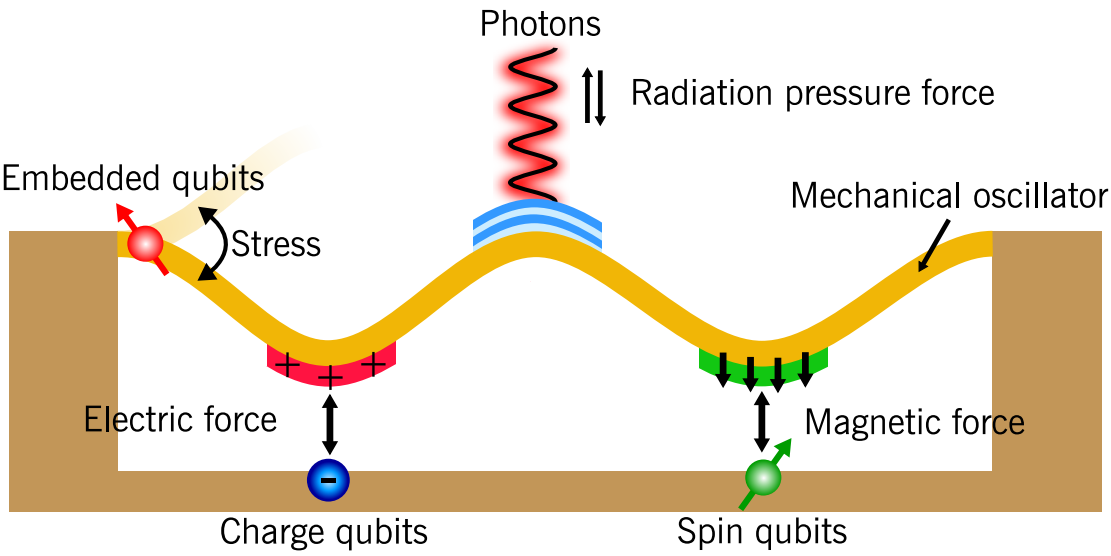

Figure 1.1: **A universal quantum bus based on a mechanical oscillator**. A mechanical oscillator can interface with a variety of qubits. For instance, a mechanical oscillator can interact with photons, charge qubits, spin qubits, and embedded qubits through radiation pressure, electrostatic interactions, magnetic dipole forces, and strain respectively.

used photonic interconnects for a variety of applications in quantum information science, such as loop-hole free Bell inequality violations [30], teleportation of quantum information between spatially separated matter qubits [31, 32], and quantum key distribution [33]. Typically, applications involving photonic quantum buses rely on quantum interference between photons emitted from each individual qubit. In order to achieve high visibility quantum interference, these photons must be indistinguishable [29]. As a result, transferring information between remote quantum systems of disparate energy scales remains an outstanding challenge, and may benefit from new types of quantum interfaces.

Mechanical oscillators in the quantum regime are an attractive solution to the challenges posed by traditional photonic interfaces due to their ability to coherently interact with a wide variety of quantum systems of differing energy scales [34, 35, 36]. For instance, mechanical systems can couple to photons through radiation pressure, charge qubits through the Coulomb interaction, spin qubits through magnetic dipole forces, or

internally embedded qubits through strain (fig.1.1). Indeed, the sensitive nature of mechanical oscillators have already enabled a host of applications in high precision metrology, ranging from detection of gravitational waves [37] to single electrons in a solid [38].

An important feature of these coupling mechanisms is that they are conservative, which allows for coherent transfer of quantum information. Consequently, a mechanical oscillator can be used as a quantum data bus to coherently couple quantum systems over an arbitrary energy scale, such as an optical photon ($\sim 10^{14}$ Hz) and a spin qubit ($\sim 10^{9}$ Hz). By the same token, phonons associated with a mechanical oscillator can extend over macroscopic distances, potentially allowing for long-range shuttling of quantum information [25, 39, 40, 41, 42].

The ability of a mechanical resonator to preserve quantum information is characterized by the quality factor Q, which determines the rate at which the resonator exchanges energy with the environment. The Q therefore determines the coherence length of a single phonon associated with the mechanical resonance, defined by $l_c = \frac{c_s Q}{\bar{n} f_m}$ where c_s is the speed of sound, $\bar{n}$ is the steady state thermal occupation number and f_m is the phonon frequency. For well designed mechanical oscillators, such as a phonon waveguide, phonons can attain a coherence length on the order of meters. The advent of novel nanofabrication techniques has led to the development of high-Q mechanical resonators over a broad range of frequencies, establishing hybrid mechanical devices as an attractive and feasible alternative to traditional quantum devices [43, 44, 45, 46, 47, 48, 49].

The synergy of hybrid mechanical architectures adds important and unique functionality to the standard toolbox of quantum devices. For instance, coherent control of qubits is traditionally carried out with electromagnetic fields that are produced by an antenna or waveguide near the system [50]. Mechanical degrees of freedom offer new ways to control qubit registers which can enable a variety of previously inaccessible applications. For example, as we discuss in this thesis, mechanically-induced crystal strain can en-

able coherent control of spin transitions that are forbidden by magnetic dipole selection rules [51, 52, 53]. Additionally, phonons associated with the vibrations of a macroscopic mechanical resonator can be used to deterministically generate long-range interactions between qubits [25, 39, 40, 41, 42].

From a mechanics perspective, qubits offer novel and powerful ways to generate and detect non-classical mechanical states due to their inherent nonlinearity. Specifically, nonlinear interactions allow for the preparation of non-Gaussian mechanical states, such as Schrodinger cat states or Fock states [54]. Realizing non-Gaussian mechanical states remains an important challenge, and has only recently been enabled by the development of hybrid qubit-mechanical devices [55, 56]. By the same token, qubits can then be used to probe the dynamics of non-Gaussian states, which may reveal the decoherence mechanisms associated with the poorly understood quantum to classical transition. In the context of quantum information science, it has been shown that non-Gaussian mechanical states are a necessary requirement for fault-tolerant quantum computing and secure quantum communication [57, 58, 59].

An important prerequisite for using a mechanical resonator as a quantum bus is the preparation of the resonator into a quantum state. Mechanical oscillators typically have resonance frequencies in the kHz-GHz regime, and under most experiment conditions, are thermally populated. The classical-to-quantum critical temperature is defined to be

$$T_c \approx \frac{\hbar\omega}{k_b} \tag{1.6}$$

where $\hbar\omega$ sets the energy scale of the physical system. It is typically difficult or impossible to passively cool a mechanical oscillator past the critical temperature. Dilution and adiabatic demagnetization refrigerators can reach temperatures as low as a few mK, which can passively cool GHz frequency oscillators to their quantum ground state [56].

However, in many cases due to experimental or financial constraints, it is desirable to operate at liquid helium temperatures (4 K) or even at ambient conditions, and therefore passive cooling is not an option.

In the past decade, the field of cavity optomechanics has pioneered efforts to actively cool mechanical oscillators to their quantum ground states using a technique similar to laser cooling atoms. A variety of mechanical oscillators spanning a wide range of frequencies (MHz to several GHz) have now been cooled to their ground state of motion [60, 61, 62, 63]. For instance, a microscale membrane oscillator coupled to a superconducting microwave cavity was cooled from an effective mode temperature of 4 K to 500 μK using optomechanical sideband cooling, well beyond the passive cooling limit [60]. Remarkably, the largest mechanical oscillator that has ever been cooled to a quantum state was a 43 nanogram SiN membrane oscillator [62]. This would correspond to a quantum state of a collection of roughly 10^{15} atoms. These pioneering experiments have validated the use of macroscopic mechanical oscillators as truly quantum elements in a hybrid quantum device.

The success of cavity optomechanics opened the door to architectures incorporating qubits, with the aim of addressing several outstanding challenges in quantum physics, ranging from quantum foundations to quantum sensing and quantum information science [34]. To date, hybrid mechanical systems have been realized with a variety of qubit platforms, including superconducting qubits [64, 56, 65, 66, 67], ultracold atoms [68, 69, 70], quantum dots [71, 72, 73], and solid-state defects [38, 74, 75, 51, 76, 77, 53, 78, 79, 80, 52, 81, 82, 79]. In the short amount of time since these efforts began, there have already been demonstrations of devices operating in the strong coupling regime. Notably, these experiments have been able to show single phonon control of a mechanical oscillator, and are positioned to generate arbitrary mechanical states [56, 67].

In this thesis, we will focus on the development of a hybrid mechanical device based

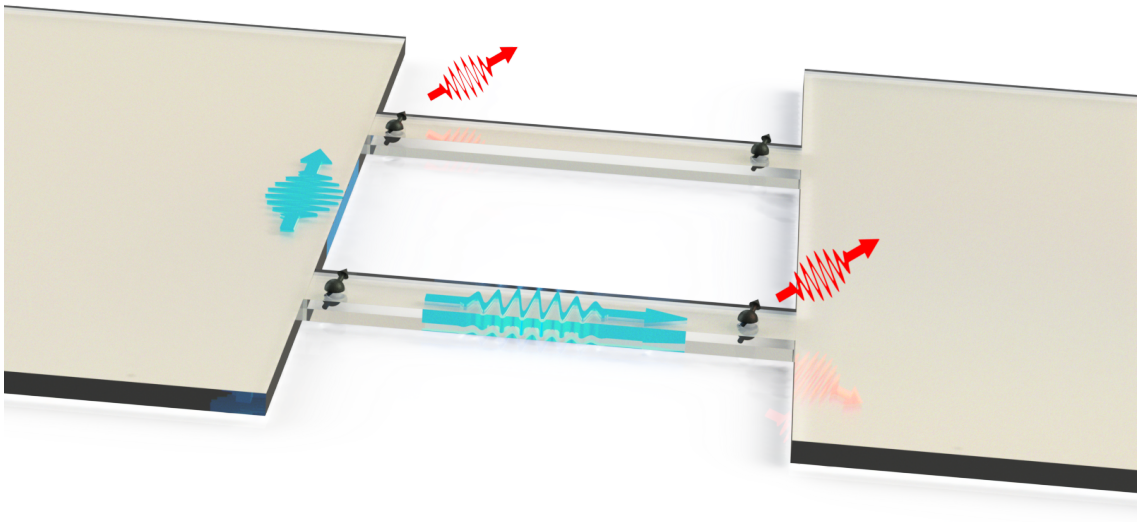

Figure 1.2: **Proposed hybrid device**. Spins (black) embedded in an array of mechanical oscillators interact through phonons (blue arrows). The device is integrated into a larger quantum network through photons (red arrows) emitted by the spins.

the nitrogen-vacancy (NV) defect center in diamond (fig.1.2). The NV center is a unique quantum system that exhibits the exquisite coherence properties of trapped atoms but in a more accessible solid-state setting. In particular, we will focus on a monolithic architecture in which single NV centers are embedded in a nanostructured diamond mechanical oscillator, and couple to mechanical motion through crystal strain. In this device, the electron spin of the NV center serves as a quantum memory and the phonons associated with a resonant mechanical mode of the diamond oscillator act as a quantum bus to generate multi-spin entanglement and to propagate information over macroscopic distances on a single chip. Using the coherent optical interface built into the electronic structure of the NV center, this device can be integrated within a larger quantum network

via a photonic channel, allowing for a modular architecture that is amenable for large scale quantum information processing [24].

There are a few important engineering challenges associated with the development of a strain-coupled NV-mechanical device. First, fabricating mechanical structures from diamond is challenging due to the chemically inert and robust nature of diamond. Second, the interaction of strain with the NV center is largely uncharacterized. In order to optimize device design, a thorough and quantitative understanding of the strain interaction is required. Finally, engineering high quality NV centers within these devices is an outstanding challenge, due to damage and impurities introduced to the diamond during fabrication. In this thesis, we aim to address all of these challenges and show that such a device is possible and can be further optimized for operation in the high cooperativity regime.

The outline for the rest of this dissertation is as follows. In Chapter 2, I will give a detailed discussion of the components of our device: the NV center and single-crystal diamond cantilevers. In particular, I will provide a full treatment of the crystal strain interaction which addresses several inaccuracies and shortcomings in previous works. In chapter 3, I will give a detailed overview of the primary experimental apparatus used in this thesis. In chapter 4, I will discuss experiments in which the mechanical motion of a diamond cantilever is used to drive the coherent dynamics of the NV spin. Using quantum control techniques, we demonstrate nanoscale strain imaging using many spins. In chapter 5, I will discuss experiments in which the mechanical motion of a diamond cantilever is used for deterministic control of the orbital states of the NV center. Remarkably, we use the strain-orbit interaction to demonstrate both frequency and polarization control of the optical transitions of a single quantum emitter. In chapter 6, we discuss experiments in which a resonant interaction between the NV spin and a diamond cantilever is used to isolate the spin from magnetic field fluctuations, significantly enhancing the spin co-

herence time. In chapter 7, we provide the theoretical framework for future experiments involving the NV center and diamond optomechanical crystals, including a discussion of phonon cooling, preparation of non-Gaussian mechanical states, spin-spin entanglement, and non-reciprocal spin-phonon interactions. Finally, in chapter 8, we will summarize the findings of this thesis and provide an outlook for future devices incorporating solid-state defects and mechanical resonators.

Chapter 2

A hybrid spin-mechanical device

> "Come on! You know... I wumbo, You wumbo, He she me... wumbo? Wumbo, wumboing, we'll have the wumbo, Wumborama... Wumbology, the study of wumbo? It's first grade, SpongeBob! " - Patrick Star

In this chapter, we will formally introduce the two components of our hybrid device: the NV center and diamond cantilevers. First, we will provide a brief overview of the optical and spin properties of the NV center, and demonstrate that the NV center meets several of the qubit criteria mentioned in chapter 1. Next, we will provide a detailed explanation of the physical and electronic structure of the NV center, including a full treatment of the Zeeman, Stark, and strain interactions. We will close the chapter with a discussion of the mechanical and elastic properties of our diamond cantilevers, along with a brief explanation of our diamond fabrication process.

2.1 The NV center in diamond

The NV center in diamond is an atomic-scale defect that balances the isolation of atomic systems with the strong interactions of solid-state quantum systems. The excel-

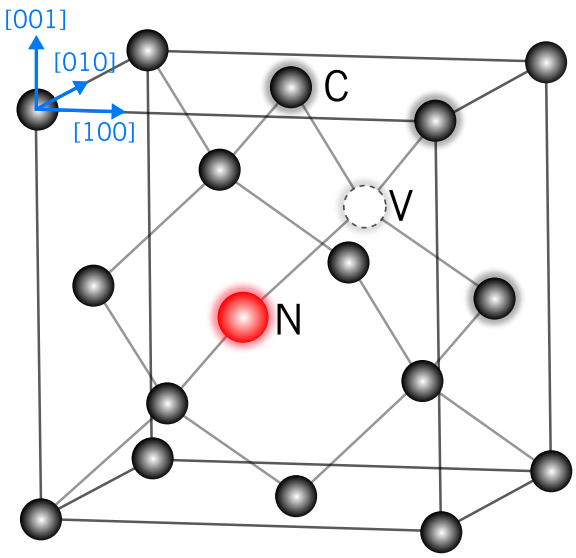

Figure 2.1: **The NV center in diamond**. The NV center is a point defect inside the carbon (black) diamond lattice, and consists of a substitutional nitrogen atom (red) adjacent to a lattice vacancy (white). The atoms that contribute to the electronic orbitals of the NV center are highlighted.

lent and robust coherence properties of the NV center combined with its sensitivity to a wide variety of external degrees of freedom make it an attractive system for applications ranging from quantum information science to quantum sensing of biological and condensed matter systems [83, 84, 85, 86, 87]. The electron spin of the NV center is remarkably isolated from its solid state environment, and exhibits long coherence times on the order of milliseconds even under ambient conditions [88, 89]. Importantly, the extended coherence time of the electron spin allows for coherent interactions with neighboring nuclear spins, such as ^{13}C, which can be used as quantum memories [90, 91]. In contrast with many other solid-state spin systems, the NV electron spin can be optically polarized and readout, mitigating the need for strong magnetic fields and cryogenic operation. An essential quality of the ground state spin levels of the NV center is the zero-field splitting of $D_0 = 2.87$ GHz (discussed in detail in this chapter), which allows

for high fidelity, coherent microwave manipulation of the spin levels with commercially available microwave sources. Moreover, the NV center contains a coherent, zero-phonon optical dipole transition that can be used for interfacing the electron spin with single photons [92, 93, 94, 95].

An important feature of the NV center is that its host crystal can be nanostructured to enhance the interactions between the NV center and photons or phonons without significantly reducing the coherence properties of the NV center. In the work presented here, the host diamond is fabricated into micron-scale mechanical resonators to enhance the coupling between single NV centers and acoustic phonons. This feature will be critical when trying to integrate the NV center into a distributed quantum network, which requires the use of flying qubits such as photons or phonons [24].

The remarkable properties of the NV center are in large part afforded by its host material: diamond [96]. Diamond is a semiconductor with a large bandgap of 5.5 eV. The bound states of the NV center reside deep within the bandgap of diamond, and thus experience negligible coupling to the valence and conduction bands. Moreover, diamond has a large Debye temperature, $T_D = 2200$ K, which results in a small thermal population of phonons even at room temperature, thereby suppressing significant phonon-mediated spin relaxation processes. Diamond's small intrinsic spin-orbit coupling also prevents unwanted spin flips during electronic transitions. In addition, advances in the engineering of synthetic diamond now allow for growth of single-crystal diamond substrates with 99.999% ^{12}C isotopic purity [88, 97], mitigating decoherence induced by fluctuating ^{13}C nuclear spins in the environment. Finally, diamond is a non-piezoelectric material due to its inversion symmetry. Low frequency acoustic phonons in piezoelectric materials can induce appreciable electric fields which can significantly affect the spin and optical coherences of an embedded defect.

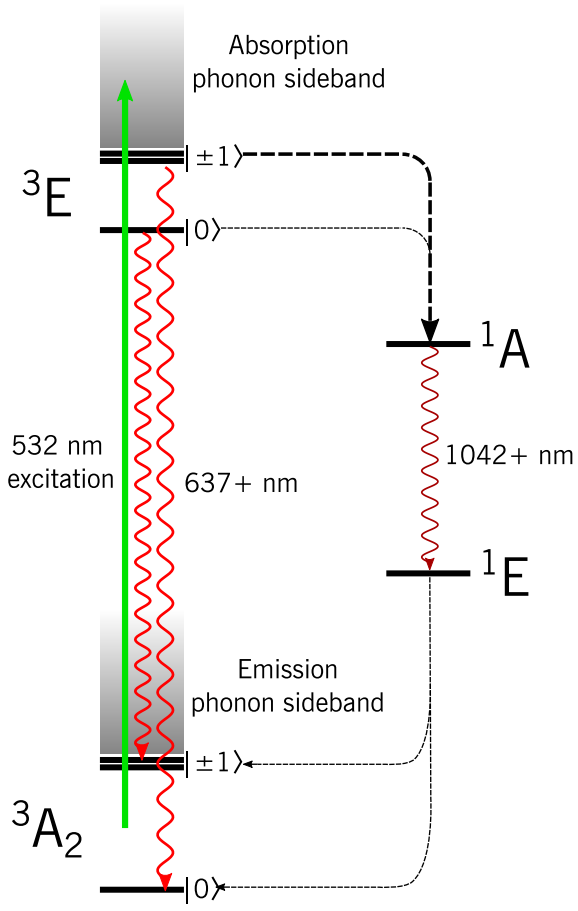

Figure 2.2: **Energy level diagram of the NV center**. The NV center can be off-resonantly excited through the absorption phonon sideband using 532 nm laser light. The NV center can radiatively decay to the ground state through emission of a photon into the ZPL or phonon sideband. However, the $m_s = \pm 1$ spin population can be transferred non-radiatively to the singlet states in an intersystem crossing. The singlet states are connected by a zero-phonon line at 1042 nm with a broad emission phonon sideband extending deep into the IR. The spin population from the singlet states is non-preferentially returned to the ground state in another intersystem crossing.

2.2 Structural, electronic, and optical properties of the NV center

Structurally, the NV center is a point defect in the diamond lattice in which a substitutional nitrogen atom is adjacent to a lattice vacancy. The electronic structure of the

NV center can be described using charge, spin and orbital degrees of freedom. There are currently three known charge states of the NV center: NV^-, NV^0, and NV^+ [98]. However, the negatively charged NV center has the most attractive quantum properties, and consequently is the one most commonly studied for quantum technologies. Throughout this thesis, we will refer to the negatively charged NV center as just "NV" and identify any other charge state as listed above.

There are six total electrons bound to the NV center: three electrons are associated with the three nearest-neighbor carbon atoms to the vacancy, two electrons are associated with the nitrogen atom, and one electron is donated from the diamond environment. These electrons are tightly bound to the four sp^3 dangling bonds surrounding the vacancy as shown on the right in fig. 2.1. Because each dangling bond can hold two electrons due to the Pauli exclusion principle, an NV center containing eight electrons would be a spin singlet with a fully symmetric orbital wavefunction, which is analogous to an atom with a completely filled shell. Therefore, the negatively charged NV center can be modeled as a two-hole defect as opposed to a six-electron defect [99]. It is convenient to use the two-hole representation due to the simplicity of constructing the NV wavefunctions, but one must be careful to take into account the positive charge of the hole when considering interactions, such as the Stark effect.

An important physical property of the NV center is its trigonal structure. As a point defect in the diamond lattice, the NV center breaks the translation symmetry of the crystal. Therefore, the symmetries of its physical structure will be determined by a collection of rotations and reflections. The particular set of rotations and reflections that represent the symmetry of the NV center are described by the C_{3v} symmetry group. As will be discussed in greater detail in a later section of this chapter, the properties of the NV electronic structure and interactions with external perturbations are intrinsically linked to the NV C_{3v} symmetry [99, 100].

Fig. 2.2 shows a simplified energy level diagram for the NV center at room temperature. The electronic ground state of the NV center is an orbital singlet/spin triplet, which is labeled $^3A_2$ for its symmetry properties under the C_{3v} group. The ground state is connected to an orbital doublet/spin triplet excited state, ^3E, through an electric dipole transition at 637 nm (471 THz). Under ambient conditions, electron-phonon interactions within the excited state manifold rapidly mix the orbital levels, averaging to an effective orbital singlet similar to the ground state [100]. In both the ground and excited states, the spin degeneracy is lifted via spin-spin interaction, and $|m_s = \pm 1\rangle$ are uniformly split from $m_s = 0$ accordingly to the Hamiltonian

$$H = DS_z^2 \tag{2.1}$$

, where D is the crystal-field or zero-field splitting and $S_z^2 = |1\rangle\langle 1| + |-1\rangle\langle -1|$. In the ground state, the zero-field splitting is approximately $D_0 = 2.87$ GHz and in the excited state, the zero-field splitting is approximately $D_{es} = 1.42$ GHz. In addition, the spin levels are affected by a variety of external fields, including magnetic [101, 102, 103], electric [104, 105], thermal [106, 107, 108], and strain fields [76, 109, 77, 51]. We will discuss these effects in greater detail in later sections of this chapter. We also note that at cryogenic temperatures (< 20 K), the orbital doublet nature of the excited state is preserved and the electronic structure becomes more complex due to spin-orbit and spin-spin interactions [100]. We will discuss the cryogenic NV center in section 2.9.

The ground to excited state transition can be directly excited with a coherent laser at 637 nm, or off-resonantly excited through an absorption phonon sideband (PSB). The phonon sidebands of the NV center originate from electron-phonon interactions with both acoustic and optical phonons which modulate the ground to excited state transition energy. As a result, the NV center exhibits a broad absorption spectrum, and can be

effectively excited using radiation from approximately 400-637 nm. In this thesis, we utilize a 532 nm laser for off-resonant excitation of the NV center. Under off-resonant excitation, the NV is promoted to a highly-excited vibrational level of the excited state, which decays rapidly ($\sim$ ps) to the vibrational ground state of the excited state. In essence, during off-resonant excitation the NV center down-converts a higher frequency photon to the resonant transition frequency by absorbing a phonon. If the NV center is resonantly pumped, no phonons are absorbed, and hence the resonant excitation line is referred to as the zero-phonon line (ZPL). It is important to note that these optical transitions are spin conserving, even under off-resonant excitation.

From the excited state, the NV center can decay radiatively back to the ground state levels through spontaneous emission. The NV center can either emit a photon directly into the ZPL at 637 nm, or emit a photon into the broad phonon sideband, which extends from approximately 638-850 nm. The ZPL accounts for approximately 3% of the total emission spectrum [100]. For photonic applications, this is a cause for concern, as photons emitted into the phonon sideband are not coherent and thus cannot be used in most experiments. Consequently, there has been a lot of experimental effort toward improving this ratio through the use of optical cavities. For the experiments in this thesis, we do not discriminate between ZPL and PSB photons and hence this ratio is not so important. However, the relative weakness of the ZPL will come into play in our discussion of phonon cooling, which is described in chapter 7.

An important aspect of the optical cycle of the NV center is that it is spin dependent. As we discuss in the following section, the NV electronic structure facilitates an all-optical spin polarization mechanism as well as spin-dependent fluorescence readout mechanism[96, 110]. Using these features, we can perform optically detected magnetic resonance of the ground state spin levels and perform single qubit gates.

2.3 Optical spin initialization

As mentioned in chapter 1, an important requirement for a good quantum system is the ability to initialize a quantum state. At thermal equilibrium for temperatures greater than 140 mK, the NV center is in its electronic ground state, and the spin is evenly distributed throughout the three spin levels. However, the spin of the NV center can be initialized with high fidelity using an optical pumping technique. Remarkably, this technique can be used to polarize the spin with high fidelity even under ambient conditions. This is in stark contrast with other spin qubits, which require strong magnetic fields and cryogenic conditions to overcome thermalization [111].

The spin polarization technique relies on the fact that the ground to excited state transition is not fully closed. Approximately 40% of the time, the $m_s = \pm 1$ spin population enters an intersystem crossing (ISC) and is non-radatively transferred to a metastable singlet manifold with an effective lifetime of 450 ns. The spin population within the singlet state is then returned to the ground state through another non-radiative ISC. The spin selectivity of the second ISC has not been firmly established, however recent measurements indicate that it is not spin-selective. Nonetheless, after several optical cycles, the spin will be mostly initialized to the $m_s = 0$ spin level of the ground state [110].

Experimentally, we initialize the spin by continuously illuminating the NV center with 532 nm laser light for several microseconds, and achieve a intialization fidelity into $|0\rangle$ of approximately 80-90%. The limits of the initialization fidelity have not been established, however charge-state hopping between NV^0 and NV^- seems to be the most commonly cited source of infidelity [112]. There has been significant research into improving the fidelity of this technique through application of different wavelength excitation lasers, with the goal of being able to stabilize the negative charge state [113]. In section 2.9.4,

we will give a more detailed discussion of the dynamics of the NV center during this initialization cycle and discuss possible avenues for improvement.

At cryogenic temperatures, the NV center can be resonantly excited through a spin-conserving transition to the ^3E manifold. Due to spin-spin interaction within ^3E, there is a small probability for the spin to flip, and upon spontaneous emission, the NV center can relax to a different spin level of the ground state. After several excitation cycles, the spin can be initialized with near-perfect fidelity [114].

2.4 Optical spin readout

Interestingly, the same mechanism that allows for spin initialization also allows for optical readout of the spin states. Due to the non-radiative nature of the ISC and the relatively long lifetime of the metastable states, the NV will exhibit diminished fluorescence when prepared in $m_s = \pm 1$ compared to $m_s = 0$. The fluorescence contrast between the spin states is approximately $PL_{\pm 1}/PL_0 \sim 70\%$, but can vary significantly across NV centers. To read out the spin, we apply a short pulse of 532 nm light that is shorter than the lifetime of the singlet manifold, (typically 350 ns) and count the number of photons measured. Due to the modest fluorescence contrast, we must perform the measurement many times to build up enough statistics to distinguish the spin states.

There are several factors that currently limit the spin readout fidelity. The primary limiting factor is the low relative strength of the ISC rate to the spontaneous emission rate [110]. If $m_s = \pm 1$ population was immediately shelved to the singlet states, then perfect fluorescence contrast could be achieved. On the other hand, the short lifetime of the singlet states limits the spin readout time to a few hundred ns, after which the spin has been significantly polarized into $m_s = 0$. Several techniques have been established to address these weaknesses and achieve higher readout fidelity or faster spin readout, which

include spin-to-charge conversion [115, 116, 117] and excitation of the infrared ZPL in the singlet states [118]. We note that at cryogenic temperatures, single shot readout of the spin levels can be achieved through resonance fluorescence techniques [114].

2.5 Optically detected magnetic resonance

The optical initialization and readout mechanism of the NV center allow for optically detected magnetic resonance (ODMR) spectroscopy of the ground state spin levels, which has been the workhorse of most NV related studies [119]. The standard ODMR protocol is continuous-wave (CW) electron spin resonance (ESR) (see fig. 2.3). During CW ESR, we illuminate the NV center with 532 nm laser light and near resonant microwave fields and monitor the NV fluorescence. To identify the spin transitions, we sweep the frequency of the applied microwave field. When the microwaves are brought into resonance with a spin transition, the NV fluorescence diminishes as a result of depopulating the $m_s = 0$ state.

In fig. 2.3, we demonstrate continuous-wave (CW) ODMR on a single NV center in the presence of an external magnetic field. Due to the Zeeman effect, the $m_s = \pm 1$ spin levels are split in energy by an amount proportional to the applied magnetic field along the NV symmetry axis, $\Delta_B = 2\gamma_{NV} B_z S_z$. We observe two dips split by approximately 25 MHz in the ODMR signal corresponding to the $|0\rangle \rightarrow |-1\rangle$ and the $|0\rangle \rightarrow |1\rangle$ transitions. The spectral position of the ESR lines are sensitive to a variety of external fields, including magnetic, electric, thermal and strain fields. By monitoring the positions of these transitions with ODMR, we can use the NV center as a nanoscale sensor of external fields [102, 88, 120, 121, 75, 74, 106, 107, 108, 104, 105, 76, 77, 82, 51].

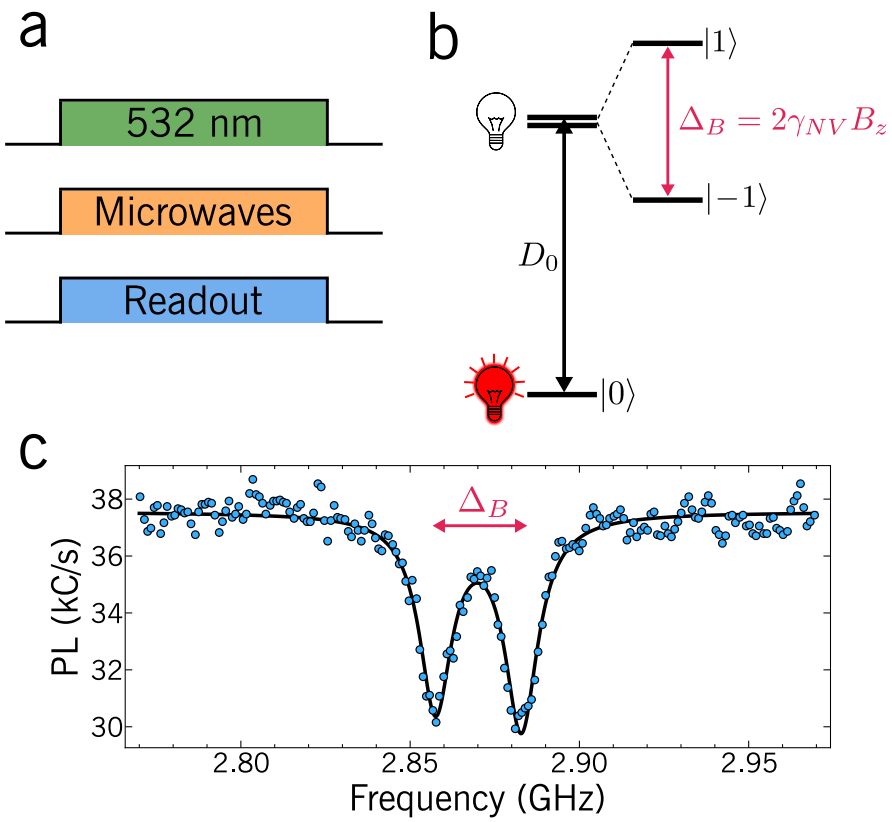

Figure 2.3: **ODMR of a single NV center**. a) Experimental protocol for continuous wave ODMR. b) Energy level diagram for the ground state spin levels. In the absence of any external fields, $|m_s = \pm 1\rangle$ are degenerate in energy and split from $|0\rangle$ by $D_0 = 2.87$ GHz. In the presence of a static magnetic field aligned to the NV axis, B_z, $|\pm 1\rangle$ split by an amount $\Delta_B = 2\gamma_{NV}Bz$. Due to the intersystem crossing, the NV fluoresces more when the spin is prepared in $|0\rangle$, as indicated by the lightbulbs. c) Experimental continuous-wave ODMR data (blue dots) shows a Zeeman splitting $\Delta_B = 25$ MHz with a fluorescence contrast of approximately 21%.

2.6 Coherent spin manipulation with microwaves

The electronic spin of the NV center can be coherently manipulated with near-resonant microwave magnetic fields. In the presence of a static magnetic field aligned to the NV axis, the $|\pm 1\rangle$ degeneracy is lifted, allowing for selective addressing of the $|0\rangle \leftrightarrow |\pm 1\rangle$ transitions. In order to isolate these transitions, the microwave Rabi frequency must be much smaller than the frequency difference between $|\pm 1\rangle$, $\Omega \ll 2\Delta_B$. In

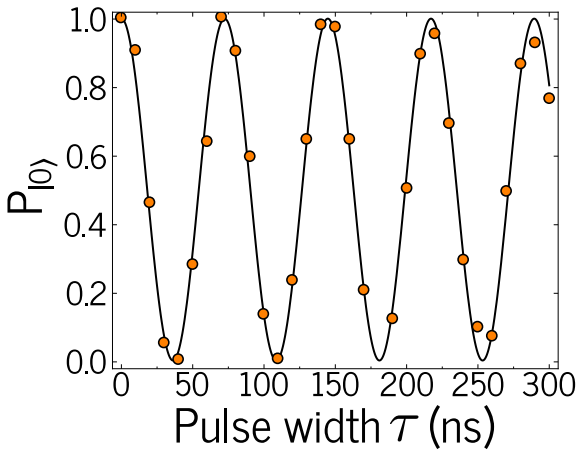

Figure 2.4: **Microwave Rabi oscillations**. Experimental data showing Rabi flopping on the $|0\rangle \leftrightarrow |1\rangle$ transition with a Rabi frequency of 13.8 MHz

this limit, we may define a spin qubit spanned by $\{|0\rangle, |-1\rangle\}$ or $\{|0\rangle, |1\rangle\}$. Let us now consider a single spin qubit interacting with a monochromatic microwave field

$$H = \frac{\omega_0}{2}\sigma_z + \Omega\cos(\omega_\mu t + \phi)\sigma_x \tag{2.2}$$

where ω_0 is the qubit frequency, ω_μ is the microwave frequency, and ϕ is a controllable microwave phase. In the interaction picture, the Hamiltonian becomes

$$H_I = \frac{\Omega}{2}\left(\sigma^+ e^{i(\delta t+\phi)} + \sigma^- e^{-i(\delta t+\phi)}\right) \tag{2.3}$$

where we have made the rotating wave approximation (RWA) and defined the microwave detuning $\delta = \omega_0 - \omega_\mu$. To solve for the qubit dynamics, we move into another frame where the Hamiltonian is time independent, and find

$$\begin{aligned} H_R &= -\frac{\delta}{2}\sigma_z + \frac{\Omega}{2}(\cos(\phi)\sigma_x - \sin(\phi)\sigma_y) \\ &= \frac{\Omega_R}{2}\sigma_R \end{aligned} \tag{2.4}$$

where $\Omega_R = \sqrt{\delta^2 + \Omega^2}$ is the generalized Rabi frequency, $\sigma_R = \frac{-\delta\sigma_z + \Omega\sigma_\phi}{\Omega_R}$ is the generalized rotation operator, and $\sigma_\phi = \cos(\phi)\sigma_x - \sin(\phi)\sigma_y$. Clearly, we can create any arbitrary superposition of the qubit states, $|\psi\rangle = \cos\left(\frac{\theta}{2}\right)|0\rangle + e^{i\varphi}\sin\left(\frac{\theta}{2}\right)|1\rangle$ by adjusting the microwave interaction time, the microwave detuning, and the microwave phase. For a resonant microwave field, we see that $\theta = \Omega_R\tau$ and $\varphi = \phi - \pi/2$, where τ is the microwave pulse length.

In figure 2.4, we demonstrate high-fidelity Rabi flopping on the $|0\rangle \leftrightarrow |1\rangle$ transition. The spin is first initialized into $|0\rangle$ via optical pumping. After applying a resonant microwave pulse of length τ, the spin is read out using spin-dependent fluorescence measurements. From fits to the data, we extract a Rabi frequency of approximately $\Omega_R/2\pi = 13.8$ MHz.

2.7 Hyperfine structure

As mentioned in the introduction of this chapter, the NV center can coherently interact with nearby nuclear spins in the diamond lattice. Because nuclear spins interact very weakly with their environments, they typically have very long coherence times, and are attractive candidates for a quantum memory. Indeed, several groups have now used nuclear spins to store quantum information that was initially prepared in the NV electron spin, leading to enhanced quantum sensing [122, 123], multipartite entanglement [124], and decoherence free quantum memory registers [90]. The electron spin of the NV interacts with nuclear spins through the hyperfine interaction [125]:

$$H_{hf} = \mu_s\mu_n\frac{8\pi|\psi_s(r_n)|^2}{3}\mathbf{S}\cdot\mathbf{I} + \langle\frac{\mu_s\mu_n}{r^3}\left(\mathbf{S}\cdot I - 3(\hat{r}\cdot\mathbf{S})(\hat{r}\cdot\mathbf{I})\right)\rangle \tag{2.5}$$

The first term is called the contact interaction, and is proportional to the electron

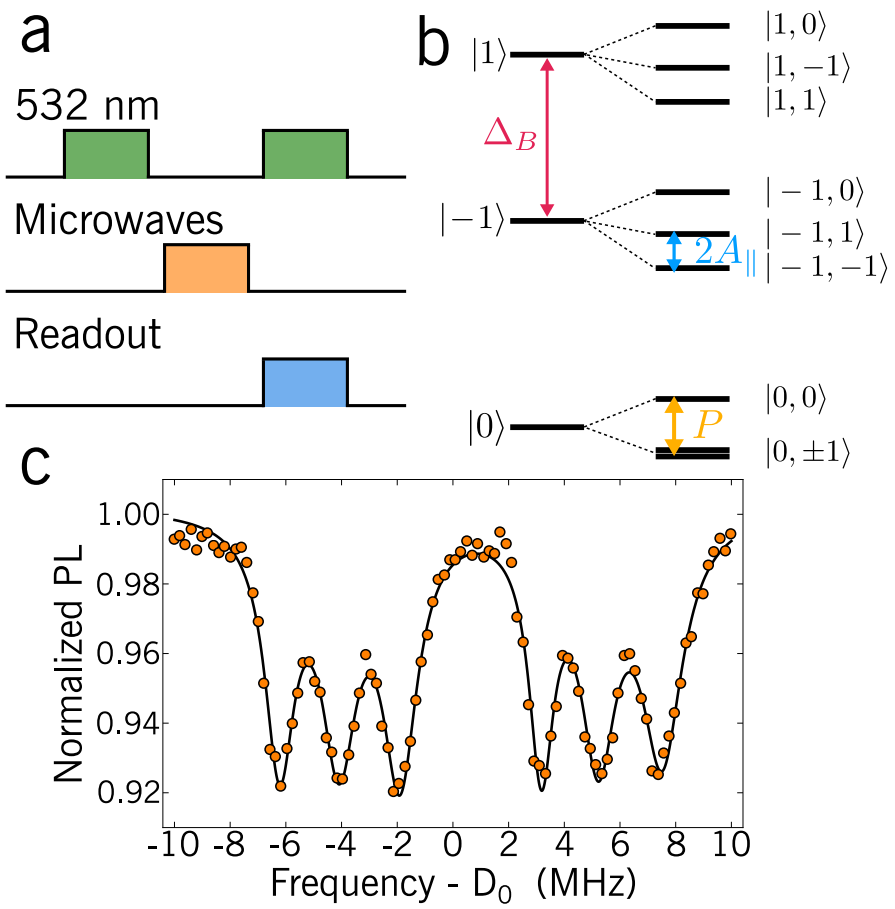

Figure 2.5: **^{14}N hyperfine structure**. a) Experimental sequence for pulsed ODMR spectroscopy. b) NV hyperfine structure for a ^{14}N nuclear spin. States are denoted by $|m_s, m_I\rangle$. c) Pulsed ODMR spectroscopy of the NV center showing the triplet hyperfine structure.

spin density at the site of the nuclear spin. The second term is the dipolar coupling between the two spins. The overall effect of this Hamiltonian is that the electron spin feels an additional magnetic field that is dependent on the spin state of the nuclear spin. The most common nuclei that couple to the NV are ^{14}N, ^{15}N, and ^{13}C [125]. In this thesis, we will only discuss hyperfine coupling to ^{14}N, which has a nuclear spin $I = 1$ [126]. The zero-field Hamiltonian for the NV center including hyperfine interaction with

^{14}N can be written as

$$H_{hf} = D_0 S_z^2 + P I_z^2 + A_\parallel S_z I_z + A_\perp (S_x I_x + S_y I_y) \tag{2.6}$$

where $A_\parallel = -2.16$ MHz and $A_\perp = -2.62$ MHz are the axial and transverse hyperfine couplings for the ground state [127, 128]. The axial hyperfine interaction produces an effective magnetic field $B_{eff} = A_\parallel m_I$ along the NV symmetry axis. The transverse hyperfine interaction induces electron-nuclear spin flip-flops when the electron and nuclear spins are near resonant. Similar to the NV electron spin, the ^{14}N nuclear spin has a preferred quantization axis at zero field which is set by the nuclear quadrupole splitting $P = -4.945$ MHz. The quadrupole interaction arises from an interaction between a nuclear spin with $I > 1/2$ and an electric field gradient. In the case of the NV center, the electric field gradient is produced by the combined charge distribution of the nuclei and electrons. We note that the ground state hyperfine interaction is purely a dipolar effect, since the ground state spin density does not overlap with the nitrogen wavefunction. However, the excited state contains a strong contact interaction leading to an axial hyperfine coupling of $A_\parallel = -40$ MHz [100, 129]. As we discuss later in this chapter, strain can mix the ground and excited state orbitals, which should increase the hyperfine interaction in the ground state.

An energy level diagram of the NV center with hyperfine interaction is shown in fig. 2.5 with eigenstates labeled by $|m_s, m_I\rangle$. To characterize the hyperfine interaction, we perform pulsed ODMR (fig. 2.5 a.), which mitigates power broadening of the ODMR signal from the microwaves and 532 nm laser [130]. To perform pulsed ODMR, we initialize the spin with a 532 nm laser pulse, and then apply a low power microwave pulse of a fixed duration to the NV center, and then readout the spin states. The microwave power is chosen such that the pulse bandwidth satisfies $\Omega_R \ll A_\parallel$, allowing us

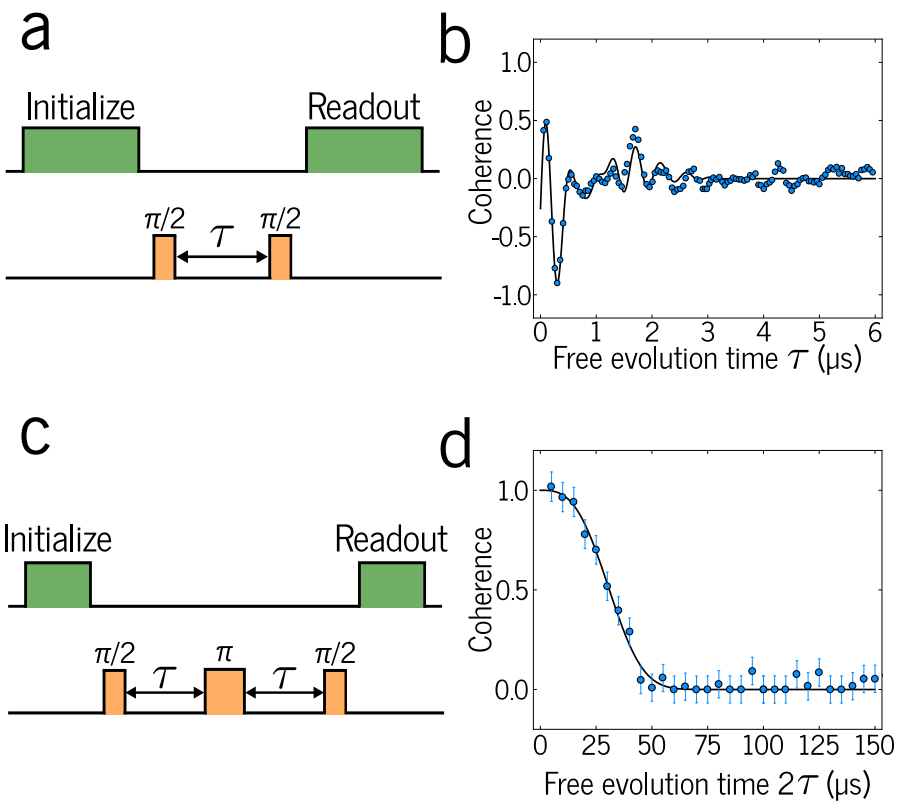

Figure 2.6: **Measurement of T_2^* and T_2.** a) Pulse sequence for a Ramsey experiment. b) Experimental Ramsey signal for a single NV center with inhomogeneous coherence time $T_2^* = 1$ μs. c) Pulse sequence for a spin-echo experiment. d) Experimental spin-echo signal for the NV in b) with homogeneous coherence time $T_2 = 34$ μs.

to resolve the hyperfine structure. Moreover, if we choose the duration of the microwave pulse such that on resonance we get a π pulse, we should achieve maximum fluorescence contrast. In the pulsed ESR data shown in fig. 2.5 c., we apply a weak magnetic field to split $m_s = \pm 1$. The data shows a triplet hyperfine structure associated with the $|0, m_I\rangle \leftrightarrow |\pm 1, m_I\rangle$ transitions, with a hyperfine splitting $A_\parallel = -2.16$ MHz.

2.8 Spin coherence

In our proposed device, the spin of the NV center will serve primarily as a quantum memory. The ability to store quantum information is given by the coherence time, T_2,

which is how long the qubit can retain information about a coherent superposition. The central decoherence mechanism for the NV center is dephasing due to noisy fluctuations of the qubit frequency [131]. The effect of dephasing can be modeled by the simple Hamiltonian

$$H = \frac{\omega_0 + \delta\omega(t)}{2}\sigma_z \tag{2.7}$$

where ω_0 is the bare qubit frequency and $\delta\omega(t)$ represents the coupling to some noisy field. For a qubit initialized onto the x axis of the Bloch sphere, the density operator in the rotating frame after a free evolution period of length τ can be written as

$$\rho(\tau) = \frac{1}{2}\left[|0\rangle\langle 0| + |1\rangle\langle 1| + e^{-i\int \delta\omega(t')dt'}|0\rangle\langle 1| + e^{i\int \delta\omega(t')dt'}|1\rangle\langle 0|\right] \tag{2.8}$$

where the has acquired a relative phase $\varphi(\tau) = \int_0^\tau \delta\omega(t')dt'$. It is important to note that this only holds for a single measurement of the qubit. In order to reconstruct the density matrix, we must repeat the experiment several times. Therefore, the measured state is given by the ensemble average and the relative phase is given by

$$\varphi(\tau) = \left\langle \int_0^\tau dt'\delta\omega(t') \right\rangle \tag{2.9}$$

If the noise is Gaussian, then the density operator can be written as

$$\rho(\tau) = \frac{1}{2}\left[|0\rangle\langle 0| + |1\rangle\langle 1| + e^{-\langle\varphi^2(\tau)\rangle}(|0\rangle\langle 1| + |1\rangle\langle 0|)\right] \tag{2.10}$$

and $\langle\varphi^2(\tau)\rangle = \int_0^\tau dt' \int_0^\tau dt''\langle\delta\omega(t')\delta\omega(t'')\rangle$. If the measurement time is sufficiently long compared to the correlation time of the noise, we can extend the bounds of the integrals to infinity, allowing us to express the relative phase in terms of the power spectral density

of the noise, $\mathcal{S}(\omega)$:

$$\langle\varphi^2(\tau)\rangle = \frac{1}{2\pi}\int_{-\infty}^{\infty} d\omega \mathcal{S}(\omega)\frac{F(\omega,\tau)}{\omega^2} \tag{2.11}$$

where $F(\omega,\tau)$ is a filter function for the noise which is determined by the measurement sequence used to determine the coherence. The coherence of the qubit is simply a measure of how much the qubit has remained in an eigenstate of σ_x, and therefore can be defined as $\mathcal{C}(\tau) = \mathrm{Tr}[\sigma_x\rho(\tau)]$.

In the case of simple white noise, $\delta\omega$ is delta correlated, and the coherence decays exponentially,

$$\mathcal{C}(\tau) = e^{-\Gamma\tau} \tag{2.12}$$

where Γ is the decay rate, and is given by the integrated noise power over all frequencies within the passband of the filter function. In practice, the noise spectral density is not uniform, which can lead to more complex coherence decays [132].

To measure the NV spin coherence, we perform a Ramsey measurement [133] in the $\{|0\rangle, |-1\rangle\}$ spin basis, as shown in fig. 2.6 a. The spin is first initialized into $|0\rangle$ with a 532 nm laser pulse. A microwave $\pi/2$ pulse initializes the spin onto the x-axis of the Bloch sphere, and then spin is allowed to freely evolve for time τ. After the free evolution period, we apply another $\pi/2$ pulse to project the qubit back onto the z axis, essentially converting the relative phase acquired into a population difference. We then readout the spin populations via spin-dependent fluorescence. In fig. 2.6 b., we show a typical Ramsey signal for a single NV center. In this case, the coherence decays according to $\mathcal{C}(\tau) = e^{-(\tau/T_2^*)^2}$ where $T_2^* = 1$ μs. In addition, there are a series of oscillations imprinted onto the coherence signal corresponding to beating of the different hyperfine states. Our microwave pulse populates all three hyperfine levels, each with a different microwave

detuning. A fit to the data yields the expected hyperfine coupling $A_{\parallel} = 2.16$ MHz.

In a Ramsey measurement, the spin is sensitive to noise at all frequencies. In particular, the spin decoherence is dominated by low frequency, quasi-static noise. For a lack of a better term, the coherence time for a Ramsey experiment is denoted the inhomogeneous coherence time, T_2^*. T_2^* is typically limited to tens of microseconds for NV centers in bulk diamond, but quickly degrades to microsecond or worse for near-surface NV centers [131].

A qubit can be decoupled from slowly varying noise through the application of a spin-echo pulse, as shown in fig. 2.6 c. If a π pulse is inserted symmetrically into the free evolution period of the qubit, the phase acquired in the second free evolution period should cancel out the phase acquired in the first, thereby extending the qubit coherence time. With the addition of more pulses, the spin can decouple from higher frequency noise sources [134, 135, 136]. This technique of applying spin-echo pulses is called dynamical decoupling [137]. The coherence time of the qubit under dynamical decoupling is called the homogeneous coherence time, T_2.

In fig. 2.6 d., we show an experimental spin-echo coherence measurement on the same NV shown in fig. 2.6 b. The spin coherence time has been extended to $T_2 = 34$ μs. Notably, the oscillations due to the static, microwave detuning of the hyperfine states have been removed. Moreover, the spin coherence is now described by an $e^{-(t/T_2)^3}$ decay envelope, suggesting that the coherence is limited by the surrounding nitrogen spin bath [132].

We can see the effect of dynamical decoupling by considering the effect of the filter function on $\mathcal{S}(\omega)$. In a Ramsey experiment, the filter function is given by

$$F(\omega, \tau)/\omega^2 = \frac{4\sin^2\left(\frac{\omega\tau}{2}\right)}{\omega^2} \tag{2.13}$$

The cut-off frequency of the Ramsey filter function is determined by the total evolution time τ. Below the cutoff frequency $1/\tau$, the Ramsey filter function is approximately constant, and hence the qubit is highly susceptible to noise from DC to $1/\tau$. Under dynamical decoupling, a periodic sequence of π pulses are applied to the qubit which is interleaved with a series of free precession periods of length τ. The filter function for an N pulse decoupling sequence for a total evolution time $T = N\tau$ can be written as

$$F_N(\omega, T)/\omega^2 = \frac{2\sin^2\left(\frac{\omega T}{2}\right)\left(1 - \sec\left(\frac{\omega T}{2N}\right)\right)^2}{\omega^2} \tag{2.14}$$

In contrast with the Ramsey filter function, the N-pulse filter function is approximately zero at low frequencies. Moreover, the filter function contains a series of narrow passbands at odd harmonics of $1/\tau$ which decay with increasing harmonic number. This feature of can be used for narrow-band sensing of time-varying fields. As the number of pulses increases, the qubit becomes decoupled from higher frequency noise and the passbands narrow.

An alternative way to think about dynamical decoupling is in the time domain through the toggling function, $f(t, \tau)$, which is a binary function that switches between the values of -1 and 1 when a π pulse is applied. The toggling function can be understood as the time domain representation of the filter function.

$$F(\omega, \tau) = \frac{\omega^2}{2}\left|\int dt f(t, \tau) e^{i\omega t}\right|^2 \tag{2.15}$$

Therefore, the phase acquired in a dynamical decoupling experiment can be written in the time domain as

$$\varphi(T) = \left\langle \int_0^T dt' \delta\omega(t') f(t', T) \right\rangle \tag{2.16}$$

For example, in the case of the spin-echo (or Hahn echo) experiment showed in fig. 2.6 c., the spin coherence obeys

$$\mathcal{C}(\tau) = \exp\left[\int_0^\tau dt' \int_0^\tau dt'' \langle \delta\omega(t')\delta\omega(t'')\rangle - \int_\tau^{2\tau} dt' \int_\tau^{2\tau} dt'' \langle \delta\omega(t')\delta\omega(t'')\rangle\right] \tag{2.17}$$

Using dynamical decoupling, the spin coherence time of the NV center has been extended to near one second at liquid nitrogen temperatures [138], and can be several milliseconds at ambient conditions [88, 97]. In addition to extending coherence, dynamical decoupling can be used to quantitatively probe the environment of the NV center [131, 139, 140]. In chapter 4, we use this result to coherently sense the mechanical motion of a diamond cantilever. In chapter 6, we use dynamical decoupling to determine the leading sources of decoherence for a mechanically-dressed spin state.

2.9 The molecular model of the NV center

In this section, we will give a more detailed description of the NV electronic structure. In particular, we will formally introduce the molecular model of the NV center [100, 99], and show how it can be used to determine the energy fine structure as well as describe the interactions with external perturbations. Using this model, we provide for the first time a complete description of the interaction of crystal strain with the spin and orbital degrees of freedom of the NV center. An understanding of this interaction is critical to understanding the internal processes of the NV center, such as the intersystem crossing [110]. In a broader context, understanding this interaction will be essential when searching for other defects which may integrated into hybrid mechanical systems.

In the experiments described in this thesis, we are interested in quasi-static processes

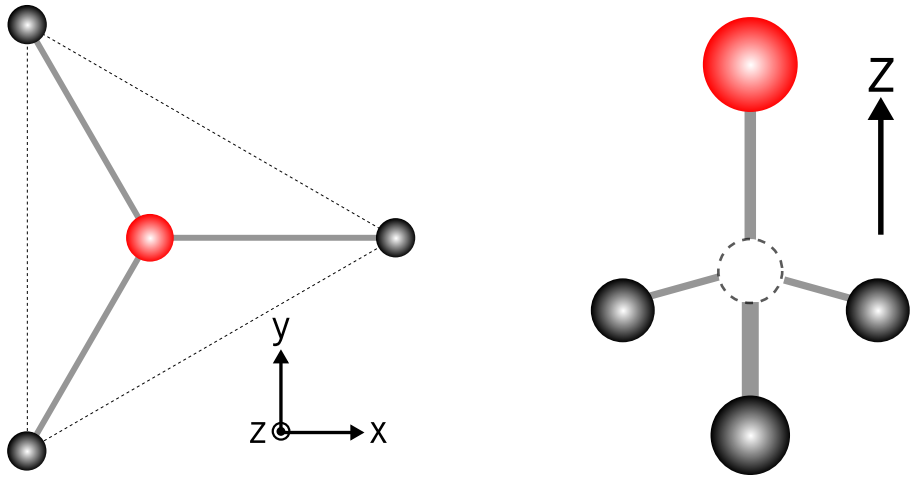

Figure 2.7: **NV coordinate system**. The NV z axis is along the nitrogen-vacancy bond, and can point along any four of the [111] crystal directions. In the calculations that follow, we assume the standard defect orientation where $z \parallel [111]$, $x \parallel [\bar{1}\bar{1}2]$, and $y \parallel [1\bar{1}0]$.

of the NV center, where the electrons move instantaneously with respect to the nuclei. In this limit, we may describe the electronic wavefunctions in the Born-Oppenheimer approximation, which allows us to separate the complicated many-body interactions between the electrons and nuclei. This will be especially important in our derivation of the crystal strain interaction.

As a crystal defect, the NV center reduces the cubic symmetry of the diamond crystal. The reduced symmetry group which describes the trigonal structure of the NV center is the C_{3v} point group (see Appendix A). In the case of the NV center, the symmetry point is at the site of the vacancy. The symmetry axis of the NV center, or NV axis, is a line passing through the nitrogen atom and vacancy. The C_{3v} point group contains 6 symmetry elements or operations under which the NV structure is preserved: $\{E, C_3, C_3^2, \sigma_v^1, \sigma_v^2, \sigma_v^3\}$. The element E is simply the identity operation. The elements C_3 and C_3^2 refer to rotations about the NV axis by $2\pi/3$ and $4\pi/3$ respectively. The elements σ_v refer to reflections in the vertical plane containing the NV axis and a single

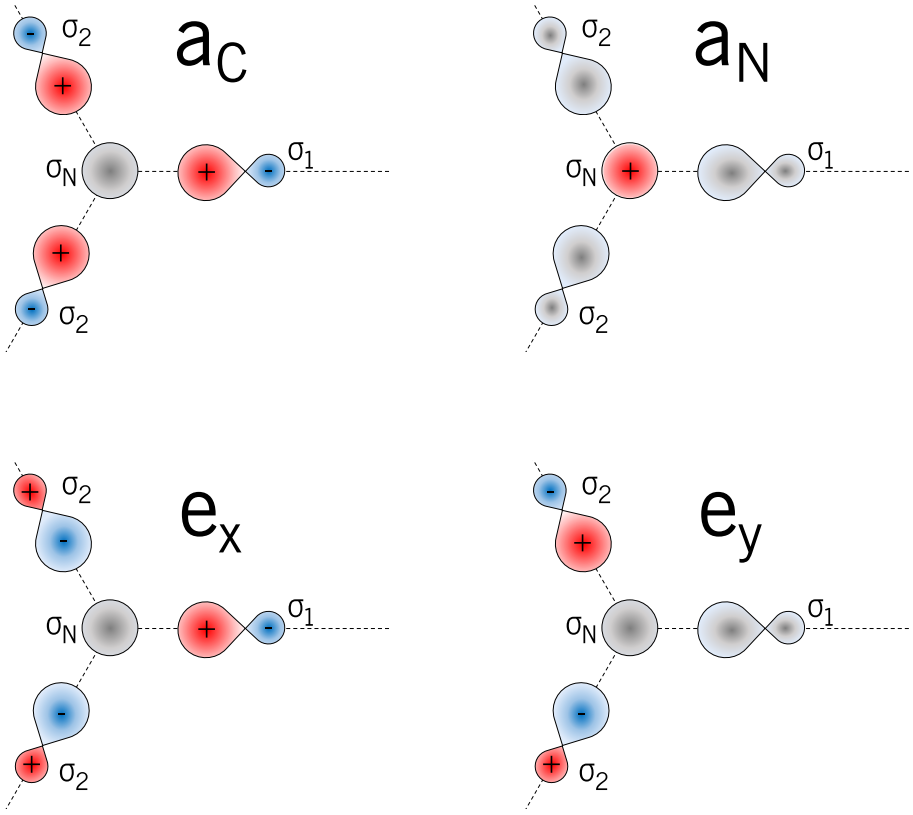

Figure 2.8: **Single-electron molecular orbitals**. Schematic of the four symmetry-adapted, single-electron molecular orbitals of the NV center. Grey indicates no contribution, red indicates a positive contribution, and blue indicates a negative contribution.

carbon atom.

The single electron molecular orbitals of the NV center are linear combinations of the sp^3 dangling bonds surrounding the vacancy, and reflect the C_{3v} symmetry of the NV center. There are four dangling bonds associated with the NV center: $\{\sigma_1, \sigma_2, \sigma_3, \sigma_N\}$. The symmetry adapted molecular orbitals of the NV center can be constructed by projecting the dangling bonds onto the irreducible representations of the C_{3v} group $\{A_1, A_2, E\}$ [99].

The resulting single electron orbitals are then

$$\begin{aligned} a_N &= \sigma_N \\ a_C &= \frac{1}{3}(\sigma_1 + \sigma_2 + \sigma_3) \\ e_x &= \frac{1}{\sqrt{6}}(2\sigma_1 - \sigma_2 - \sigma_3) \\ e_y &= \frac{1}{\sqrt{2}}(\sigma_2 - \sigma_3) \end{aligned} \tag{2.18}$$

The orbitals a_N and a_C are fully symmetric orbitals and transform as the irreducible representation A_1 whereas e_x and e_y are degenerate orbitals that transform as the irreducible representation E. Due to the Coulomb interaction, the a_N and a_C orbitals will mix slightly (see appendix A), resulting in two A_1 symmetric orbitals $a_1(1)$ and $a_1(2)$. *Ab initio* calculations have shown that the e_x and e_y orbitals are higher in energy than the a orbitals and moreover, that the $a_1(1)$ orbital lies in the valence band of diamond [100].

It is useful to relate the single electron orbitals to the internal coordinate system of the NV center, which is shown schematically in fig. 2.7. A geometric understanding of these orbitals is critical to understanding how the NV center interacts with various external perturbations. The z axis of the NV center is equivalent to the NV symmetry axis, and can point in any one of the four [111] crystal directions. The x axis lies along the projection of any one of the carbon bonds onto the plane perpendicular to the z axis. The geometric relationship between the molecular orbitals and the NV coordinate system can be seen through group theory. Because the molecular orbitals transform as the linear basis functions of the C_{3v} group, we see that each orbital transforms according to a different cartesian variable. For instance, $a_1(2)$ transforms as A_1, and hence transforms identically to the operator z. Similarly, the orbitals e_x and e_y transform as E_1 and E_2,

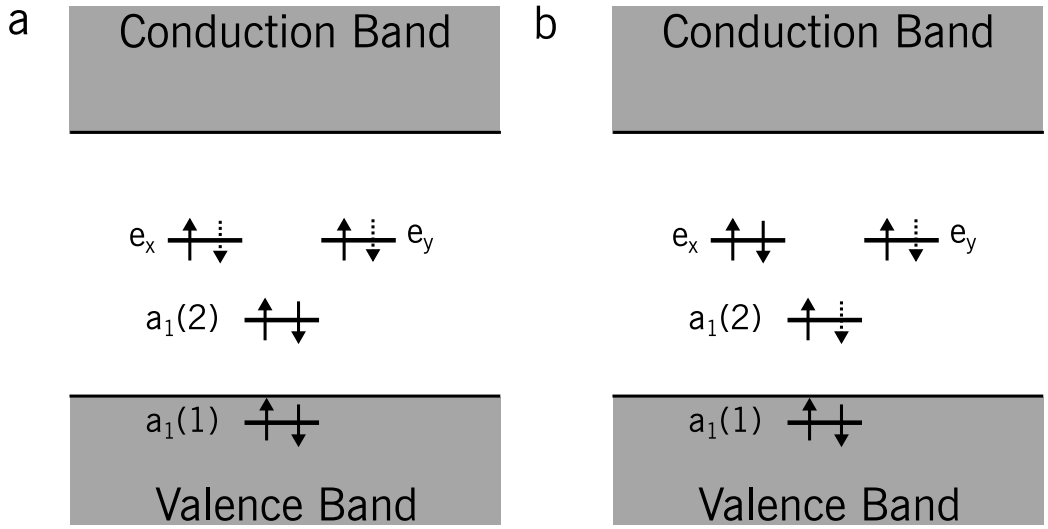

Figure 2.9: **Electronic configuration for the ground and excited states**. Electronic configuration of the NV center for the ground state (a) and first excited state (b). The lowest lying molecular orbital, $a_1(1)$ lies in the valence band, and the rest lie within the bandgap. The orbitals e_x and e_y are degenerate in the absence of external perturbations. Black arrows indicate electrons and dashed arrows indicate holes. Note that b) shows only one of the two possible electronic configurations, $\{|ae_y\rangle, |ae_x\rangle\}$

and hence transform identically to the operators x and y respectively.

2.9.1 Constructing the NV wavefunctions

Now that we have constructed the molecular orbitals of the NV center, we may compute the relevant electronic bound states of the NV center. As mentioned previously, there are six electrons that occupy the NV center. In the ground state electronic configuration, the a_1 orbitals are fully occupied and the remaining two electrons occupy the e_x and e_y orbitals. In the first excited state, an electron is promoted from the $a_1(2)$ orbital to the e_x and e_y orbitals. A diagram of these configurations is shown in fig. 2.9, where the electrons are indicated with black arrows.

If the molecular orbitals of the NV were fully occupied, the NV wavefunction would resemble that of an atom with a completely filled shell, such as a noble gas. Therefore,

the NV center can be modeled as a two-hole defect as opposed to a six-electron defect [99]. In the hole representation, the ground state configuration would consist of two holes occupying the e_x and e_y orbitals. For this reason, the ground state configuration is typically referred to as the e^2 electronic configuration. Similarly, the first excited state would consist of a hole occupying $a_1(2)$ and a hole occupying either one of the e_x and e_y orbitals. For this reason, the first excited state is typically referred to as the ae electronic configuration. The hole configuration is represented by dashed arrows in fig. 2.9. Due to the simplicity of the hole representation (2 particles vs. 6 particles), we will henceforth use the hole representation of the NV center.

We may write the overall NV wavefunctions as a product state of the orbital and spin wavefunctions, $|\Psi\rangle = |\ell\rangle \otimes |s\rangle$. The symmetry of $|\Psi\rangle$ can be determined by a direct product of each hole, $\Gamma_\Psi = (\Gamma_1 \otimes D_{1/2})(\Gamma_2 \otimes D_{1/2})$, where Γ_i denotes the orbital symmetry for the i^{th} hole and $D_{1/2}$ is the representation of a spin 1/2 particle in the C_{3v} group. The corresponding wavefunctions can be constructed by projecting the two-hole wavefunctions onto the irreducible representations of the C_{3v} group using a series of projection operators (see appendix A).

In the triplet ground state, the orbital wavefunction is a singlet $|^3A_2\rangle = |e_x e_y - e_y e_x\rangle$ with overall A_2 symmetry. The total wavefunction including the spin degree of freedom is simply $|^3A_{2m_s}\rangle = |e_x e_y - e_y e_x\rangle\,|m_s\rangle$. Using the decomposition $D_{1/2} \otimes D_{1/2} = A_1 + A_2 + E$, we find that $|^3A_{20}\rangle$ has overall A_1 symmetry and $|^3A_{2\pm}\rangle$ have E symmetry. The triplet excited state consists of a degenerate orbital doublet, with eigenstates $|X\rangle = |ae_x - e_x a\rangle$ and $|Y\rangle = |ae_y - e_y a\rangle$ with E_1 and E_2 symmetry respectively. In the absence of fine structure, the total excited state wavefunctions including the spin degree of freedom are $|E_x\rangle = |X\rangle\,|m_s\rangle$ and $|E_y\rangle = |Y\rangle\,|m_s\rangle$. As we will show in the next section, the spin-orbit and spin-spin interactions lift the orbital and spin degeneracies of the excited state, producing six distinct eigenstates. There are two (E_x and E_y) with $m_s = 0$ and

Configuration	State	Name	Symmetry
e^2	$\|e_x e_y - e_y e_x\rangle \otimes \|\downarrow\downarrow\rangle$	${}^3A_{2-}$	E_1
	$\|e_x e_y - e_y e_x\rangle \otimes \|\uparrow\downarrow + \downarrow\uparrow\rangle$	${}^3A_{20}$	A_1
	$\|e_x e_y - e_y e_x\rangle \otimes \|\uparrow\uparrow\rangle$	${}^3A_{2+}$	E_2
ae	$\|E_-\rangle \|\uparrow\uparrow\rangle - \|E_+\rangle \|\downarrow\downarrow\rangle$	A_1	A_1
	$\|E_-\rangle \|\uparrow\uparrow\rangle + \|E_+\rangle \|\downarrow\downarrow\rangle$	A_2	A_2
	$\|E_-\rangle \|\downarrow\downarrow\rangle - \|E_+\rangle \|\uparrow\uparrow\rangle$	E_1	E_1
	$\|E_-\rangle \|\downarrow\downarrow\rangle + \|E_+\rangle \|\uparrow\uparrow\rangle$	E_2	E_2
	$\|a_1(2)e_y - e_y a_1(2)\rangle \otimes \|\uparrow\downarrow + \downarrow\uparrow\rangle$	E_y	E_1
	$\|a_1(2)e_x - e_x a_1(2)\rangle \otimes \|\uparrow\downarrow + \downarrow\uparrow\rangle$	E_x	E_2

Table 2.1: NV wave functions for the triplet ground and first excited states along with their names and symmetry. The left column denotes the electronic configuration. The last two columns denote the name and overall symmetry of each wavefunction. Note that we have defined $e_\pm = \mp(e_x \pm i e_y)$ and $|E_\pm\rangle = |a_1(2)e_\pm - e_\pm a_1(2)\rangle$

four (A_1, A_2, E_1, and E_2) that are entangled states of non-zero spin and orbital angular momentum. The explicit definitions of the ground and excited state eigenstates including fine structure are shown in table 2.1. We note that the singlet states of the NV center can be constructed using the same process, and are explicitly calculated in appendix A.

2.9.2 Fine structure

Let us now introduce the fine structure of the NV center, which is a result of spin-orbit and spin-spin interactions. Although the magnitudes of these interactions are relatively small, they are responsible for a few important properties of the NV electronic structure, including the intersystem crossing [110], the zero-field splitting [100, 99], and spin-strain coupling [128]. In the following section, we will explicitly calculate the effect of the spin-orbit and spin-spin interactions on the both the ground and excited states of the NV center.

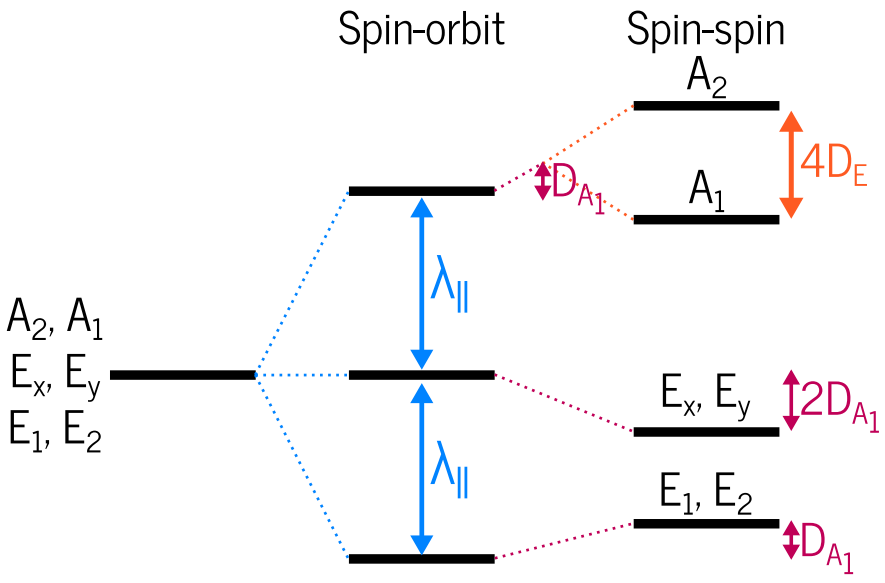

Figure 2.10: **Fine structure of the ^3E excited state.**

Spin-orbit interaction

Spin-orbit coupling is a relativistic correction to the NV Hamiltonian that breaks any orbital degeneracies for states with non-zero angular momentum, such as in the ^3E excited state. Physically, the spin-orbit interaction arises due to the relative, relativistic motion between the crystal ions and the electrons associated with the NV center. In the reference frame of the electrons, the electric field from the crystal ions appears as a magnetic field which can influence the electron spin. Therefore, the angular momentum of the electron is inherently coupled to the spin, and the spin-orbit interaction obeys the Hamiltonian $H_{SO} \sim \mathbf{L} \cdot \mathbf{S}$. However, because the NV center is hosted inside of a crystal, the spin-orbit interaction has a discrete rotational symmetry as prescribed by C_{3v} symmetry. If we project the spin-orbit Hamiltonian onto the irreducible representations of the C_{3v} group, we see (L_x, L_y, L_z) transform as (E_1, E_2, A_2). This implies that the

spin-orbit Hamiltonian can be written in the following way

$$H_{SO} = \lambda_{\parallel} L_z \sigma_z + \lambda_{\perp}(L_x \sigma_x + L_y \sigma_y) \tag{2.19}$$

To see the effect of the spin-orbit interaction, we first evaluate the Hamiltonian in the basis of the single-electron orbitals $\{e_x, e_y, a_1(2)\}$. To do that, it is useful to consider a new set of single electron orbitals, $\{e_+, e_-, a_1(2)\}$, where $e_+ = -\frac{1}{\sqrt{2}}(e_x + ie_y)$ and $e_- = \frac{1}{\sqrt{2}}(e_x - ie_y)$. The orbitals $\{e_+, a_1(2), e_-\}$ are analogous to p orbitals of an atoms, corresponding to states of $m_\ell = \{1, 0, -1\}$. Therefore, the spin-orbit Hamiltonian can be written in terms of the raising and lowering operators in the following way.

$$H = \lambda_{\parallel} L_z \sigma_z + \frac{\lambda_{\perp}}{2}(L_+ \sigma^- + L_- \sigma^+) \tag{2.20}$$

In terms of $\{e_x, e_y, a_1(2)\}$, the Hamiltonian is then

$$\begin{aligned} H_{SO} =& \lambda_{\parallel}(|e_x\rangle \langle e_x| + |e_y\rangle \langle e_y|)\sigma_z + \frac{\lambda_{\perp}}{2}(|a_1(2)\rangle (\langle e_x| + i \langle e_y|) - (|e_x\rangle + i |e_y\rangle) \langle a_1(2)|)\sigma^- \\ &+ \frac{\lambda_{\perp}}{2}(|a_1(2)\rangle (- \langle e_x| + i \langle e_y|) + (|e_x\rangle - i |e_y\rangle) \langle a_1(2)|)\sigma^+ \end{aligned} \tag{2.21}$$

The effect of spin-orbit coupling on the electronic structure can then be calculated by generalizing H_{SO} to the two-hole picture via $H = H_{SO} \otimes \mathbf{I} + \mathbf{I} \otimes H_{SO}$.

$$H = \lambda_{\parallel} (|A_2\rangle \langle A_2| + |A_1\rangle \langle A_1| - |E_2\rangle \langle E_2| - |E_1\rangle \langle E_1|) \tag{2.22}$$

The only observable aspect of the NV fine structure is due to the axial spin-orbit interaction in the ${}^3E$ manifold. Specifically, the axial spin-orbit interaction splits $A_{1,2}$ and $E_{1,2}$ from $E_{x,y}$ by $\lambda_{\parallel} = 5.5$ GHz, as shown in fig. 2.10. However, there are other

important effects of spin-orbit coupling that do not result in fine structure [99, 100]. First, the axial spin-orbit interaction can couple states of $m_s = 0$ spin projection and of the same orbital configuration. For instance, this allows $|E_x\rangle$ and $|E_y\rangle$ to directly couple to the singlet ${}^1E_{x,y}$ manifold, which may play an integral part in the intersystem crossing. Second and more importantly, the transverse spin-orbit interaction couples states of different spin multiplicities and electronic configuration. Because the spin-orbit interaction is a fully A_1 symmetric interaction, this means that the transverse spin-orbit interaction may only couple states of the same overall symmetry. For instance, transverse spin-orbit coupling directly couples $|A_1\rangle$ with $|{}^1A_1\rangle$ and is the primary mechanism for the intersystem crossing, as we discuss in a later section. Additionally, transverse spin-orbit coupling directly couples ${}^3A_2$ with ${}^3E$, which is partially responsible for the spin-strain interaction, which we discuss below.

Spin-spin interaction

The spin-spin interaction in the NV center plays an important rule in the fine structure of the ground and excited states. The spin-spin interaction results from a direct dipolar coupling between the unpaired spins of the NV center, and can be written as

$$H_{SS} = \frac{\mu_0}{4\pi}\frac{g^2\mu_B^2}{r^3}(3(\sigma_{\mathbf{1}}\cdot\hat{r})(\sigma_{\mathbf{2}}\cdot\hat{r}) - \sigma_{\mathbf{1}}\cdot\sigma_{\mathbf{2}}) \tag{2.23}$$

where $g \approx 2$ is the Landé g factor of the NV center and μ_B is the Bohr magneton. To see how the spin-spin interaction affects the NV electronic structure, it is useful to separate the spin and orbital components and project them onto the irreducible repre-

sentations of the C_{3v} group [99]. Generalizing to the two-hole picture, we find

$$\begin{aligned} H_{SS}^{A_1} &= \frac{\mu_0}{4\pi}\frac{g^2\mu_B^2}{4}\left\langle\frac{1-3z^2}{r^3}\right\rangle S_z^2 \\ H_{SS}^{E} &= \frac{\mu_0 g^2\mu_B^2}{4\pi}\Bigg[\left\langle\frac{3(x^2-y^2)}{4r^3}\right\rangle(S_+^2+S_-^2) - i\left\langle\frac{3xy}{2r^3}\right\rangle(S_+^2-S_-^2) \\ &\quad + \left\langle\frac{3xz}{2r^3}\right\rangle(S_xS_z+S_zS_x) - i\left\langle\frac{3yz}{2r^3}\right\rangle(S_yS_z+S_zS_y)\Bigg] \end{aligned} \tag{2.24}$$

In a perfect crystal, the ground state has A_2 orbital symmetry, and hence the only non-zero component of the spin-spin interaction is $H_{SS}^{A_1}$, since $E \otimes A_2 = E$. Therefore, the spin-spin interaction in the ground state can be written as

$$H_{SS} = D_0 S_z^2 \tag{2.25}$$

where $D_0 = \frac{\mu_0}{4\pi}\frac{g^2\mu_B^2}{4}\left\langle e_x\left|\frac{1-3z^2}{r^3}\right|e_x\right\rangle = 2.87$ GHz is the zero-field splitting at room temperature that was introduced earlier in the chapter. Not surprisingly, the value of D_0 is sensitive to both temperature, strain, and electric fields, as all of these directly affect the unpaired spin density. We will directly show this later in the chapter.

The spin-spin interaction in the excited state is slightly more complicated, due to the fact that the orbitals are E symmetric. Indeed, all terms of the spin-spin interaction are non-zero, resulting in additional fine structure and mixing between states of different

spin projections. In the excited state, the spin-spin interaction obeys

$$\begin{aligned} H_{SS} =& D_{A_1}\left(|A_1\rangle\langle A_1| + |A_2\rangle\langle A_2| + |E_1\rangle\langle E_1| + |E_2\rangle\langle E_2|\right) \\ & - 2D_{A_1}\left(|E_x\rangle\langle E_x| + |E_y\rangle\langle E_y|\right) \\ & + 2D_E(|A_2\rangle\langle A_2| - |A_1\rangle\langle A_1|) \\ & + D_{E'}\left(|E_y\rangle\langle E_1| + |E_1\rangle\langle E_y| + i\,|E_x\rangle\langle E_2| - i\,|E_2\rangle\langle E_x|\right) \end{aligned} \tag{2.26}$$

where we have defined $D_{A_1} = \frac{\mu_0}{4\pi}\frac{g^2\mu_B^2}{4}\left\langle X\left|\frac{1-3z^2}{r^3}\right|X\right\rangle$, $D_E = \frac{\mu_0 g^2\mu_B^2}{4\pi}\left\langle X\left|\frac{3(x^2-y^2)}{4r^3}\right|X\right\rangle = \frac{\mu_0 g^2\mu_B^2}{4\pi}\left\langle X\left|\frac{3xy}{2r^3}\right|X\right\rangle$, and $D_{E'} = \frac{\mu_0 g^2\mu_B^2}{4\pi}\left\langle X\left|\frac{3xz}{2r^3}\right|X\right\rangle = \frac{\mu_0 g^2\mu_B^2}{4\pi}\left\langle X\left|\frac{3yz}{2r^3}\right|X\right\rangle$. An energy level diagram showing the fine structure due to spin-orbit and spin-spin interaction in ${}^3E$ is shown in fig. 2.10 [99, 141]. The D_E term lifts the degeneracy of $|A_1\rangle$ and $|A_2\rangle$ and splits them by an amount $4D_E = 3.3$ GHz. In addition, the D_{A_1} uniformly shifts states of non-zero spin projection from states of zero spin projection by an amount $3D_{A_1} = 1.4$ GHz. The last term mixes $|E_y\rangle$ with $|E_1\rangle$ and $|E_x\rangle$ with $|E_2\rangle$ with a strength given by $D_{E'}$. The value of $D_{E'}$ has not directly been measured, but its effect is significant enough to cause spin-flips in the optical cycle of the NV center at cryogenic temperatures. This mechanism allows for the high fidelity optical pumping technique described earlier in the chapter. Furthermore, in the presence of large E symmetric strain or electric fields, $|E_y\rangle$ and $|E_1\rangle$ form an avoided level crossing and spin-mixing increases considerably. This feature can be exploited to form a Λ system, providing an all-optical route for coherent control of the spin [142, 141].

2.9.3 Interactions

The electronic structure of the NV center is sensitive to several external degrees of freedom, including magnetic fields, electric fields, temperature, and crystal strain. In

this thesis, we are particularly concerned with the NV interaction with crystal strain. In a solid-state system, there are several ways that strain can interact with a defect. For instance, in a piezoelectric crystal, the electric dipole moment can interact with the stress-induced electric polarization field. In the case of diamond which is non-piezoelectric, the strain interaction arises from a modification of the Coulomb interaction between the electrons and nuclei. These models of the strain interaction are well established, and have been used for careful studies of crystal defects since the 1960s [143, 144]. However, the origin of the spin-strain interaction until very recently has not been established. Until now, the strain interaction has been treated entirely phenomenologically using the formalism for the spin-Stark effect observed in the EPR community [76, 77, 51, 82]. In the following subsections, we will calculate the effects of magnetic, electric and strain fields on the electronic structure of the triplet manifolds of the NV center, and provide for the first time a full treatment of the NV-strain interaction. We note that the approach taken here can be easily generalized to the singlet levels of the NV center and other solid-state defects.

Zeeman interaction

Magnetic fields couple to both the spin and orbital degrees of freedom of the NV center through the Zeeman interaction, which is described by the Hamiltonian

$$H_B = \gamma_\ell \mathbf{L} \cdot \mathbf{B} + \gamma_s \sigma \cdot \mathbf{B} \tag{2.27}$$

where $\mathbf{L}$ and σ are the single-electron orbital and spin operators, and $\gamma_\ell = 1.4$ MHz/G and $\gamma_s = 2.8$ MHz/G are the orbital and spin gyromagnetic ratios respectively. The ${}^3A_2$ ground state is an orbital singlet, and hence the Zeeman interaction only contains a spin component. Therefore, the Zeeman interaction within the ground state manifold can be

written as

$$H_B = \gamma_{NV} \mathbf{S} \cdot \mathbf{B} \tag{2.28}$$

where $\mathbf{S}$ is the spin-1 operator and $\gamma_{NV} = \gamma_s = 2.8$ MHz/G.

At room temperature, the orbital excited state averages to an effective orbital singlet due to the dynamic Jahn Teller effect, and the Zeeman interaction is identical to that of the ground state. However, at cryogenic temperatures, the orbital excited state is an orbital doublet, and hence the Zeeman interaction will also contain an orbital component. Moreover, the presence of spin-orbit and spin-spin interactions leads to a highly non-trivial response to magnetic fields. A discussion of this effect is beyond the scope of this thesis, but a detailed calculation can be found in ref. [141].

A magnetic field applied along the NV axis breaks the degeneracy of the $|\pm 1\rangle$ spin levels according to $H_Z = \gamma_{NV} S_z B_z$. In addition, microwave magnetic fields near-resonant with the $|0\rangle \leftrightarrow |\pm 1\rangle$ transitions can be used to coherently rotate the spin. Interestingly, the associated dipole selection rules are dictated by the value of B_z. In the absence of an applied B_z, the microwaves couple $|0\rangle$ to a new set of spin states, $|\pm\rangle = \frac{1}{\sqrt{2}}(|1\rangle \pm |-1\rangle)$ which require $\hat{x}$ and $\hat{y}$ polarized microwaves respectively. In the presence of an applied field such that $2\gamma_{NV} B_z \gg \Omega_R$, the microwaves directly couple $|0\rangle$ to the usual $|\pm 1\rangle$ spin levels, which require $\sigma^{\pm}$ polarized microwaves. In our experiments, we use a single gold wire to generate our microwave field, which is inherently linearly polarized. Therefore, we will be able to drive the $|0\rangle \leftrightarrow |\pm 1\rangle$ transitions equally. However, as we show in the following sections, the presence of crystal strain can alter the microwave selection rules such that the $|0\rangle \leftrightarrow |\pm 1\rangle$ transitions are driven by linearly polarized microwave fields.

Strain-orbit coupling

The primary interaction of the NV center with crystal strain is through the orbital degree of freedom. Strain-induced relative displacements of the crystal ions modifies the ion-electron Coulomb interaction, which deforms the molecular orbitals of the NV center [99, 100]. Here, we will consider the effects of a small strain where the ionic displacements are small. In the Born-Oppenheimer approximation, we can then expand the ion-electron Coulomb interaction to first order in the displacements of the crystal ions.

Let's suppose that the ion-electron Coulomb interaction can be written as as a sum of one-particle potentials for the electrons:

$$U_{el-ion}(\mathbf{r}^i;\mathbf{R}^l) = \sum_i U_{el-ion}(\mathbf{r}^i;\mathbf{R}^l) \tag{2.29}$$

where $\mathbf{r}^i$ denotes the position of the i^{th} electron and $\mathbf{R}^l$ denotes the position of the l^{th} ion of the NV center. For small ionic displacements, $\delta\mathbf{R}^l$,the modified Coulomb potential is linear in $\delta\mathbf{R}^l$. If we denote the equilibrium positions of the ions by $\mathbf{R}^{l0}$, the potential may be written and expanded as

$$\begin{aligned} U_{el-ion}(\mathbf{r}^i;\mathbf{R}^l) &= U_{el-ion}(\mathbf{r}^i;\{\mathbf{R}^l+\delta\mathbf{R}^l\}) \\ &= U_{el-ion}(\mathbf{r}^i;\mathbf{R}^{l0}) + \delta U_{el-ion}(\mathbf{r}^i,\delta\mathbf{R}^l) \end{aligned} \tag{2.30}$$

where

$$\delta U_{el-ion} = \sum_j \left.\frac{\partial U_{el-ion}}{\partial R^l_j}\right|_{\mathbf{R}^{l0}} \delta R^l_j \tag{2.31}$$

Using the chain rule, we can rewrite the modified Coulomb interaction in terms of

the displacement tensor, $u^l_{jk} = \frac{\partial(\delta R^l_j)}{\partial R^l_k}$,

$$\delta U_{el-ion} = \sum_{j,k} \frac{\partial U_{el-ion}}{\partial(\delta R^l_j)} u_{jk} \delta R^l_k \tag{2.32}$$

The displacement tensor can be broken up into symmetric and anti-symmetric parts, $\mathbf{u} = \boldsymbol{\epsilon} + \mathbf{f}$, where ϵ is the strain tensor and f is the rotation tensor.

$$\begin{aligned} \epsilon_{ij} &= \frac{1}{2}(u_{ij} + u_{ji}) \\ f_{ij} &= \frac{1}{2}(u_{ij} - u_{ji}) \end{aligned} \tag{2.33}$$

However, the modified Coulomb interaction will only be proportional to the strain tensor ϵ_{ij}. The rotation tensor f_{ij} corresponds to rigid rotations of the crystal, which should not affect the energy of the defect. Therefore, the strain Hamiltonian is given by

$$H_{strain} = \sum_{j,k} V_{jk} \epsilon_{jk} \tag{2.34}$$

where $V_{jk} = \sum_l \frac{\partial U_{el-ion}}{\partial(\delta R^l_j)}|_{\mathbf{R}^{l0}} \delta R^l_k$ is a symmetric, second rank orbital tensor operator. Because $\mathbf{V}$ and $\boldsymbol{\epsilon}$ are both second rank symmetric tensors, their components transform as the quadratic basis functions of the C_{3v} group. Therefore, we may project H_{strain} onto the irreducible representations of the C_{3v} group [99, 80], which reflect the symmetry of the orbital wavefunctions.

$$\begin{aligned} H_{strain} =& \frac{1}{2}(V_{xx} + V_{yy})(\epsilon_{xx} + \epsilon_{yy}) + V_{zz}\epsilon_{zz} - \frac{1}{2}(V_{xx} - V_{yy})(\epsilon_{xx} - \epsilon_{yy}) \\ &+ \frac{1}{2}(V_{xy} + V_{yx})(\epsilon_{xy} + \epsilon_{yx}) - \frac{1}{2}(V_{xz} + V_{zx})(\epsilon_{xz} + \epsilon_{zx}) \\ &+ \frac{1}{2}(V_{yz} + V_{zy})(\epsilon_{yz} + \epsilon_{zy}) \end{aligned} \tag{2.35}$$

For ease of notation, we will write the Hamiltonian in a more compact form and label each term of the Hamiltonian by their symmetry:

$$\begin{aligned} V_{A_1} &= V_{zz} & & \epsilon_{A_1} = \epsilon_{zz} \\ V_{A_1'} &= \frac{1}{2}(V_{xx} + V_{yy}) & & \epsilon_{A_1'} = \epsilon_{xx} + \epsilon_{yy} \\ V_{E_1} &= \frac{1}{2}(V_{xx} - V_{yy}) & \leftrightarrow & \epsilon_{E_1} = \epsilon_{xx} - \epsilon_{yy} \\ V_{E_2} &= \frac{1}{2}(V_{xy} + V_{yx}) & & \epsilon_{E_2} = \epsilon_{xy} + \epsilon_{yx} \\ V_{E_1'} &= \frac{1}{2}(V_{xz} + V_{zx}) & & \epsilon_{E_1'} = \epsilon_{xz} + \epsilon_{zx} \\ V_{E_2'} &= \frac{1}{2}(V_{yz} + V_{zy}) & & \epsilon_{E_2'} = \epsilon_{yz} + \epsilon_{zy} \end{aligned} \tag{2.36}$$

The orbital operators V_Γ can be represented in the basis spanned by the single electron molecular orbitals of the NV center $\{e_x, e_y, a_1(2)\}$. The matrix elements of V_Γ can be determined from symmetry considerations. We explicitly define them below

$$V_{A_1,A_1'} = \begin{pmatrix} V^{xx}_{A_1,A_1'} & 0 & 0 \\ 0 & V^{xx}_{A_1,A_1'} & 0 \\ 0 & 0 & V^{aa}_{A_1,A_1'} \end{pmatrix} \tag{2.37}$$

$$V_{E_1,E_1'} = \begin{pmatrix} V^{xx}_{E_1,E_1'} & 0 & 0 \\ 0 & -V^{xx}_{E_1,E_1'} & V^{ax}_{E_1,E_1'} \\ 0 & V^{ax}_{E_1,E_1'} & 0 \end{pmatrix} \tag{2.38}$$

$$V_{E_2,E_2'} = \begin{pmatrix} 0 & V^{xx}_{E_1,E_1'} & V^{ax}_{E_1,E_1'} \\ V^{xx}_{E_1,E_1'} & 0 & 0 \\ V^{ax}_{E_1,E_1'} & 0 & 0 \end{pmatrix} \tag{2.39}$$

Here, we have defined $V_\Gamma^{aa} = \langle a_1(2)|V_\Gamma|a_1(2)\rangle$,$V_\Gamma^{ax} = \langle a_1(2)|V_\Gamma|e_x\rangle$, and $V_\Gamma^{xx} =$

$\langle e_x|V_\Gamma|e_x\rangle$. Extending the strain Hamiltonian to the two-hole picture allows us to write the Hamiltonian in terms of the orbital wavefunctions $\{|X\rangle, |Y\rangle, |A\rangle\}$, where we have defined $|A\rangle = |^3A_2\rangle$. Furthermore, the Hamiltonian can be decomposed into $H_{strain} = H^E + H^A + H^{AE}$: H^E is the strain-orbit interaction within ^3E, H^A is the strain-orbit interaction within $^3A_2$, and H^{AE} is the strain-orbit interaction coupling the two manifolds.

$$\begin{aligned} H^E =& \left[(V^{aa}_{A_1} + V^{xx}_{A_1})\epsilon_{zz} + (V^{aa}_{A_1'} + V^{xx}_{A_1'})(\epsilon_{xx} + \epsilon_{yy})\right](|X\rangle\langle X| + |Y\rangle\langle Y|) \\ &- \left[V^{xx}_{E_1}(\epsilon_{xx} - \epsilon_{yy}) + V^{xx}_{E_1'}(\epsilon_{xz} + \epsilon_{zx})\right](|X\rangle\langle X| - |Y\rangle\langle Y|) \\ &+ \left[V^{xx}_{E_1}(\epsilon_{xy} + \epsilon_{yx}) + V^{xx}_{E_1'}(\epsilon_{yz} + \epsilon_{zy})\right](|X\rangle\langle Y| + |Y\rangle\langle X|) \end{aligned} \tag{2.40}$$

$$H^A = \left[2V^{xx}_{A_1}\epsilon_{zz} + 2V^{xx}_{A_1'}(\epsilon_{xx} + \epsilon_{yy})\right]|A\rangle\langle A| \tag{2.41}$$

$$\begin{aligned} H^{AE} =& -\left[V^{ax}_{E_1}(\epsilon_{xx} - \epsilon_{yy}) + V^{ax}_{E_1'}(\epsilon_{xz} + \epsilon_{zx})\right](|A\rangle\langle Y| + |Y\rangle\langle A|) \\ &+ \left[V^{ax}_{E_1}(\epsilon_{xy} + \epsilon_{yx}) + V^{ax}_{E_1'}(\epsilon_{yz} + \epsilon_{zy})\right](|A\rangle\langle X| + |X\rangle\langle A|) \end{aligned} \tag{2.42}$$

As expected, H^A contains only A_1 symmetric terms, which results in a uniform shift in energy with respect to the excited state. In any real experiment, the absolute shifts of the ground and excited states will not be detectable. Spectroscopy of the two states will only indicate the relative shifts of the ground and excited states. Therefore, it is instructive to set the ground state to always be at zero energy and absorb H^A into the definition of H^E.

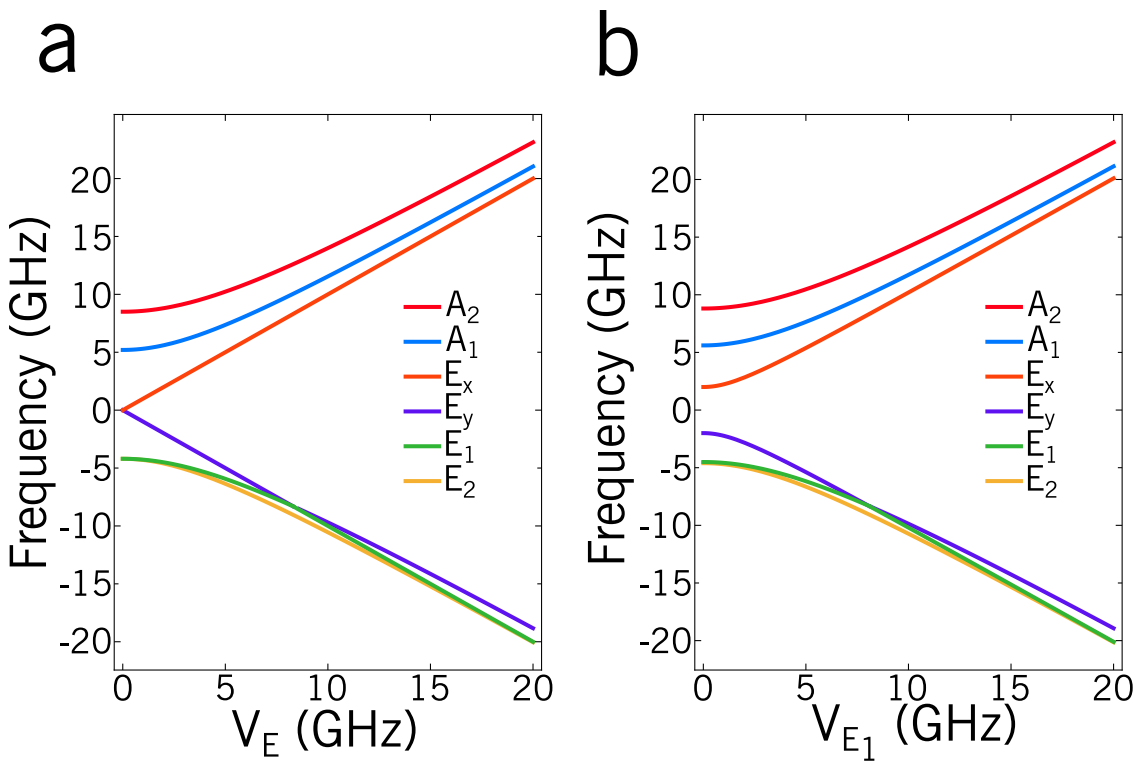

Figure 2.11: **Interaction of E strain in the ^3E excited state**. a). In a perfect crystal, the application of E_1 or E_2 strain splits $|E_x\rangle$ and $|E_y\rangle$ and mixes $|A_{1,2}\rangle$ and $|E_{1,2}\rangle$. Under high strain (>20 GHz), the fine structure is washed out and the ^3E manifold converges into two orbital branches, $|X\rangle$ and $|Y\rangle$. b) Energy of the ^3E fine structure levels as a function of E_1 strain for an intrinsic E_2 strain of 2 GHz.

Finally, we may write the strain-orbit interaction in terms of the fine structure states and define the strain-orbit coupling constants. We label the ground state levels by their spin projection $\{|1\rangle, |0\rangle, |-1\rangle\}$ and label the excited levels by their symmetry as shown in table 2.1: $\{|E_x\rangle, |E_y\rangle, |A_1\rangle, |A_2\rangle, |E_1\rangle, |E_2\rangle\}$. Furthermore, we separate each strain-orbit interaction in terms of their symmetries such that $H^E = H^E_{A_1} - H^E_{E_1} + H^E_{E_2}$ and

$H^{AE} = H^{AE}_{E_1} + H^{AE}_{E_2}$. In the excited state manifold, we obtain

$$\begin{aligned}
H^{E}_{A_1} &= \left[\lambda_{A_1}\epsilon_{zz} + \lambda_{A_1'}(\epsilon_{xx}+\epsilon_{yy})\right]\mathbf{I} \\
H^{E}_{E_1} &= \left[\lambda_{E}(\epsilon_{xx}-\epsilon_{yy}) + \lambda_{E'}(\epsilon_{xz}+\epsilon_{zx})\right]\Big(|E_x\rangle\langle E_x| - |E_y\rangle\langle E_y| \\
&\quad + (|E_1\rangle\langle A_1| - |E_2\rangle\langle A_2| + h.c.)\Big) \\
H^{E}_{E_2} &= \left[\lambda_{E}(\epsilon_{xy}+\epsilon_{yx}) + \lambda_{E'}(\epsilon_{yz}+\epsilon_{zy})\right]\Big(|E_x\rangle\langle E_y| \\
&\quad + i\,|E_2\rangle\langle A_1| - i\,|E_1\rangle\langle A_2| + h.c.\Big)
\end{aligned} \tag{2.43}$$

where $\lambda_{A_1} = V^{aa}_{A_1} - V^{xx}_{A_1}$, $\lambda_{A_1'} = V^{aa}_{A_1'} - V^{xx}_{A_1'}$, $\lambda_E = V^{xx}_{E_1}$, and $\lambda_{E'} = V^{xx}_{E_1'}$. A_1 symmetric strain uniformly shifts the excited state in energy with respect to the ground state. Under E_1 symmetric strain, the $m_s = 0$ eigenstates (E_x and E_y) split linearly while states of non-zero spin momentum mix with each other. Under E_2 strain, the $m_s = 0$ eigenstates mix while states of non-zero spin momentum mix with each other.

These effects of the strain-orbit interaction within the excited state are demonstrated in fig. 2.11. On the left, an NV in a perfect crystal is subject to E symmetric strain. There are a few important things to point out. First, the application of E strain breaks the E_x and E_y degeneracy. This is directly related to the fact that E symmetric strain reduces the C_{3v} of the NV center. Second, for an E symmetric strain-orbit coupling of approximately 8 GHz, the E_y and E_1 states are nearly degenerate in energy. At this avoided level crossing, the E-symmetric spin-spin interaction results in significant spin-mixing between $m_s = 0$ and $m_s = \pm 1$. Finally, at high strain, the spin-orbit coupling is washed out and the excited state converges to two orbital branches $|X\rangle$ and $|Y\rangle$ which are linearly sensitive to strain. In chapter 5, we quantitatively characterize H^E and determine the strain-orbit coupling constants.

The strain-orbit interaction H^{AE} can be written as

$$\begin{aligned} H^{AE}_{E_1} =& d_E \Bigg[|0\rangle \langle E_y| + \frac{i}{\sqrt{2}} \Big(\big(|1\rangle - |-1\rangle \big) \big(\langle A_1| - \langle E_1| \big) \\ &+ \big(|1\rangle + |-1\rangle \big) \big(\langle A_2| + |E_2\rangle \big) \Big) + h.c. \Bigg] \\ H^{AE}_{E_2} =& - d_E \Bigg[|0\rangle \langle E_x| + \frac{1}{\sqrt{2}} \Big(\big(|1\rangle - |-1\rangle \big) \big(\langle E_2| - \langle A_2| \big) \\ &- \big(|1\rangle + |-1\rangle \big) \big(\langle A_1| + |E_1\rangle \big) \Big) + h.c. \Bigg] \end{aligned} \tag{2.44}$$

where the coupling constants $d_E = V^{ax}_{E_1}$ and $d_{E'} = V^{ax}_{E'_1}$ have not yet been determined. Given previous measurements and *ab initio* calculations of the electric dipole moment of the NV center [145, 146], it seems likely that d_E and $d_{E'}$ are approximately an order of magnitude larger than the strain-orbit coupling constants within the ^3E manifold. Traditionally, H^{AE} has been ignored in the discussion of the NV electronic structure. In measurements of the optical transitions of the NV center, this effect is essentially negligible, as non-resonant terms are suppressed by the zero-phonon line energy and generating phonons at 471 THz is unrealistic. However, H^{AE} is responsible for the spin-strain interaction, as we show in the following section.

Spin-strain coupling

The spin-strain interaction arises through two different mechanisms, as shown in fig.2.12. The first is transverse spin-orbit coupling between the ground and excited state manifolds [128]. The second is a modification of the spin-spin interaction via distortion of the unpaired spin density [109]. Let us first consider the effect of spin-orbit coupling on the ground state manifold, $|^3A_{2m_s}\rangle$. It is easy to see that the axial spin-orbit term does not affect the ground state spin levels. On the other hand, the transverse spin-orbit

interaction connects the ground state manifold to the ^3E manifold. After simplification, we obtain the transverse spin-orbit Hamiltonian

$$\begin{aligned} H_{SO} =& \frac{\lambda_\perp}{2}\left(|^3A_{2+}\rangle\left(\langle E_y| - i\langle E_x|\right) + \left(|E_y\rangle - i|E_x\rangle\right)\langle^3A_{2+}|\right) \\ &- \frac{\lambda_\perp}{2}\left(|^3A_{2-}\rangle\left(\langle E_y| + i\langle E_x|\right) + \left(|E_y\rangle + i|E_x\rangle\right)\langle^3A_{2-}|\right) \\ &- \frac{i\lambda_\perp}{2}\left(|A_1\rangle\langle^3A_{20}| + |^3A_{20}\rangle\langle A_1|\right) \end{aligned} \tag{2.45}$$

The transverse spin-orbit interaction connects the $|\pm1\rangle$ spin levels of the ground state to $|E_x\rangle$ and $|E_y\rangle$ while it connects the $|0\rangle$ spin level to A_1. From here, we can calculate the spin-orbit perturbed ground state spin levels:

$$|1\rangle \rightarrow |1\rangle + \frac{\lambda_\perp}{2f_{ZPL}}\Big(|E_y\rangle - i|E_x\rangle\Big) \tag{2.46}$$

$$|0\rangle \rightarrow |0\rangle + i\frac{\lambda_\perp}{2f_{ZPL}}|A_1\rangle \tag{2.47}$$

$$|-1\rangle \rightarrow |-1\rangle - \frac{\lambda_\perp}{2f_{ZPL}}\Big(|E_y\rangle + i|E_x\rangle\Big) \tag{2.48}$$

where f_{ZPL} is the zero-phonon line frequency of 471 THz. Now using the strain-orbit interaction H^E, we can derive the spin-strain interaction.

$$\begin{aligned} H_{strain} =& \frac{\lambda_\perp^2}{4f_{ZPL}^2}\Big[U_{A_1}\Big(|1\rangle\langle1| + |-1\rangle\langle1| - |0\rangle\langle0|\Big) + U_{E_1}\Big(|1\rangle\langle-1| + |-1\rangle\langle1|\Big) \\ &- iU_{E_2}\Big(|1\rangle\langle-1| - |-1\rangle\langle1|\Big)\Big] \end{aligned} \tag{2.49}$$

Note that we have defined the shorthand $U_{A_1} = \lambda_{A_1}\epsilon_{zz} + \lambda_{A_1'}(\epsilon_{xx} + \epsilon_{yy})$, $U_{E_1} = \lambda_E(\epsilon_{xx} - \epsilon_{yy}) + \lambda_{E'}(\epsilon_{xz} + \epsilon_{zx})$, and $U_{E_2} = \lambda_E(\epsilon_{xy} + \epsilon_{yx}) + \lambda_{E'}(\epsilon_{yz} + \epsilon_{zy})$. Now, let us add

the contributions from the spin-spin interaction.

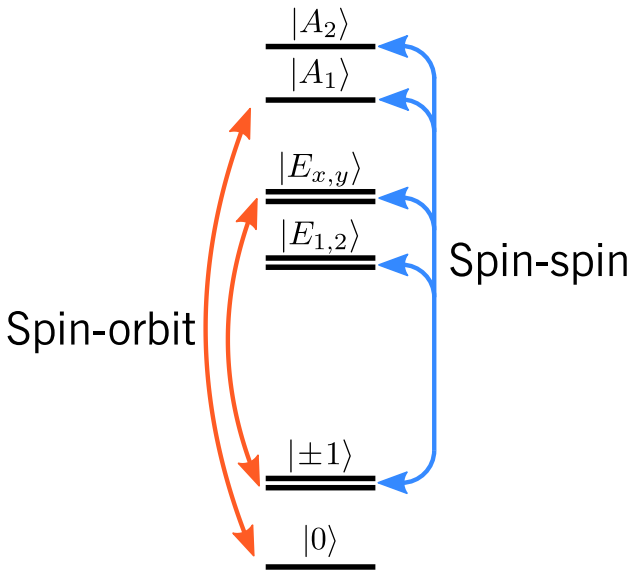

Figure 2.12: **Fine structure required for spin-strain coupling**. Spin-strain coupling is partially enabled via spin-orbit (orange) and spin-spin (blue) interactions between the triplet ground and excited states. Spin-orbit interaction introduces both A_1 and E symmetric spin-strain interactions and spin-spin interaction introduces only an E symmetric spin-strain interaction.

Strain distorts the unpaired spin density of the NV center, which directly modifies the spin-spin interaction. A_1 symmetric strain, which corresponds to contractions and dilations of the molecular structure that preserve the NV C_{3v} symmetry, directly affects the spin-spin interaction of the ground state. If the NV has perfect C_{3v} symmetry, the E symmetric components of the ground state spin-spin interaction are zero. However, E symmetric strain distorts the unpaired spin density and reduces its symmetry. In this situation, the E symmetric spin-spin interaction terms are no longer negligible.

To calculate the effect of E strain on the spin-spin interaction, we will treat both strain and the spin-spin interactions to first order. It is easiest to see the effect by first examining how the spin-spin interaction couples the ${}^3A_2$ and ${}^3E$ manifolds. Applying

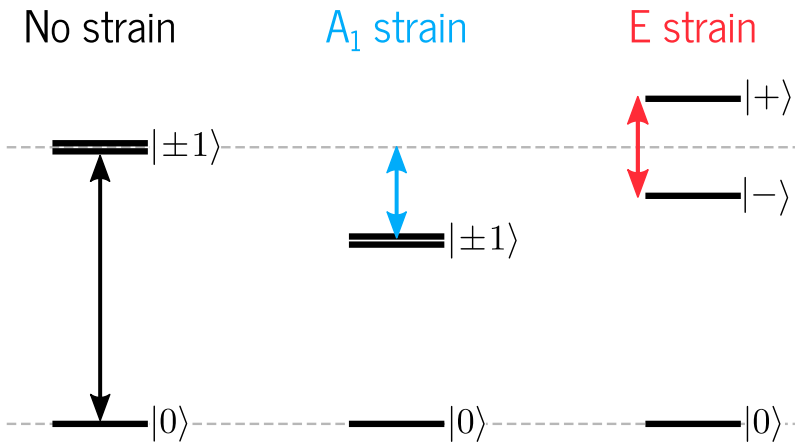

Figure 2.13: **Spin-strain interaction**. In the absence of strain, $|\pm 1\rangle$ are degenerate and split from $|0\rangle$ by spin-spin interaction. In the presence of A_1 strain, $|\pm 1\rangle$ remain degenerate and shift uniformly with respect to $|0\rangle$. In the presence of E strain, the $|\pm 1\rangle$ degeneracy is broken and the levels mix producing new spin eigenstates, $|\pm\rangle$.

first order perturbation theory, we obtain the perturbed ground state spin levels:

$$\begin{aligned} |1\rangle &\to |1\rangle + \frac{\Delta_E}{f_{ZPL}}(|A_1\rangle - |A_2\rangle) + \frac{\Delta'_E}{f_{ZPL}}(|E_y\rangle + i\,|E_x\rangle) \\ |-1\rangle &\to |-1\rangle + \frac{\Delta_E}{f_{ZPL}}(|E_2\rangle - |E_1\rangle) - \frac{\Delta'_E}{f_{ZPL}}(|E_y\rangle + i\,|E_x\rangle) \\ |0\rangle &\to |0\rangle \end{aligned} \tag{2.50}$$

where we have defined $\Delta_E = \frac{\mu_0 g^2 \mu_B^2}{4\pi} \left\langle A \left| \frac{3(x^2-y^2)}{4r^3} \right| X \right\rangle = \frac{\mu_0 g^2 \mu_B^2}{4\pi} \left\langle A \left| \frac{3xy}{2r^3} \right| X \right\rangle$ and $\Delta'_E = \frac{\mu_0 g^2 \mu_B^2}{4\pi} \left\langle A \left| \frac{3xz}{2r^3} \right| X \right\rangle = \frac{\mu_0 g^2 \mu_B^2}{4\pi} \left\langle A \left| \frac{3yz}{2r^3} \right| X \right\rangle$. Note that we have neglected terms coupling $|0\rangle$ to the excited state, which would introduce terms in the spin-strain Hamiltonian coupling $|0\rangle$ to $|\pm 1\rangle$ that are suppressed by the large zero-field splitting.

If we apply the strain-orbit Hamiltonian, H^{AE} to the perturbed eigenstates, we see

that an effective spin-strain interaction arises of the form

$$H = \frac{\Delta_E + \Delta'_E}{4f_{ZPL}}\Big[- V_{E_2}(|1\rangle\langle -1| + |-1\rangle\langle 1|) + iV_{E_2}(|1\rangle\langle -1| - |-1\rangle\langle 1|)\Big] \tag{2.51}$$

The effective spin-strain coupling constants are a product of the strain-orbit coupling and the spin-spin coupling between the ground and excited states. Therefore, the spin-strain interaction can be interpreted as an enhancement of the spin-spin interaction due to the distortion of the unpaired spin density from mixing of the ground and excited state electronic orbitals [147]. Combining the spin-orbit and spin-spin terms, we obtain overall spin-strain Hamiltonian,

$$\begin{aligned} H_{strain} = &\left[d_{A_1}\epsilon_z z + d_{A'_1}(\epsilon_{xx} + \epsilon_{yy})\right](|1\rangle\langle 1| + |-1\rangle\langle -1|) \\ &- \left[d_E(\epsilon_{xx} - \epsilon_{yy}) + d_{E'}(\epsilon_{xz} + \epsilon_{zx})\right](|1\rangle\langle -1| + |-1\rangle\langle 1|) \\ &+ i\left[d_E(\epsilon_{xy} + \epsilon_{yx}) + d_{E'}(\epsilon_{yz} + \epsilon_{zy})\right](|1\rangle\langle -1| - |-1\rangle\langle 1|) \end{aligned} \tag{2.52}$$

where d_{A_1}, $d_{A'_1}$, d_E, and $d_{E'}$ are the spin-strain coupling constants. As shown in fig. 2.13, the A_1 component of the spin-strain interaction results in a modification of the zero-field splitting, uniformly shifting $|\pm 1\rangle$ with respect to $|0\rangle$. The E components of the spin-strain interaction mix $|\pm 1\rangle$. In a perfect crystal with no external perturbations, the E symmetric spin-strain interaction breaks the $|\pm 1\rangle$ spin degeneracy. Notably, the degeneracy of the spin levels cannot be restored with a magnetic field, as the Zeeman interaction does not commute with the E strain interaction.

Traditionally, the spin-strain interaction has been treated phenomenologically using the Hamiltonian for the linear electric field effect derived in electron paramagnetic reso-

nance of transition ions [148, 76, 51, 77], which can be written as

$$\begin{aligned} H_{strain} = &\left[d_{A_1}\epsilon_z z + d_{A_1'}(\epsilon_{xx}+\epsilon_{yy})\right] S_z^2 \\ &- \left[d_E(\epsilon_{xx}-\epsilon_{yy}) + d_{E'}(\epsilon_{xz}+\epsilon_{zx})\right](S_x^2 - S_y^2) \\ &+ \left[d_E(\epsilon_{xy}+\epsilon_{yx}) + d_{E'}(\epsilon_{yz}+\epsilon_{zy})\right](S_xS_y + S_yS_x) \end{aligned} \tag{2.53}$$

By using the spin raising and lowering operators, it can be shown that the spin-strain Hamiltonian derived in this chapter coincides with this phenomenological model.

Stark Effect

The Stark effect can be immediately calculated by recognizing an equivalence between strain and electric fields. Because the NV center lacks inversion symmetry, strain and electric fields transform identically under C_{3v} symmetry [99]. Physically, this means that the polarization of the NV electron cloud has the same effect as the relative motion of the crystal ions. This is closely related to the piezoelectric effect, in which mechanical stress induces a net electric polarization in the crystal. The electric field Hamiltonian is simply given by

$$H_E = -\vec{d}\cdot\vec{E} \tag{2.54}$$

where $\vec{d} = q\vec{r}$ is the electric dipole operator. Because the dipole operator is a vector quantity, its components will transform as the linear elements of the C_{3v} group. In particular, $d_z \sim z$, and thus it will transform as the A_1 irreducible representation. The transverse components $\{d_x, d_y\} \sim \{x, y\}$, and thus they will transform as the E irreducible representation. Therefore, we may identify the following equivalence relations

$$E_z \leftrightarrow \epsilon_{zz}, \epsilon_{xx} + \epsilon_{yy} \tag{2.55}$$

$$E_x \leftrightarrow \epsilon_{xx} - \epsilon_{yy}, \epsilon_{xz} + \epsilon_{zx} \tag{2.56}$$

$$E_y \leftrightarrow \epsilon_{xy} + \epsilon_{yx}, \epsilon_{yz} + \epsilon_{zy} \tag{2.57}$$

Therefore, the dipole operators in the $\{|X\rangle, |Y\rangle, |A\rangle\}$ basis can be written as

$$d_z = \begin{bmatrix} d_\parallel + \tilde{d}_\parallel & 0 & 0 \\ 0 & d_\parallel + \tilde{d}_\parallel & 0 \\ 0 & 0 & 2\tilde{d}_\parallel \end{bmatrix} \tag{2.58}$$

$$d_x = \begin{bmatrix} \tilde{d}_\perp & 0 & 0 \\ 0 & -\tilde{d}_\perp & d_\perp \\ 0 & d_\perp & 0 \end{bmatrix} \tag{2.59}$$

$$d_y = \begin{bmatrix} 0 & \tilde{d}_\perp & -d_\perp \\ \tilde{d}_\perp & 0 & 0 \\ -d_\perp & 0 & 0 \end{bmatrix} \tag{2.60}$$

where we have defined

$$\begin{aligned} d_\parallel &= \langle a_1(2)| \, d_z \, |a_1(2)\rangle \\ \tilde{d}_\parallel &= \langle e_x| \, d_z \, |e_x\rangle \\ d_\perp &= \langle e_x| \, d_x \, |a_1(2)\rangle \\ \tilde{d}_\perp &= \langle e_x| \, d_x \, |e_x\rangle \end{aligned} \tag{2.61}$$

By relating the dipole operators to the orbital operators for the strain interaction,

we can characterize the piezoelectric effect for the NV center, which is described by $\epsilon_{ij} = R_{ijk}E_k$, where R_{ijk} is the third-rank piezoelectric tensor. The components of R_{ijk} can be calculated via

$$\begin{aligned}(d_{\parallel} - \tilde{d}_{\parallel})E_z &= \lambda_{A_1}\epsilon_{zz} + \lambda_{A_1'}(\epsilon_{xx} + \epsilon_{yy}) \\ \tilde{d}_{\perp}E_x &= \lambda_E(\epsilon_{xx} - \epsilon_{yy}) + \lambda_{E'}(\epsilon_{xz} + \epsilon_{zx}) \\ \tilde{d}_{\perp}E_y &= \lambda_E(\epsilon_{xy} + \epsilon_{yx}) + \lambda_{E'}(\epsilon_{yz} + \epsilon_{zy})\end{aligned} \tag{2.62}$$

Using the strain-electric field equivalent relations, we can similarly construct the spin-Stark Hamiltonian. Exactly like strain, the electric field couples to the spin through the spin-orbit and spin-spin interactions. The spin-Stark Hamiltonian written in terms of the Pauli matrices is

$$H_E = k_{\parallel}E_z S_z^2 - k_{\perp}\left[E_x(S_x^2 - S_y^2) - E_y(S_xS_y + S_yS_x)\right] \tag{2.63}$$

where $k_{\parallel} = 0.35$ Hz $\cdot$ cm/V and $k_{\perp} = 17$ Hz $\cdot$ cm/V are the spin-electric coupling constants [149, 104]. Electric fields applied along the NV axis uniformly shifted $|\pm 1\rangle$ with respect to $|0\rangle$ and transverse electric fields mix $|\pm 1\rangle$.

Optical selection rules

Using the results from the previous sections, we can derive the selection rules for electric dipole transitions between the $^3A_2$ ground state and the ^3E excited state and how they change in the presence of crystal strain. In the presence of E symmetric strain, the charge distribution of the NV center is deformed, which alters the electric dipole moment. Here, we will focus on the selection rules for the E_x, E_y, and A_2 transitions, which have the most ideal for photonic applications due to their low coupling to the

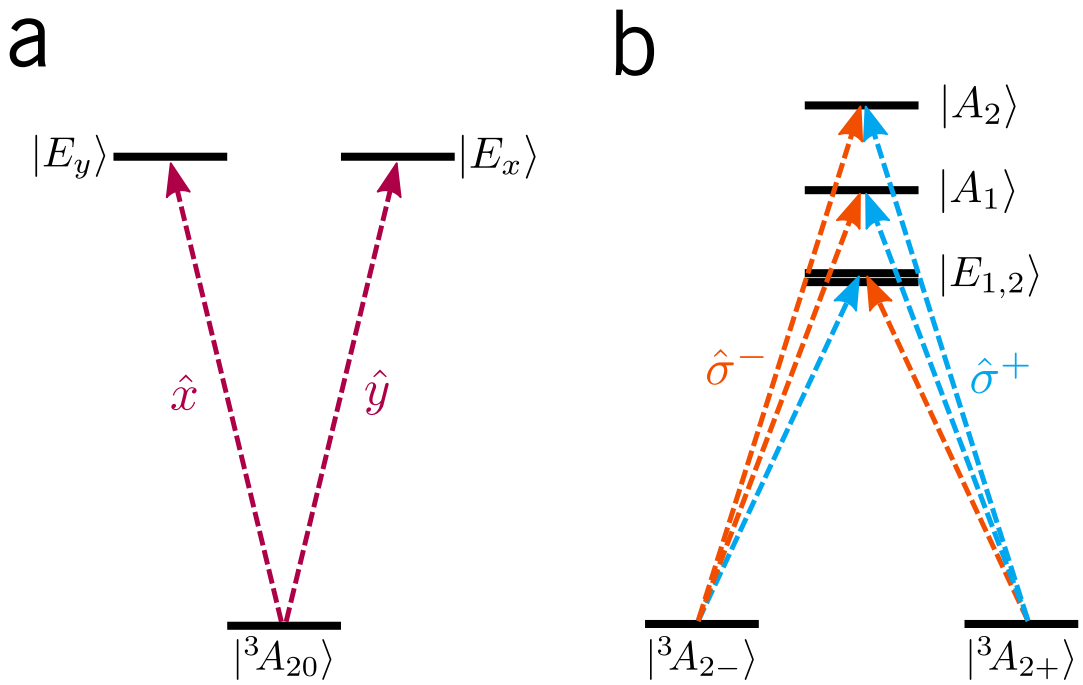

Figure 2.14: **Selection rules for the NV optical transitions in a perfect crystal**. Dipole transitions involving $m_s = 0$ (a) are driven with linearly polarized light. Dipole transitions involving $m_s = \pm 1$ (b) are driven with circularly polarized light.

intersystem crossing. These transitions have all been used for spin-photon entanglement as well as photon-mediated spin-spin entanglement [92, 30, 150]. The fidelity of these operations are intrinsically linked to the strain environment of the NV center, and hence it is critical to have a full understanding of the optical transitions under strain.

Let us first consider the selection rules for the E_x and E_y transitions which correspond to spin projection $m_s = 0$. From the dipole operators derived in the last section, we see that the $|0\rangle \rightarrow |E_x\rangle$ and $|0\rangle \rightarrow |E_y\rangle$ transitions are driven by $\hat{y}$ and $\hat{x}$ polarized light respectively. To calculate the selection rules under E strain, we consider the following simplified strain Hamiltonian

$$H^E_{E_{1,2}} = U_{E_1}(|E_x\rangle\langle E_x| - |E_y\rangle\langle E_y|) + U_{E_2}(|E_x\rangle\langle E_y| + |E_y\rangle\langle E_x|) \tag{2.64}$$

The corresponding eigenstates are linear combinations of the $\{|E_x\rangle, |E_y\rangle\}$ states, which we will denote by $|\phi^{\pm}\rangle$

$$|\phi^{+}\rangle = \cos(\theta)|E_x\rangle + \sin(\theta)|E_y\rangle \tag{2.65}$$

$$|\phi^{-}\rangle = -\sin(\theta)|E_x\rangle + \cos(\theta)|E_y\rangle \tag{2.66}$$

where $\tan(2\theta) = U_{E_2}/U_{E_1}$. The presence of E_2 strain mixes the $|E_x\rangle$ and $|E_y\rangle$. Consequently, E_2 strain rotates the transition dipole moment for the E_x an E_y transitions [80]. We can rewrite the transverse electric dipole operators in the new basis spanned by $\{|\phi^{+}\rangle, |\phi^{-}\rangle, |A\rangle\}$.

$$d_x = \begin{bmatrix} \tilde{d}_\perp \cos(2\theta) & \tilde{d}_\perp \sin(2\theta) & d_\perp \sin(\theta) \\ \tilde{d}_\perp \sin(2\theta) & -\tilde{d}_\perp \cos(2\theta) & d_\perp \cos(\theta) \\ d_\perp \sin(\theta) & d_\perp \cos(\theta) & 0 \end{bmatrix} \tag{2.67}$$

$$d_y = \begin{bmatrix} \tilde{d}_\perp \sin(2\theta) & -\tilde{d}_\perp \cos(2\theta) & -d_\perp \cos(\theta) \\ -\tilde{d}_\perp \cos(2\theta) & -\tilde{d}_\perp \sin(2\theta) & d_\perp \sin(\theta) \\ -d_\perp \cos(\theta) & d_\perp \sin(\theta) & 0 \end{bmatrix} \tag{2.68}$$

From here, we see the two new polarizations required to excite the $m_s = 0$ transitions are

$$\begin{aligned} \hat{e}_+ &= \cos(\theta)\hat{x} + \sin(\theta)\hat{y} \\ \hat{e}_- &= -\sin(\theta)\hat{x} + \cos(\theta)\hat{y} \end{aligned} \tag{2.69}$$

where $\hat{e}_+$ and $\hat{e}_-$ polarizations drive the ϕ^- and ϕ^+ transitions respectively. As

expected, the polarizations remain orthogonal under strain, and hence either transition can be selectively addressed by tuning the polarization of the incident light regardless of the energy splitting.

Now let us look at the $|A_2\rangle$ excited state. Because electric dipole transitions may not change the spin, we must consider the following transitions: ${}^3A_{2+} \leftrightarrow A_2$ and ${}^3A_{2-} \leftrightarrow A_2$. Recall that $|A_2\rangle = \frac{1}{\sqrt{2}}(|E_-\rangle|1\rangle + |E_+\rangle|-1\rangle)$ where $|E_\pm\rangle = |a_1 e_\pm - e_\pm a_1\rangle$. With some algebra, we find that these transitions are driven by circularly polarized light,

$$\begin{aligned} \langle A_2| \frac{d_x + id_y}{2} |{}^3A_{2+}\rangle &= d_\perp \\ \langle A_2| \frac{d_x - id_y}{2} |{}^3A_{2-}\rangle &= d_\perp \end{aligned} \tag{2.70}$$

Specifically, σ^+ light will be required to excite this the $|{}^3A_{2+}\rangle \rightarrow |A_2\rangle$ transition, whereas σ^- light will be required to excite the $|{}^3A_{2-}\rangle \rightarrow |A_2\rangle$. Note that an emission of a σ^+ photon results in a decay to the $|{}^3A_{2-}\rangle$ state and the emission of a σ^- photon results in a decay to the $|{}^3A_{2+}\rangle$ state. In a perfect crystal, the Clebsch-Gordan coefficients for the transitions are equal, which allows the the A_2 transition to be used for spin-photon entanglement. Specifically, the polarization of the photon is maximally entangled with the spin in the Bell state $|\Psi^+\rangle = \frac{1}{\sqrt{2}}(|1\rangle|\sigma^-\rangle + |-1\rangle|\sigma^+\rangle)$ [92].

The change from linear to circular polarization is a direct result of the spin-orbit coupling in the excited state. However, in the limit of large strain, the spin-orbit interaction is washed out and spatial and spin components of the wavefunction are decoupled. In this limit, the A_2 state converges to $|X\rangle|-1\rangle$, and the transition is driven by linearly polarized light. This would destroy the ability to perform the spin-photon entanglement protocol based on photon polarization [99]. The exact polarization dependence as a function of strain can be calculated using the same procedure used for the E_x and E_y transitions.

2.9.4 Intersystem crossing

The intersystem crossing (ISC) is an important internal mechanism of the NV center that enables the optical initialization and readout techniques mentioned at the beginning of this chapter [110]. An intersystem crossing generally refers to a non-radiative transition between states of the different electronic configurations and total spin. In the NV center there are two ISCs between the triplet and singlet manifolds that are relevant to the optical cycle. The first is a state-selective ISC between ^3E and $^1A_1$, which preferentially shelves $m_s = \pm 1$ spin population. The second ISC is between $^1E_{1,2}$ and the ground state $^3A_2$, and does not appear to be appreciably state-selective. Therefore, the first ISC appears to be the primary cause behind the optical spin initialization and readout [151]. In this section we will briefly review the ISC mechanism and outline the relevant rates that determine the spin polarization and fluorescence contrast. We will henceforth refer to the $^3E \rightarrow^1 A_1$ intersystem crossing as "ISC."

The ISC mechanism is demonstrated in fig. 2.15 [151]. The transverse spin-orbit interaction directly couples $|A_1\rangle$ with $|^1A_1\rangle$. However, the states are separated in energy by an amount $\Delta \sim 400$ meV. To conserve energy, the transition from $|A_1\rangle$ must be to a highly excited vibrational level of $|^1A_1\rangle$. The NV will quickly relax (ps timescale) to the vibrational ground state of $|^1A_1\rangle$ through emission of A_1 phonons. Because the vibrational relaxation happens on such fast timescales, the ISC rate is dominated by the transition $|A_1\rangle|\Xi_{\nu_n}\rangle \rightarrow |^1A_1\rangle|\Xi'_{\nu_n}\rangle$, where we have defined $|\Xi_{\nu_n}\rangle$ and $|\Xi'_{\nu_n}\rangle$ to be the n^{th} vibrational levels of the ^3E and $^1A_1$ with energies ν_n. The ISC rate is then determined by the value of the transverse spin-orbit interaction and the vibrational overlap between the triplet and singlet, $F(\Delta) = |\langle\Xi_{\nu_n}|\Xi_{\nu_n}\rangle|^2$. In addition, due to the E symmetric strain interaction, phonons of E symmetry can drive transitions between $|E_{1,2}\rangle$ and $|A_1\rangle$, allowing them to enter the ISC in a second order process. The ISC from these states

is therefore proportional to the spectral density of E phonons interacting with the NV center. It is important to note that this rate is not dominated by direct, single-phonon processes, but rather multi-phonon processes such as Raman transitions.

There have been several experimental determinations of the intersystem crossing rates through lifetime measurements [151, 152, 153, 154], which are shown in fig. 2.15 b. and c. At cryogenic temperatures of less than 22 K, it was determined that the ISC from $|A_1\rangle$ is $\Gamma_{A_1} = 16$ MHz and the ISC rate from $|E_{1,2}\rangle$ is $\Gamma_{E_{1,2}} = 8$ MHz. The ISC rates of A_2 and $E_{x,y}$ are significantly smaller, as each state would enter as a third-order or higher process, either through electron phonon-interactions or the spin-spin interaction. These rates are comparable with the radiative lifetime of the NV center, which is Γ_{Rad} =13.2 MHz. Above 22 K, electron-phonon interactions rapidly mix the orbital levels of the NV center and wash out the orbital doublet of the excited state. The ISC rate of the $|\pm 1\rangle$ spin levels is then given by the average of the ISC rates from the non-zero spin states $\Gamma_{\pm 1} = \frac{1}{4}(\Gamma_{A_1} + 2\Gamma_{E_{1,2}}) = 8.2$ MHz. The ISC rate from the $m_s = 0$ spin level is still fairly low at room temperature, with a value of $\Gamma_0 = 200$ kHz. Given the radiative decay rate of the excited state, there is approximately a 38% chance that $m_s = \pm 1$ population enters the ISC and is transferred to $|^1A_1\rangle$. The population in $|^1A_1\rangle$ rapidly decays to $|E_{1,2}\rangle$ in under a nanosecond. This rate appears to be dominated by non-radiative processes. The lifetime of the $^1E_{1,2}$ state is approximately 450 ns, and is the longest timescale in the optical cycle of the NV center.

Because there exists a high-fidelity initialization protocol at cryogenic temperatures, the focus of theoretical and experimental work relating to the ISC has been on improving the room temperature spin initialization protocol [151]. The primary way to improve the initialization fidelity is to increase the intersystem crossing rate $\Gamma_{\pm 1}$. Because the spin-orbit coupling is fixed, an improvement in the ISC rate will depend on increasing the spectral density of E phonons or the vibrational overlap $F(\Delta)$. Improving the vibrational

overlap could potentially be accomplished by changing Δ. However, strain and electric fields are unable to produce a significant relative shift of these levels. Therefore, the ISC rate must be improved by increasing the spectral density of E phonons [110].

One possible avenue to increase the spectral density is to embed the NV center in a broadband phononic cavity, such as a surface acoustic wave cavity. This should shrink the phonon mode volume while mostly conserving the mode structure of bulk diamond. As our understanding of the ISC improves, there may be other mechanisms that can be exploited to improve the spin polarization.

2.10 Single-crystal diamond mechanical oscillators

Diamond's excellent mechanical properties make it an attractive platform material for high quality factor mechanical resonators [43, 44, 155]. In addition, the large Young's modulus of diamond ($E = 1.2$ TPa) [156] allows for high frequency mechanical resonators to be fabricated with relatively large features, potentially mitigating Q degradation associated with scaling down device dimensions. As we discuss in the final chapter, this will be an important factor in the success of future diamond optomechanical devices. Importantly, diamond mechanical resonators could be used in an integrated hybrid quantum device where embedded crystal defects can couple to the motion of the resonator through crystal strain.

2.10.1 Fabrication of diamond mechanical oscillators

Fabrication of high-quality diamond mechanical structures thus far has been limited due to challenges in processing and growth. Processing of single-crystal diamond (SCD) is difficult due to diamond's chemically inert and robust nature, and is underdeveloped compared to other technologies such as silicon processing. Moreover, challenges in the

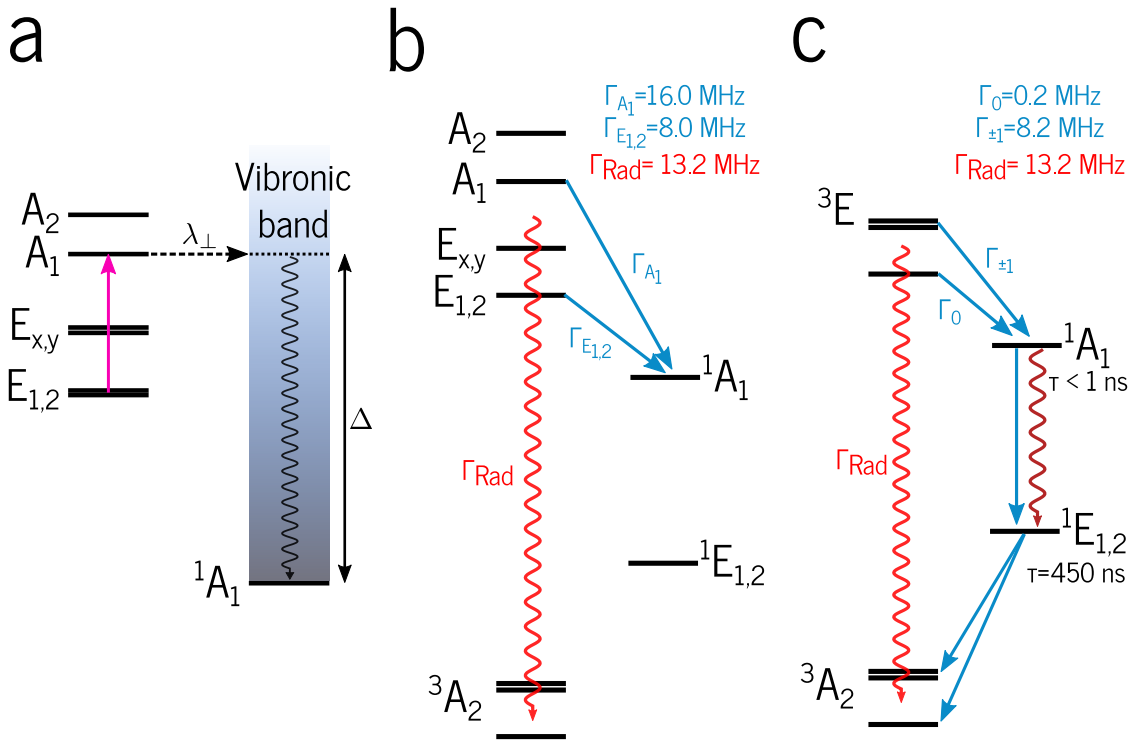

Figure 2.15: **Intersystem crossing mechanism**. a) The primary mechanism for the ISC. Transverse spin-orbit coupling couples $|A_1\rangle$ to a highly excited vibrational level of $|^1A_1\rangle$. The NV center relaxes to the vibrational ground state on the ps timescale through emission of an A_1 symmetric phonon. The $|E_{1,2}\rangle$ states can also enter the ISC via A_1 through electron-phonon interactions (pink arrow). b) Energy diagram of the NV center at cryogenic temperatures (<20 K) with the timescales for each transition involved in the optical pumping mechanism c) Energy diagram of the NV center at room temperature with the timescales for each transition involved in the optical pumping mechanism.

growth of high quality single-crystal diamond has limited the availability of suitable substrates. Nonetheless, SCD mechanical oscillators have now been successfully fabricated in many different forms, including clamped beams [43, 44, 46, 45], bulk acoustic resonators [51], phononic crystals [48], and nano-disk resonators [157, 47] (Fig. 3a).

In this thesis, a"diamond-on-insulator" (DOI) approach is used [43, 44], in which a thin film of diamond is bonded to an oxide-bearing substrate (Fig. 3b). Due to the

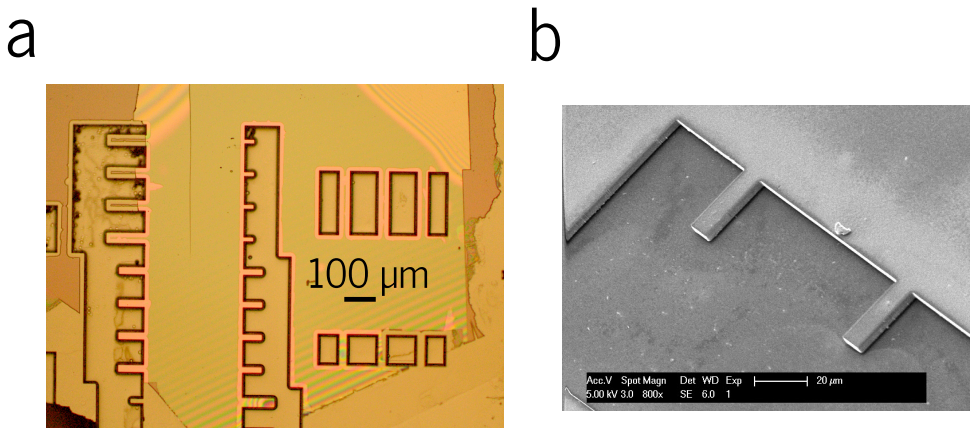

Figure 2.16: **Single-crystal diamond cantilevers**. a) Optical micrograph. b) SEM micrograph

prominent lack of commercially available diamond thin films, this technique requires an additional, time-intensive step of producing the thin film, which can be accomplished with ion-implantation techniques [158, 159] or inductively-coupled plasma/reactive ion (ICP/RIE) etching [43]. The mechanical structures are lithographically defined and subsequently created via ICP etching. The sacrificial oxide layer is etched away using a buffered hydrofluoric (HF) solution, which releases the diamond mechanical structure.

2.10.2 Single-crystal diamond cantilevers

The mechanical oscillators in this thesis consist of micron-scale, single-crystal diamond cantilevers. The use of cantilevers addresses a few important challenges in our experiment. First, we would like to generate a well-characterized and controlled strain in order to quantitatively characterize the strain response of the NV center. We demonstrate exquisite control over the cantilever motion using the mature characterization techniques established in the AFM community. Moreover, the mechanical and elastic properties of cantilevers are well-known and can be described with Euler-Bernoulli beam theory [160]. This allows us to quantitatively determine the NV response to crystal strain, which is

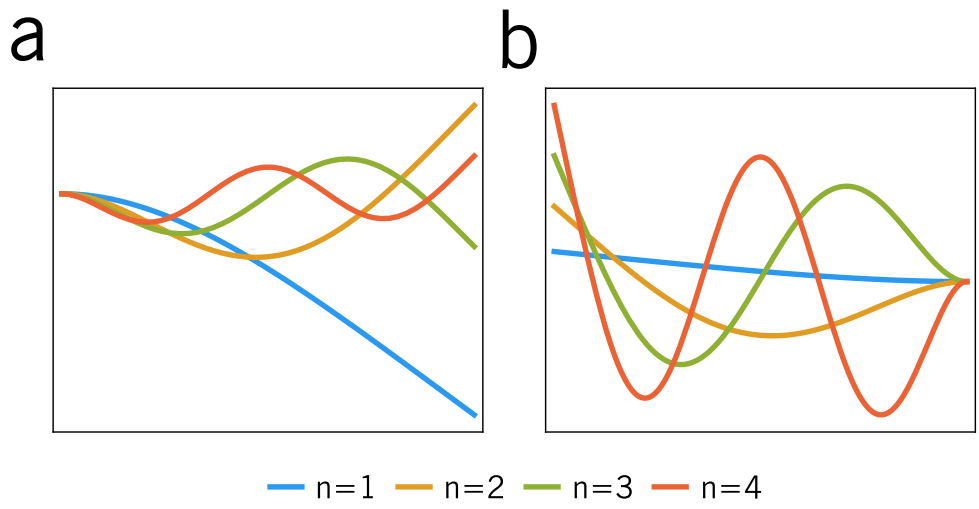

Figure 2.17: **Mechanics of a cantilevered beam**. a) Modeshapes for the first four flexural modes of a cantilever. b) Strain profiles for the first four flexural modes of a cantilever

important for future engineering of mechanical devices. Finally, cantilevers offer a simple device geometry, and can be fabricated with high quality factors.

In the following sections, we will review the mechanical properties of cantilevers. We will first describe the resonant mechanical modes of the cantilever using Euler-Bernoulli beam theory, followed by a derivation of the associated strain profiles. We will conclude the section with experimental data characterizing the diamond cantilevers employed in this thesis. We note that a more detailed discussion of Euler-Bernoulli beam theory can be found in ref. [161].

Cantilever modeshapes for flexural vibrations

The mode shape of a diamond cantilever undergoing flexural vibrations can be described by Euler-Bernoulli beam theory [160]. Here, we calculate the modeshape and resonant frequencies of the first four flexural modes of the cantilever. Consider a singly-clamped diamond beam of length l, width w, and thickness t. The wave equation for

beam deflections of the neutral axis obeys

$$EI\frac{\partial^4 U}{\partial z^4} = -\rho A\frac{\partial^2 U}{\partial t^2} \tag{2.71}$$

where U represents the beam deflection in the y direction and z is along the length of the beam, as shown in the below figure. Here, E is Young's modulus ($E = 1.2$ TPa for diamond), $I = \frac{wt^3}{12}$ is the moment of inertia of the beam, ρ is the mass density ($\rho = 3500$ kg/m^3 for diamond), and $A = tw$ is the cross-sectional area of the beam. The solutions to the above wave equation take the form $U_n(t, z) = u_n(z)e^{-i\omega_n t}$, where $u_n z$ is given by

$$u_n(z) = a_n[\cos(\beta_n z) - \cosh(\beta_n z)] + b_n[\sin(\beta_n z) - \sinh(\beta_n z)] \tag{2.72}$$

which obeys the boundary conditions $u_n(0) = u_n'(0) = u_n''(l) = u_n'''(l) = 0$. The coefficients a_n and b_n satisfy the condition $c_n = a_n/b_n = -1.3622, -0.0919, -1.008, -1.000, ...$ and β_n satisfies the condition $\cos(\beta_n l)\cosh(\beta_n l) = -1$. For the first four flexural modes, we have $\beta_n l = (1.875, 4.694, 7.855, 10.996)$.

The eigenfrequencies of the cantilever are given by

$$\omega_n = \beta_n^2\sqrt{\frac{EI}{\rho A}} = (\beta_n l)^2\sqrt{\frac{E}{12\rho}}\frac{t}{l^2} \tag{2.73}$$

To normalize the modeshapes, we set the potential energy of the beam equal to half of the zero point energy $\sqrt{\frac{\hbar}{4\mu\omega_n}}$, where $\mu = \frac{1}{4}ltw\rho$ is the effective mass of the cantilever. This normalization satisifies the Virial theorem, which states $\langle T\rangle = \langle V\rangle = \frac{\langle E\rangle}{2}$. The modeshapes for the first four flexural vibrations are shown in fig 2.17.

Strain due to flexural vibrations

The strain due to the flexural motion of the beam is constant across the width of the beam, and only varies along z and y. If we look at a point that is R_0 away from the neutral axis of the beam in the y direction, then the strain associated with flexural modes as a function of z is given by $\epsilon_n(z) \simeq -R_0 \frac{d^2 u_n}{dz^2}$, and we obtain

$$\epsilon_n(z) \simeq R_0 \frac{x_0}{\sqrt{2}} \beta_n^2 \left[\cos(\beta_n z) + \cosh(\beta_n z) - c_n(\sin(\beta_n z) + \sinh(\beta_n z))\right] \tag{2.74}$$

In this thesis, we are concerned with the strain felt by an NV center that is near the diamond surface. For an NV center that is implanted at a depth d_i from the surface of the cantilever, then $R_0 = t/2 - d_i$.

If the beam is displaced some amount x_c from its equilibrium point, then the strain will be multiplied by a factor $\frac{x_c\sqrt{2}}{x_0}$ (accounting for comparing absolute versus RMS displacement). Therefore, under a coherent mechanical drive in which the beam is maximally displaced by x_c, then the strain profile for the n^{th} mode can be written as

$$\epsilon_n(z,t) \simeq \left(\frac{t}{2} - d_i\right) \frac{x_c}{2} \beta_n^2 \left[\cos(\beta_n z) + \cosh(\beta_n z) - c_n(\sin(\beta_n z) + \sinh(\beta_n z))\right] \cos(\omega_n t + \phi) \tag{2.75}$$

Mechanical characterization using Fabry-Perot Interferometry

The mechanical properties of the cantilevers can be characterized using Fabry-Perot interferometry [162]. Because our devices are fabricated using the diamond-on-insulator technique, a low-finesse Fabry-Perot cavity exists between the diamond cantilever and the polished silicon substrate with a resting length d. The length of the cavity is modulated by

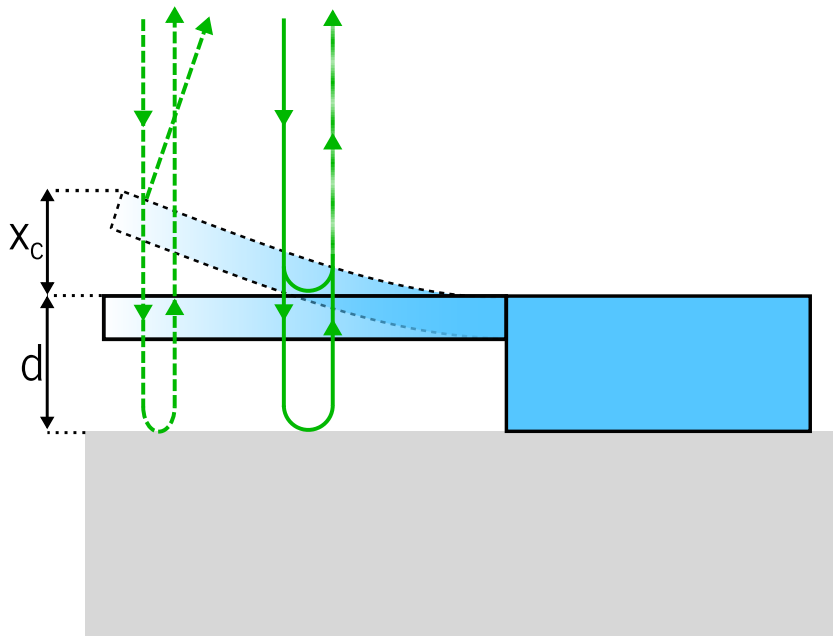

Figure 2.18: **Fabry-Perot interferometry**. A low finesse, Fabry-Perot cavity exists between the surface of the cantilever and the polished silicon that sits below the diamond sample. The resting length of the cavity, d, is defined by the distance between the silicon surface and the equilibrium position of the cantilever. Light that reflects off the cantilever surface interferes with light that passes through the cantilever and reflects off of the silicon. When the cantilever is deflected by an amount x_c, the light passing through the cantilever picks up an additional $2kx_c$ phase due to the change in path length difference.

the motion of the cantilever. Therefore, the light reflected by the cavity will experience a phase shift that is dependent on the position of the cantilever. This is essentially the reverse goal of standard Fabry-Perot interferometry, in which a cavity with a well-controlled length is used to measure frequency changes of a laser.

A critical requirement for this technique is that the coherence length of the laser must exceed the length of the cavity. Another way to say this is that the laser must maintain phase coherence while passing through the cavity so as to not wash out the phase imprinted by the mechanical motion. Measuring the coherence length of a laser can be accomplished by sending the laser through a Mach-Zender interferometer and measuring the interference contrast as a function of the path length difference. In our

experiments, we use a 532 nm or a 450 nm laser as our probe, both of which have coherence lengths of approximately 1 cm, greatly exceeding the resting cavity length.

The light coming back from the cavity will be a combination of light reflected from the cantilever surface and light that has passed through the cantilever and reflected off of the silicon and back through the cantilever. Due to the curvature of the cantilever, the light reflected from the cantilever surface will be slightly displaced at a small angle from the light reflected off of the silicon. This is known as the optical lever effect. The electric field for the light reflected off of the cantilever can be written as

$$\mathbf{E}_1(t) = (1 - \beta x_c(t))\mathbf{E}_0 \left(e^{-i(kx_c(t)-\omega_L t)} + e^{i(kx_c(t)-\omega_L t)}\right) \tag{2.76}$$

where $x_c(t)$ is the cantilever position in time and β quantifies the optical lever effect for small displacements of the cantilever. The light reflected from the silicon surface will pick up a $2kd$ phase shift from traversing the length of the cavity, can be written as

$$\mathbf{E}_2(t) = \alpha\mathbf{E}_0 \left(e^{-i(2kd-kx_c(t)-\omega_L t)} + e^{i(2kd-kx_c(t)-\omega_L t)}\right) \tag{2.77}$$

where α is a scaling factor that takes into account the reflectivity of the silicon and transmission coefficient of diamond.

The signal at the monitor photodiode is given by $S_{PD} = |\mathbf{E}_1 + \mathbf{E}_2|^2$. The photodetector will only pick up time-dependent terms within its detection bandwith (10 MHz for the PDA36A at 0 gain), and hence we will only focus on quasi-static terms of S_{PD}.

$$S_{PD}(t) = |\mathbf{E}_0|^2 \left((1 - \beta x_c(t))^2 + \alpha^2 + 2\alpha(1 - \beta x_c(t)) \left(e^{-i(2k(x_c(t)-d)} + e^{i(k(x_c(t)-d)}\right)\right) \tag{2.78}$$

The output of the photodiode is then sent to a lock-in amplifier for spectral analysis

of the signal. In many cases, we coherently excite the cantilever with a piezoelectric transducer that is electrically driven with the lock-in. The excitation signal can then serve as a reference for lock-in detection of the cantilever motion. For weak mechanical excitation, the cantilever exhibits a linear mechanical response, and the driven motion is well-described by

$$\begin{aligned} x_c(t) &= x(\omega)\cos(\omega t) \\ &= x\frac{(\gamma/2)}{\sqrt{(\gamma/2)^2+(\omega-\omega_m)^2}}\cos(\omega t) \end{aligned} \tag{2.79}$$

where $\gamma = \omega_m/Q$ is the damping rate of the cantilever, ω is the drive frequency of the lock-in amplifier. If we remove DC terms and keep terms to first order in β, we find

$$S_{PD} = -2\beta x_c(t) + 2\alpha(1-\beta x_c(t))\left[\cos(2kd)\cos(2kx_c(t)) + \sin(2kd)\sin(2kx_c(t))\right] \tag{2.80}$$

The lock-in signal essentially picks out the Fourier component of the photodiode signal at frequency ω, and can be written as

$$S_{lockin}(\omega) = \frac{1}{T}\int_0^T S_{PD}(t)\cos(\omega t)dt \tag{2.81}$$

where T is the total measurement time at a particular drive frequency. To properly characterize the mechanics, T must be longer than the correlation time of the mechanical oscillator, or the mechanical ringdown time. In the limit of large T, the integral can be thought of a sum of $N = T\omega/2\pi$ integrals over the range $[0, 2\pi/\omega]$ and we can use orthogonality to simplify the lock-in expression. In our experiments, we typically choose $T = 5T_{ringdown}$.

The lock-in signal can be simplified using the Jacobi-Anger expansion and isolating terms that oscillate at ω.

$$\begin{aligned} S_{lockin}(\omega) = &- 2\beta x(\omega) + 4\alpha J_1\left(2kx(\omega)\right)\sin\left(2kd\right) \\ &- 2\alpha\beta x(\omega)\cos\left(2kd\right)\Big(J_0\left(2kx(\omega)\right) - J_2(2kx(\omega))\Big) \end{aligned} \tag{2.82}$$

where $J_n(z)$ is the n^{th} order Bessel function of the first kind. Because the lock-in will measure the rms voltage, S_{lockin} is always positive, and

$$\begin{aligned} S_{lockin}(\omega) = \Big| &- 2\beta x(\omega) + 4\alpha J_1\left(2kx(\omega)\right)\sin\left(2kd\right) \\ &- 2\alpha\beta x(\omega)\cos\left(2kd\right)\Big(J_0\left(2kx(\omega)\right) - J_2(2kx(\omega))\Big)\Big| \end{aligned} \tag{2.83}$$

Brownian motion

A simple technique that can be used to calibrate the lock-in signal is to use the interferometer to measure the Brownian motion of the cantilever. When the cantilever is at thermal equilibrium, it exhibits motion with a random amplitude and phase at its resonance frequency. The mean displacement of the cantilever in thermal equilbrium is precisely zero, but its variance is non-zero and determined by the equilibrium temperature, as predicted by equipartition theorem.

$$\langle x^2\rangle = \frac{k_B T}{\mu\omega_m^2} \tag{2.84}$$

The variance of the mechanical motion is directly related to the autocorrelation func-

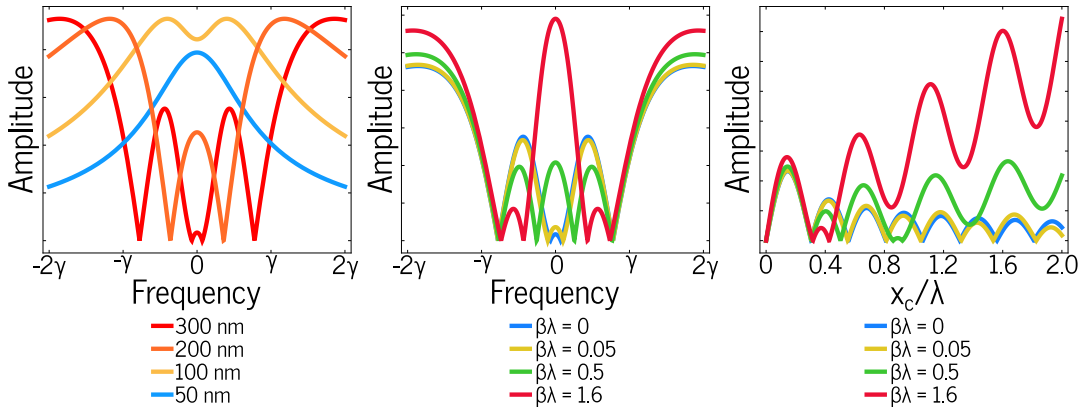

Figure 2.19: **Interferometer signal**. Left: The theoretical interferometer signal as a function of frequency for various drive amplitudes assuming no optical lever effect and a probe laser with $\lambda = 532$ nm. As the amplitude of motion increases, the signal transforms from a Lorentzian lineshape to a series of interference fringes. Center: The theoretical interferometer signal as a function of frequency for a fixed drive amplitude of 300 nm, variable optical lever constant, and a probe laser with $\lambda = 532$ nm. As the optical lever effect increases, the interference fringes are washed out. Right: The theoretical interferometer signal for a resonantly driven oscillator as a function of drive amplitude for various optical lever constants and a probe laser with $\lambda = 532$ nm. As the optical lever effect increases, the signal becomes dominated by amplitude modulation of the photodiode signal and washes out the phase modulation signal

tion of the position operator

$$G_{xx}(t) = \langle x(t)x(t')\rangle \tag{2.85}$$

The autocorrelation function G_{xx} measures the degree to which the position fluctuations at times t and t' are correlated. The decay constant of the position autocorrelation function, τ, is the correlation or ringdown time and is related to the mechanical Q of the cantilever. Using our interferometer, we measure the power spectral density of the position. The power spectral density is formally defined as

$$S_{xx}(\omega) = \int_0^T dt \int_0^T dt' \langle x(t)x(t')\rangle e^{i\omega(t-t')} \tag{2.86}$$

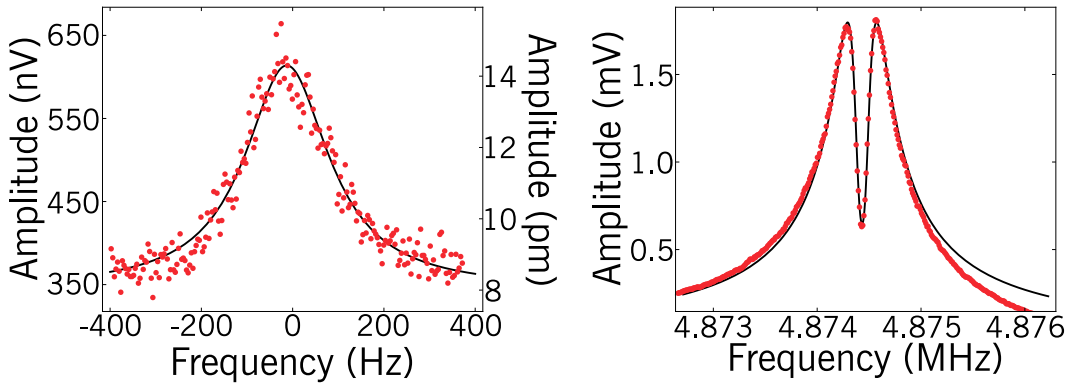

Figure 2.20: **Mechanical response of a diamond cantilever**. Left: Interferometric signal showing the brownian motion of a cantilever with dimensions $30 \times 2 \times 0.67$ μm taken in vacuum (10^-2 torr) and at room temperature. A Lorentzian fit to the data is shown in black. Right: Interferometric signal (red dots) showing the driven motion of the cantilever with an amplitude of motion $x_c = 188$ nm. A fit to the expected response is plotted in black.

where again T is the measurement time. If $T \gg \tau$, then we may extend the bounds on the inner integral to infinity. The bandwidth of the spectral density is $1/\tau$, and hence the major contributions to the spectral density will lie in the interval $\{-T, T\}$. If we utilize the fact that Brownian motion is time-translation invariant, we find that the power spectral density can be written as

$$S_{xx}(\omega) = \int_{-\infty}^{\infty} dt \langle x(t)x(0)\rangle e^{i\omega t} \tag{2.87}$$

This is known as the Wiener-Khinchin theorem. In the limit that $Q > 1$, the power spectral density of the position is a Lorentzian centered around the cantilever resonance frequency with a width determined by the quality factor.

$$S_{xx}(\omega) = \frac{k_B T}{\pi \mu \omega_m^2} \frac{(\gamma/2)}{(\gamma/2)^2 + (\omega - \omega_m)^2} \tag{2.88}$$

The mechanical linewidth is defined to be $\gamma = \omega_m/Q$. The units of the position spectral density are m^2/Hz. To get the total amplitude of Brownian motion, one must integrate the spectral density over the entire frequency spectrum. The rms position is merely

$$\begin{aligned} x_{rms} &= \sqrt{\langle x^2 \rangle} \\ &= \sqrt{\frac{k_B T}{\mu \omega_m^2}} \end{aligned} \tag{2.89}$$

To calibrate the interferometer signal, we compare the peak height of the Brownian motion signal to the peak height of the mechanical response under a weak coherent drive. In fig. 2.20 a., we show a measurement of the Brownian motion of a cantilever with a resonance frequency $\omega_m/2\pi = 4.8745$ MHz. The measurement was performed at room temperature in a vacuum environment of approximately 1 torr. The measured linewidth of the cantilever is $\gamma/2\pi = 220$ Hz, implying a quality factor $Q = 2.2 \times 10^4$. Alternatively, the the quality factor can be determined by a mechanical ringdown measurement, which mitigates line broadening due to drifts in the mechanical frequency [43].

Mechanical quality factors

The cantilevers studied in this thesis have frequencies ranging from 600 kHz to about 5.3 MHz. All of these cantilevers have relatively high quality factors, where the lowest Q is approximately 1.2×10^4 for the 5.3 MHz cantilever and the highest Q is approximately 3×10^5 for a cantilever with a frequency of approximately 900 kHz. These Qs are comparable to state of the art cantilevers employed in atomic force microscopy [163]. Typically, as the mechanical frequency increases, the quality factor will decrease, and hence it is useful to discuss the Qf product. At room temperature, the largest ever

Qf product ever reported is 1.66×10^{14} [49] for a 1.6 MHz silicon nitride membrane resonator embedded in a phononic shield. By comparison, the resonators in this thesis at that frequency achieve a Qf product of roughly 10^{11}. The limits to the cantilever quality factor have not been determined, but have been attributed to two-level defects, surface chemistries, surface roughness, and clamping losses [43, 44, 164].

Chapter 3

Experimental setup

> "You know what they say. 'Fool me once, strike one, but fool me twice,... strike three' " - Michael Scott

In this chapter, we will review the experimental setup used for measuring our hybrid NV-mechanical devices. The primary setup consists of a homebuilt laser scanning confocal microscope integrated with a cryogen-free cryostat. The confocal microscope is used to locate, analyze, and manipulate individual NV centers embedded in our diamond samples, which are hosted inside the cryostat. The cryostat provides a low-temperature environment necessary for resolving the fine structure of the orbital excited state of the NV center, and also provides a high vacuum environment to mitigate viscous damping of the mechanical resonators. In addition, the cryostat is equipped with a microwave antenna for coherent spin manipulation and a low-capacitance piezoelectric transducer for resonant mechanical excitation. In the following sections, we will review the basics of confocal microscopy, the design and components of our apparatus, and relevant experimental constraints that were considered during the design process.

3.1 Scanning confocal microscope

The confocal microscope is a powerful and versatile imaging tool that has been critical to experiments throughout the natural sciences. In contrast to a standard optical microscope which uniformly illuminates a sample, a confocal microscope illuminates and images a single point on the sample [165]. To illuminate a single point of the sample, the *excitation* or *illumination* light is sent through a high numerical aperture (NA) microscope objective and focused onto the sample to a diffraction-limited spot size. The (NA) of an objective quantifies the amount of light that the objective can collect, and is given by

$$NA = n \sin(\theta) \tag{3.1}$$

where n is the index of refraction of the medium the objective is working in and θ is the maximum angle of light emanating from the focal point that makes it into the objective. A higher NA objective allows for tighter focusing of the excitation beam and greater collection efficiencies. Consequently, the NA essentially determines the spatial resolution of the confocal microscope. Only the fluorescence of objects located in the illumination volume will contribute to the confocal microscope image. The fluorescence can be imaged onto a pinhole aperture in the image plane, which rejects light that is out of focus or not in the image plane, hence defining the detection or collection volume. Under these conditions, the illumination and collection volumes are said to be $confocal$ [165].

The spatial resolution of a confocal microscope is determined by the point spread function of the microscope, and under ideal conditions is [166]

$$\phi_r = \frac{\kappa\lambda}{NA} \tag{3.2}$$

$$\phi_z = \frac{n\lambda}{NA^2} \tag{3.3}$$

whereλ is the wavelength of the excitation light, and κ is a constant typically around 1 that varies depending on the apparatus. In our experiments, κ is determined by the diffraction limit, or the Airy unit diameter, giving $\kappa = 1.22$. In our experiments, we uniformly illuminate the back aperture of our microscope objective ($NA = 0.7$) with $\lambda = 532$ nm laser light, which is then focused onto the sample with a diffraction limited spot size of $\phi_r \sim 920$ nm. The axial resolution of the microscope is then $\phi_z \sim 1.1$ μm. Therefore, the excitation/detection volume is confined to about 1 μm^3. While the confocal microscope affords exceptional spatial resolution, it comes at a cost when trying to image a large sample. In order to get an image of a large sample, the excitation light must be rastered across the sample. To get a fully three-dimensional image, the light must then be rastered at different focal planes.

3.1.1 Design of the confocal microscope

In this subsection, we will give a brief description of the confocal microscope, and provide a detailed description of the important components in further sections. A schematic of our homebuilt scanning confocal microscope is shown in fig. 3.1. The excitation light is provided by a 532 nm laser (shown schematically in green), which enters the apparatus through a fiber port. The excitation light is sent through polarization optics before being introduced into the confocal path through a longpass dichroic beam splitter (Semrock Di01-R532-25) which reflects approximately 94% of the laser light. A fast scanning mirror (FSM-300-02) is used to raster the excitation laser across the sample. Piezoelectric

actuators tilt the fast scanning mirror in two orthogonal directions which deflect the beam at an angle with respect to the confocal axis. The excitation light passes through a scanning telescope (see following section for design details) to direct the beam onto the back aperture of the objective. The excitation light then passes through an infinity corrected objective (Olympus LCPLFLN50xLCD) with $NA = 0.7$ and focused onto the diamond sample, which sits inside a closed cycle cryostat. The NV fluorescence collected by the objective is sent back through the confocal path and is passed through the dichroic beam splitter (transmission $\sim 93\%$.) The fluorescence is further passed through longpass filters (BLP01-594R-25) to reject any light outside of the NV photoluminescence band. The light is then coupled into a single mode fiber (SM800) which is sent directly to an avalanche photodiode (APD) single photon detector (Perkin Elmer SPCM-AQR-14) with a measured dark count rate of 100 Hz.

3.1.2 The scanning telescope

In order to direct the beam into the objective, a scanning telescope consisting of two convex lenses, L_1 and L_2, with focal lengths f_1 and f_2, is placed in between the fast scanning mirror and objective. If the scanning telescope is positioned correctly, the laser's position and size will be matched to that of the back aperture of the objective while the entrance angle is varied. For the beam to not move off of the back aperture of the objective as the fast scanning mirror moves, the lenses L_1 and L_2 must be a distance f_1 and f_2 away from the fast scanning mirror and back aperture of the objective respectively. Any deviation from this will result in not only a loss of excitation power, but also a decrease in the photon collection efficiency.

This loss can be calculated by considering the overlap between two Gaussian beams of waist w. Consider a scanning telescope such that L_1 is a distance $d_1 = f_1 + \delta d_1$ from the

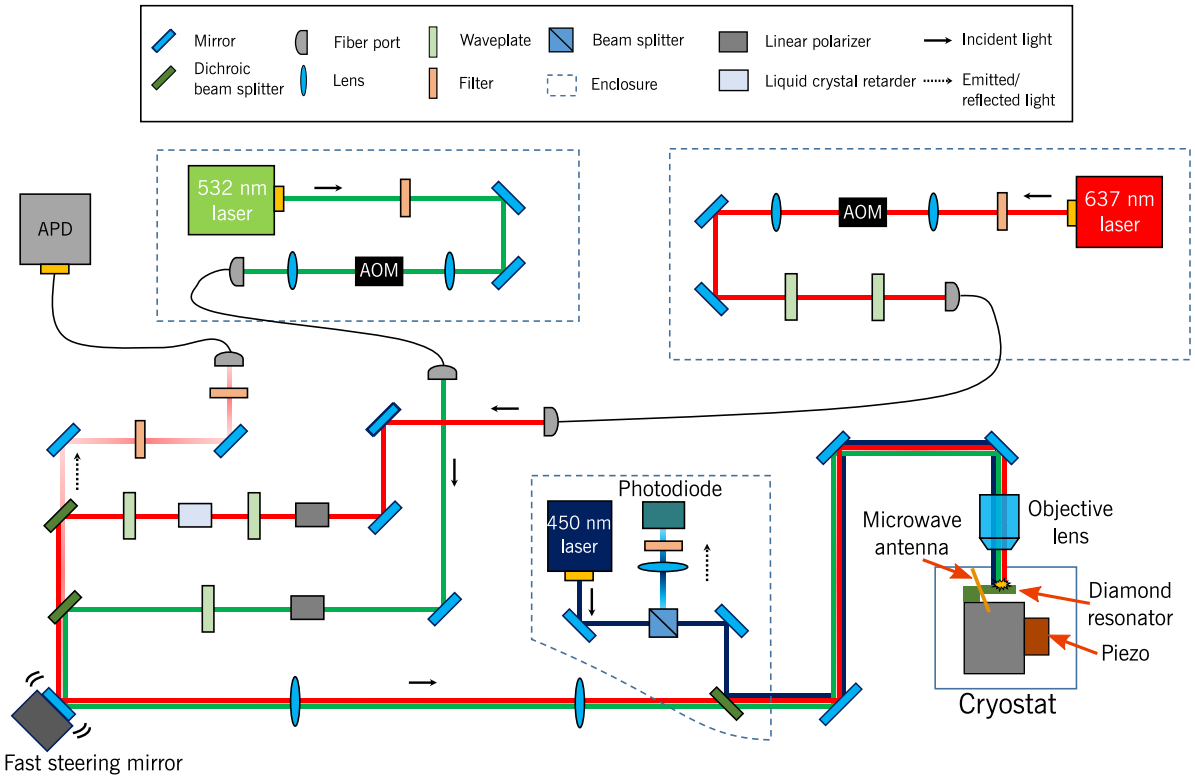

Figure 3.1: **Schematic of the cryogenic scanning confocal microscope**. The optical path of each laser is shown in color and the relevant propagation directions are shown in black arrows. A legend for the schematic is found above.

fast scanning mirror and L_2 is a distance $d_2 = f_2 + \delta d_2$ away from the back aperture of the objective. Assuming that the telescope input and output is collimated, the displacement of the laser center due to an angular displacement θ from the confocal axis is

$$\delta r = \left(\frac{f_2}{f_1} \delta d_1 + \frac{f_1}{f_2} \delta d_2 \right) \theta \tag{3.4}$$

The loss in excitation power and collection is then quantified by

$$P_{loss} = 1 - e^{-\delta r^2 / 2w^2} \tag{3.5}$$

In addition, the scanning telescope will determine the field of view of the confocal microscope. The field of view is determined by the maximum entrance angle into the

objective, and is given by

$$FOV = 2 \times WD \times \tan\left(\frac{f1}{f2}\theta_{max}\right) \tag{3.6}$$

where WD is the working distance of the objective and $\theta_{max} = 1.5°$ is the maximum deflection angle of the fast steering mirror. The FOV for our apparatus is approximately 100×100 μm.

3.1.3 Microscope objective

The primary microscope objective used on this apparatus is an infinity-corrected, Olympus LCPLFLN50xLCD microscope objective with a $NA = 0.7$. The objective is apochromatic to mitigate chromatic aberrations, and displays a nearly constant transmission of $\sim 90\%$ over the relevant wavelength ranges for our experiment (450-850 nm). The objective is equipped with a coverslip correction collar, which allows the objective to correct for spherical aberrations from imaging through glass up to 1.2 mm in thickness. In our experiments, we image through two 200 μm windows (the cryostat lid and the radiation shield window), and hence set the correction collar to a value of 0.4. The objective was partially chosen for its large working distance of 2.7 mm, which maximizes the space inside of the cryostat. The large working distance, however, comes at the cost of NA and hence collection efficiency. The objective is mounted on an NPoint nanopositioning piezo stage for fine adjustment of the focus. The NPoint stage is mounted to a large breadboard supported by three 1.5 in. stainless steel posts, as shown in fig. 3.2. The breadboard height can be coarse adjusted using a series of adjustable height collars (Thorlabs PSHA) over a range of 8.2 mm (640 μm per revolution). It is important that the breadboard be kept level with the optical table during adjustment. To minimize the effect of vibrations from the compressor, these collars are left unlocked. This allows the

objective platform to vibrate in phase with the sample inside of the cryostat.

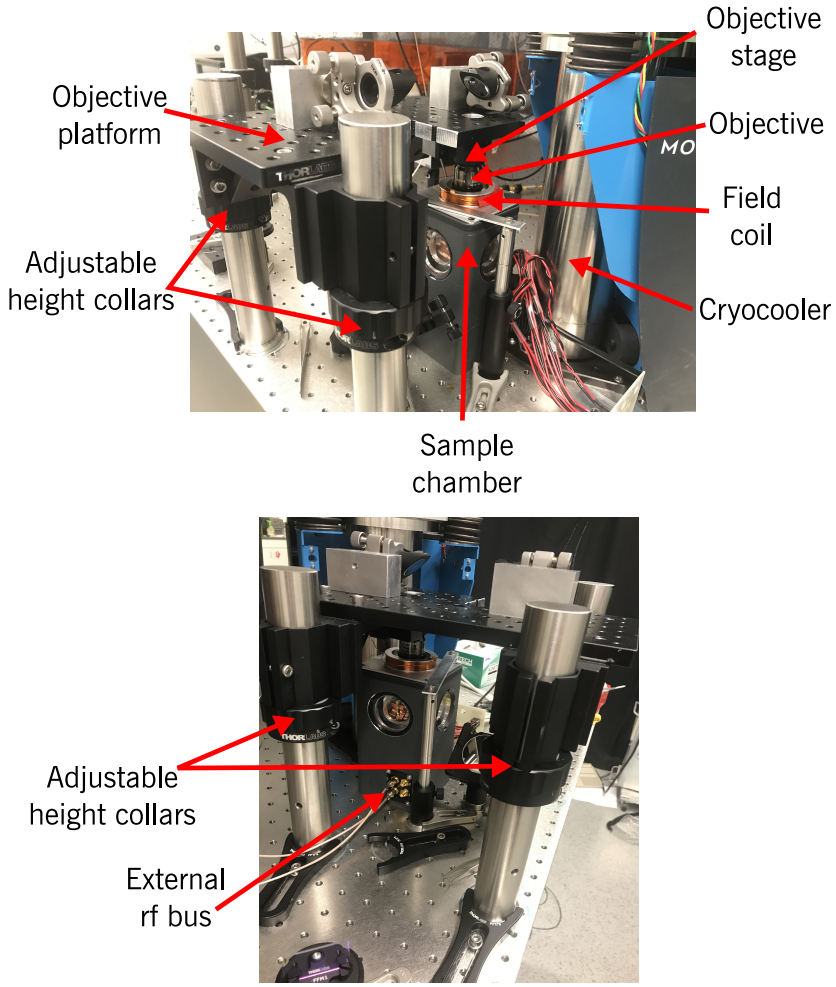

Figure 3.2: **Photographs of the cryogenic confocal microscope (external).** Top: The sample is hosted inside the chamber of the cryostat. A magnetic field coil is clamped to the lid of the cryostat. The objective is mounted on a piezoelectric nanopositioner and placed inside the field coil. The objective stage is mounted onto a platform breadboard. The height of the breadboard can be adjusted using three adjustable height collars (two shown). Bottom: Alternative view showing the third height collar and the external rf bus located on the side of the sample chamber.

3.1.4 Laser systems

The confocal microscope is equipped with 3 different laser systems, which are used for optically addressing single NV centers and characterizing the mechanical properties of our diamond mechanical oscillators. The primary science laser is a continuous-wave (cw) diode laser at 532 nm (Laser Quantum gem 532) with a maximum power of 100 mW and a coherence length of approximately 1 cm. As described later, this laser is used for optically addressing the NV center as well as characterizing the mechanical resonances of single-crystal diamond cantilevers. The 532 nm laser is sent through an Intraaction acousto-optic modulator (AOM) and the first order diffracted beam is coupled to a single mode fiber (460HP) which is sent to the confocal microscope. The AOM is primarily used as a switch, and has a rise time of about 12 ns with a maximum extinction ratio exceeding 10^6. The AOM is driven with an Isomet driver operating at 200 MHz integrated with a passive noise-eating circuit, which improves the extinction ratio of the AOM from 10^3 to greater than 10^6.

The laser power is adjusted with a series of neutral density filters of varying strengths that are hosted in a Thorlabs filter wheel. The laser polarization is controlled with a linear polarizer and a half-wave plate. The linear polarization is matched to the optical transition dipole moment of the NV center by monitoring the PL as a function of the half-wave plate angle and choosing the maximizing angle. At room temperature, the optimal polarization is roughly the same for all NVs, in contrast with NVs at cryogenic temperatures. This can be explained by electron-phonon interactions and the dynamic Jahn Teller effect, which washes out the orbital-doublet nature of the excited state [167].

The confocal microscope is also equipped with a cw narrow-linewidth ($\sim$ 300 kHz), tunable, external cavity diode laser operating near 637 nm (New Focus Velocity). As described in chapter 5, this laser is used for resonant excitation of the optical transitions

of the NV center. The 637 nm laser can be coarse tuned over a 3 nm range spanning 636-639 nm with 0.01 nm resolution, and can be fine tuned over a 38 GHz frequency band by scanning the laser cavity piezo. The 637 nm laser also outputs a significant amount of yellow light which can couple into the APD and significantly increase the background counts. We filter out the yellow light using a series of bandpass filters centered around 637 nm. The laser is passed through an AOM similar to the 532 nm laser and coupled into a single-mode fiber (SM600) and sent to the confocal microscope. The AOM in this case is driven by a homebuilt rf driver that consists of a voltage controlled oscillator, voltage variable attenuator, microwave switch, and a microwave amplifier. The extinction ratio of the AOM using the homebuilt driver is greater than 10^6, and hence does not require a noise-eating circuit.

The 637 nm laser is introduced into the confocal microscope through a dichroic beamsplitter with a cutoff wavelength of 640 nm as depicted in fig. 3.1. To minimize background 637 nm light reflected from the sample, a series of longpass filters are placed in front of the collection fiber. This results in a slightly reduced photon collection rate from the NV center (10-20% loss), but completely extinguishes scattered excitation light. The extinction ratio is very sensitive to the relative angle between the optical axis and the filters. To calibrate the angle, we focused on a single NV center and varied the position of the filters while optimizing the fluorescence collection rate.

To perform fine scans of the 637 nm laser frequency, we apply a series of voltages generated by the DAQ directly to the laser piezo. The relative frequency shift per piezo voltage was calibrated via Fabry-Perot interferometry using a scanning invar cavity with a free spectral range of 1.5 GHz. Although the laser piezo can handle voltages spanning (-10, 10) V, we found that the scan is only linear in piezo voltage from (-7.5, 7.5) V and is highly nonlinear otherwise (see fig. 3.3). We note that our measurements of the scanning range differ by a factor of 2 from the New Focus specifications.

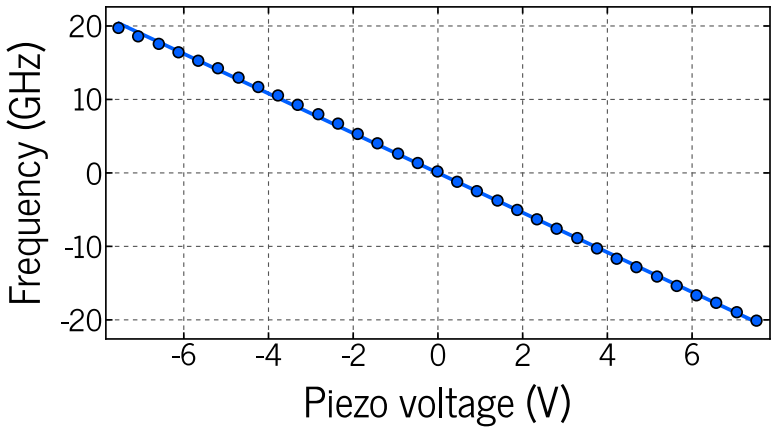

Figure 3.3: **Laser calibration**. Calibration of the 637 nm laser fine scan. The frequency sweep is linear in voltage from -7.5 to 7.5 V, yielding a frequency shift of -2.725 GHz/V

The laser power was controlled by either changing the laser diode current or passing the laser through a series of neutral density filters. The polarization of the 637 nm laser was controlled with a linear polarizer and a liquid crystal retarder. The liquid crystal retarder allows for rotation of the laser polarization while keeping the laser intensity constant. In the experiments of chapter 5, we characterize the orientation of the electric dipole moment of the NV center, which requires precise calibration of the laser polarization with respect to the crystal axes. To this end, we used a polarimeter (Thorlabs) to determine the absolute polarization of the laser.

The final laser used in the confocal microscope is a cw diode laser at 450 nm with a maximum power of 5 mW and a coherence length exceeding 1 cm. This laser was used for characterizing and stabilizing the driven mechanical motion of diamond cantilevers. This laser is directly introduced into the confocal microscope with a long-pass dichroic beamsplitter.

3.1.5 Control of the confocal microscope

The experimental apparatus is controlled using custom software written in MATLAB. The program contains two GUIs: one to control the confocal microscope (ImageScan) and one to interface with the control electronics (ESRControl). Both GUIs communicate with a data acquisition and DAQ board (NI PXIe-6361). Two DAQ outputs are used to control the orientation and position of the fast scanning mirror. A single DAQ output is used to control the objective piezo stage (NPoint) for fine tuning of the microscope focus over a 100 μm range. A counter on the DAQ board is used to process the APD signal. For a comprehensive overview of the control software, I refer the reader to ref. [168].

3.2 Microwave electronics

As discussed in chapter 2, the spin of the NV center can be coherently manipulated using near resonant microwave magnetic fields at approximately 2.87 GHz. Microwave fields are delivered to the sample through a gold wirebond that is placed just above the sample. The microwave circuit is shown schematically in fig. 3.4. Microwaves are generated using a microwave signal generator (SG384).The frequency and power settings of the signal generator are controlled with the MATLAB control software. The output of the signal generator is first sent through a SPDT high isolation switch (ZASWA-2-50-DR) with a rise time of 5 ns to generate microwave pulses. As described in the following section, this switch is gated by a pulse timing generator. The output of the switch is then sent through a high power microwave amplifier (ZHL-16W-43+). The amplified signal is passed through a circulator (NARDA 4923) and to the microwave SMA interface of the cryostat (see fig. 3.2). A combination of stiff and flexible SMP cables are used to deliver the microwave signal to the coplanar waveguide (CPW) sample holder. A gold wirebond with a diameter of approximately 30 μm connects the inner conductors

of the CPW and is placed nearby the diamond sample. The transmitted signal through the CPW is sent back through the cryostat interface and either terminated with a high power 50 Ω terminator or measured using a SRS spectrum analyzer. For an optimally placed antenna, a 1 mW output from the signal generator will produce a field of about 9 G at the NV, corresponding to a microwave Rabi frequency of 25 MHz.

In some of the pulsed measurements described in this thesis, we require phase control of the microwave source, which is accomplished through IQ modulation. The total microwave signal can be written as

$$\begin{aligned} V(\omega) =& I\cos(\omega t) + Q\sin(\omega t) \\ =& A\sin(\omega t + \varphi) \end{aligned} \tag{3.7}$$

where $A = \sqrt{I^2 + Q^2}$ and $\varphi = \tan^{-1}(Q/I)$. I and Q are controlled with by an external voltage input located on the real panel of the signal generator. The allowable voltage range for each input spans (-0.5, 0.5) V.

3.3 Pulse timing electronics

To perform pulsed measurements, we use a SpinCore PulseBlasterESR-PRO 500 MHz card (Pulseblaster) to generate TTL control pulses. The Pulseblaster can generate up to 24 independent TTL signals (assigned to bit 1, 2, 3, ...) that are synchronized to a single clock. The outputs of the Pulseblaster are sent through a homebuilt TTL interface for ease of access. Bit1 is assigned to the AOM driver for the 532 nm laser, and is used for switching the laser on and off. Bit2 is assigned to the trigger of the DAQ counter input which measures the signal from the APD. Bit3 is assigned to the microwave switch, is used to create square microwave pulses. Bits 5-8 are used to for IQ modulation of the

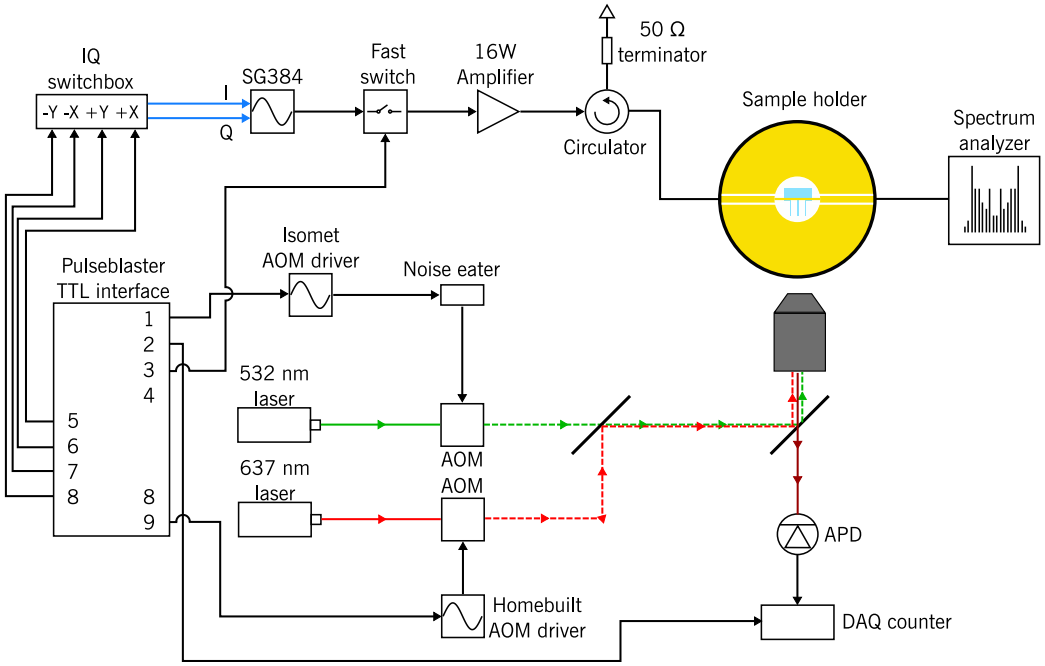

Figure 3.4: **Electrical schematic of the apparatus**. The schematic shows the microwave and pulse timing control electronics.

microwave signal. The TTL pulses are sent through a homebuilt circuit board which attenuates the pulses from 3.3 V to ±0.5 V and then sent to the IQ modulation inputs of the SG384. In our setup, we map bits (bit5, bit6, bit7, bit8) to $\varphi = (0, 90°, 180°, 270°)$. For a more detailed discussion of the pulse timing, we refer the reader to ref. [168].

3.4 Magnetic field electronics

As discussed in chapter 2, we apply a small magnetic field to the NV center in order to break the degeneracy of the $m_s = \pm 1$ spin levels. In the experiments described in chapter 4, the magnetic field is generated by a rare earth magnet. In the experiments described in chapter 6, the magnetic field is generated by a half-Helmholtz coil, which sits on the lid of the cryostat as depicted in fig 3.5. The coil is approximately 2 in. in

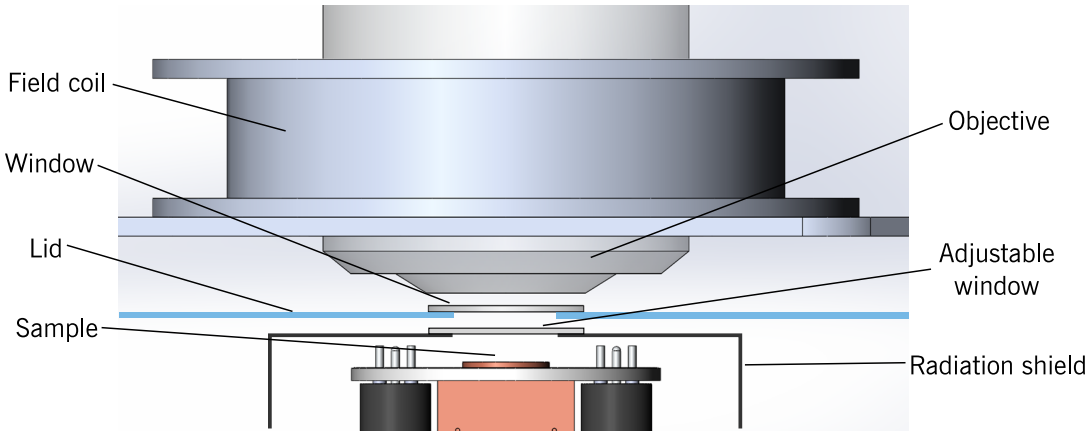

Figure 3.5: **Cross section of the cryostat**. A cross section of the cryostat shows the relative positions of the magnetic field coil, objective, and sample. The sample–to-window distance varies with temperature, but is typically on the order of 1 mm. The sample to coil center distance is approximately 1 cm.

diameter and contains 100 turns of wire. The field coil is driven with a custom-built, low-noise current source that can supply current up to 1 A. The value of the current is set by an external voltage supplied by a DAQ output, where the current is given by 1 A/V. To further reduce noise in the current, the control voltage output from the DAQ is sent through a differential amplifier to break the ground loop with the computer power supply. The current source is connected to the external electrical bus of the fridge, as shown in fig 3.9.

The field coil sits approximately 1 cm above the sample, depending on the operating temperature of the cryostat. If the sample sits laterally in the center of the coil, the magnetic field will be approximately perpendicular to the plane of the diamond sample (along the (001) crystal direction), producing a field $B_{(001)} = (24\ \mathrm{mG/mA})I_{coil}$. Note that this field will generate the same longitudinal magnetic field for all four NV orientations, $B_z = \frac{B_{(001)}}{\sqrt{2}}$. The use of the field coil allows for precise tuning of the Zeeman splitting, which is a crucial requirement for the coherent strain-driving measurements presented in chapter 6.

3.5 Mechanical resonance characterization

The resonant modes of our diamond mechanical oscillators are actuated with a low capacitance ($\sim$ 25 nF), piezoelectric transducer (Noliac NAC2011) that is electrically driven using a lock-in amplifier (Zurich Instruments HF2). The piezo is soldered to two phosphor-bronze wires which are wrapped around a copper bobbin for thermal anchoring and lagging and connected to the fridge at a user interface (see figure). The piezo is mounted to the sample holder with a set screw and flat copper clamp. The piezo-cantilever coupling is very sensitive to the clamping conditions, due to its small surface area. Once the coupling is maximized, the clamp is never touched again unless it needs to be tuned. To remove the sample holder from the fridge, the piezo must be disconnected from the fridge.

The lock-in amplifier contains two channels that can be independently controlled. In addition, the lock-in is equipped with two phase-locked loops and four PID servo controllers. We control the lock-in externally through commercial software (ziControl). To characterize the driven motion of the cantilevers, we use the "Sweeper" function within ziControl. The Sweeper function measures the demodulated input signal for either a varying output frequency or amplitude. To characterize the brownian motion of the cantilevers, we use the FFT function within ziControl.

As discussed in Chapter 2, the mechanical properties of the cantilevers are characterized using Fabry-Perot interferometry where either the 450 nm or 532 nm lasers are used as the probe laser. In this section, we will describe the interferometer setup for the 450 nm laser, which is shown schematically in fig. 3.6. The 450 nm laser is first sent through a non-polarizing 50:50 beamsplitter, which is used to send light reflected from the sample to a photodiode with a bandwith of 125 MHz (Newport 1801-FS). The light is then introduced into the confocal path through a dichroic beamsplitter. The beam

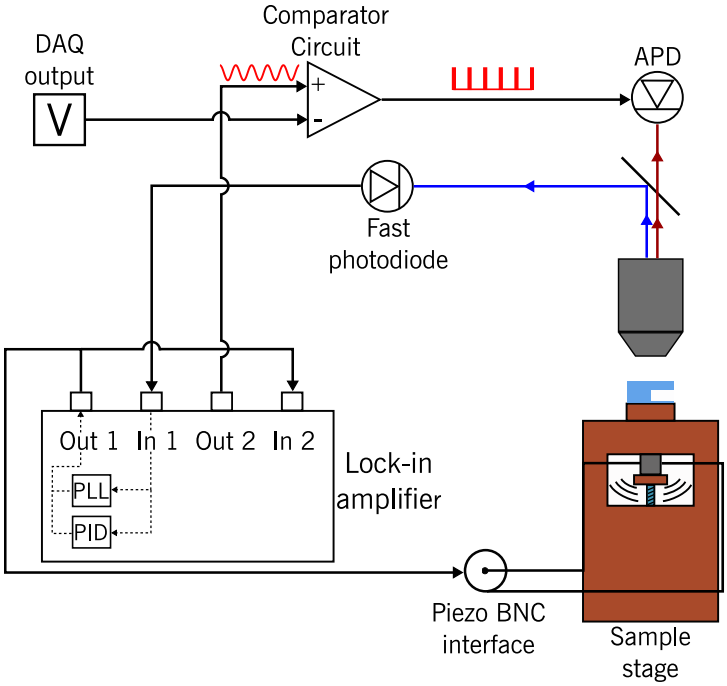

Figure 3.6: **Circuit for mechanical characterization**. A lock-in amplifier is used to actuate a piezoelectric transducer clamped to the sample stage. The interferometer signal is demodulated with the lock-in amplifier. Using feedback, the mechanical resonance can be stabilized. Furthermore, the lock-in can be used to perform stroboscopic PL measurements using a homebuilt ADC circuit.

is introduced after the fast-steering mirror due to space constraints, and its position is determined by a two-mirror periscope. The blue light is focused to a spot of roughly 3 microns in diameter onto the cantilever. Light reflected from the diamond surface and the underlying silicon substrate interfere and are sent to the photodiode for spectral analysis. A band-pass filter centered at 450 nm is placed in front of the photodiode to minimize crosstalk introduced by the 532 nm laser.

The output of the photodiode is sent directly to the input of the lock-in amplifier, and is demodulated using the piezo excitation signal as the reference. The extracted amplitude and phase from the demodulated signal can then be used to for stabilization of the mechanical motion. We use a phase-locked loop to keep the mechanical excitation on resonance with the cantilever and a PID to stabilize the amplitude of driven motion.

3.5.1 Stroboscopic measurements

All of the strain related measurements in this paper are performed when the cantilever is in motion. Therefore, any spectroscopic measurements of the NV spin or optical transitions average over the cantilever motion. At times, it can be difficult to separate the internal dynamics of the NV center from the mechanical motion, and it is desirable to look at static bending of the cantilever. Static bending could be achieved with an atomic force microscope or an electrostatic interaction with metal electrodes [77]. However, the required overhead for these methods would add unnecessary complications to the experiment. As an alternative, we perform stroboscopic measurements of the NV center which isolate a particular phase of the cantilever motion. This is accomplished by directly gating the APD with a periodic sequence of short TTL pulses that is phase locked with the mechanical motion (see fig. 3.6).

A small portion of the mechanical drive signal (output 1 of the lock-in) is sent to input 2 of the lock-in, which then serves as a reference for output 2. The signal from output 2 has the same frequency as the mechanical drive signal but an adjustable, relative phase that can be set in the control software. The signal from output 2 is then sent to a homebuilt comparator circuit which converts the sinusoidal signal into a TTL pulse train of the same frequency and phase. The threshold voltage of the comparator is supplied by a DAQ output, and sets the logic "HI" threshold. We adjust the threshold voltage such that the TTL pulse train has pulses with an "ON" length of approximately 60 ns, which is short compared to the length of a cantilever oscillation period (typically 1 μs). The TTL output of the comparator then directly gates the APD. The APD will only generate pulses from incident photons during the TTL "HI" period.

3.6 Cryogenic and vacuum environment

The diamond samples studied in this experiment are housed inside of small cryostat operating at liquid He temperatures and high vacuum (10^{-9} torr). The cryogenic and high vacuum environment is necessary for resolving the fine structure of the NV excited state and minimizing damping of the cantilever motion. In the following sections, we will provide a detailed discussion of the cryostat and the additional equipment that has been incorporated into the cryogenic environment.

3.6.1 Cryostat description

The cryogenic environment is provided by a closed-cycle cryostat (Montana Instruments Cryostation) with a base temperature of 3.2 K and 150 mW of cooling power at 4.2 K with no experimental heatload. The term closed-cycle refers to the fact that there is no direct liquid helium bath to provide cooling. Instead, a cryocooler is used to conductively cool the sample to base temperature. For this reason, the closed-cycle systems are often called "cryogen-free" systems, even though the cooling process still relies on helium. One important advantage of a closed-cycle system is that helium can be recycled. This feature allows for continuous operation of the cryostat without having to refill the helium supply.

The main cooling apparatus for the cryostat is a two-stage Gifford-McMahon cryocooler. The primary cooling mechanism involves pulsing high pressure helium, typically at frequencies of a couple Hz. The helium supply is run through a variable-flow helium compressor, which also controls the speed of the cold head and hence the cooling power. The cryocooler has two stages for cooling that are equipped with three pre-calibrated Cernox thermometers. The first stage is thermally coupled to the radiation shield and reaches a temperature of approximately 28 K at base temperature. The second stage is

thermally coupled to the cold plate, or platform. At base temperature, stage 2 reaches a temperature of approximately 3 K and the platform reaches a temperature of approximately 3.5 K. The sample stage, which is mounted directly on the platform, reaches a base temperature of approximately 3.9 K. We note that during cooldown, the platform temperature significantly lags stage 1 and stage 2 in order to prevent particles from condensing onto the sample.

One significant drawback of a closed-cycle system is the vibrations that are introduced from the pulsing of the helium gas. To address this issue, the cryostat chamber is vibrationally isolated from the coldhead. The only mechanical connection between the crycooler and the sample chamber is provided by the copper coldfinger. The platform of the cryostat is thermally connected to the coldfinger through a copper mesh, which is designed to further minimize vibrations carried by the coldfinger. The optical table is vibrationally isolated from the coldhead with both passive and active elements.

To reach base temperature, the sample chamber must be at a high vacuum level, as background gas can add unwanted heat loads. High vacuum is achieved with a combination of mechanical pumping and cryopumping. Before the compressor is turned on, the sample chamber is evacuated with a mechanical pump or a turbopump to pressures of approximately 100 mTorr. During cooldown, high vacuum is established through cryopumping with activated charcoal sorbs that are thermally coupled to the cold plate. Material floating in the chamber adsorbs onto the charcoal surface, reducing the pressure in the chamber. As the temperature decreases, the charcoal sorbs "activate", and adsorbed material on the surface does not have the required energy to overcome the binding energy of the carbon and escape. Through cryopumping, pressures down to approximately 10^{-9} torr can be achieved.

After long periods of time, the charcoal sorbs become saturated (usually with water) and need to be re-activated. At 4 K, we find that significant saturation begins after

approximately one month. As a consequence of the charcoal saturation, the pressure in the sample chamber rises. To reactivate the charcoal, we bake the charcoal sorbs at 150 °C for three hours in atmosphere. Ideally, this would be done in a dry nitrogen environment or a high vacuum environment.

3.6.2 Calculating vacuum pressure from mechanics measurements

At cryogenic temperatures, our diamond sample also becomes an effective cryopump for any material floating around in the fridge. As material is adsorbed onto the diamond surface, the resonance frequency of the cantilevers will decrease due to the increase in mass. The adsorption rate onto the surface in equilibrium is given by the impingement equation, which is defined to be

$$J = \frac{fP}{\sqrt{2\pi M k_B T}} \tag{3.8}$$

where J is the adsorption rate per unit area, f is the sticking coefficient, P is the pressure, M is the molar mass of the material, and T is the temperature. In the cryostat, the primary gases adsorbing onto the surface are nitrogen and water. At 4 K, the sticking constant is approximately 1. We can measure the adsorption rate J by measuring the cantilever frequency drift rate and converting it into an adsorbed mass.

In this experiment, we measured the resonance frequency of a cantilever with dimensions $(l, w, t) = (60, 15, 1)$ μm and found that the resonance frequency drifted about 20 mHz/second. Using an average of the molar masses of nitrogen and water, this corresponds to roughly 10^6 atoms impinging the surface per second, which corresponds to a change in mass of about 10^{-20} kg. From this measurement, we infer a pressure of about 10^{-9} torr. When the charcoal sorbs begin to saturate, the pressure in the chamber starts

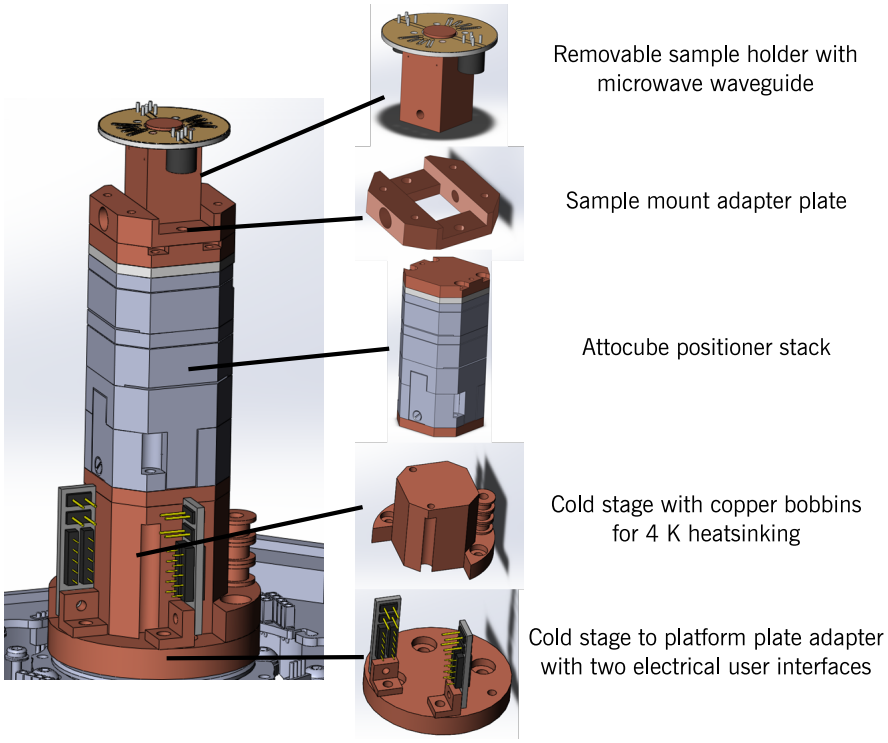

Figure 3.7: **Schematic of the cryostat interior**. A rendering of the sample stage stack showing the cold stage, the attocube stack, and the sample holder.

to rise and the adsorption rate begins to accelerate. After significant saturation, the adsorbed mass on the cantilever reduces the cantilever quality factor to the point that mechanical resonance can no longer be detected.

3.6.3 Sample stage

The sample stage consists of three main components which are shown in fig. 3.7: a copper cold stage, the Attocube stack, and the sample mount. The copper cold stage is thermally anchored to the platform and contains a series of copper bobbins and two custom electrical user interfaces. The copper bobbins serve two main purposes. The first is for 4 K heatsinking to the coldplate. The second is to allow wires to be wound several times for thermal lagging. The electrical interfaces are used to organize and

reroute electrical connections between the inner fridge connectors shown in fig. 3.9 and the components inside of the radiation shield. All electrical wiring entering the radiation shield is clamped to the platform for heat sinking and passed underneath the radiation shield and up through the platform. This prevents any thermal contact with the radiation shield, which is at the elevated temperature of stage 1.

The attocube stack contains 3 separate nanopositioning piezo stages to control the sample position in all three dimensions. The travel range of each attocube is approximately 5 mm. The attocubes are controlled with a dedicated controller provided by Attocube. The controller is connected to the homebuilt external electrical bus shown in fig. 3.9. Due to the poor heatsinking between the attocube stacks, a several copper ribbons are placed between the attocube stacks and thermally anchored to the cold plate, as shown in fig. 3.8. The thermal anchoring of the copper ribbons to the cold plate in part is provided by the mechanical pressure provided by the z attocube, which sits at the bottom of the stack. When the z attocube is raised from its fully retracted position, the thermal connection is slightly worsened, resulting in a slightly elevated sample temperature. Furthermore, we have found that when the z attocube is extended more than a few hundred microns, the vibrations become worse. For that reason, we typically keep the z attocube fully retracted.

The sample mount consists of an adapter plate and the sample holder. The sample holder consists of a copper post with a circular pillar at the top. The sample is firmly attached to the surface of the pillar with silver conductive paint. The microwave CPW is anchored to the copper post with four 0-80 screws. The sample holder is machined so that the piezoelectric actuator can be clamped underneath of the sample, as depicted in fig. 3.6. The piezo is electrically connected to the custom electrical bus at the cold plate with phosphor-bronze wiring. To electrically insulate the piezo leads from the copper clamp, we wrap the piezo in a thin layer of teflon tape. The sample holder screws into the

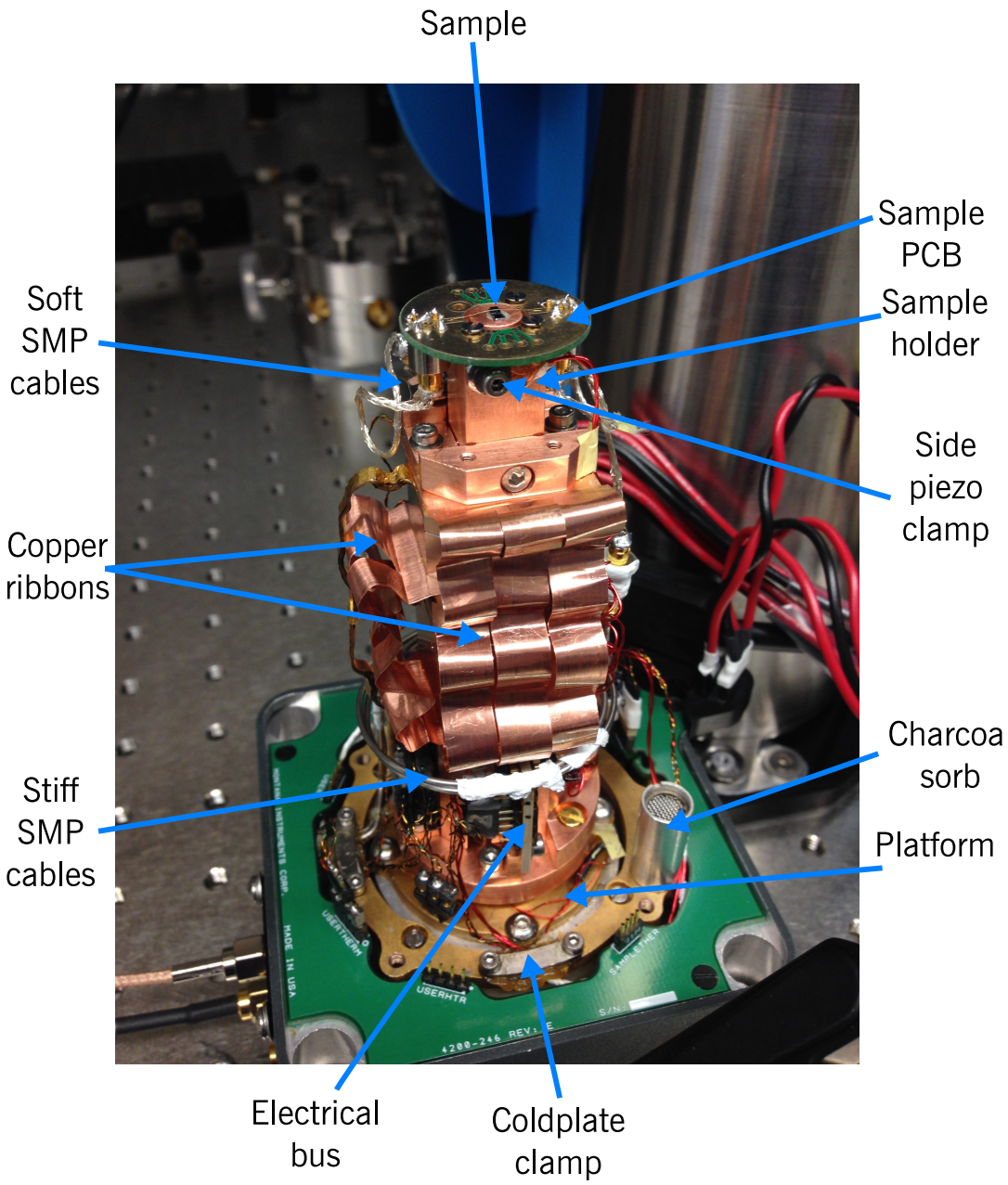

Figure 3.8: **Photographs of the sample chamber**. A photograph of the sample chamber of the cryostat with no radiation shield.

sample mount adapter plate, which allows for simple removal of the sample holder. The sample mount adapter plate is also equipped with a self-calibrated Cernox thermometer to measure the temperature

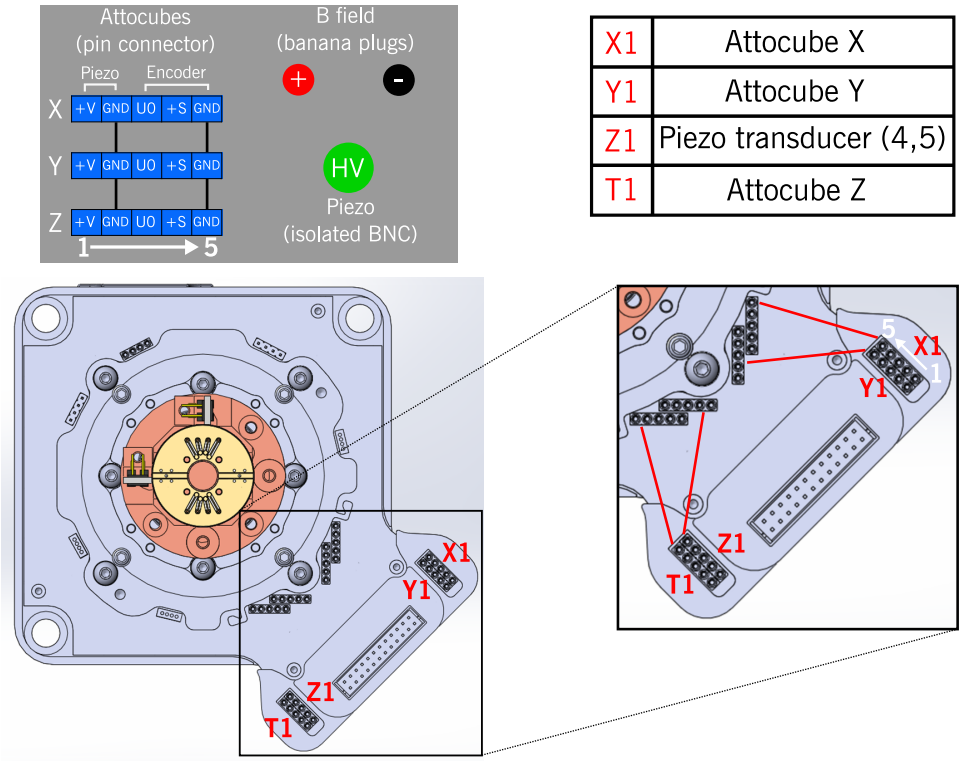

Figure 3.9: **External electrical connections of the cryostat**. Schematic of the external electrical bus and wiring for the cryostat, including connections for the attocubes, piezo, and magnetic field coil

The sample stage sits approximately 2 mm below the top window of the cryostat, and approximately 1 mm below the top radiation shield window.

3.6.4 Electrical wiring

The cryostat is equipped with several external electrical buses to organize the electrical wiring for the attocubes, microwaves, piezo, and thermometers. A homemade bus interface (fig whatever A) handles the connections for the X, Y, and Z attocubes, the magnetic field coil, and the piezo. The homemade bus is directly connected to the built-in external electrical bus of the fridge, with connectors X1, Y1, Z1, and T1, as shown in fig. 3.9. These external connectors are internally routed to their counterparts X2 Y2 Z2

and T2 inside of the cryostat.

The attocubes are driven by a commercial high voltage supply provided by Attocube. Each attocube is driven with a separate controller that is connected to the homemade electrical bus, as shown in fig. 3.9. The attocube signals enter the fridge through the X, Y and T connectors of the cryostat electrical bus. Inside of the cryostat, the attocube signal enters the radiation shield through a clamp that heatsinks the wires to the cold stage. The wires are then directed to the homebuilt electrical bus and connected to the respective attocubes.

The electrical drive signal for the piezo is generated by a lock-in amplifier. The lock-in amplifier is directly connected to an isolated BNC bulkhead located on the homebuilt electrical bus to ensure that the piezo has a floating ground with respect to the fridge. The piezo signal enters the fridge through the Z1 and Z2 connectors as shown in fig. 3.9. Inside of the cryostat, two phosphor bronze wires carry the electrical signal to the piezo. The wires first enter the radiation shield through a clamp that heat sinks the wires to the platform. The wires are then wrapped around copper bobbins for thermal lagging and then are connected to the electrical interface mounted on the cold stage. From there, another set of phosphor-bronze wires carry the signal to the piezo. To keep the piezo in place during sample removal, another connector is placed just before the piezo enters the sample mount. Each time the sample holder is removed from the cryostat, the piezo must be unplugged at this connector.

The microwaves used for coherent spin manipulation enter the cryostat through the external RF electrical bus, as shown in fig. 3.2. Inside of the cryostat, the microwaves are transmitted through rigid SMP cables that enter the sample chamber through the platform. The stiff cables wrap around the sample stage several times and are then exchanged for semi-rigid SMP cables, which connect directly to the sample PCB board, as shown in fig. 3.8. There is approximately 5 dB of rf loss at 3 GHz through the cryostat

when the sample PCB is bypassed. The loss is mostly in the semi-rigid cables. Including the sample PCB, the total loss ranges from 9-15 dB depending on the quality of the gold on the conducting layer of the sample PCB.

In addition to the thermometers on stage 1, 2 and the platform, the cryostat has another Cernox thermometer located on the sample mount adapter. The thermometer is soldered to two phosphor-bronze wires that are thermally lagged and connected to the "USERTHM" connector on the sample chamber PCB board. The USERTHM pins can be accessed externally through the user bridge located on the back of the cryostat. The thermometer can be read out in the Montana Instruments Cryostation control software.

Chapter 4

Dynamic strain-mediated coupling of a single spin to a mechanical oscillator

"You rarely win, but sometimes you do" - Atticus Finch

This chapter has been adapted with edits from ref. [76]

4.1 Introduction

Hybrid quantum systems are central to several emerging quantum technologies, ranging from quantum information processing to quantum-assisted sensing. Very recently, hybrid quantum systems incorporating high quality factor (Q) mechanical oscillators coupled to quantum two-level systems have been developed to address both fundamental and practical problems in quantum technology [24, 23]. One promising architecture for a such a device consists of a mechanical oscillator whose motion is coupled to the spin of an embedded nitrogen-vacancy (NV) center through crystal strain [24, 39]. Utilizing the

superior coherence properties of the NV center and the low intrinsic mechanical losses of diamond, this device offers unique opportunities to engineer long-range spin-spin interactions such as entanglement or squeezing [24, 39, 25]. In the regime of strong coupling, the spin-mechanical interaction can be used for phonon cooling and creating non-classical mechanical states, such as a Schrödinger cat state [54, 169, 170].

An important consideration in the design of hybrid devices lies in the quantum interface. Ideally, the the interface should combine the merits of the individual elements to mitigate the weaknesses of each element. A crystal strain interface not only meets this requirement, but also offers distinct engineering advantages over other designs, such as magnetic interfaces. For example, strain coupling is intrinsic to the device, and requires no additional external components, such as magnetic tips or cavities, which typically require precise alignment to the target qubit [75, 76]. This allows for a monolithic architecture, which should eliminate drifts in the coupling strength associated with drifts in the alignment. In contrast with other monolithic mechanical devices, this NV-mechanical device requires no functionalization of the oscillator, which could adversely affect the Q. Importantly, strain coupling does not generate noisy, stray fields such as Johnson noise, which introduce decoherence channels to the spin. Overall, these engineering features are particularly important for device scalability. As these devices are scaled to host large numbers of qubits and mechanical oscillators, it will be crucial to minimize the number of individual components and channels for decoherence.

NV centers in diamond are among the most promising qubit platforms due to their superior quantum coherence and their ability to coherently interact with a wide variety of external fields, including magnetic, electric, and thermal fields [171]. To date, NV centers have been integrated into several different hybrid systems consisting of photons [92, 150, 93], nuclear spins [91, 90], magnons [172], and magnetically-coupled mechanical resonators [75, 74]. Despite numerous theoretical proposals, there has not yet been

any experimental demonstrations of a strain-coupled spin-oscillator device, primarily due to the inability to reliably produce high quality diamond mechanical oscillators. At a more fundamental level, the NV spin-strain interaction has not been fully characterized due to the inability to controllably probe the interaction, and there exist competing theoretical models of the interaction itself [100, 99]. However, the recent and rapid development of diamond nanofabrication techniques has led to several demonstrations of high Q single-crystal diamond mechanical resonators, stimulating significant experimental efforts towards developing a strain-coupled NV-mechanical system [43, 44].

In this chapter, we discuss experiments in which the coherent dynamics of a single NV center in diamond are driven by crystal strain associated with the mechanical motion of a high quality factor diamond cantilever. Using a piezoelectric actuator, we resonantly drive the fundamental vibration mode of the cantilever and carefully monitor and control the motion with an optical interferometer and feedback electronics. Coherent control of the spin through pulsed dynamical decoupling allows the mechanical resonator to imprint a relative phase on the spin through a parametric spin-strain coupling [136]. Combining our measurements with elasticity theory and Euler-Bernoulli beam theory, we quantitatively determine the previously unknown spin-strain coupling constants and identify the primary mechanism for the spin-strain interaction. Our measurements therefore enable the use of the NV center as a calibrated strain sensor,. As a proof-of-principle, we demonstrate nanoscale strain imaging of the cantilever, with a strain sensitivity of 10^{-6} $\mathrm{Hz}^{-1/2}$. Importantly, we demonstrate for the first time a strain-coupled NV-mechanical system in an scalable architecture, and show that by scaling down the device dimensions, it should be possible to enter the regime of strong coupling between spins and single phonons.

4.2 Spin-strain model

In this chapter, we model strain as an effective electric field and adopt the phenomenological formalism for the linear electric field effect developed in the context of EPR [104, 148, 149]. Within this model, the ground state spin Hamiltonian for the NV center in the presence of magnetic and strain fields can be written as ($h = 1$),

$$H_{NV} = (D_0 + d_{\parallel}\epsilon_{zz})S_z^2 + \gamma_{NV}\mathbf{S}\cdot\mathbf{B} - d_{\perp}\left[\epsilon_{xx}(S_x^2 - S_y^2) + \epsilon_{yy}(S_xS_y + S_yS_x)\right] \tag{4.1}$$

where D_0 is the zero-field splitting (D_0 =2.87 GHz at room temperature), $\gamma_{NV} = 2.8$ MHz/G is the gyromagnetic ratio, $\{S_i\}_{i=x,y,z}$ are the spin-1 Pauli operators, $\{\epsilon_j\}_{j=x,y,z}$ are the uniaxial components of the strain tensor defined in the NV coordinate basis, and $d_{\parallel}$ and $d_{\perp}$ are the strain susceptibility parameters for axial and transverse strain. A uniaxial strain along the NV axis results in a parametric interaction from a modification of the zero-field splitting whereas, a uniaxial strain tranvserse to the NV axis mixes and splits the $m_s = \pm 1$ spin levels. It is important to note that this simplified model makes two important assumptions that differ from the full model provided in chapter 2. First, strain is treated somewhat like a vector, and hence shear strain is neglected and the full A_1 character of the strain tensor is not captured. Second, only two strain susceptibility parameters appear in the Hamiltonian, which neglects the coupling to A_1 symmetric ($\epsilon_{xx} + \epsilon_{yy}$) strain and E symmetric shear strain. Later in this chapter, we will discuss how this affects our measurements of the strain susceptibilities.

The above Hamiltonian can be rewritten in a more accessible form using the spin

raising and lowering operators that captures the spin mixing induced by transverse strain:

$$H_{NV} = (D_0 + d_{\parallel}\epsilon_{\parallel})S_z^2 + \gamma_{NV}\mathbf{S}\cdot\mathbf{B} - \frac{d_{\perp}\epsilon_{\perp}}{2}\left(e^{i\phi_s}S_+^2 + e^{-i\phi_s}S_-^2\right) \tag{4.2}$$

Here, $S_{\pm} = S_x \pm iS_y$ are the raising and lowering operators, $\epsilon_{\parallel} = \epsilon_{zz}$ is the axial strain, $\epsilon_{\perp} = \sqrt{(\epsilon_{xx})^2 + (\epsilon_{yy})^2}$ is the tranverse strain, and $\phi_s = \tan^{-1}(\epsilon_{yy}/\epsilon_{xx})$ is the strain phase. Although we have somewhat neglected the tensor nature of strain in our Hamiltonian, we include elastic effects such as the Poisson effect in our analysis. The Poisson effect accounts for uniaxial strain that is generated in directions tranverse to the direction of applied stress. This effect cannot be ignored, and will be discussed in detail later.

4.3 Spin-mechanical coupling

In this experiment, the spin of a single NV center interacts with the fundamental flexural mode of a single-crystal diamond cantilever through crystal strain. For small displacements of the cantilever, the strain in the crystal is proportional to the beam displacement, which can be quantized in terms of the phonon creation and annihilation operators:

$$\epsilon = \epsilon_0 X = \epsilon_0(a + a^{\dagger}) \tag{4.3}$$

Here, ϵ_0 is the strain induced by the zero-point fluctuations of the cantilever and $X = x_c/x_0$ is the cantilever displacement normalized to the zero-point motion. If the NV is in the presence of a small magnetic field closely aligned to its symmetry axis, we can make the secular approximation and equation 4.2 can be diagonalized with eigenstates

$\{|0\rangle, |\pm\rangle\}$, whose energies can be written as a function of X

$$\begin{aligned} \omega_0(X) &\simeq 0 \\ \omega_\pm(X) &\simeq D_0 + g_\parallel X \pm \sqrt{(\gamma_{NV} B_z)^2 + (g_\perp X)^2} \end{aligned} \tag{4.4}$$

Here, we have defined the quantum spin-phonon couplings $g_\parallel = d_\parallel \epsilon_{\parallel 0}$ and $g_\perp = d_\perp \epsilon_{\perp 0}$, which quantify the axial and transverse coupling of the spin to the zero-point motion of the beam. Alternatively, these couplings can be thought of as the spin energy shift due to the absorption or emission of a single phonon, and hence g is typically referred to as a single phonon coupling. In the experiments here, the resonator is in a classical coherent state containing many phonons, and hence it is useful to consider the classical strain coupling parameters $G_\parallel = g_\parallel X$ and $G_\perp = g_\perp X$. Here, the normalized position of the cantilever is given by $X(t) = \frac{x_c}{x_0} \cos(\omega_m t + \phi)$, where ω_m is the cantilever frequency.

The corresponding spin eigenstates can then be written as

$$\begin{aligned} |0\rangle &= |0\rangle \\ |\pm\rangle &= \cos(\alpha) |1\rangle \mp e^{-i\phi_s} \sin(\alpha) |-1\rangle \end{aligned} \tag{4.5}$$

where α is the mixing angle and $\tan(2\alpha) = \frac{G_\perp}{\gamma_{NV} B_z}$. Note that for increasing B_z the effect of transverse strain is suppressed. In our experiments, we tune the value of B_z in order to suppress or enhance the effects of transverse strain, which allows for selective characterization of axial and transverse strain.

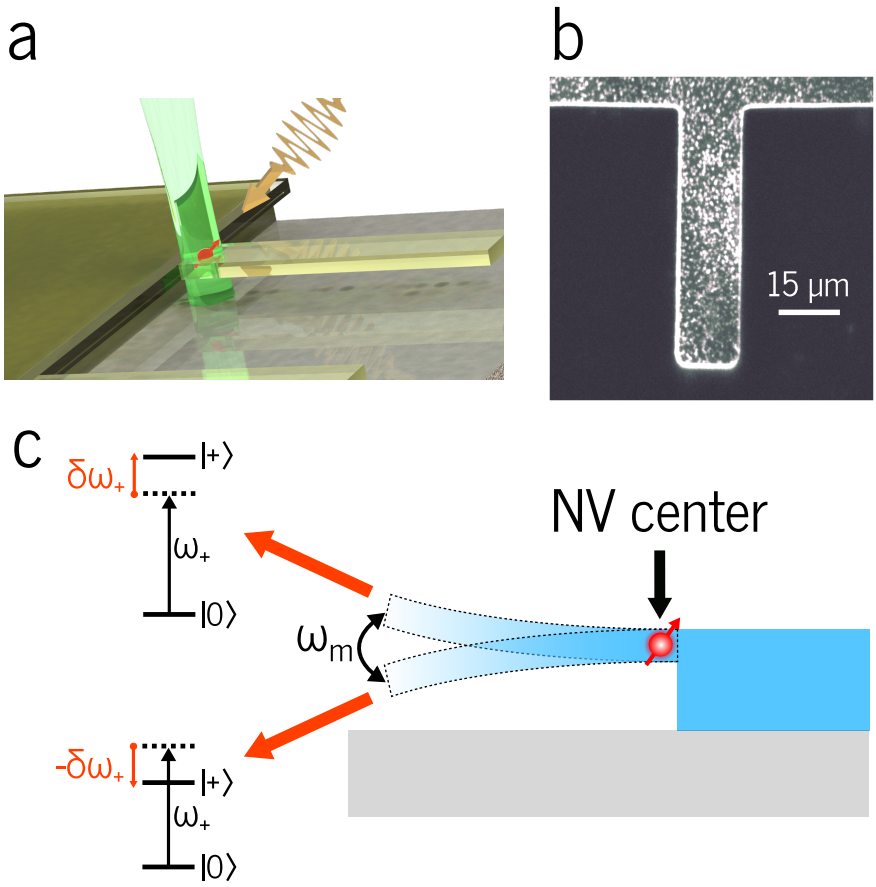

Figure 4.1: **A hybrid spin-mechanical system**. a) Schematic of the hybrid device. A 532 nm laser is focused onto a single NV spin embedded in a cantilever for spin initialization and readout. Microwaves are used for pulsed spin manipulation. b) Confocal fluorescence image of a cantilever showing the presence of embedded NV centers. c) Strain induced by the motion of a diamond cantilever modulates the spin levels of an embedded NV center.

4.4 Experimental setup

The device in this experiment consists of a single spin embedded inside of a SCD cantilever, as shown in fig. 4.1 a. The cantilevers were fabricated using the silicon-on-insulator technique described in chapter 2 and have dimensions of approximately $60 \times 15 \times 1$ μm. The fundamental flexural modes of the cantilever have resonance frequencies $\omega_m/2\pi$ ranging from approximately 600 kHz to 1.4 MHz and quality factors exceeding 10^5 [43]. NV centers were formed via ^{14}N ion implantation with a dosage of 3×10^9 ion/cm^2 at

40 keV and a 0° tilt, which yields an expected nitrogen layer at a depth of 51.5 nm below the surface (calculated by Stopping and Range of Ions in Matter (SRIM) simulations). To create NV centers, the sample was annealed under high vacuum ($\sim 10^{-6}$ torr at 800°C for 3 hours.

The measurement apparatus consists of a homebuilt confocal microscope integrated with a vacuum chamber, as described in chapter 3. A confocal microscope image of the the device is shown in fig. 4.1 b., showing the existence of single NV centers embedded in the structure. The experiments were performed at room temperature and high vacuum ($\sim 10^{-5}$ torr) to reduce viscous damping of the cantilever mode. A continuous wave laser at 532 nm is used for optical pumping and readout of the spin, and is gated with an acousto-optic modulator (AOM). Photons emitted into phonon sideband are collected into a single-mode fiber and directed to an avalanche photodiode. For pulsed measurements, we apply a DC magnetic field supplied by a rare earth magnet to break the degeneracy of the $m_s = \pm 1$ spin levels. The position and orientation of the magnet is controlled in all 3 dimensions using a combination of goniometers and translation stages. We identify the crystallographic orientation of the NV center with respect to the cantilever by the monitoring the Zeeman splitting in the ESR spectrum. In our measurements, we align the field close to the NV axis and encode our qubit in the $|0\rangle$ and $|+\rangle$ spin states. Microwaves used for resonant spin manipulation are delivered to the sample by a nearby gold wirebond. Phase control of the microwaves is accomplished via IQ modulation. Microwave pulses are generated by gating a high isolation switch placed in the microwave circuit with a Spincore Pulseblaster ESR-Pro 500 MHz card.

The cantilevers are mechanically driven with a piezoelectric actuator that is electrically driven with a lock-in amplifier, as discussed in chapter 3. To maximize the piezo coupling to the sample, the piezo is clamped directly to the sample holder. The mechanical motion of the cantilever is characterized using Fabry-Perot interferometery as

discussed in detail in chapter 3. To calibrate the amplitude of driven motion, we find the piezo voltage required for the cantilever to hit the silicon substrate which sits 1 μm below the cantilever. This manifests as an interruption of the Bessel oscillations shown in 2.19.

4.5 Coherent strain detection using spin-echo spectroscopy

The interaction between the cantilever motion and the spin qubit results in a parametric modulation of the qubit frequency, as shown in fig. 4.1 c. To measure this effect, we perform spin-echo spectroscopy on the spin qubit while mechanically driving the cantilever. During the free evolution periods, the mechanical motion of the cantilever imprints a relative phase onto the spin qubit, which is then converted into a population difference and readout via spin-dependent fluorescence. Importantly, the use of a spin-echo pulse allows the spin to decouple from quasi-static noise while enhancing the spin sensitivity to the mechanical motion over a narrow frequency band [75]. In the following measurements, we set the axial magnetic field to $B_z = 22$ G, which should suppress the effects of transverse strain.

The protocol for the strain detection as well as the spin evolution on the Bloch sphere is depicted in 4.2 a. The cantilever is driven at its resonant frequency while a Hahn echo sequence is performed on the spin. The experiment begins by initializing the spin into $|0\rangle$ via optical pumping. A microwave $\pi/2$-pulse tuned to the $|0\rangle \leftrightarrow |+\rangle$ transitions prepares the spin in a coherent superposition along the x-axis of the Bloch sphere. The spin then freely evolves for a time τ, during which the mechanical motion imprints a relative phase onto the qubit (blue shaded region). The spin is then inverted with a microwave

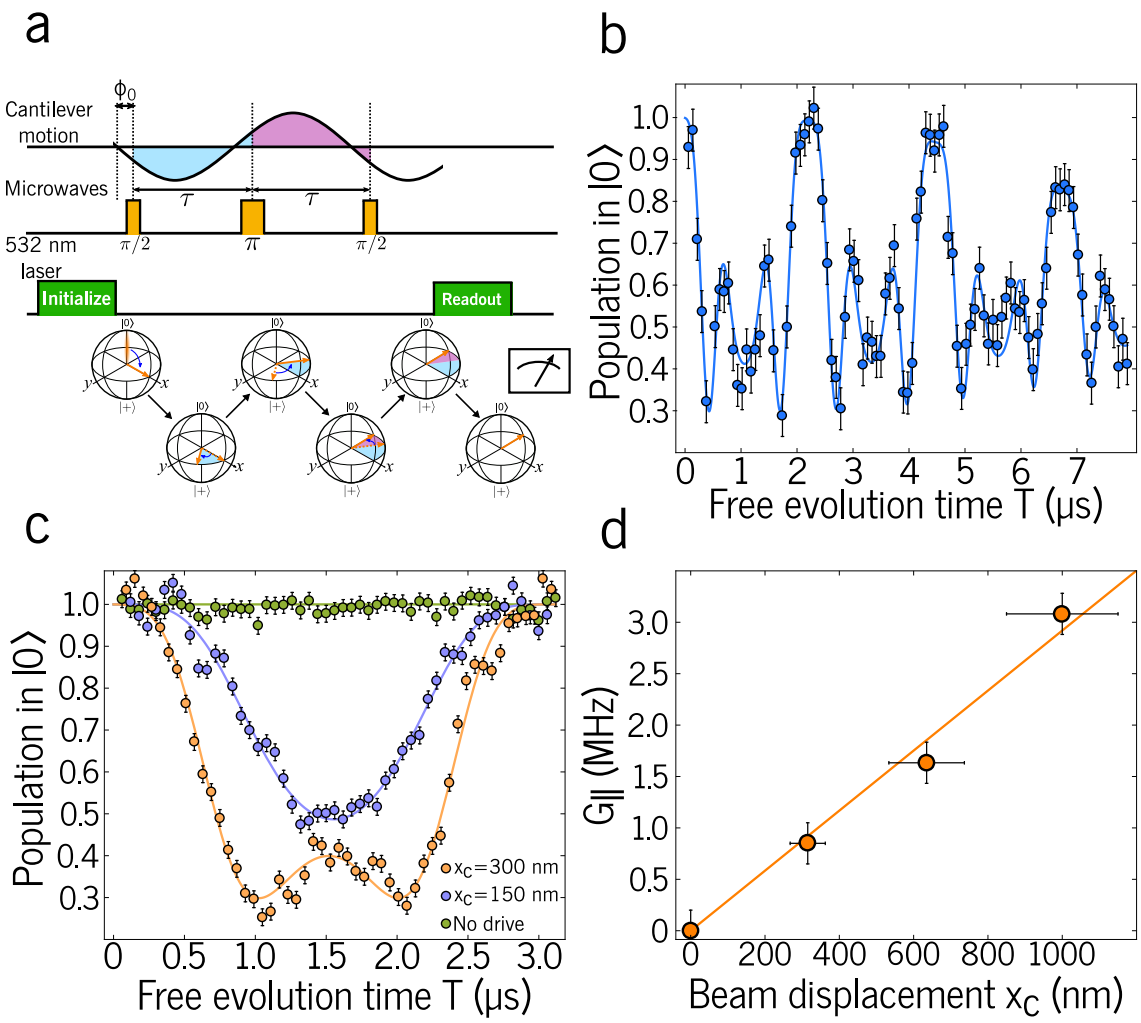

Figure 4.2: **Mechanically driven spin dynamics**. a)Strain-induced modulations of the qubit frequency are detected with a Hahn echo sequence. The spin-echo pulse allows the phases from the first (blue) and second (purple) free evolution periods to add constructively. Below is a cartoon showing the spin evolution on the Bloch sphere. b) Hahn echo signal for an NV center demonstrating coherent spin dynamics driven by the mechanical motion. c) As the amplitude of motion increases, the modulation depth increases. d) The measured strain coupling $G_{||}$ is plotted as a function of x_c, demonstrating the linear nature of the coupling.

π-pulse and allowed to freely evolve for a time τ, during which the spin acquires a relative phase shown by the purple shaded region. The acquired phase is then converted into a population difference with a final $\pi/2$-pulse and then the spin is readout with a 532 nm laser pulse.

In figure 4.2 b., we show the Hahn echo signal for a single NV center located at the base of a cantilever with $\omega_m/2\pi = 884$ kHz and an oscillation amplitude $x_c = 650$ nm. The dynamic, axial strain produced by the cantilever motion results in a modulation of the spin population that is correlated with the cantilever motion. In particular, when the total free evolution time, $T = 2\tau$ is equal to an odd integer multiple of the cantilever period, the phases acquired in each free evolution period add constructively, resulting in a collapse of the spin population in $|0\rangle$. When T is equal to an even integer multiple of the cantilever period, the phases cancel out and the qubit acquires no net phase, resulting in a revival of spin population in $|0\rangle$. Because we do not keep track of the cantilever phase, the signal averages of a uniform distribution of the initial phase of motion. A fit to the theoretical Hahn echo signal (discussed in the following section) yields an axial strain coupling $G_{\parallel} = 2.1 \pm 0.1$ MHz. The data shown here indicates that the mechanical motion of the cantilever is driving the coherent evolution of the spin.

To demonstrate the tunability of our coupling, we performed a series of Hahn echo experiments for various amplitudes of cantilever motion, which is shown in fig. 4.2 c. When the cantilever is not driven, the spin is coherent over a single cantilever oscillation period and the spin population is fixed in $|0\rangle$. As x_c increases, the axial strain coupling increases, resulting in stronger modulation of the spin population difference. For sufficiently high strain couplings, multiple oscillations of the spin populations appear, indicating that the spin has precessed more than once around the equator of the Bloch sphere. This is responsible for the faster frequency response in fig. 4.2 b. To confirm that the strain coupling is linear in x_c, we plot the extracted strain couplings, $G_{\parallel}$, for four different values of x_c, which is shown in fig. 4.2 d.

4.5.1 Theoretical spin evolution for axial strain under dynamical decoupling

In this section, we derive the theoretical spin evolution signal under generic dynamical decoupling for a parametric spin-strain coupling induced by axial strain [173]. The Hamiltonian for the system can be written as

$$H = \frac{\omega_+}{2}\sigma_z + \omega_m a^\dagger a + 2\pi\frac{g_\parallel}{2}(a + a^\dagger)\sigma_z \tag{4.6}$$

where $\omega_+ = 2\pi(D_0 + \gamma_{NV}B_z)$ is the qubit frequency in the absence of strain, ω_m is the cantilever frequency, and a is the annihilation operator of the cantilever mode. In the experiment, we resonantly drive the cantilever mode with a piezoelectric transducer. In this situation, the cantilever mode can be described by a large amplitude coherent state.

$$|\alpha\rangle = e^{-\alpha^2/2}\sum_{n=0}^{\infty}\frac{\alpha^n}{\sqrt{n!}}|n\rangle \tag{4.7}$$

where $|n\rangle$ represent the Fock states of the cantilever mode and α is a dimensionless number giving the amplitude of the coherent state. Working in the Schrodinger picture, we see the the time-dependent coherent state obeys

$$|\alpha(t)\rangle = e^{-\alpha^2/2}\sum_{n=0}^{\infty}\frac{\alpha^n}{\sqrt{n!}}e^{-i(n+1/2)\omega_m t}|n\rangle \tag{4.8}$$

We are interested in the expectation value of the position operator, $X(t) = \langle\alpha(t)|\, x_0(a+$

$a^\dagger)\,|\alpha(t)\rangle$, which will govern the dynamics of the spin evolution. We see

$$\begin{aligned}
X(t) =& x_0 e^{-\alpha^2}\left(\sum_m \frac{\alpha^m}{\sqrt{m!}} e^{i(m+1/2)\omega_m t}\,\langle m|\right) a + a^\dagger \left(\sum_n \frac{\alpha^n}{\sqrt{n!}} e^{i(n+1/2)\omega_m t}\,|n\rangle\right) \\
=& x_0 e^{-\alpha^2} \sum_m \sum_n \frac{\alpha^{m+n}}{\sqrt{m!n!}} e^{-i(n-m)\omega_m t}(\sqrt{n}\delta_{m,n-1} + \sqrt{n+1}\delta_{m,n+1}) \\
=& x_0 e^{-\alpha^2} \sum_n \left(\frac{\alpha^{2n-1}}{\sqrt{(n-1)!n!}} e^{-i\omega_m t}\sqrt{n} + \frac{\alpha^{2n+1}}{\sqrt{(n+1)!n!}} e^{i\omega_m t}\sqrt{n+1}\right) \\
=& x_0 e^{-\alpha^2}\left(\sum_{l=0}^{\infty} \frac{\alpha^{2l+1}}{\sqrt{(l+1)!l!}} e^{-i\omega_m t}\sqrt{l+1} + \sum_{n=0}^{\infty} \frac{\alpha^{2n+1}}{\sqrt{(n+1)!n!}} e^{i\omega_m t}\sqrt{n+1}\right) \\
=& x_0 \alpha e^{-\alpha^2} \sum_n \frac{\alpha^{2n}}{n!}\left(e^{-i\omega_m t} + e^{i\omega_m t}\right) \\
=& 2x_0\alpha\cos(\omega_m t)
\end{aligned} \tag{4.9}$$

Defining $X = 2\alpha$, the Hamiltonian may be written as

$$H = \frac{\omega_+}{2}\sigma_z + 2\pi\frac{g}{2} X\cos(\omega_m t + \phi)\sigma_z \tag{4.10}$$

In the experiment, we initialize the qubit into an eigenstate of σ_x, $|\psi\rangle = \frac{1}{\sqrt{2}}(|0\rangle + |+\rangle)$ with a microwave $\pi/2$ pulse. During the free evolution period, the qubit acquires a relative phase from the mechanical motion of the cantilever. To enhance the mechanically-induced phase accumulation and decouple the qubit from quasi-static noise, we apply a periodic sequence of π pulses to the qubit. In such dynamical decoupling pulse sequences, a π pulse swaps the qubit populations, or equivalently, takes $\sigma_z \to -\sigma_z$ and vice versa. In the rotating frame of the qubit, the sign of the parametric spin-phonon coupling then "toggles" each time a π pulse is applied. Therefore, it is convenient to write out the Hamiltonian in the interaction picture with respect to the qubit and introduce the so-

called "toggling frame"

$$H_I = \pi g X \cos(\omega_m t + \phi) f(t,\tau)\sigma_z \tag{4.11}$$

where $f(t,\tau)$ defines the toggling frame generated by the microwave π pulse train and τ is the length of a free evolution period [173]. Mathematically, $f(t,\tau)$ is a square wave that switches between values of ± 1 when a π pulse is applied. The explicit definitions of $f(t,\tau)$ for the Hahn echo sequence and XY-4 sequence are shown below

$$f_{echo}(t,\tau) = \begin{cases} +1 & 0 < t < \tau \\ -1 & \tau < t < 2\tau \end{cases} \tag{4.12}$$

$$f_{XY4}(t,\tau) = \begin{cases} +1 & 0 < t < \tau \\ -1 & \tau < t < 3\tau \\ +1 & 3\tau < t < 5\tau \\ -1 & 5\tau < t < 7\tau \\ +1 & 7\tau < t < 8\tau \end{cases} \tag{4.13}$$

The dynamics of the qubit are then determined by the time evolution operator in the interaction picture

$$\begin{aligned} U(T) &= \exp\left[-i\int_0^T H_I(t)dt\right] \\ &= \mathcal{T}\exp\left[-i\pi g_{\parallel} X\sigma_z \int_0^T \cos(\omega_m t + \phi) f(t,\tau)\right] \end{aligned} \tag{4.14}$$

where we have introduced the time ordering $\mathcal{T}$. After a free evolution period of length T, the qubit has acquired a relative phase, $\theta(T)$. In our measurements, we convert this

relative phase into a population difference by projecting the qubit back on the z axis with a $\pi/2$ pulse. The phase can then be readout by reading out the qubit populations via spin-dependent fluorescence. Our signal can then be written in terms of the probability for the qubit to be in $|0\rangle$,

$$P(T) = \frac{1}{2}(1 \pm \cos(\theta(T)) \tag{4.15}$$

where the sign of the phase term is determined by the phase of the last $\pi/2$ pulse. In our analysis, we map this probability to the fluorescence signal to infer the qubit populations.

4.5.2 Hahn echo signal

For a Hahn echo experiment, the qubit undergoes free evolution for a time $T = 2\tau$, and acquires a relative phase

$$\theta(2\tau) = 2\pi G_{\parallel}\left[\int_0^{\tau}\cos(\omega_m t + \phi)dt - \int_{\tau}^{2\tau}\cos(\omega_m t + \phi)dt\right] \tag{4.16}$$

Carrying out the integration and accounting for the phase of the microwave pulse train, the probability to be in $|0\rangle$ is given by

$$P(T) = \frac{1}{2}\left[1 + \cos\left[\frac{8\pi G_{\parallel}}{\omega_m}\sin^2\left(\frac{\omega_m T}{8}\right)\sin\left(\frac{\omega_m T}{2} + \phi\right)\right]\right] \tag{4.17}$$

In our experiments, we do not keep track of the cantilever phase, and hence the Hahn echo signal will average over an initial, uniform distribution of the cantilever phase, ϕ.

$$P(T) = \frac{1}{2}\left[1 + J_0\left(\frac{8\pi G_{\parallel}}{\omega_m}\sin^2\left(\frac{\omega_m T}{8}\right)\right)\right] \tag{4.18}$$

To take into account decoherence, we introduce a exponential phase decay

$$P(T) = \frac{1}{2}\left[1 + e^{-(T/T_2)^n} J_0\left(\frac{8\pi G_\parallel}{\omega_m}\sin^2\left(\frac{\omega_m T}{8}\right)\right)\right] \tag{4.19}$$

where T_2 is the spin coherence time and n is a free parameter that is determined by the decoherence mechanism for the system.

4.6 Nanoscale strain imaging with a single spin

The electron spin of the NV center is an extraordinarily robust quantum sensor that can be used to probe a variety of external fields [174]. As an atomic scale defect, the NV center offers the ability to perform quantum field imaging with nanometer scale resolution. Here, we demonstrate nanoscale strain imaging of a diamond cantilever using single NV spins embedded in the structure. To this end, we perform a Hahn echo measurement for a fixed mechanical drive amplitude and measured the classical strain coupling, $G_\parallel$, for several NV centers located at different positions in the cantilever.

The strain profile for the fundamental flexural mode of a cantilever is shown in fig. 4.3 a(calculated using COMSOL). The strain is highest at the clamping point of the cantilever, and decreases approximately linear along the cantilever axis, reaching a strain of zero at the cantilever tip. With the exception of the corners of the clamping points, the simulated strain profile is in good agreement with the strain profile predicted from Euler-Bernoulli beam theory.

In fig. 4.3 b., we plot the measured values of $G_\parallel$ for a fixed mechanical drive amplitude $x_c = 250$ nm as a function of NV position along the cantilever axis (orange circles). As expected, the measured strain couplings are highest for spins located near the clamping point, and near zero for spins located near the tip. Indeed, the measured couplings are

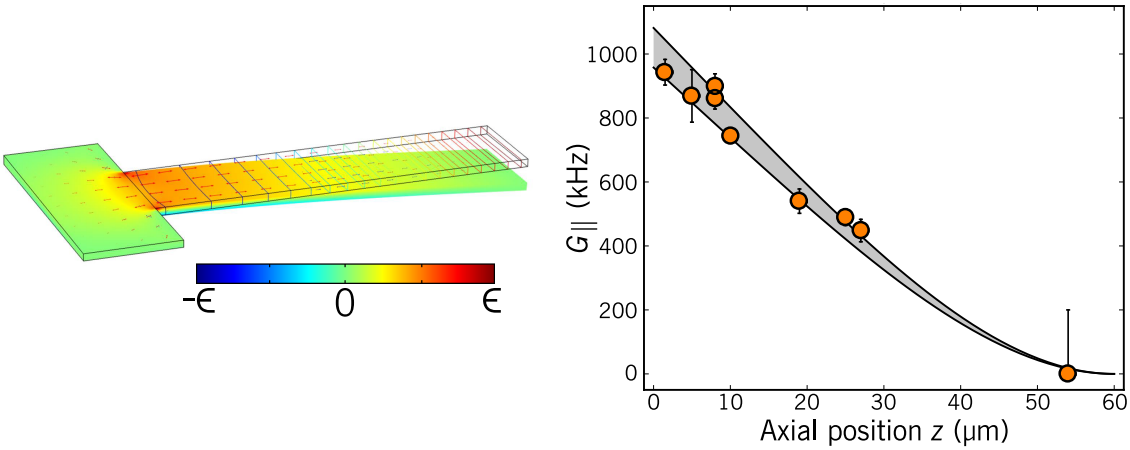

Figure 4.3: **Nanoscale strain imaging**. a) Strain profile for the cantilever used in this experiment simulated using a finite element method. b) Measured strain coupling as a function of NV position along the cantilever axis. The grey shaded area shows the region of expected strain couplings from theory including uncertainties in the NV depth (13 nm) and amplitude of driven motion (10 nm). Vertical error error bars correspond to standard error in the fit from the spin-echo measurement.

in excellent agreement with the theoretical strain profile calculated from Euler-Bernoulli beam theory, indicated by the gray shaded region. The width of the shaded region is determined by the uncertainty in the depth of the NV centers from ion implantation (13 nm), and the data error bars are determined by errors in the fit to the expected Hahn echo signal. Notably, the excellent agreement between the data and theory provides convincing evidence that strain is responsible for the spin evolution.

Because Euler-Bernoulli theory appears to accurately predict the strain coupling to the NV center, we can quantitatively infer the axial spin-strain coupling constant, $d_{\parallel}$. The confocal microscope allows for precise, three dimensional localization of the NV centers, allowing us to predict the cantilever strain at the site of the NV center with Euler-Bernoulli theory (see supporting information for this chapter). Using the data from fig. 4.3 b., we extract an average value of $d_{\parallel} = 13.4 \pm 0.8$ GHz. Note that our measured value should average over the expected inhomogeneities in the NV depth and local strain environments.

4.7 Spin-strain sensitivity

An important result of our determination of $d_{\parallel}$ is that the NV can be used as a calibrated strain sensor. To evaluate the strain sensing ability of the NV, we must calculate the strain sensitivity. The strain sensitivity, η_s, can be thought of as the minimum value of the field that can be detected with a signal-to-noise ratio (SNR) of 1 in a 1 second measurement. Here, we provide a shot-noise limited estimation of the strain sensitivity of our hybrid spin-mechanical device, following a similar procedure provided in ref. [101].

The sensing measurement consists of a Hahn echo experiment performed in the $\{|0\rangle, |+\rangle\}$ basis that senses AC strain introduced from the motion of the cantilever. The free evolution period, τ, is matched to half of the cantilever oscillation period, and the phase of the microwave control pulse train is fixed with respect to the phase of the cantilever motion, maximizing the accumulated phase. In the analysis that follows, we will only consider the sensitivity to axial strain, but note that this analysis may be extended to transverse strain as well.

The strain sensitivity may be written as

$$\eta_s = \frac{2\pi A}{d_{\parallel} t} e^{(t/T_2)^n} \tag{4.20}$$

where A is defined to be

$$A = \sqrt{\frac{2(1+C)}{(N\alpha_0(1-C)^2}} \tag{4.21}$$

Here, t is the total measurement time, N is the total number of measurements, n is the exponent in the coherence decay (determined by the decoherence mechanism), T_2, is the Hahn echo coherence time, α_0 is the number of photons detected in a single shot for an initial spin state $|0\rangle$, and C is the fluorescence contrast between $|0\rangle$ and $|+\rangle$. For a readout

time of $350ns$, we collect approximately $\alpha_0 = 0.01$ per shot. The fluorescence contrast varies between NVs, but on average is $C = 0.85$. These values are limited primarily by the collection efficiency of the confocal microscope, and can be significantly improved with higher numerical aperture objectives or resonator geometries that waveguide NV fluorescence into the confocal microscope. The spin coherence times in these devices vary from $10 - 60$ μs, which we estimate to be limited by fluctuating paramagnetic spins within the diamond. The coherence decays observed in our experiments can be modeled with several values of n in the range $[1, 3]$, and we will henceforth set $n = 1$. Assuming no dead time between measurements, the total interrogation time, T, can be written as $T = Nt$.

It can be shown that the SNR is maximized with $t = T_2/2$, and hence the strain sensitivity can be written as

$$\eta_2 = \frac{2\pi\sqrt{2}A}{d_{\parallel}\sqrt{TT_2}}e^{1/2} \tag{4.22}$$

Substituting typical values for the parameters from this device, we extract a minimum detectable strain of 10^{-6} in a 1 second measurement, implying the sensitivity of our device is $\eta_s = 1 \times 10^{-6}$ Hz$^{-1/2}$. Given the minimum detectable strain, the minimum detect amplitude of motion is estimated to be 2 nm.

4.8 Coherent detection of transverse strain

In the previous measurements, we suppressed the effects of transverse strain by applying a strong axial magnetic field. However, to quantitatively understand the spin-strain interaction, we must understand how the spin evolves under a general strain. To this end, we measured an NV center perpendicular to the cantilever stress direction. indi-

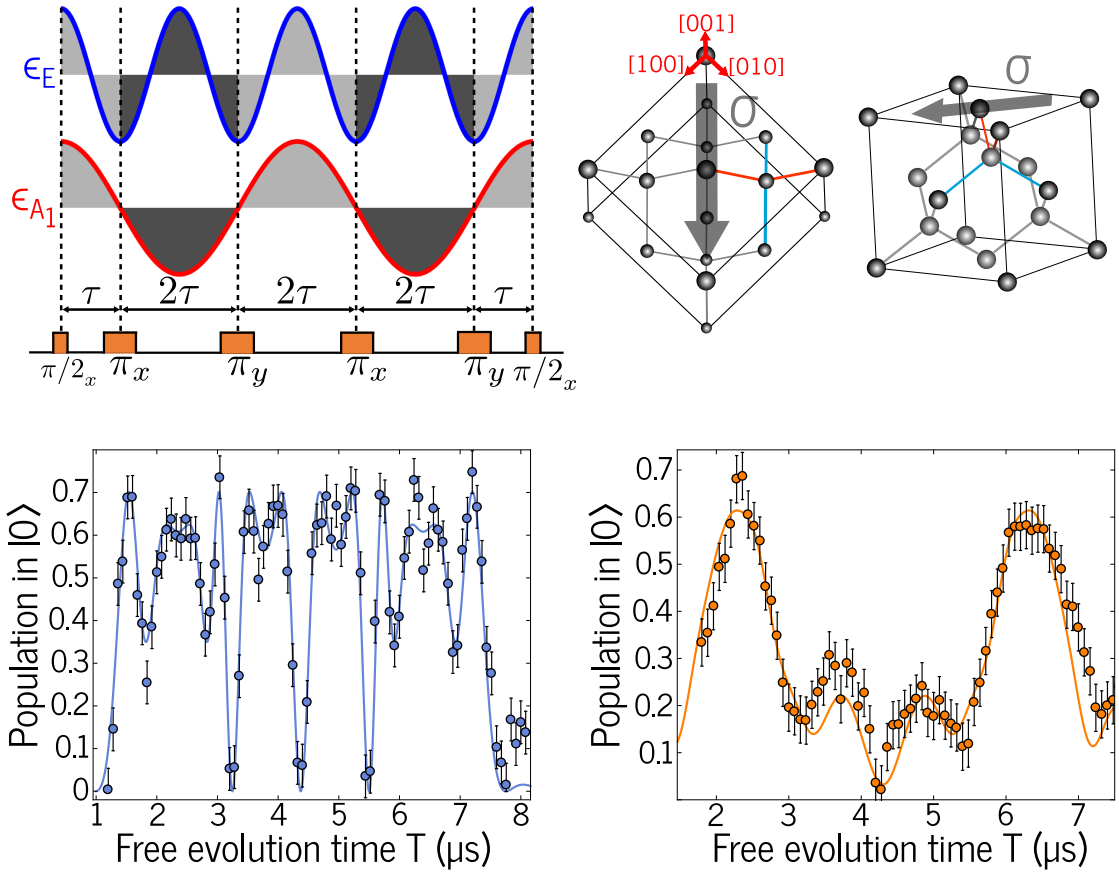

Figure 4.4: **Measurement of transverse strain**. a) XY-4 control sequence used to measure transverse strain. Dynamic transverse strain (blue) modulates the qubit splitting at approximately twice the cantilever frequency, whereas dynamic axial strain modulates the qubit splitting at the cantilever frequency. b) Schematic showing the orientation of the cantilever stress (grey arrow) with respect the crystal frame. NVs oriented nearly parallel to the cantilever stress are indicated by blue bonds. NVs oriented perpendicular to the cantilever stress are indicated by orange bonds. c) XY-4 signal for a parallel NV when the cantilever is driven at 250 nm d) XY-4 signal for a perpendicular NV center for $x_c = 675$ nm.

cated with orange bonds in fig. 4.4 b. Additionally, we lowered the axial magnetic field to $B_z = 16$ G, allowing the transverse strain to have a more significant effect. We note that although the strain for this NV center will be predominantly transverse to the symmetry axis, the NV will experience a small amount of axial strain due to the Poisson effect.

Interestingly, because the magnetic field and transverse strain interactions do not commute, the time dependence of the transverse strain interaction will be inherently different from the axial strain interaction, as indicated by the energy eigenvalues in equation 4.5. Specifically, the axial strain modulation frequency will be at ω_m, whereas the transverse strain modulation frequency will be at $\sim 2\omega_m$. Therefore, the effects of the axial and transverse strain can be identified by beatnotes in the spin evolution.

To enhance our sensitivity to these beatnotes, we applied an XY-4 control sequence to the NV center, as shown in fig. 4.4 a. This sequence increases the spin sensitivity to strain by extending the coherence time and correcting for first-order, pulse timing errors [136, 135]. To demonstrate the geometric dependence of the NV orientation on the cantilever stress, we performed an XY-4 sequence for an NV whose symmetry axis is approximately parallel to the cantilever stress (fig. 4.4 c.) and an NV whose symmetry axis is perpendicular to the cantilever stress (fig. 4.4 d.). For the data in fig. 4.4 c., we investigated an NV center at the base of a cantilever that was being driven at 250 nm. The data is in good agreement with the expected XY-4 signal (discussed in next section) for an NV center experiencing only axial strain, and shows the presence of several cycles around the equator of the Bloch sphere. In fig. 4.4 d., we plot the XY-4 signal for an NV 3 μm from the base for the same cantilever being driven at 675 nm. A fit to the expected signal indicates the presence of transverse strain. Using this data, we extract $G_\perp = 6.7 \pm 0.4$ MHz and $G_\parallel = 270 \pm 50$ kHz. Using Euler-Bernoulli theory, we extract a value of $d_\perp = 21.5 \pm 1.2$ GHz and $d_\parallel = 13.1 \pm 1.1$ GHz, showing excellent agreement with the previously determined $d_\parallel$.

4.8.1 XY-4 signal for an NV under dynamic axial strain

In the XY-4 sequence, the qubit undergoes free evolution for a time $T = 8\tau$, and acquires a relative phase

$$\begin{aligned}\theta(8\tau) =& 2\pi G_{\parallel}\Bigg[\int_0^{\tau}\cos(\omega_m t+\phi)dt - \int_{\tau}^{3\tau}\cos(\omega_m t+\phi)dt \\ &+ \int_{3\tau}^{5\tau}\cos(\omega_m t+\phi)dt - \int_{5\tau}^{7\tau}\cos(\omega_m t+\phi)dt + \int_{7\tau}^{8\tau}\cos(\omega_m t+\phi)dt\Bigg]\end{aligned} \tag{4.23}$$

Using the same procedure described in the Hahn echo section and taking into account the microwave phase, we obtain the XY-4 signal

$$P(T) = \frac{1}{2}\left[1 - e^{-(T/T_2)^n} J_0\left[\frac{4\pi G_{\parallel}}{\omega_m}\sin\left(\frac{\omega_m T}{2}\right)\left(1-\sec\left(\frac{\omega_m T}{8}\right)\right)\right]\right] \tag{4.24}$$

4.8.2 Spin evolution for general strain under dynamical decoupling

In this section, we provide a theoretical model for the XY-4 signal for an NV experiencing significant coupling to both axial and transverse strain. The Hamiltonian in the interaction picture is

$$H_I = \left[2\pi G_{\parallel}\cos(\omega_m t+\phi) + \sqrt{(\gamma_{NV}B_z)^2 + 4\pi^2 G_{\perp}^2\cos^2(\omega_m t+\phi)}\right]\sigma_z \tag{4.25}$$

Because the Zeeman and transverse strain interactions do not commute, they add in quadrature. As a result, axial and transverse strain will oscillate at different frequencies,

allowing us to distinguish the two effects in the spin evolution. We see that axial strain will oscillate at ω_m and transverse strain will oscillate at approximately $2\omega_m$. This will result in beatnotes in the spin evolution, which we measure with the XY-4 pulse sequence. The probability to be in $|0\rangle$ after a measurement time T is given by

$$P(T) = \frac{1}{2}\left[1 - e^{-(T/T_2)^n}\cos\left(\theta_\parallel(T) + \theta_\perp(T)\right)\right] \tag{4.26}$$

where

$$\theta_\parallel = \frac{4\pi G_\parallel}{\omega_m}\sin\left(\frac{\omega_m T}{2}\right)\left(1 - \sec\left(\frac{\omega_m T}{8}\right)\right)\sin\left(\omega_m T + \phi\right) \tag{4.27}$$

represents the phase accumulated due to axial strain. To evaluate the phase $\theta_\perp$, we use the incomplete elliptic integral of the second kind, $E(m,k)$. If the elliptic modulus, k, satisfies the condition $0 < k^2 < 1$, then we define $E(m,k) = \int_0^m dx\sqrt{1 - k^2\sin^2(x)}$. With some algebra, we can write $\theta_\perp$ as

$$\begin{aligned}\theta_\perp(T) =& \frac{2\pi R}{\omega_m}\left[2E\left(\frac{\omega_m T}{8} + \phi, \frac{G_\perp}{R}\right) - E\left(\phi, \frac{G_\perp}{R}\right) - 2E\left(\frac{3\omega_m T}{8} + \phi, \frac{G_\perp}{R}\right)\right. \\ &+ 2E\left(\frac{5\omega_m T}{8} + \phi, \frac{G_\perp}{R}\right) - 2E\left(\frac{7\omega_m T}{8} + \phi, \frac{G_\perp}{R}\right) \\ &\left.+ E\left(\omega_m T + \phi, \frac{G_\perp}{R}\right)\right]\end{aligned} \tag{4.28}$$

where have defined $R = \sqrt{(\gamma_{NV}B_z)^2 + G_\perp^2}$ for ease of notation. Finally, we must average over the initial phase of the cantilever motion. We note that this has no closed-form solution. In the analysis of our data, we used a simple least-squares model that compared a series of numerically integrated fit functions to the data. In the analysis, we sample various values of ω_m, $g_\parallel$ and $g_\perp$ while keeping the Zeeman splitting and amplitude of driven motion constant.

4.9 Discussion of the spin-strain coupling constants

As we mentioned in the beginning of the chapter, the simple model used for the spin-strain interaction is not strictly correct. One important discrepancy is that our description fails to completely project the elements of the strain tensor onto the irreducible representations of the C_{3v} group. For instance, in our model we treat ϵ_{xx} and ϵ_{yy} as terms of only E_1 and E_2 symmetry. As we showed in chapter 2, both ϵ_{xx} and ϵ_{yy} have A_1 and E_1 character and hence our model of A_1 symmetric spin-strain coupling is incomplete. In addition, our model incorrectly neglects the effects of shear strain, specifically ϵ_{xz}, which introduces an E symmetric spin-strain interaction.

In this work, we use two strain coupling constants to characterize the spin-strain interaction. While this description can phenomenologically explain the effects observed in this work, it does not provide a complete description of the spin-strain interacton. As we showed in chapter 2, we require four parameters to fully characterize the spin-strain interaction. This is a result of the fact that the NV center has C_{3v} symmetry and is hosted inside a cubic crystal. Very recently, a study by Barson *et al.* measured all four spin-stress coupling constants using static uniaxial stress [109]. In their experiments, a pneumatically actuated push press was used to apply uniaxial stress to a diamond anvil cell while continuous wave ODMR was performed on an ensemble of embedded NV centers. The coupling constants were measured by monitoring the uniform shift (corresponding to A_1 strain) and splitting (corresponding to E strain) of the ESR peaks as a function of applied stress.

Despite our incomplete model, we can make some comparisons between our measured strain coupling constants and the stress coupling constants in Barson *et al.* The stress coupling constants can be converted into strain coupling constants by transforming into

the crystal frame and applying the elastic stiffness matrix:

$$\begin{aligned} d_{A_1} &= -3.0 \text{ GHz} \\ d_{A_1'} &= 11.2 \text{ GHz} \\ d_E &= 2.0 \text{ GHz} \\ d_{E'} &= 6.6 \text{ GHz} \end{aligned} \tag{4.29}$$

We can compare our value for $d_\parallel$ to these measured coupling constants by calculating the A_1 symmetric strain coupling for a unit strain, $d_{A_1}\epsilon_{zz} + d_{A_1'}(\epsilon_{xx} + \epsilon_{yy})$. Because we measured $d_\parallel$ with NVs in group A, we substitute the unit strain tensor for an NV in group A and find an equivalent $d_\parallel = 0.6$ GHz, which does not agree with our result. Interestingly, if we use the strain tensor for group B, Barson would predict a value of $d_\parallel = 12$ GHz, which agrees relatively well with the result found here. In addition, our measured value of $d_\perp$ does not agree with the measurement of Barson. Interestingly, our value of $d_\perp$ agrees well with a related study by Teissier *et al.*, which measured the strain coupling constants using static bending of a diamond cantilever [77].

4.10 Origin of the spin-strain interaction

In chapter 2, we showed that the spin-strain interaction can be explained by both spin-orbit and spin-spin interactions between the ground and excited state manifolds. However, it is not obvious if one of these interactions is the dominant mechanism. Interestingly, the experiments shown here along with recent work by Doherty *et al.* indicate that the spin-spin interaction is the primary mechanism for the spin-strain interaction [175]. *Ab initio* calculations by Doherty showed that under hydrostatic pressure, the

change in the zero-field splitting is approximately 6.5 GHz per unit strain, which is of the same order of magnitude as our result. This semi-classical calculation considered the modification of the spin-spin interaction within the ground state triplet due to isotropic changes in the sp^3 bond lengths. Further calculations performed by Doherty using density functional theory estimate that the distortion in the unpaired spin density from crystal strain strongly modifies the spin-spin interaction within the ground state. The calculated spin-strain couplings are again of the same order of magnitude as our results, suggesting that the spin-spin interaction is the dominant factor in the spin-strain interaction

4.11 Toward spin-phonon interactions in the quantum regime

Looking ahead toward quantum spin-phonon interactions, we observe that the zero point motion coupling for our current devices is quite small, with $g_\perp = 40$ mHz. However, this value can be significantly increased by reducing the device dimensions to the nanoscale. For instance, a doubly-clamped beam with dimensions of 2 μm $\times$ 50 nm $\times$ 50 nm and $\omega_m/2\pi = 238$ MHz would have a coupling $g_\perp \sim 180$ Hz. Although the NV spin exhibits smaller strain couplings than other systems, such as quantum dots [72], the NV center has a significantly longer coherence time. Assuming a bath temperature of $T = 100$ mK, a mechanical quality factor $Q = 10^6$ and $T_2 = 100$ ms, this doubly clmaped beam achieves a single spin cooperativity, $\eta = 2\pi\frac{g_\perp^2 T_2}{\gamma\bar{n}} \approx 1.6$, where $\gamma = \omega_m/Q$ is the damping rate and $\bar{n}$ is the equilibrium thermal occupation number of the resonator. These parameters have been demonstrated independently in a variety of systems. For instance, single crystal diamond cantilevers have been shown to exhibit $Q > 10^6$ at temperatures of less than 50 K [44]. In our current devices, the spin coherence times

are limited to tens of microseconds. By utilizing nitrogen delta-doping techniques and higher order dynamical decoupling pulse sequences, it should be possible to significantly increase T_2 [97, 131]. Very recently, coherence times exceeding 500 ms were recorded for a single NV center at liquid nitrogen temperatures [138]. We note that although smaller resonators could increase $g_\perp$, clamping losses would limit their quality factors [164]. However, the strain coupling to the orbital levels of the NV center is significantly higher, and for the resonator described here, would give a coupling exceeding 10 MHz [80]. Therefore, a device utilizing strain-orbit coupling presents an alternative route to accessing the regime of strong spin-phonon coupling.

4.12 Conclusion

In conclusion, we have presented for the first time a novel, hybrid quantum system coupling a spin electron spin to a mechanical oscillator through crystal strain. We demonstrated mechanically driven, coherent spin evolution, which enabled nanoscale strain imaging as well as a quantitative analysis of the spin-strain coupling mechanism. We note that the measurements and analysis utilized here can be generalized to measure all four spin-strain coupling constants of the NV center, and can be used to measure strain couplings to other solid-state defects, such as color centers in SiC [176, 177]. As a nanoscale strain sensor, the NV could be critical to identifying the poorly understood origins of dissipation in mechanical oscillators, which is instrumental in engineering high-Q mechanical resonators [178]. Moreover, our results could provide insight into the role of strain in the decoherence of the ground state spin levels. Most importantly, we have demonstrated that our device architecture provides a feasible route to accessing coherent spin-phonon interactions, with applications ranging from quantum control of a macroscopic mechanical oscillator to long-range spin-spin interactions.

4.13 Supporting information

4.13.1 Cantilever strain profile

The strain introduced by the mechanical motion of the cantilever can be modeled theoretically using Euler-Bernoulli beam theory [160], which describes the bending modes of long, thin beams. We consider a singly-clamped diamond beam of length l, width w, and thickness t. We define the cantilever coordinate system (X, Y, Z), such that the Z axis (cantilever axis) lies along the length of the beam and flexural vibrations occur along the Y direction. The strain associated with pure bending is given by the radius of curvature of the beam and hence is directly proportional to the amplitude of bending. Using the results from chapter 2, we find that the strain experienced by an NV center at a position Z along the cantilever axis can be written as

$$\begin{aligned}\varepsilon(Z, x_c) \simeq & R_0 \frac{x_c}{2l^2}(1.875)^2 \Bigg[\cos\left(1.875\frac{Z}{l}\right) + \cosh\left(1.875\frac{Z}{l}\right) \\ & - \frac{1}{1.3622}\left(\sin\left(1.875\frac{Z}{l}\right) + \sinh\left(1.875\frac{Z}{l}\right)\right)\Bigg]\end{aligned} \tag{4.30}$$

where R_0 refers to the distance in the Y direction from the neutral axis of the beam. For an NV that is at a depth d_i from the surface of the cantilever, $R_0 = (t/2) - d_i$. The NV depth is determined by the nitrogen implantation process, and $d_i = 51.5 \pm 13.0$ nm. The quoted uncertainty in d_i corresponds to one standard deviation in the straggle of nitrogen ions during ion implantation (calculated by Stopping Range of Ions in Matter (SRIM) simulations).

4.13.2 Strain tensor in the NV coordinate system

To understand the spin response to cantilever motion, it is necessary to calculate the mechanical strain tensor in the NV coordinate system. The strain tensor for a cantilever under pure bending in the cantilever coordinate system is

$$\Xi = \begin{vmatrix} -\nu\varepsilon & 0 & 0 \\ 0 & -\nu\varepsilon & 0 \\ 0 & 0 & \varepsilon \end{vmatrix} \tag{4.31}$$

where ε is the mechanically induced strain along the Z direction in the previous section and $\nu = 0.069$ is the Poisson ratio of CVD diamond. The cantilevers are cut along the (110) crystal plane and the diamond is grown along the (100) plane. Therefore, we find $Z \parallel [110]$, $X \parallel [\bar{1}10]$, and $Y \parallel [001]$. t.

The NV coordinate system depends on its orientation within the diamond crystal. There are 4 possible crystallographic orientations for the NV z axis

$$\begin{aligned} \hat{v}_1 &= [\bar{1}\bar{1}\bar{1}] \\ \hat{v}_2 &= [\bar{1}11] \\ \hat{v}_3 &= [1\bar{1}1] \\ \hat{v}_4 &= [11\bar{1}] \end{aligned} \tag{4.32}$$

The x axis of the NV center lies along the projection of any of the 3 carbon atoms in the plane perpendicular to the NV axis. We will define the NV reference frame T^{ik}, where the NV z axis lies along $\hat{v}_i$ and the NV x axis lies along the projection of a carbon bond that lies along $\hat{v}_j$. To obtain the strain tensor in the NV reference frame, we apply a similarity transformation of the form $\mathbf{P}^{ik}\Xi(\mathbf{P}^{ik})^T$. We note that although there are 3 unique transformations and strain tensors that can be made for each NV orientation

(due to the C_3 rotational symmetry), the spectral response of the NV center is invariant to the choice of x axis.

Due the symmetry of the cantilever, we can group NV centers into two separate groups, A and B, within which NV centers experience the same strain tensor. Group A contains NV centers oriented along $\hat{v}_1$ and $\hat{v}_4$, and group B contains NV centers oriented along $\hat{v}_2$ and $\hat{v}_3$. For NVs in group A we choose the transformations

$$\mathbf{P}^{14} = \begin{vmatrix} 0 & -\sqrt{\frac{2}{3}} & \frac{1}{\sqrt{3}} \\ -1 & 0 & 0 \\ 0 & -\frac{1}{\sqrt{3}} & -\sqrt{\frac{2}{3}} \end{vmatrix} \tag{4.33}$$

$$\mathbf{P}^{41} = \begin{vmatrix} 0 & -\sqrt{\frac{2}{3}} & -\frac{1}{\sqrt{3}} \\ 1 & 0 & 0 \\ 0 & -\frac{1}{\sqrt{3}} & \sqrt{\frac{2}{3}} \end{vmatrix} \tag{4.34}$$

and for NVs in group B we choose the transformations

$$\mathbf{P}^{23} = \begin{vmatrix} -\frac{1}{\sqrt{3}} & \sqrt{\frac{2}{3}} & 0 \\ 0 & 0 & 1 \\ \sqrt{\frac{2}{3}} & \frac{1}{\sqrt{3}} & 0 \end{vmatrix} \tag{4.35}$$

$$\mathbf{P}^{32} = \begin{vmatrix} \frac{1}{\sqrt{3}} & \sqrt{\frac{2}{3}} & 0 \\ 0 & 0 & -1 \\ -\sqrt{\frac{2}{3}} & \frac{1}{\sqrt{3}} & 0 \end{vmatrix} \tag{4.36}$$

From these transformations we see that the strain tensors for each group are

$$\Xi_A = \begin{vmatrix} \frac{\varepsilon}{3}(1-2\nu) & 0 & -\frac{\sqrt{2}\varepsilon}{3}(1+\nu) \\ 0 & -\nu\varepsilon & 0 \\ -\frac{\sqrt{2}\varepsilon}{3}(1+\nu) & 0 & \frac{\varepsilon}{3}(2-\nu) \end{vmatrix} \tag{4.37}$$

$$\Xi_B = \begin{vmatrix} -\nu\varepsilon & 0 & 0 \\ 0 & \varepsilon & 0 \\ 0 & 0 & -\nu\varepsilon \end{vmatrix} \tag{4.38}$$

NV centers in group A are oriented nearly parallel with cantilever axis, and will predominantly experience axial strain, whereas NV centers in group B are oriented perpendicular to the cantilever axis, and will experience predominantly transverse strain. The classical strain coupling parameters $G_\parallel$ and $G_\perp$ can then be defined for each group

$$\begin{aligned} G_\parallel^A &= \frac{1-2\nu}{3} d_\parallel \varepsilon \\ G_\perp^A &= \sqrt{\nu^2 + \frac{1}{9}(2-\nu)^2}\, d_\perp \varepsilon \\ G_\parallel^B &= -\nu d_\parallel \varepsilon \\ G_\perp^B &= \sqrt{1+\nu^2}\, d_\perp \varepsilon \end{aligned} \tag{4.39}$$

4.13.3 Estimation of the single-spin backaction force

In the measurements performed in this chapter, we have described the parametric spin-phonon interaction in terms of a shift of the qubit frequency due to the motion of a mechanical oscillator. Alternatively, this interaction can also be interpreted as a reciprocal spin-dependent force on the oscillator. The Hamiltonian for the parametric spin-phonon interaction is linear in position, $H = \frac{g}{2} X \sigma_Z$, and hence the force exerted by a

single spin on the oscillator is simply $F = \frac{g}{2x_0}\sigma_z$. For the devices in this chapter, we expect a backaction force of $F \sim 8 \times 10^{-21}$ N. If the spin is driven with resonant microwaves with a Rabi frequency equal to the mechanical resonance frequency, this would induce a $x_c = \frac{FQ}{\omega_m^2 \mu} = 800$ fm displacement. This is small compared to the amplitude of Brownian motion, $x_{th} = 10$ pm, and hence would not be detectable in our experiments.

Chapter 5

Mechanical control of the optical properties of a single quantum emitter

> Fry: "I heard one time you single-handedly defeated a horde of rampaging somethings in the something something system"
>
> Zapp Brannigan: "The killbots? A trifle. It was simply a matter of outsmarting them."
>
> Fry: "Wow, I never would've thought of that."
>
> Zapp Brannigan: "You see, killbots have a preset kill limit. Knowing their weakness, I sent wave after wave of my own men at them until they reached their limit and shut down.
>
> - *Futurama*

The contents of this chapter have been adapted with minor edits from ref. [80].

5.1 Introduction

Hybrid quantum devices involving mechanical systems are attractive candidates for future quantum technologies. Mechanical systems are sensitive to a diverse array of external forces, and with recent advancements made in nanofabrication techniques, these systems can be precisely engineered with high quality factors. Several experiments have exploited this sensitivity to engineer magnetic, electric, and strain couplings between mechanical resonators and two-level systems in atoms, quantum dots, superconducting Josephson junctions and defects in semiconductors [56, 75, 72, 74, 68, 66, 73]. These experiments have demonstrated coherent mechanical control of two-level systems and in some cases, coupling of the two-level system to the quantum motion of the resonator. Ultimately, these devices strive to address several outstanding challenges in the development of quantum technologies, including the realization of long-range interactions between a wide variety of quantum systems, and the preparation of non-classical states of a macroscopic mechanical object [54, 24].

Hybrid spin-mechanical devices that utilize a crystal strain interface offer several promising applications in the fields of quantum information science and sensing. For example, crystal strain associated with the spatially extended phonon modes of mechanical resonators can be used as a quantum data bus to transmit quantum information between disparate qubits [179, 41], prepare spins in entangled or squeezed states [39, 25], or provide an interface between photons of disparate energy scales [180, 181]. This interaction can similarly be used to cool mechanical resonators to their quantum ground state, enabling fundamental studies of quantum mechanics in macroscopic objects [170, 169, 60, 61].

From a practical standpoint, using crystal strain to interface a mechanical resonator with a two-level system has many advantages. Strain directly couples the two systems without the need for external components or functionalization of the resonator, and there-

fore allows for a monolithic architecture. Importantly, the coupling does not generate noisy stray fields, which may degrade the coherence of the system. Furthermore, a monolithic architecture eliminates drifts in the coupling strength and allows for more facile device fabrication, which is crucial when scaling the device to large numbers of quantum systems.

A leading candidate for a strain-coupled hybrid device consists of nitrogen-vacancy (NV) defect center spins and diamond mechanical resonators [76, 77, 51, 82]. The electron spin of the NV center has been shown to exhibit long coherence times near one second at 77 K and single-crystal diamond mechanical resonators have been fabricated with high quality factors in excess of one million [138, 44]. To date, experiments coupling mechanical oscillators to the NV spin have realized mechanically driven spin dynamics, enabling coherent spin manipulation in the strong coupling regime [53], nanoscale strain sensing [76], and continuous dynamical decoupling from magnetic field noise [53, 78]. However, proposed hybrid quantum devices involving the NV center, photons, and phonons will also require a mechanical coupling to the orbital states of the NV center [40]. The orbital degree of freedom is inherently more sensitive to crystal strain than the spin degree of freedom, and thus provides higher single-phonon couplings. In addition, coupling to the orbital states allows for direct tuning of the optical transitions of the NV center, which is essential for photonic applications that require generation of indistinguishable photons, such as entanglement of distant spins [150]. Importantly, strain-orbit coupling enables several applications that are inaccessible with spin-strain coupling, such as phonon cooling of a mechanical resonator and phonon routing [169, 40]. Very recently, coherent control of the NV orbital states was demonstrated using a combination of optical fields and strain fields associated with propagating surface acoustic waves generated by an interdigitated transducer [79].

In this chapter, we realize a dynamic, strain-mediated coupling between the orbital

states of a single NV center in diamond and the resonant mechanical motion of a diamond cantilever. The time-varying strain field generated by the cantilever displacement modulates both the energy and polarization dependence of the optical transitions of the NV center, which we characterize using resonant excitation spectroscopy (RES). With mechanical driving, we observe large (10 GHz) NV strain-orbit coupling and precisely characterize the strain-orbit coupling constants. Notably, we observe strain-mediated single phonon coupling strengths of a few kHz, which are three to five orders of magnitude higher than those previously demonstrated with the NV spin [76, 77, 51, 82]. Finally, we use this coupling to match the energy and polarization dependence of the zero-phonon lines of two spatially separated NV centers.

5.2 Experimental setup and sample preparation

Our experiments are performed on single, negatively-charged NV centers embedded in a single-crystal diamond cantilever as depicted in fig. 5.1a. In fig. 5.1c., we show a simplified energy level diagram of the NV center that depicts the relevant energy levels investigated here. An orbital-singlet/spin-triplet ground state, $^3A_2$, is connected to an orbital-doublet/spin-triplet excited state, ^3E, by a zero-phonon dipole transition at 637 nm. Here, we focus on electronic states with spin projection $m_s = 0$, consisting of two excited state levels ($|E_x\rangle, |E_y\rangle$) and one ground state level ($|A\rangle$) (although $|E_x\rangle$ and $|E_y\rangle$ are slightly mixed via spin-spin interaction with $m_s = 1$ spin projections under perfect C_{3v} symmetry, we neglect this effect and approximate them as the $m_s = 0$ spin projections of the excited state). Experiments are carried out at cryogenic temperatures ($\sim$7 K) where phonon broadening of the optical transitions is negligible and the excited state fine structure is accessible [100]. We use a home-built confocal microscope to optically address single NV centers in diamond cantilevers and to interferometrically monitor the

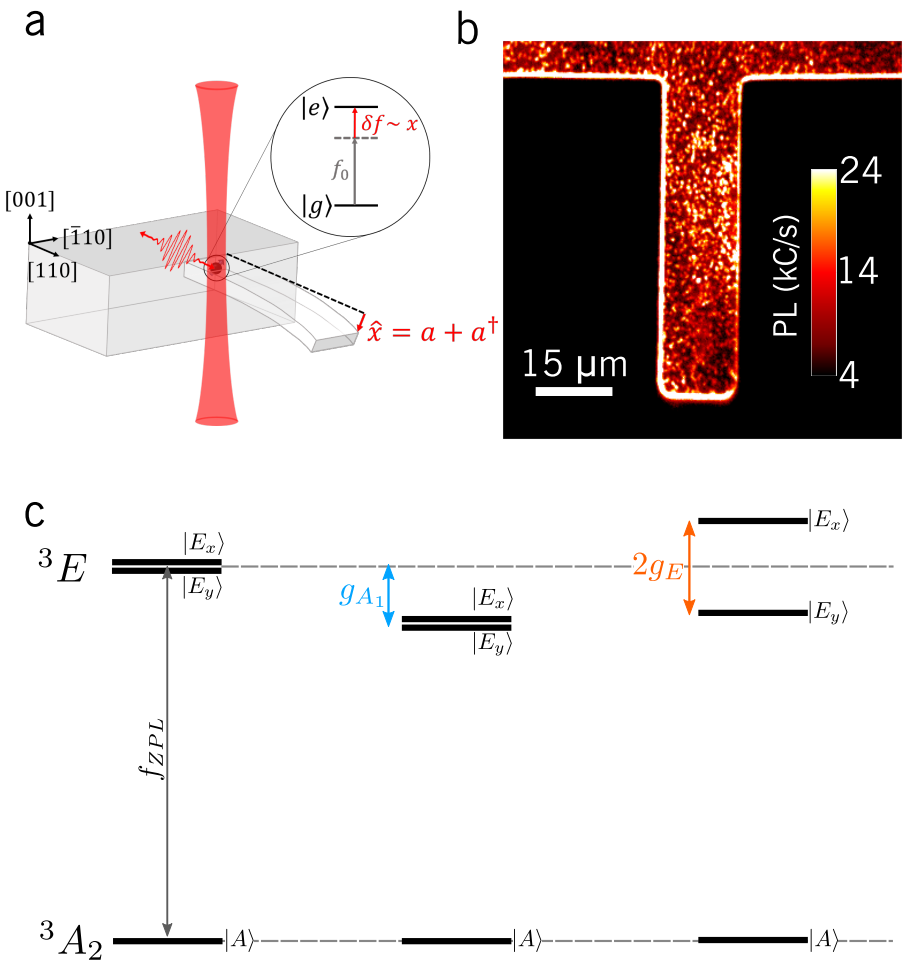

Figure 5.1: **Strain-orbit coupling and experimental setup**. a) An NV center is embedded in a diamond cantilever and strain produced by the cantilever motion shifts the resonance frequency of the zero-phonon line. A 637 nm lase probes the shifts using resonant excitation spectroscopy. b) A photoluminescence image of a diamond cantilever shows the presence of embedded NV centers. c) Simplified energy level diagram depicting the optical transitions between the $m_s = 0$ electronic levels. Under no strain, the E_x and E_y states are degenerate (left panel). Strain of A_1 symmetry shifts the E_x and E_y states together (center), while strain of E symmetry splits the E_x and E_y levels (right).

cantilevers motion. In our experiments, we off-resonantly excite the NV center with 532 nm laser light to identify NV centers in the cantilever (fig. 5.1b.), optically pump the NV center into the $m_s = 0$ spin sublevel of the ground state, and to initialize the NV^- charge state. A tunable diode laser near 637 nm (New Focus Velocity) is used for resonant

excitation of the NV zero-phonon line, and is gated with an acousto-optic modulator (Intraaction). A combination of linear polarizers and a liquid-crystal retarder is used to control the linear polarization of the resonant excitation light. The relative polarization of the laser light with respect to the diamond crystallographic orientations is monitored with a polarimeter. Photons emitted by the NV are collected into a single-mode fiber and subsequently detected by an avalanche photodiode (APD).

A piezoelectric transducer with a capacitance of 17 nF is mounted just below the sample for resonant mechanical driving of the diamond cantilevers. A continuous wave diode laser at 450 nm (Thorlabs) is used for interferometric detection of the mechanical motion of the cantilever. The mechanical motion of the cantilever phase modulates the reflected light off the cantilever surface and interferes with light that passes through the cantilever and reflects off the silicon substrate located 1 μm below the cantilever. The 450 nm light is filtered out of the collection path using a longpass dichroic filter (Semrock).

The cantilever used in this experiment was fabricated using the silicon-on-insulator technique [43] described in chapter 3. NV centers were formed via nitrogen implantation, with a dosage of 3×10^9 ion/cm^2 at 40 keV and a 0° tilt, yielding an expected nitrogen depth of 51.5 nm (calculated by Stopping and Range of Ions in Matter (SRIM)). The sample was annealed under high vacuum (10^{-6} Torr) at 800 °C for 3 hours to create NV centers.

5.3 Optical characterization using resonant excitation spectroscopy (RES)

To characterize the coherent optical transitions of the NV center, we perform resonant excitation spectroscopy (RES), which directly probes the absorption spectrum of the NV

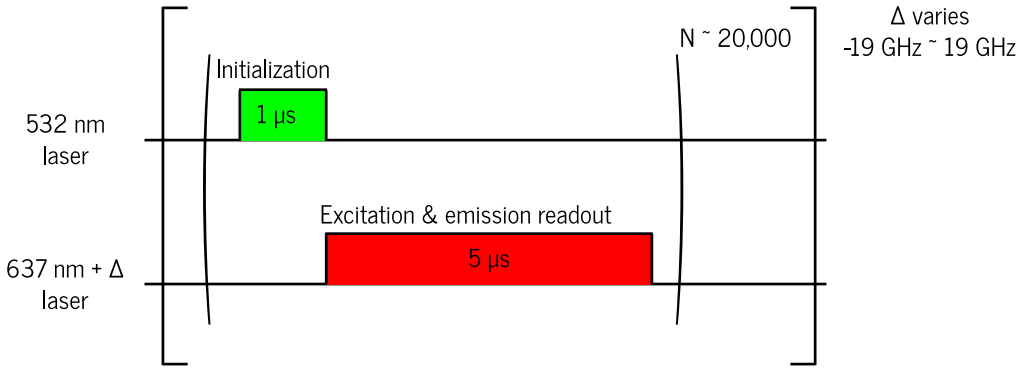

Figure 5.2: **Resonant excitation spectroscopy**. Experimental sequence describing resonant excitation spectroscopy.

center. The experimental protocol for RES is shown in fig. 5.2. The experiment begins with a short 1 μs pulse of 532 nm laser light generated by an acousto-optic modulator (AOM). This pulse initializes the NV negative charge state and also optically pumps the NV into the $m_s = 0$ spin level of the ground state, $|A\rangle$. Next, a 5 μs pulse of light near 637 nm from the tunable diode laser is sent to the NV for resonant excitation of the zero-phonon line (ZPL). During this pulse, we monitor the NV fluorescence using an avalanche photodiode. If the laser is resonant with one of the optical transitions, the NV center will fluoresce. This two-pulse sequence is repeated 20,000 times for a particular laser frequency. The laser frequency is swept by changing the voltage of a piezoelectric element that controls the laser cavity length. In each scan, the laser is swept over a 38 GHz frequency band, which is the maximum frequency window allowed by the laser piezo (see chapter 3). The laser frequency sweep is calibrated with a scanning Fabry-Perot invar cavity with a free spectral range of 1.5 GHz.

It is important to note that the experimental parameters used in this sequence were optimized specifically for the NV centers in this sample. The optimal values of the 532 nm laser power, 532 nm laser pulse length, 637 nm laser power, and the 637 nm laser pulse

length may vary significantly across samples, and even across NV centers within a sample. The reason for this is unclear, but is likely linked to the photoionization rate of the NV center. The 637 nm laser efficiently ionizes the NV center from the negative charge state to the neutral charge state via a two-photon photoionization process [113, 115]. The first photon promotes an NV electron into the ^3E manifold and the second photon promotes the electron into the conduction band. The 532 nm laser then restores the negative charge state by promoting an electron from the valence band to the bound states of the NV center. Despite this simple model, it is clear that the electrostatic environment of the NV center significantly contributes to the ionization dynamics. Near-surface NV centers typically photoionize or "blink" more often than bulk NV centers [182, 183]. This is also true of implanted NV centers compared to bulk, naturally occurring NV centers [184]. During optical measurements, it is possible to alter the local electrostatic environment, producing photo-induced fields at the NV center which can alter the relevant energy scales for photoionization [145]. Interestingly, this effect is closely related to the spectral diffusion of the zero-phonon line. We will discuss spectral diffusion in more detail in the final chapter of this thesis.

5.4 Strain-orbit interaction

The strain-orbit Hamiltonian arises from a modification of the Coulomb interaction between the crystal ions and the electrons of the NV center due to small, relative displacements of the crystal ions. To analyze the effect of crystal strain, let us consider a generic strain experienced by the NV center as defined in its own coordinate basis, which

is characterized by the strain tensor, ϵ.

$$\epsilon = \begin{vmatrix} \epsilon_{xx} & \epsilon_{xy} & \epsilon_{xz} \\ \epsilon_{yx} & \epsilon_{yy} & \epsilon_{yz} \\ \epsilon_{zx} & \epsilon_{zy} & \epsilon_{zz} \end{vmatrix} \tag{5.1}$$

The NVs coordinate system is shown in fig. 2.1 from chapter 2. The z-axis, or NV axis, lies along the nitrogen bond, and can point in 4 crystallographic directions: $[\bar{1}\bar{1}\bar{1}]$, $[11\bar{1}]$, $[\bar{1}11]$, or $[1\bar{1}1]$. The NV x-axis lies along the projection of a carbon bond in the plane perpendicular to the NV axis. The strain Hamiltonian can be written in terms of individual components of the strain tensor, as shown in chapter 2

$$H_{strain} = \sum_{i,j} \Lambda_{ij} \epsilon_{ij} \tag{5.2}$$

where i, j refer to Cartesian indices of the NV coordinate system and Λ_{ij} are orbital operators. The NV center has C_{3v} symmetry, and hence it is useful to project the strain Hamiltonian onto the irreducible representations of the C_{3v} group, $\Gamma = \{A_1, A_2, E\}$ [99, 100].

$$H_{strain} = \sum_{\Gamma} \Lambda_{\Gamma} \epsilon_{\Gamma} \tag{5.3}$$

In the above Hamiltonian we take advantage of the fact that since strain is a symmetric second-rank tensor, its components transform as the quadratic basis functions of the C_{3v} group. Therefore, H_{strain} will only contain components that transform as A_1 and E. For instance, ϵ_{zz} transforms like z^2, and hence it will transform as A_1. Strains that transform as A_1 will preserve the C_3 rotational symmetry and σ_v reflection symmetry of the NV center; whereas, strains that transform as E will break both the rotation and reflection symmetries.

In our experiments, we focus on the $m_s = 0$ eigenstates of the triplet manifolds, $\{|A\rangle, |E_x\rangle, |E_y\rangle\}$. In this basis, the NV-strain interaction can be written as

$$\begin{aligned} H_{strain} =& \big[\lambda_{A_1}\epsilon_{zz} + \lambda_{A_1'}(\epsilon_{xx}+\epsilon_{yy})\big]\big[\,|E_x\rangle\langle E_x| + |E_y\rangle\langle E_y|\,\big] \\ &- \big[\lambda_E(\epsilon_{xx}-\epsilon_{yy}) + \lambda_{E'}(\epsilon_{xz}+\epsilon_{zx})\big]\big[\,|E_x\rangle\langle E_x| - |E_y\rangle\langle E_y|\,\big] \\ &+ \big[\lambda_E(\epsilon_{xy}+\epsilon_{yx}) + \lambda_{E'}(\epsilon_{yz}+\epsilon_{zy})\big]\big[\,|E_x\rangle\langle E_y| + |E_y\rangle\langle E_x|\,\big] \end{aligned} \tag{5.4}$$

where λ_{A_1}, $\lambda_{A_1'}$, λ_E, and $\lambda_{E'}$ are the strain-orbit coupling constants in units of Hz.

5.5 NV-resonator interaction

In our experiments, the strain induced by the cantilever motion is linear in the cantilever tip deflection, $\epsilon = \epsilon_0(a + a^\dagger)$. Here, ϵ_0 is the strain induced by zero point fluctuations of the cantilever and a is the annihilation operator of the cantilever mode. In the $\{|A\rangle, |E_x\rangle, |E_y\rangle\}$ basis, the strain-coupled NV-resonator Hamiltonian ($h = 1$) takes the form

$$\begin{aligned} H_{NV} =& f_{ZPL}\Big(\,|E_x\rangle\langle E_x| + |E_y\rangle\langle E_y|\,\Big) + \frac{\omega_m}{2\pi}a^\dagger a + \Bigg[g_{A_1}\Big(\,|E_x\rangle\langle E_x| + |E_y\rangle\langle E_y|\,\Big) \\ &+ g_{E_1}\Big(\,|E_x\rangle\langle E_x| - |E_y\rangle\langle E_y|\,\Big) + g_{E_2}\Big(\,|E_x\rangle\langle E_y| + |E_x\rangle\langle E_y|\,\Big)\Bigg] \end{aligned} \tag{5.5}$$

where f_{ZPL} is the natural zero-phonon line frequency, ω_m is the cantilever frequency, g_Γ is the single phonon coupling strength for phonons with symmetry Γ, $a(a^\dagger)$ are the creation (annihilation) operators for the phonon mode of the cantilever, and we have defined $|A\rangle$ to be at zero energy. In a perfect crystal lattice with no applied external fields, the NV has perfect C_{3v} symmetry and $|E_x\rangle$ and $|E_y\rangle$ are degenerate in energy. Strain of A_1 symmetry corresponds to dilations and contractions of the NV molecular

structure that preserve the C_{3v} symmetry. An A_1-symmetric strain preserves the $|E_x\rangle$ and $|E_y\rangle$ degeneracy and uniformly shifts the two states in energy with respect to $|A\rangle$. Conversely, strains of E_1 and E_2 symmetry break all symmetries of the NV center, and therefore split and mix $|E_x\rangle$ and $|E_y\rangle$ respectively (Fig 1c). From the NV-resonator Hamiltonian, the E_x and E_y transition frequencies, f_+ and f_- , can be expressed in terms of the normalized cantilever displacement, $x = x_c/x_0$,

$$f_\pm(x) = f_{ZPL} + \delta f_{A_1} + g_{A_1} x \pm \sqrt{(g_{E_1} x + \delta f_{E_1})^2 + (g_{E_2} x + \delta f_{E_2})^2} \tag{5.6}$$

where x_0 is the amplitude of zero-point motion, x_c is the peak displacement of the cantilever, and δf_Γ corresponds to the frequency shift due to local, intrinsic strain of symmetry Γ.

5.6 Dynamic NV-mechanical coupling

We demonstrate strain-mediated NV-phonon coupling by mechanically driving the fundamental flexural mode of a cantilever with a resonance frequency $\omega_m/2\pi = 870$ kHz and performing RES on a single embedded NV (fig. 5.3). In the absence of mechanical driving, we observe two Lorentzian peaks within the RES spectrum (gray) corresponding to the E_x and E_y transitions. Under a resonant mechanical drive the peaks are modulated (red) by the AC strain field produced by the cantilevers flexural motion, which is given by $x(t) = x_c/x_0 \cos(\omega_m t)$. The time-varying strain modulates the optical transition frequencies, and hence the center frequency of these Lorentzian peaks. In addition, the strain field will modulate the polarization selection rules for the transitions. Since the laser polarization is kept constant throughout the measurement, this modulation will manifest as a modulation of the peak PL emission intensity. The broadened, double-

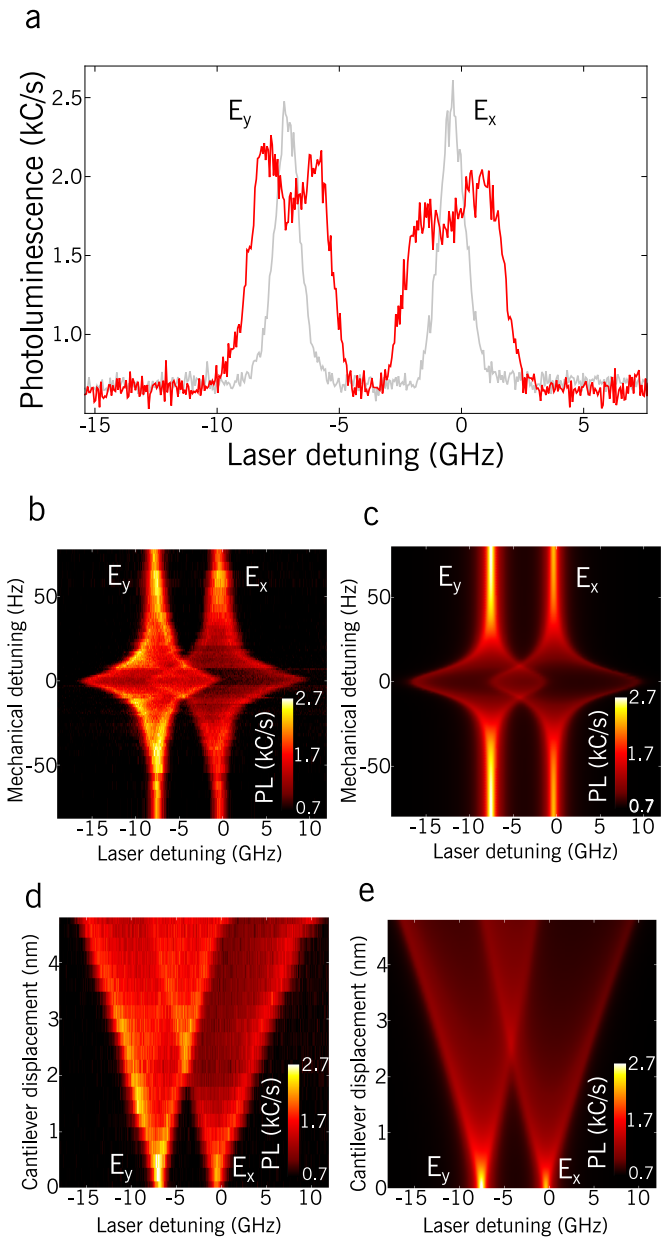

Figure 5.3: **Dynamic strain-orbit coupling**. a) RES measurement of a single NV center embedded in a cantilever. In the absence of mechanical driving (gray curves), the optical transition lineshapes are Lorentzian. Under resonant mechanical driving (red), the transitions are modulated and the lineshapes are broadened. b) Experimental and c) simulated excitation spectra of the E_x and E_y transitions as a function of mechanical drive detuning, showing the resonant nature of the coupling. d) Experimental and e) simulated excitation spectra as a function of the amplitude of the mechanical excitation.

peaked lineshape results from averaging over the cantilever motion and can be modeled by a Lorentzian with an oscillating center frequency and modulated peak intensity,

$$\mathcal{S}_{\pm}(f) = \frac{2\pi}{\omega_m}\int_0^{2\pi/\omega_m} \mathcal{I}_{\pm}\left(x(t)\right)\frac{(\Gamma/2)^2}{(\Gamma/2)^2+\left(f-f_{\pm}\left(x(t)\right)\right)^2}dt \tag{5.7}$$

where $\mathcal{I}_{\pm}$ refers to the PL intensity of each peak (measured in kC/s). In the data shown in figure, the linewidth of these peaks is $\Gamma = 1.4$ GHz.

Next, we show the dynamic modulation of the E_x and E_y transitions as the drive frequency is swept through the cantilever resonance. Due to the finite quality factor of the cantilever, the cantilever will respond to mechanical excitations over a small frequency band around its resonance frequency. For weak mechanical excitation, the cantilever exhibits a Lorentzian mechanical response whose linewidth is determined by its quality factor. Therefore, the normalized cantilever tip position can be written as

$$x(t) = \frac{x_c(\omega_{piezo})}{x_0}\cos\left(\omega_{piezo}t\right) \tag{5.8}$$

where

$$x_c(\omega_{piezo}) \sim x_{max}\frac{(\gamma/2)^2}{(\gamma/2)^2+(\omega_{piezo}-\omega_m)^2} \tag{5.9}$$

Here, x_{max} refers to the maximum tip deflection when driven on resonance, ω_{piezo} is the actuation frequency, and $\gamma = \omega_m/Q$ is the linewidth of the mechanical resonance.

The resonant behavior of the mechanical mode is clearly imprinted on the spectral response of the NV center (fig. 5.3b). Far detuned from the mechanical resonance, the transitions are unaffected and maintain their Lorentzian lineshape. Approaching resonance, the lineshapes broaden due to the increasing deflection of the cantilever. The spectral response of the NV is in good agreement with simulations shown in fig. 5.3c, which take into account the intrinsic strain environment and the mechanical quality

factor of 20,000. The asymmetric frequency modulation of the optical transitions, most clearly seen at zero mechanical detuning, arises from intrinsic crystal strain of E_1 and E_2 symmetry, which we discuss in greater detail later. In addition, the intrinsic E_1- and E_2- symmetric strains are responsible for the splitting between $|E_x\rangle$ and $|E_y\rangle$ when the cantilever is at rest, $\Delta f_0 = 2\sqrt{(\delta f_{E_1})^2 + (\delta f_{E_2})^2}$.

Next, we probe the strength of the strain-mediated NV-phonon coupling as a function of cantilever deflection for a resonant mechanical drive (fig. 5.3d). As the amplitude of beam deflection increases, the strain-modulation of the optical transitions increases approximately linearly, as predicted by equation (2). For the NV measured in fig. 5.3, we observe strain-mediated NV-phonon couplings exceeding 10 GHz for cantilever displacements of only a few nanometers. Our measurement is in good agreement with simulations (fig. 5.3e) and demonstrates the large coupling of the orbital states to the mechanical motion of the cantilever. We note that the observed coupling strengths are limited by the scanning range of the resonant excitation laser and not by the device itself. The cantilevers can be driven a maximum of $x_c = 1$ μm, which would correspond to a coupling strength of approximately 1 THz.

5.7 Determination of the single-phonon couplings and strain-orbit coupling constants

To accurately determine the single-phonon coupling parameters, we must isolate the effects of strain for each symmetry, which cannot be accomplished with the continuous wave (CW) spectroscopy technique employed above. The CW spectral response of the NV is a time-averaged response that samples all points of the cantilevers motion, making it difficult to distinguish between common mode shifts and splittings of $|E_x\rangle$ and

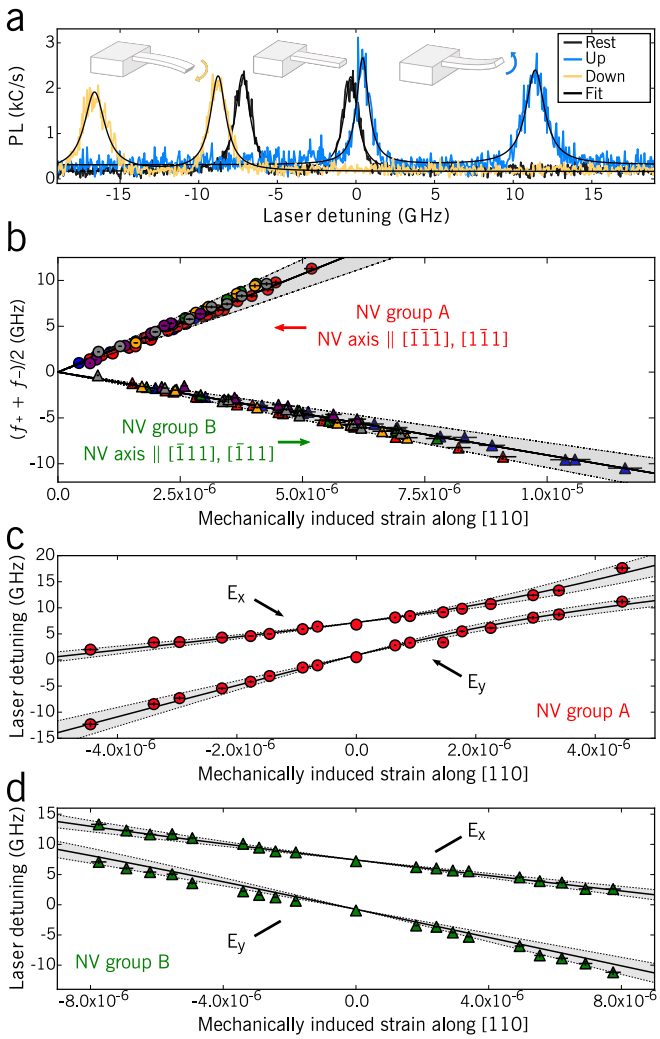

Figure 5.4: **Stroboscopic strain-orbit coupling**. a) A stroboscopic RES measurement shows shifts of the E_x and E_y transitions when the cantilever tip is deflected upward (blue curve) or downward (yellow curve) by 24 nm. The transitions when the cantilever is at rest are shown in gray. The line shapes are fit with Lorentzians (black curve). b) Plot of the common mode shift of theE_x and E_y states for 12 different NV centers, each marked by a different color. Circles (triangles) indicate NV centers in group A (B). Linear fits to the data are shown in black. The gray shaded area indicates a 15% uncertainty in the amplitude of driven motion determined from optical-interferometry measurements. c) and d) plot the total frequency shifts of the E_x and E_y transitions for NV centers in groups A and B. Error bars in b)d) correspond to 5° phase uncertainties in the relative phase between the measurement window and the cantilevers motion in the stroboscopic measurement (vertical) and 13-nm uncertainties in the NV depth (horizontal).

$|E_y\rangle$. However, by performing stroboscopic RES synchronized to the cantilevers motion, we can deconvolve the orbital dynamics from the mechanical motion [81]. Specifically, we measure the NV fluorescence in 60 ns windows that are much shorter than the cantilevers 1.15 μs oscillation period, thus enabling RES at a well-defined cantilever position (see supporting information). In fig. 5.4a, we demonstrate stroboscopic RES when the cantilever is maximally deflected upward (blue) and maximally deflected downward (orange) with $x_c = 24$ nm. Importantly, we can distinguish the effects of uniform shifts of the transitions due to A_1 strain from splittings due to E strain, and with the well-known strain profile of a cantilever, we may extract the strain-orbit coupling constants [76, 77]. The single-phonon coupling parameters can be written explicitly in terms of the strain-orbit coupling constants and the strain induced by the zero-point motion of the cantilever: $g_{A_1} = \lambda_{A_1}\epsilon_{zz} + \lambda_{A_1'}(\epsilon_{xx} + \epsilon_{yy})$, $g_{E_1} = \lambda_E(\epsilon_{xx} - \epsilon_{yy}) + \lambda_{E'}(\epsilon_{xz} + \epsilon_{zx})$, and $g_{E_2} = \lambda_E(\epsilon_{xy} + \epsilon_{xy}) + \lambda_{E'}(\epsilon_{yz} + \epsilon_{zy})$.

In fig. 5.4b, we study the A_1-symmetric common mode shifts of $|E_x\rangle$ and $|E_y\rangle$ for 12 different NV centers as a function of the mechanically induced strain along the cantilever axis, which lies along the [110] crystal direction. We observe two distinct spectral responses corresponding to NV centers of different crystallographic orientations. Due to the crystallographic orientation of the cantilever, the NV centers can be categorized into two distinct groups: group A with NVs oriented along $[\bar{1}\bar{1}\bar{1}]$ and $[11\bar{1}]$, and group B with NVs oriented along $[\bar{1}11]$ and $[1\bar{1}1]$. Within each group, NV centers experience the same type of strain induced by the cantilever motion (see supporting information). Fitting this data, we find $\lambda_{A_1} = -1.95 \pm 0.29$ PHz and $\lambda_{A_1'} = 2.16 \pm 0.32$ PHz. To extract the two remaining coupling constants, we analyze the total frequency shifts of the E_x and E_y transitions for group A NV centers and group B NV centers. To accurately fit the data, we must take into account the intrinsic E- symmetric strain environment of each NV center that generates δf_{E_1} and δf_{E_2}. E-symmetric strain rotates the orthogonal transition dipole moments

for the E_x and E_y transitions, and thus modifies the polarization dependence of the transitions. The rotation angle, θ, is defined by $\tan(2\theta) = (\delta f_{E_2} + g_{E_2} x)/(\delta f_{E_1} + g_{E_1} x)$ and is defined relative to the NV x-axis (see supporting information). Measuring both Δf_0 and θ allows for complete characterization of the intrinsic strain environment of an NV center. From the fits of the transition frequencies in fig. 5.4c-d, we obtain $\lambda_E = -0.85 \pm 0.13$ PHz and $\lambda_{E'} = 0.02 \pm 0.01$ PHz. From the 12 NVs measured in this paper (data shown in supporting information of this chapter), we observe maximal single phonon couplings of $g_{A_1} \sim 1$ kHz and $g_{E_1} \sim 3$ kHz, and note that due to the crystallographic orientation of the cantilever, g_{E_2}.

5.8 Comparison with uniaxial stress measurements

In this section, we do a direct comparison of our strain-orbit coupling constants with those measured by Davies *et al.* [144]. The experiments in ref. [144] were performed on type 1a and 1b diamond anvil cells at liquid nitrogen temperatures (77 K). Uniaxial stress was applied to the diamond with simple push rods driven by pressurized oil. In the experiments, Davies measured the effect of stress on both the absorption and emission zero-phonon lines for an ensemble of NV centers, including the optical polarization and frequency. The Hamiltonian provided by Davies is written in terms of the stress tensor defined in the crystal frame, where $\hat{x} \parallel [100]$, $\hat{y} \parallel [010]$ and $\hat{z} \parallel [001]$.

$$\begin{aligned} V =& \mathbf{A_1}(s_{xx} + s_{yy} + s_{zz}) + \mathbf{A_1'}(s_{yz} + s_{zx} + s_{xy}) \\ &+ \mathbf{E_X}(s_{xx} + s_{yy} - 2s_{zz}) + \mathbf{E_Y}\sqrt{3}(s_{xx} - s_{yy}) \\ &+ \mathbf{E_X'}(s_{yz} + s_{zx} - 2s_{xy}) + \mathbf{E_Y'}\sqrt{3}(s_{yz} - s_{zx}) \end{aligned} \tag{5.10}$$

Here, $\mathbf{A_1}$, $\mathbf{E_X}$,... are orbital operators labeled by their symmetry under C_{3v} oper-

ations, and s_{ij} refer to components of the stress tensor in the crystal frame. We can rewrite the above Hamiltonian explicitly in terms of the eigenstates of the NV center as follows:

$$\begin{aligned} V =& \Big(A_1(s_{xx}+s_{yy}+s_{zz}) + 2A_2(s_{yz}+s_{zx}+s_{xy})\Big)\Big(\,|E_x\rangle\langle E_x| + |E_y\rangle\langle E_y|\,\Big) \\ &+ \Big(B(s_{xx}+s_{yy}-2s_{zz}) + C(s_{yz}+s_{zx}-2s_{xy})\Big)\Big(\,|E_x\rangle\langle E_x| - |E_y\rangle\langle E_y|\,\Big) \\ &- \sqrt{3}\Big(B(s_{xx}-s_{yy}) + C(s_{yz}-s_{zx})\Big)\Big(\,|E_x\rangle\langle E_y| + |E_y\rangle\langle E_x|\,\Big) \end{aligned} \tag{5.11}$$

Here, we have set ${}^3A_2$ to be at zero energy and introduced the stress coupling constants $\{A_1, A_2, B, C\}$. The values for the stress coupling constants were measured to be

$$\begin{aligned} A_1 &= 1.92 \text{ meV/GPa} \\ A_2 &= -5.02 \text{ meV/GPa} \\ B &= -1.36 \text{ meV/GPa} \\ C &= -2.20 \text{ meV/GPa} \end{aligned} \tag{5.12}$$

To compare our coupling constants, we must convert our strain Hamiltonian into a stress Hamiltonian. This can be done using the elastic stiffness matrix, $\mathbf{C}$, which converts stress into strain via $\vec{\sigma} = \mathbf{C}\vec{\epsilon}$. Here $\vec{\sigma} = (\sigma_{xx}, \sigma_{yy}, \sigma_{zz}, \sigma_{yz}, \sigma_{zx}, \sigma_{xy})$ and $\vec{\epsilon} = (\epsilon_{xx}, \epsilon_{yy}, \epsilon_{zz}, 2\epsilon_{yz}, 2\epsilon_{zx}, 2\epsilon_{xy})$ are the stress and strain six-vectors respectively.

For an isotropic material, the elastic stiffness matrix is defined by 3 physical quantities of the material: the Young's modulus (E), the shear modulus (G), and the Poisson ratio

(ν). This allows the elastic stiffness matrix to be written in the following way

$$\mathbf{C} = \begin{bmatrix} c_{11} & c_{12} & c_{12} & 0 & 0 & 0 \\ c_{12} & c_{11} & c_{12} & 0 & 0 & 0 \\ c_{12} & c_{12} & c_{11} & 0 & 0 & 0 \\ 0 & 0 & 0 & c_{44} & 0 & 0 \\ 0 & 0 & 0 & 0 & c_{44} & 0 \\ 0 & 0 & 0 & 0 & 0 & c_{44} \end{bmatrix} \tag{5.13}$$

These value were measured as a function of temperature in ref. [185], and were found to be

$$\begin{aligned} c_{11} &= 1080 \text{ GPa} \\ c_{12} &= 124 \text{ GPa} \\ c_{44} &= 578 \text{ GPa} \end{aligned} \tag{5.14}$$

Next, we transform into the crystal frame from the NV coordinate system. Davies assumes the the standard NV orientation, with $z \parallel [111]$, $x \parallel [\bar{1}\bar{1}2]$, and $y \parallel [1\bar{1}0]$, and hence we choose that as the starting NV coordinate system. Applying the proper transformation and grouping stress terms of the correct symmetry, we obtain a relationship between the strain coupling constants defined in this chapter and the Davies stress

	Lee *et al.* [80]	Davies *et al.* [144]
λ_{A_1}	-1.95 ± 0.29 PHz	-2.18 PHz
$\lambda_{A_1'}$	2.16 ± 0.32 PHz	2.01 PHz
λ_E	-0.85 ± 0.13 PHz	-0.93 PHz
$\lambda_{E'}$	0.02 ± 0.01 PHz	0.01 PHz

Table 5.1: Comparison of the strain-orbit coupling constants measured in refs. [80, 144].

coupling constants.

$$\begin{aligned}
\lambda_{A_1} &= (c_{11} + 2c_{12})A_1 + 4c_{44}A_2 \\
\lambda_{A_1'} &= (c_{11} + 2c_{12})A_1 - 2c_{44}A_2 \\
\lambda_E &= (c_{11} - c_{12})B + 2c_{44}C \\
\lambda_{E'} &= \sqrt{2}\left((c_{11} - c_{12})B + c_{44}C\right)
\end{aligned} \tag{5.15}$$

A comparison of our measured coupling constants with Davies constants is shown in table 5.1.

These values are in excellent agreement with those measured in this chapter. In a related study, Doherty *et al.* measured the shift in the zero phonon line as a function of hydrostatic pressure [175], which determines the value of A_1. Since hydrostatic pressure induces a stress $s = s_{xx} = s_{yy} = s_{zz}$, the measured shift corresponds to a value of $3A_1$, which was measured to be $3A_1 = 5.75$ meV/GPa. This result is the most accurate measurement to date, since it was calibrated with the well-established pressure response of the spectral lines of Ruby. Importantly, this measurement is in good agreement with the values measured in our experiments.

5.9 Mechanical tuning of the zero-phonon line frequency

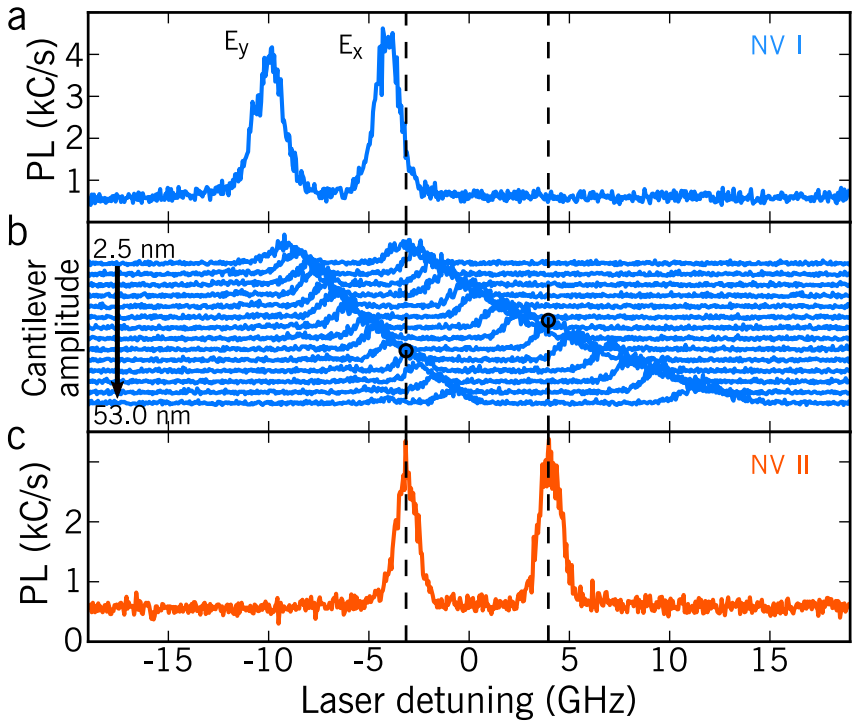

Figure 5.5: **Deterministic frequency tuning**. a)c) RES measurements for two NV centers (NV I, NV II). With no mechanical driving, the E_x and E_y transitions of NV I (a) differ in frequency from those of NV II (c). (b) RES measurements of NV I for increasing cantilever-tip-deflection amplitudes. At amplitudes of 30 nm and 43 nm, respectively, the E_x and E_y transition frequencies match those of NV II, as indicated by the black circles.

A common way to couple remote, matter qubits via a photonic channel is to interfere and detect single photons emitted by the qubits [92, 150]. However, protocols employing quantum interference typically require the photons to be indistinguishable. As a quantum emitter in the solid state, the NV center faces the challenge of overcoming spectral inhomogeneities resulting from locally varying electrostatic and strain environments in the host diamond. In many cases, the optical transitions for different emitters can vary by

many optical linewidths, precluding the use of quantum interference. The conventional solution to this challenge utilizes multi-axis DC electric fields that are delivered via metal electrodes placed nearby or on the diamond sample [145, 146]. While this technique has found success, it introduces additional channels for spectral diffusion through electric field noise produced by the electrodes or changes in the electrostatic environment. Here, we take a promising alternative approach that uses our hybrid strain-mediated coupling to deterministically control the frequency of the E_x and E_y transitions. This control will allow for dynamic matching of the optical transition frequencies of two spatially separated NV centers. For weakly or non-piezoelectric host materials such as diamond, strain-control should introduce minimal spectral diffusion to embedded quantum emitters.

Fig. 5.5a and c show RES measurements of two NVs: one located in the cantilever (NV I) and one located in the bulk of our sample (NV II). In the absence of mechanical driving, their optical transitions differ in frequency by several linewidths. By resonantly driving the cantilever, we can tune the E_x and E_y transitions of NV I into resonance with NV II. Fig. 5.5b shows stroboscopic RES measurements of NV I for various cantilever deflection amplitudes. At amplitudes of 43 nm and 30 nm respectively, the E_x and E_y transition frequencies of NV I match those of NV II. Importantly, this technique introduces very minimal spectral broadening, which can be attributed to the finite duration of the detection window. In the future, this technique could be extended to a large array of cantilevers, each with a different resonant frequency, enabling on-chip, multiplexed tuning of many NV centers for multipartite entanglement. In this architecture, a high density of emitters can be addressed without crosstalk between photonic channels using nanoscale cantilevers without the need for individual electrical leads for each emitter. Excitation of multiple resonators is straightforward and can be carried out by driving a single piezoelectric transducer at multiple frequencies. This AC strain tuning modality is also more tractable than protocols involving static strain, which may suffer from

an unknown strain profile and may require significantly more fabrication, alignment, and stabilization steps to individually address each structure. In addition, strain tuning could be used for dynamic feedback control of the transitions to reduce spectral diffusion caused by local charge fluctuations [146].

5.10 Mechanical tuning of the orientation of the NV electric dipole moment

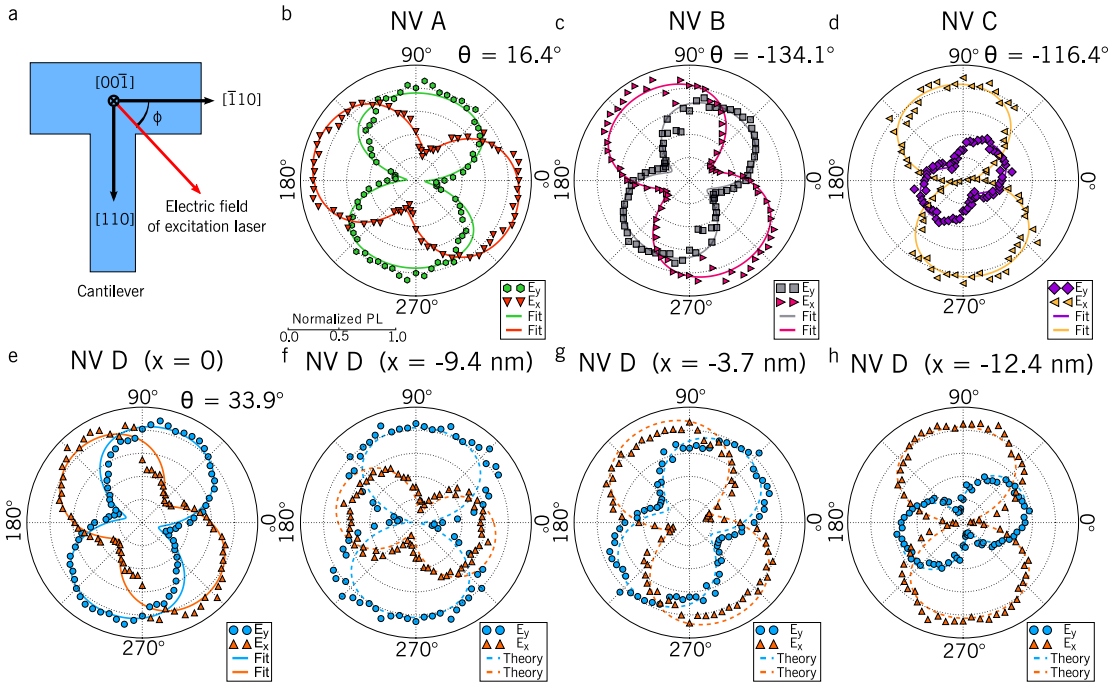

Figure 5.6: **Deterministic polarization tuning**. a) Schematic showing the electric–field vector (red arrow) of the excitation laser ($\hat{k} \parallel [00\bar{1}]$) and the linear-polarization angle, ϕ, defined with respect to the [$\bar{1}$10-crystal axis. b)e) ϕ-dependent RES measurements for NV centers A-D with no mechanical excitation showing the distinct polarization dependences of the E_x and E_y transitions due to local, intrinsic strain. Data points plot the PL amplitudes of the E_x/E_y peaks versus ϕ, and solid lines are fits (see supporting information). f)h) ϕ-dependent stroboscopic RES measurements for NV center D at tip deflections of (9.4, 3.7, and 12.4 nm), matching the dipole-excitation pattern of NV center D to those of NV centers A-C. The dashed lines are theoretical predictions using the tip-deflection amplitude as the input.

The polarization dependence of the optical transitions of spatially separated NV centers can also be matched using our strain-mediated control scheme. We characterize the polarization dependence of the zero-phonon line by performing RES for as a function of laser polarization angle (fig. 5.6a) and measuring the corresponding PL amplitudes of the transition peaks. Infig. 5.6b-e, we plot the polarization dependence of the E_x and E_y transitions for 4 different NV centers, where NVs A, B, and C are located in the sample bulk, and NV D is located inside the cantilever. Due to their inhomogeneous environments, they all exhibit different polarization dependences, with $\theta = (16.4°, -134.1°, -116.4°, 33.9°)$ for NVs A, B, C and D, respectively. In fig. 5.6f-h, we match the polarization dependence of the E_x and E_y transitions of NV D to those of NV A, B and C by driving the cantilever at tip amplitudes of 9.4 nm, 3.7 nm, and 12.4 nm respectively, and measuring when the cantilever is maximally deflected downward. The dashed curves in fig. 5.6f-h correspond to the expected polarization dependence, taking into account the cantilever amplitude and distortions in the shape of the dipole excitation patterns caused by non-zero ellipticity in the laser beam and saturation of the optical transitions (see supporting information). The excellent agreement between measured and expected polarization dependences highlights the deterministic nature of our strain-control. To the best of our knowledge, this is the first demonstration of $in-situ$ polarization tuning of a NV center. Typically, the polarization state of spontaneously emitted photons is manipulated after the collection optics with a combination of polarization control elements, such as waveplates and fiber paddles. For fully chip-integrated systems where many quantum emitters need to be individually addressed, it can be difficult to utilize these external components for selective control of a photonic channel. In-situ control allows for selective control while minimizing cross-talk between photonic channels. We note that in-situ control can also be accomplished with electric fields [186] or optical microcavities [187]. However, the fabrication and alignment required for indi-

vidual addressing with electric fields and cavities may present a significant challenge as the number of emitters increases.

In our current resonator geometry we do not have independent control of E_1 and E_2 strain, and are thus unable to arbitrarily tune the frequency and polarization dependence of an optical transition simultaneously. Universal control could be enabled by simultaneous excitation of two mechanical modes that generate different strain profiles. Interestingly, this approach could offer novel opportunities to study multimode optomechanics by utilizing the inherent nonlinearity of a two level system [54]. Alternatively, generation of indistinguishable photons can still be accomplished by a combination of frequency matching and polarization filtering [95, 94].

5.11 Conclusion and outlook

Future quantum-enabled applications such as long-range interactions between distant qubits or phonon routing will require the single phonon coupling strength to be larger than the intrinsic dissipation in the hybrid system. This high cooperativity regime is defined by $\eta = (g^2/\Gamma_2\gamma_{th}) > 1$, where η is the cooperativity, Γ_2 is the dephasing rate of the optical transition, and γ_{th} is the thermalization rate of the resonator with the environment. By scaling our device down to the nanoscale and improving optical linewidths, it should be possible to enter the high cooperativity regime. For instance, the fundamental flexural mode of a doubly-clamped diamond beam of dimensions 2 μm $\times$ 100nm $\times$ 50nm with $\omega_m/2\pi$ = 238 MHz and $Q = 10^5$, coupled to a near surface NV center with Γ_2 = 100 MHz, would have a coupling g = 21.5 MHz and a cooperativity $\eta \sim 5$ at T = 4 K, residing deep within the high cooperativity regime. Moreover, this device could be used for single-defect cooling of the fundamental mode of the nanobeam to its quantum ground state with phonon occupation number $\bar{n} < 1$, allowing for preparation and observation

of quantum states of the mechanical oscillator (see supporting information).

The strain-mediated frequency tuning technique employed here should in principle preserve the coherence of the optical transitions. Due to the finite duration of our stroboscopic measurement window, we observe minimal broadening of the optical transitions, and are only limited by the Brownian motion of the cantilever. In the devices here, the broadening of the zero-phonon line due to the cantilever Brownian motion would be approximately 1 MHz, which is much lower than the lifetime limited linewidth of 13.6 MHz. In a future experiment, one could perform a $g^{(1)}$ correlation measurement to probe the coherence of the transition and definitively prove that strain does not introduce significant spectral diffusion.

In summary, we have presented a hybrid quantum device in which the orbital states of a single solid-state quantum emitter are coupled via strain to a single vibrational mode of a high quality factor mechanical resonator. We used our device to carefully control the frequency and polarization dependence of the optical transitions of single NV centers. Several additional and diverse applications could be enabled by our device. For instance, our hybrid coupling mechanism could be used to generate large, broadly-tunable light phase shifts, enabling novel applications in all-optical signal processing [188]. Moreover, by combining our strain-mediated NV-phonon coupling with electron spin resonance at the cryogenic temperatures employed here, it should be possible to significantly enhance the optically detected magnetic resonance signal through phonon assisted optical pumping [110]. Additionally, our dynamic strain-tuning experiments may be extended for manipulation and control of the NV hyperfine transitions, which may facilitate the use of nuclear spins as quantum memories [189, 91]. Furthermore, our device architecture and its applications are compatible with other solid-state emitters, such as the silicon-vacancy center in diamond or defects in silicon carbide [176]. Most importantly, we have demonstrated for the first time strain-coupling of a mechanical oscillator to the orbital states

of the NV center. Scaling down our device dimensions and reducing optical linewidths should allow for operation in the resolved sideband regime, enabling phonon cooling and lasing, spin-dependent force quantum gates, and phononic routing applications. The single phonon couplings shown here are the largest ever demonstrated for an NV-based system, and constitute a major step toward quantum applications enabled by a hybrid quantum device based on spins, phonons and photons.

5.12 Supporting information

5.12.1 Stroboscopic measurement procedure

The fundamental mechanical mode of the cantilever is actuated by a piezoelectric transducer that is electrically driven with a lock-in amplifier. During the measurement, both the frequency detuning from resonance and amplitude of the driven motion are kept constant with a phase-locked loop and feedback circuits. The amplitude of driven motion is measured with an interferometer whose signal is calibrated by the Brownian motion of the cantilever. The stroboscopic measurement is accomplished by gating the photon detection. A home-built comparator circuit converts the mechanical drive signal from the lock-in amplifier into a TTL pulse train of the same frequency with a finite phase offset. The duty cycle and hence the width of the ON region of the pulse train is controlled by the threshold voltage of the comparator chip. The finite phase offset is tuned with a phase shifter, and can be tuned over a full 360 degrees. This pulse train directly gates the APD through an external modulation input. For the data shown in Fig. 3b-d, the TTL pulse train is frequency doubled, allowing for measurements of two cantilever positions that are 180 degrees out of phase from each other.

5.12.2 Stroboscopic RES signal

During stroboscopic measurements, RES signals average over a small segment of the cantilever motion, as described in the previous section. Therefore, the general stroboscopic RES signal can be written as

$$\mathcal{S}_{\pm}^{strob}(f) = \frac{1}{\tau}\int_{T}^{T+\tau} \mathcal{I}_{\pm}\left(x(t)\right) \frac{(\Gamma/2)^2}{(\Gamma/2)^2 + \left(f - f_{\pm}\left(x(t)\right)\right)^2} dt \tag{5.16}$$

Where T indicates the start time of the PL detection and τ is the length of the detection window of 60 ns. The start time, T, is set by the relative phase between the TTL pulse train gating the single photon counter and the mechanical driving signal. In our experiments, we set T such that the detection window lies symmetrically around an antinode of the cantilevers motion. For instance, when we are interested in the maximum downward deflection of the cantilever (corresponding to negative x), we set $T = (\pi/\omega_m) - (\tau/2)$.

The detection window is much shorter than the oscillation period of the cantilever, and we approximately measure the NV spectral response for a well-defined positon of the cantilever. When the detection window is placed symmetrically around an antinode of motion, the stroboscopic RES signal can be approximated by a Lorentzian.

$$\mathcal{S}_{\pm}^{strob}(f) \approx \mathcal{I}_{\pm}\left(x_{max/min}\right) \frac{(\Gamma/2)^2}{(\Gamma/2)^2 + \left(f - f_{\pm}\left(x_{max/min}\right)\right)^2} \tag{5.17}$$

Here, $x_{max/min}$ is the maximum or minimum normalized displacement of the cantilever tip depending on which antinode is selected. The fits to the stroboscopic RES data shown in Fig. 3a in the main text reflect this approximation. For data shown in Figs. 3b-d and in Figs. 5f-h, the center frequency and amplitudes of the stroboscopic RES peaks as calculated by fits to eq. (9) are used respectively.

An important note to make is that this approximation breaks down at other phases of the cantilever motion. Although our measurement window is short compared to the cantilever period, it is still long enough that measurements at other phases fail to isolate a single position of the cantilever. This can be understood by considering the dynamics of a harmonic oscillator. At the classical turning points, the velocity of the beam is zero, and hence the cantilever is essentially static during our measurement window. However, when the beam passes through its equilibrium position, the velocity is largest and hence our measurement window will average over a significant portion of the motion. Therefore, if one were to use this method to perform frequency tuning, the cantilever displacement must be adjusted as opposed to the position of the detection window. Alternatively, one could make a lower frequency cantilever so that the ratio of the measurement time to the cantilever period is reduced.

5.12.3 Cantilever strain profile

The mechanical modes of our diamond cantilevers are well-described by Euler-Bernoulli beam theory. We consider a singly-clamped diamond beam of length l, width w, and thickness t. The cantilever coordinate system (X, Y, Z) can be described in terms of the diamond crystallographic directions, as shown in Fig. 7a. The Z-axis is the cantilever axis, and is parallel to the [110] crystal direction. The strain profile for the cantilevers fundamental flexural motion along the Y direction as function of axial position Z and cantilever tip deflection x_c is given by

$$\begin{aligned}\varepsilon(Z, x_c) \simeq & R_0 \frac{x_c}{2l^2}(1.875)^2 \Bigg[\cos\left(1.875\frac{Z}{l}\right) + \cosh\left(1.875\frac{Z}{l}\right) \\ & - \frac{1}{1.3622}\left(\sin\left(1.875\frac{Z}{l}\right) + \sinh\left(1.875\frac{Z}{l}\right)\right)\Bigg]\end{aligned} \tag{5.18}$$

where R_0 refers to the distance in the Y direction from the center of the beam (neutral axis). A more detailed derivation is provided in chapter 2.

For an NV that is at a depth d_i from the surface of the cantilever, $R_0 = (t/2) - d_i$. For the devices in this paper, the NV depth is determined by the nitrogen implantation process, and $d_i = 51.5 \pm 13.0$ nm, where the uncertainty in d_i is derived from Stopping Range of Ions in Matter (SRIM) simulations, representing one standard deviation in the straggle of nitrogen ions during ion implantation.

5.12.4 Strain tensor in the NV coordinate system

For the purposes of this paper, we treat diamond as an isotropic solid. In this approximation, the strain tensor generated by the cantilevers flexural motion can be written in the cantilevers coordinate system (X, Y, Z) as follows

$$\epsilon_c = \begin{vmatrix} -\nu\varepsilon & 0 & 0 \\ 0 & -\nu\varepsilon & 0 \\ 0 & 0 & \varepsilon \end{vmatrix} \tag{5.19}$$

where ε is the mechanically induced strain along the Z direction as defined above and $\nu = 0.11$ is the Poisson ratio of diamond. Our cantilevers are fabricated such that $X \parallel [\bar{1}10]$, $Y \parallel [001]$ and $Z \parallel [110]$. We transform the above strain tensor from the cantilever coordinate system, (X, Y, Z), into the coordinate system of the NV center, (x, y, z). For NVs in group A ($z \parallel [\bar{1}\bar{1}\bar{1}]$ or $[11\bar{1}]$), the transformed strain tensor is

$$\epsilon_A = \begin{vmatrix} \frac{\varepsilon}{3}(1-2\nu) & 0 & -\frac{\sqrt{2}\varepsilon}{3}(1+\nu) \\ 0 & -\nu\varepsilon & 0 \\ -\frac{\sqrt{2}\varepsilon}{3}(1+\nu) & 0 & \frac{\varepsilon}{3}(2-\nu) \end{vmatrix} \tag{5.20}$$

For NVs in group B ($z \parallel [\bar{1}11]$ or $[1\bar{1}1]$), the transformed strain tensor is

$$\epsilon_B = \begin{vmatrix} -\nu\varepsilon & 0 & 0 \\ 0 & \varepsilon & 0 \\ 0 & 0 & -\nu\varepsilon \end{vmatrix} \tag{5.21}$$

With the above strain tensors, we can diagonalize the Hamiltonian in eq. (6) and write the E_x and E_y transition frequencies for NVs in both groups in terms of ε. We obtain

$$\begin{aligned} f_{\pm}^{A} =& f_{ZPL} + \delta f_{A_1} + \lambda_{A_1}\frac{2-\nu}{3}\varepsilon + \lambda_{A_1'}\frac{1-5\nu}{3}\varepsilon \\ & \pm \sqrt{\left(-\lambda_E\frac{1+\nu}{3}\varepsilon - \lambda_{E'}\frac{2\sqrt{2}(1+\nu)}{3}\varepsilon + \delta f_{E_1}\right)^2 + \left(\delta f_{E_2}\right)^2} \end{aligned} \tag{5.22}$$

for group A and

$$f_{\pm}^{B} = f_{ZPL} + \delta f_{A_1} - \lambda_{A_1}\nu\varepsilon + \lambda_{A_1'}(1-\nu)\epsilon \pm \sqrt{\left(\lambda_E(1+\nu)\varepsilon + \delta f_{E_1}\right)^2 + \left(\delta f_{E_2}\right)^2} \tag{5.23}$$

for group B.

5.12.5 Characterization of intrinsic strain and polarization selection rules with strain

To properly model the NV response to crystal strain and extract the single phonon coupling parameters, it is necessary to characterize the intrinsic local E-symmetric strain environment of the NV center. The intrinsic strain can be completely characterized by measuring the splitting between $|E_x\rangle$ and $|E_y\rangle$ and measuring the orientation of the

transition dipole moments. For intrinsic strains δf_{E_1} and δf_{E_2}, we see that the splitting between $|E_x\rangle$ and $|E_y\rangle$ can be written as

$$\Delta f_0 = 2\sqrt{(\delta f_{E_1})^2 + (\delta f_{E_2})^2} \tag{5.24}$$

The orientation of the transition dipole moments can be extracted by measuring the polarization dependence of the E_x and E_y transitions. The interaction of the resonant laser with the NV is described by electric dipole interaction, $H_E = -\mathbf{d} \cdot \mathbf{E}$, where $\mathbf{d}$ is the NV electric dipole operator and $\mathbf{E}$ is the electric field of the excitation laser. The axial dipole moment, d_z, does not connect the ground and excited state manifolds, but merely shifts them relative to each other. The transverse electric dipole moments d_x and d_y split and mix $|E_x\rangle$ and $|E_y\rangle$, but also couple the ground and excited state manifolds.

In the $\{|A\rangle, |E_x\rangle, |E_y\rangle\}$ basis and in the absence of strain, the transverse electric dipole moments d_x and d_y can be expressed as

$$d_x = \begin{vmatrix} 0 & 0 & d_\perp \\ 0 & \tilde{d_\perp} & 0 \\ d_\perp & 0 & -\tilde{d_\perp} \end{vmatrix} \tag{5.25}$$

$$d_y = \begin{vmatrix} 0 & d_\perp & 0 \\ d_\perp & 0 & \tilde{d_\perp} \\ 0 & \tilde{d_\perp} & 0 \end{vmatrix} \tag{5.26}$$

Clearly, the E_x and E_y transitions are driven by linearly polarized light along the $\hat{y}$ and $\hat{x}$ directions of the NV center. In the presence of E-symmetric strain, $|E_x\rangle$ and $|E_y\rangle$ are mixed, and new eigenstates are formed. Simultaneously, this leads to a rotation of the transverse electric dipole moments. The rotated dipole operators, $\tilde{d_x}$ and $\tilde{d_y}$ can be expressed as

$$\tilde{d}_x = \cos(\theta) d_x + \sin(\theta) d_y \tag{5.27}$$

$$\tilde{d}_y = -\sin(\theta) d_x + \cos(\theta) d_y \tag{5.28}$$

where 2θ is the Stuckelberg angle and $\tan(2\theta) = (\delta f_{E_2} + g_{E_2} x)/(\delta f_{E_1} + g_{E_1} x)$.The electric field of the incident light, $\mathbf{E}$, can be written in terms of the crystallographic directions and polarization angle ϕ, $\mathbf{E} = \frac{|E|}{2}\big(\cos(\phi)[\bar{1}10] + \sin(\phi)[110]\big)$. The absorption intensity is proportional to $|\mathbf{d} \cdot \mathbf{E}|^2$. Therefore, the normalized absorption intensity of the two excited states are given by

$$\begin{aligned} I_{E_y} &= \left(\frac{\cos(\theta)\cos(\phi)}{\sqrt{3}} - \sin(\theta)\sin(\phi)\right)^2 \\ I_{E_x} &= \left(\frac{\sin(\theta)\cos(\phi)}{\sqrt{3}} - \cos(\theta)\sin(\phi)\right)^2 \end{aligned} \tag{5.29}$$

for group A, and

$$\begin{aligned} I_{E_y} &= \left(\frac{\cos(\theta)\sin(\phi)}{\sqrt{3}} - \sin(\theta)\cos(\phi)\right)^2 \\ I_{E_x} &= \left(\frac{\sin(\theta)\sin(\phi)}{\sqrt{3}} - \cos(\theta)\cos(\phi)\right)^2 \end{aligned} \tag{5.30}$$

for group B.

In our polarization dependence measurements, we need to account for saturation of the optical transitions and non-zero ellipticity of the excitation laser. Here, we assume a simple model of saturation in which the normalized absorption intensity is given by $I = 1 - e^{-P_{eff}/P_{sat}}$, where P_{eff} is the effective laser power seen by the NV and P_{sat} is the

saturation power. The effective laser power is determined by the polarization dependence of the transition as well as the total incident laser power, P_{in}. To account for ellipticity, we introduce a relative phase delay, ψ, between the x and y components of the electric field: $\mathbf{E} = \frac{|E|}{2}\left(\cos(\phi)[\bar{1}10] + e^{i\psi}\sin(\phi)[110]\right)$ (refer to fig. 5.6a. for a diagram). Putting it all together, the normalized absorption intensities for the E_x and E_y transitions including these two effects are given by

$$I_{E_y} = 1 - \exp\left[-\frac{P_{in}}{P_{sat}}\left(\sin^2(\theta)\sin^2(\phi) + \frac{\cos^2(\theta)\cos^2(\phi)}{3} - \frac{\cos(\psi)\sin(2\theta)\sin(2\phi)}{2\sqrt{3}}\right)\right] \quad (5.31)$$

$$I_{E_x} = 1 - \exp\left[-\frac{P_{in}}{P_{sat}}\left(\cos^2(\theta)\sin^2(\phi) + \frac{\sin^2(\theta)\cos^2(\phi)}{3} - \frac{\cos(\psi)\sin(2\theta)\sin(2\phi)}{2\sqrt{3}}\right)\right] \quad (5.32)$$

for group A, and

$$I_{E_y} = 1 - \exp\left[-\frac{P_{in}}{P_{sat}}\left(\sin^2(\theta)\cos^2(\phi) + \frac{\cos^2(\theta)\sin^2(\phi)}{3} - \frac{\cos(\psi)\sin(2\theta)\sin(2\phi)}{2\sqrt{3}}\right)\right] \quad (5.33)$$

$$I_{E_x} = 1 - \exp\left[-\frac{P_{in}}{P_{sat}}\left(\cos^2(\theta)\cos^2(\phi) + \frac{\sin^2(\theta)\sin^2(\phi)}{3} - \frac{\cos(\psi)\sin(2\theta)\sin(2\phi)}{2\sqrt{3}}\right)\right] \quad (5.34)$$

for group B. Note that to calculate the dipole excitation patterns, we must transform from the cantilever frame used to describe the laser polarization into the NV coordinate system. The fits of the polarization plots are shown in Fig. 5 as well as Figs. 8 and 9. where θ, P_{sat}, and ψ are used as fit parameters. The fit results obtained from 12 NVs yield $P_{sat} = 0.4 \pm 0.1$ μW, $\psi = 54 \pm 10°$, and the results of θ are used to determine the intrinsic strain.

5.12.6 Extracting the strain coupling constants and error bars

To measure the strain-orbit coupling constants, we measure the E_x and E_y transition frequencies, f_+ and f_-, for NVs in groups A and B as function of the strain induced along the cantilever axis. Flexural motion of the cantilever introduces a strain ε along the cantilever axis, while producing strains $-\nu\varepsilon$ in the transverse directions due to the Poisson effect ($\nu = 0.11$). To extract the A_1-symmetric strain coupling constants, we monitor the uniform shifts of the E_x and E_y transition frequencies as a function of ε, $\Delta_{A_1} = (f_+ + f_-)/2$. Neglecting the static frequency offset, $f_{ZPL} + f_{A_1}$, we obtain

$$\Delta^A_{A_1}(\varepsilon) \quad = \lambda_{A_1}\tfrac{2-\nu}{3}\varepsilon + \lambda_{A_1}\tfrac{1-5\nu}{3}\varepsilon \tag{5.35}$$

$$\Delta^B_{A_1} = (\varepsilon \quad = -\lambda_{A_1}\nu\varepsilon + \lambda_{A_1'}(1-\nu)\varepsilon \tag{5.36}$$

The vertical error bars in Fig. 3b-d reflect the uncertainty in peak positions in the RES measurements, which is dominated by the 5° phase uncertainty in the location of the stroboscopic measurement window with respect to the cantilever motion. The horizontal error bars in Fig. 3b-d are given by the uncertainty in 3-D position of the NV, which is dominated by the 13 nm uncertainty in the NV depth in the diamond, which is the expected straggle of nitrogen ions during our implantation process (as calculated by SRIM). To extract λ_{A_1} and $\lambda_{A_1'}$, we simultaneously fit the data in Fig. 3b to the above equations for Δ_{A_1}. The error reported forλ_{A_1} and $\lambda_{A_1'}$ is limited by our calibration in the uncertainty of ε, which is determined in the uncertainty in the optical interferometry measurement of the cantilever tip deflection. We estimate a 15% uncertainty in this calibration, and hence quote a 15% uncertainty in the values of λ_{A_1} and $\lambda_{A_1'}$. With this information, we next extract λ_E and $\lambda_{E'}$ by extracting the overall shifts of the E_x and

E_y transition frequencies for 12 NVs (6 NVs in each group), as a function of ε. The uncertainty in the measured values of λ_E and $\lambda_{E'}$ also reflect the 15% uncertainty in the interferometric measurement of the cantilever tip deflection. Data for all measured NVs are shown in Figs. 10 and 11.

5.12.7 Cooperativity and phonon cooling calculations

The device described in the conclusion section is a doubly-clamped diamond nanobeam with dimensions (2 μm, 100 nm, 50 nm) containing a near-surface NV center located at one of the clamping points. We will focus on the fundamental mode of this resonator, which has a resonance frequency $\omega_m/2\pi = 238$ MHz. Moreover, we assume that the nanobeam has the same crystallographic orientation as the device shown in this chapter. In this calculation, we will consider an NV center from group B, whose symmetry axis is transverse to the resonator axis. For simplicity, we will assume that the NV is hosted in a perfect crystal with no intrinsic strain. Using the strain tensor calcaulated above, the NV-resonator interaction Hamiltonian is

$$\begin{aligned} H_{int} = \left(-\lambda_{A_1}\nu\varepsilon + \lambda_{A_1'}(1-\nu)\varepsilon\right)\left(|E_x\rangle\langle E_x| + |E_y\rangle\langle E_y|\right) \\ + \left(\lambda_E(1+\nu)\varepsilon\right)\left(|E_x\rangle\langle E_x| - |E_y\rangle\langle E_y|\right) \end{aligned} \tag{5.37}$$

where ε is the strain induced along the axis of the nanobeam. Next, we quantize the strain field in terms of the phonon creation and annihilation operators for the resonator mode such that $\varepsilon = \varepsilon_0(a + a^\dagger)$ and ε_0 is the strain due to zero point motion. Based on the signs of the strain coupling constants, the highest single phonon coupling occurs for the $A \rightarrow E_y$ transition. We can isolate this transition and neglect $|E_x\rangle$ by using $\hat{x}$ polarized

light. We find the effective interaction Hamiltonian for the $|E_y\rangle$ state is

$$H_{eff} = g_{\parallel} |E_y\rangle \langle E_y| (a + a^{\dagger}) \tag{5.38}$$

where $g_{\parallel} = \left(-\lambda_{A_1}\nu + \lambda_{A_1'}(1-\nu) - \lambda_E(1+\nu)\right)\varepsilon_0 = (2.31 \text{ PHz})\varepsilon_0$ is the effective single-phonon coupling parameter. For the device described here, we expect $g_{\parallel} = 21.5$ MHz for the fundamental mode.

The single phonon cooperativity is defined to be $\eta = (g_{\parallel}^2/\Gamma_2\gamma_{th})$, where Γ_2 is the dephasing rate of the optical transition, and γ_{th} is the heating rate of the mechanical resonator [10]. The heating rate is defined by $\gamma_{th} = (\bar{n}\omega_m)/2\pi Q$, where $\bar{n}$ is the equilibrium phonon occupation number of the resonator at temperature T, and Q is the quality factor of the mechanical mode. For the calculation of the cooperativity in the conclusion section, we assume a value of $\Gamma_2 = 100$ MHz for the $A \rightarrow E_y$ transition, which has been observed in ref. [190]. This value was limited primarily by electron-phonon interactions within the excited state manifold. In addition, we assume that the quality factor of the mechanical mode is $Q = 10^5$, which has already been demonstrated with micron-scale diamond resonators [43]. At a temperature $T = 4$ K, the diamond resonator has an equilibrium thermal occupation number of $\bar{n} = 367$. Putting it all together, we find the cooperativity of this device to be $\eta = 5.2$. To evaluate the prospects for ground state cooling, we consider the protocol for sideband cooling as detailed in ref. [169, 170] and chapter 7 of this thesis. In this protocol, we resonantly address the first red vibrational sideband of the $A \rightarrow E_y$ transition associated with the fundamental mechanical mode of the resonator. The steady state thermal occupation number for the resonator under sideband cooling obeys

$$\bar{n} \approx \frac{\gamma_{th}}{\Gamma_C} \tag{5.39}$$

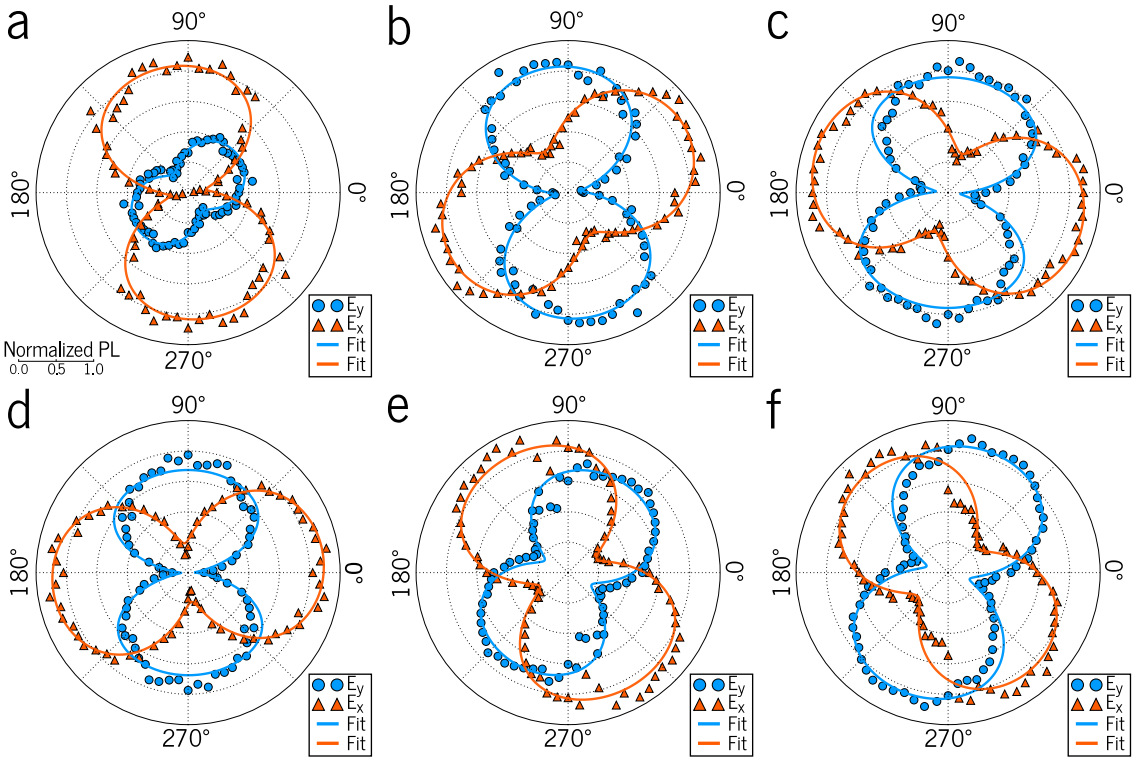

Figure 5.7: **Supplementary Data 1**. Measured dipole excitation patterns for all NVs in group A

where Γ_C is the sideband cooling rate. The sideband cooling rate is given by

$$\Gamma_C = 4\pi^2 \frac{g_{\parallel}^2 \Omega^2}{\Gamma \omega_m^2} \tag{5.40}$$

where Ω is the optical Rabi frequency and Γ is the linewidth of the optical transition. Assuming an optical Rabi frequency Ω, a linewidth of $\Gamma = 100$ MHz, and the γ_{th} described above, we find $\Gamma_C = 843$ kHz and $\bar{n} \approx 0.9$.

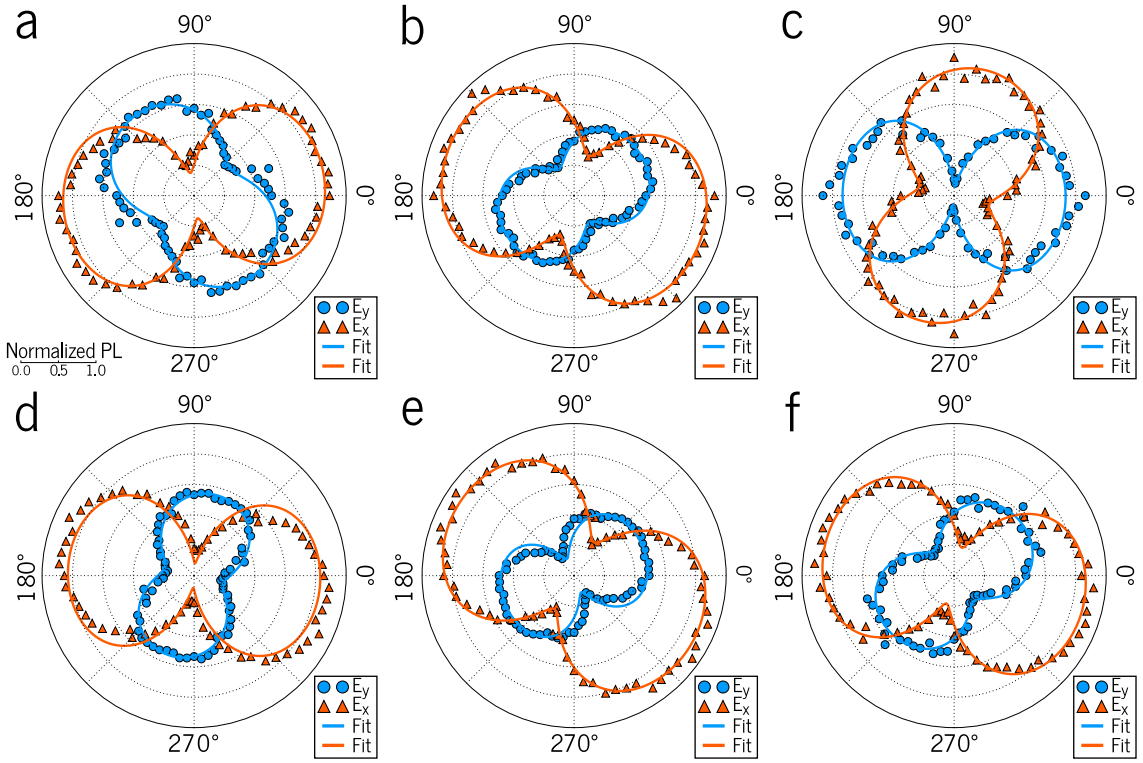

Figure 5.8: **Supplementary Data 2**. Measured dipole excitation patterns for all NVs in group B

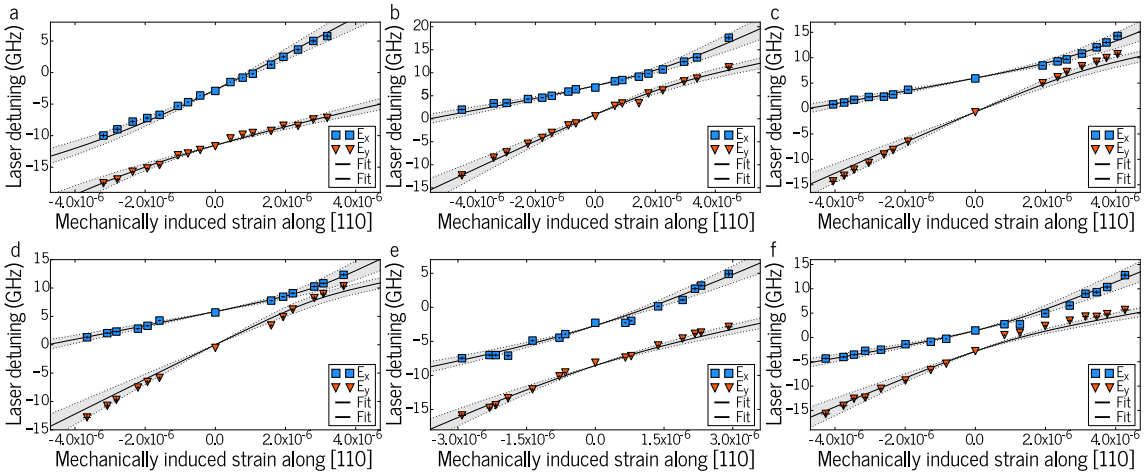

Figure 5.9: **Supplementary Data 3**. Measured total frequency shift of all measured NVs in group A as function of cantilever strain

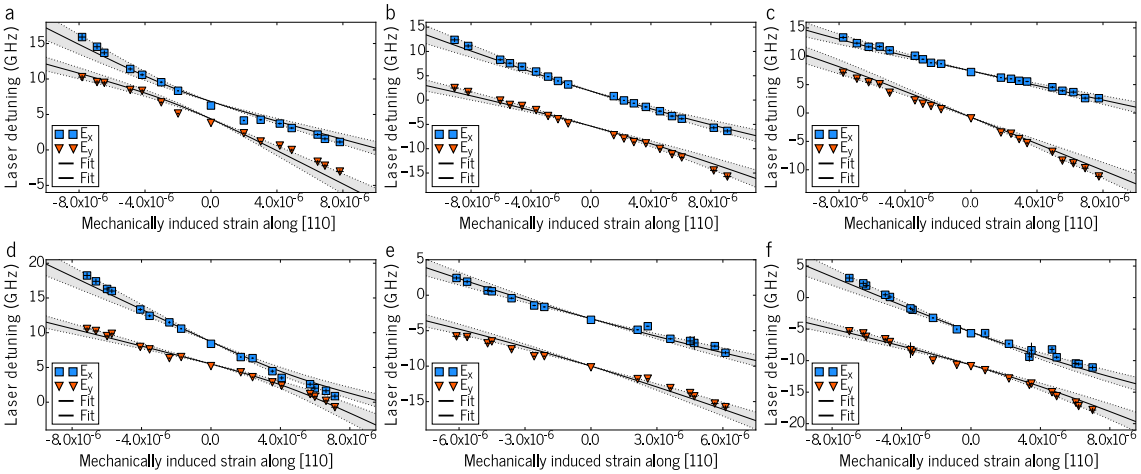

Figure 5.10: **Supplementary Data 4**. Measured total frequency shift of all measured NVs in group B as function of cantilever strain

Chapter 6

Enhanced spin coherence in a hybrid spin-mechanical oscillator system

"Though some of you may see me as a celebrity, you should know that I once sat where you sit. Literally. Late last night I snuck out here and sat in every seat. I did it to prove a point: I am not bright and I have a lot of free time."

- Conan O'Brien

6.1 Introduction

The electron spin of the nitrogen-vacancy (NV) center in diamond is among the most technologically advanced platforms for nanoscale quantum sensing and quantum information processing due to its exceptional coherence properties. To date, NV centers have been integrated into complex quantum devices that are capable of imaging nanoscale magnetic systems, such as superconducting vortices [121], single electron spins [191], and nuclear spins in proteins [192]. Furthermore, NV centers have been successfully imple-

mented in small qubit registers that can be integrated into a large-scale quantum network [124, 90]. However, many of these applications require NV centers that are either near the surface of diamond or embedded in a fabricated diamond nanostructure, where the NV spin experiences significant dephasing from surface-related noise [131, 139, 193, 140]. As a result, engineering highly coherent, near-surface NV centers in nanostructures remains an outstanding challenge, and will require a detailed understanding of the underlying decoherence mechanisms.

One way to decouple the spin from environmental fluctuations is through dynamical decoupling [194]. In periodic dynamical decoupling (PDD), the spin is coherently addressed with a periodic sequence of control pulses, which decouple the spin from quasi-static noise while enhancing the spin sensitivity in a narrow frequency band set by the interpulse spacing. In continuous dynamical decoupling (CDD), the spin is continuously and coherently driven with an external control field, creating new "dressed" spin states that are inherently less sensitive to environment fluctuations. Both techniques have been utilized to extend the NV spin coherence time by orders of magnitude [138, 78, 53, 195, 196, 197].

In this chapter, we take a hybrid approach to dynamical decoupling which combines continuous and periodic control of the NV spin. We utilize the time-varying strain field generated by the motion of a diamond mechanical oscillator to drive a magnetic dipole-forbidden $|1\rangle \leftrightarrow |-1\rangle$ spin transition and perform continuous dynamical decoupling [78, 53]. The resulting strain dressed states, $\{|0\rangle, |+\rangle, |-\rangle\}$, where $|\pm\rangle$ are linear combinations of $|\pm 1\rangle$, are insensitive to all magnetic field noise to first order. We encode our qubit in the $\{|0\rangle, |-\rangle\}$ states and demonstrate a 50-fold increase in the inhomogeneous spin coherence time, T_2^*. We then perform conventional periodic dynamical decoupling on the $\{|0\rangle, |-\rangle\}$ qubit, and demonstrate that the mechanically dressed spin states exhibit an extended homogeneous spin coherence time, T_2, compared to the bare spin states of the

NV center.

Our approach to dynamical decoupling has a few important advantages over previous demonstrations. First, CDD is traditionally performed on the $|0\rangle \leftrightarrow |\pm 1\rangle$ transitions with microwave magnetic fields. The resulting dressed states cannot be distinguished using spin-dependent fluorescence, and hence any protocol utilizing $|0\rangle \leftrightarrow |\pm 1\rangle$ CDD requires undressing the spin in an adiabatic fashion, which adds significant overhead. The CDD protocol employed here does not address $|0\rangle$, and hence the standard spin-dependent fluorescence readout protocol can be used. Furthermore, previous work with magnetic CDD has shown that the coherence of the dressed states is limited by high frequency amplitude fluctuations in the driving field. Our approach leverages the narrow linewidth of a high quality factor mechanical oscillator to filter out high frequency noise in the continuous driving field. Finally, a microwave dressed spin qubit typically has a frequency splitting on the order of MHz due to the experimental constraints on the drive field amplitude, and hence the manipulation speed of the dressed qubit is limited. The mechanically dressed qubit employed here is in the GHz range, and hence theoretically it is possible to perform rapid manipulation of the qubit. We take advantage of this feature to perform PDD with microwave magnetic fields to further extend the spin coherence time past the CDD limit.

6.2 Bare spin states

The traditional NV spin qubit is encoded in a magnetic dipole transition between two of the bare S_z eigenstates, such as $|m_s = 0\rangle$ and $|m_s = 1\rangle$. The spin Hamiltonian for the NV center in this basis can be written as

$$H_{NV} = DS_z^2 + \gamma_{NV}\mathbf{S}\cdot\mathbf{B} - \frac{1}{2}E(S_+^2 + S_-^2) \tag{6.1}$$

where D is a function of the zero-field spin-spin interaction, temperature, axial electric fields, and A_1 symmetric strain, and E is a function of transverse electric fields and E symmetric strain (see supporting information). A static magnetic field applied along the NV quantization axis breaks the $m_s = \pm 1$ degeneracy and allows for selective addressing of the $|0\rangle \leftrightarrow |\pm 1\rangle$ transitions. For a qubit encoded in the bare spin states $\{|0\rangle, |\pm 1\rangle\}$, dephasing is dominated by noise terms that couple to S_z and S_z^2, as the E terms are suppressed by the Zeeman interaction. Therefore, the spin decoherence of the bare dressed states can be induced by magnetic, electric, strain, and thermal noise.

6.3 Hyperfine interaction

As described in chapter 2, the NV center can couple to the nuclear spin of the nitrogen atom through hyperfine interaction. In our experiments, the NV center couples to the $I = 1$ nuclear spin of ^{14}N, characterized by the hyperfine interaction

$$H_{hyp} = -A_{\parallel} m_I S_z \tag{6.2}$$

where $A_{\parallel} = 2.16$ MHz is the hyperfine coupling and m_I denotes the nuclear spin projection along the quantization axis. Here, we work entirely within the $m_I = 1$ manifold. Therefore, the resonance condition for mechanically driven Rabi oscillations is given by $\Delta_B = 2(\gamma_{NV} B_z - A_{\parallel}) = \omega_m / 2\pi$.

6.4 Mechanically dressed spin states

In our experiments, we perform CDD by coherently driving the $|1\rangle \leftrightarrow |-1\rangle$ transition. To this end, we resonantly address the $|1\rangle \leftrightarrow |-1\rangle$ transition with a time-varying, E-symmetric strain field generated by the motion of a single-crystal diamond cantilever.

We model the system with the following Hamiltonian

$$H = DS_z^2 + \frac{\Delta_B}{2}S_z + \frac{\Omega_m}{4}\cos(\omega_m t)(S_+^2 + S_-^2) \tag{6.3}$$

where Ω_m is the mechanical Rabi frequency, and ω_m is the mechanical frequency. The dynamics of the system can be solved by moving into the interaction picture with respect to S_z and making a rotating wave approximation. In the time-independent frame, we obtain

$$H_I = DS_z^2 + \frac{\Delta}{2}S_z + \frac{\Omega_m}{4}(S_+^2 + S_-^2) \tag{6.4}$$

where we have defined the mechanical detuning $\Delta = \Delta_B - \omega_m$. From here, we may diagonalize the Hamiltonian to obtain the mechanical dressed states

$$\begin{aligned} |0\rangle &= |0\rangle \\ |+\rangle &= \cos(\theta)|1\rangle + \sin(\theta)|-1\rangle \\ |-\rangle &= -\sin(\theta)|1\rangle + \cos(\theta)|-1\rangle \end{aligned} \tag{6.5}$$

where $\tan(2\theta) = \Omega_m/\Delta$. When $\Delta = 0$, the dressed states are equal superpositions of $|\pm 1\rangle$ that are split in energy by an amount Ω_m. Importantly, we observe that $\langle \pm| S_z |\pm\rangle = 0$. Therefore, the mechanical dressed states are insensitive to fluctuations in the magnetic field to first order. However, we note that $\langle \pm| S_z^2 |\pm\rangle \neq 0$, and hence the mechanically dressed spin states will still be sensitive to fluctuations in D. In addition, as the $|\pm\rangle$ splitting is set by Ω_m, the dressed states will also be sensitive to amplitude fluctuations in the mechanical driving field. Because we employ a high Q mechanical oscillator, we filter out amplitude noise above a cutoff frequency $f_c = \frac{\omega_m}{4\pi Q} = 250$ Hz. This is an important

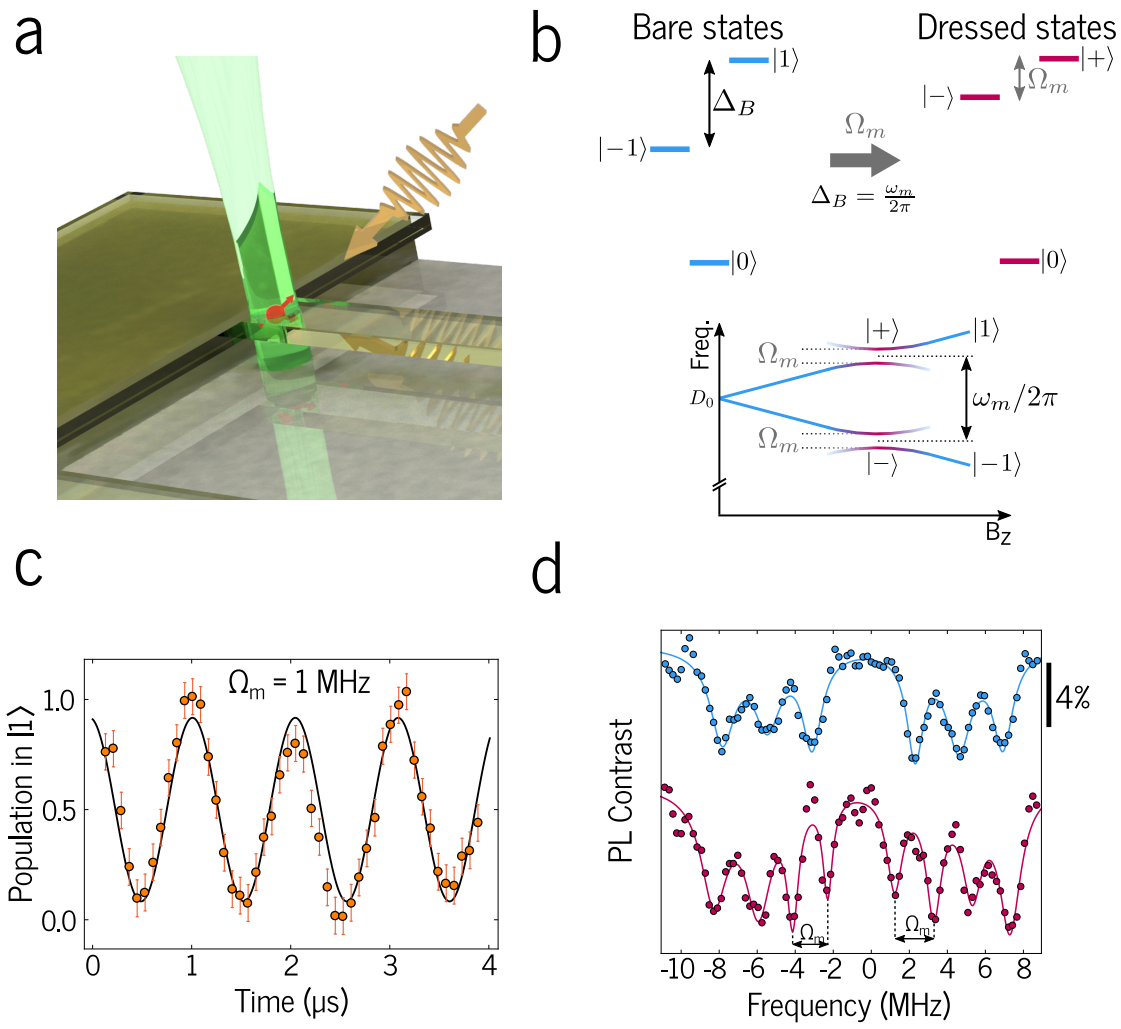

Figure 6.1: **A mechanically-dressed spin**. a) Schematic of the device. A single NV center (red) embedded in a diamond cantilever coherently interacts with the strain induced by the cantilever motion and microwave magnetic fields. The spin is initialized and readout using a 532 nm laser. b) Energy level diagram of the bare spin levels (left) and strain-dressed spin levels (right) of the NV center. The bare spin levels are sensitive to magnetic fields. Under resonant mechanical driving, the spin evolves into new eigenstates which are insensitive to magnetic fields to first order (bottom). c) Rabi flopping on the $|1\rangle \leftrightarrow |-1\rangle$ transition with Rabi frequency Ω_m. d) ODMR spectroscopy of the bare (blue) spin levels and the mechanically-dressed spin levels (maroon) reveals the hyperfine structure of the NV center. When the $|m_s = 1, m_I = 1\rangle \leftrightarrow |m_s = -1, m_I = 1\rangle$ transition frequency matches the mechanical oscillator frequency, an Autler-Townes splitting emerges with energy gap Ω_m.

feature of our device, as high frequency noise can be difficult to mitigate with PDD.

6.5 Experimental setup

Our experiments are performed on single NV centers embedded in a single-crystal diamond cantilever, as depicted in fig. 6.1a. The cantilever has dimensions $30 \times 10 \times 1.7$ μm and a fundamental flexural mode frequency of $\omega_m/2\pi = 5.28$ MHz. The cantilevers were fabricated using a diamond-on-insulator technique, as described in ref. [43]. NV centers were created through ^{14}N ion implantation and subsequent annealing at 850°C. A homebuilt, cryogenic scanning confocal microscope is used to optically address individual NV centers in the cantilevers and perform Fabry-Perot interferometry for mechanical characterization. The fundamental mode of the cantilever is actuated with a piezoelectric transducer located nearby the diamond sample. Electron spin resonance and pulsed dynamical decoupling are performed with resonant microwave fields produced by a microwave antenna placed nearby the sample. A half-Helmholtz coil is used for precise tuning of the $|1\rangle \leftrightarrow |-1\rangle$ transition energy.

The experiments are performed at 180 K and under high vacuum conditions (10^{-5} torr). This unconventional choice of operating conditions addresses four important issues associated with operating at liquid helium temperatures or ambient conditions. First, the high vacuum environment mitigates damping of the cantilever, which should improve the noise filtering ability of the CDD protocol. Second, we observe the formation of anomalous bright spots on the sample under vacuum conditions. The formation of these bright spots is significantly suppressed at cryogenic temperatures. The origin of these bright spots is not understood, but may be related to graphitization of the diamond or accumulation of impurities on the surface. For a short discussion of these bright spots, we refer the reader to the supporting information for this chapter. Third, at temperatures below 50 K, the diamond sample becomes an effective cryopump. Due to the finite pressure in the cryostat, the cantilever will adsorb material floating in the chamber,

causing a slow drift in the mechanical frequency and a slow reduction in the mechanical quality factor. Finally, we observe a significant temperature dependence of the cantilever quality factor [44, 43], with a significant drop in quality factor as the temperature is lowered from 180 K. To overcome all of these constraints, we operate the cryostat at an elevated temperature by heating the sample stage. Under these conditions, we observe a mechanical quality factor $Q = 12,000$ with no apparent drift of the mechanical frequency, and no formation of bright spots.

6.6 Mechanically driven Rabi flopping

We first demonstrate that the strain field produced by the mechanical oscillator can be used to coherently drive the $|1\rangle \leftrightarrow |-1\rangle$ spin transition [51, 53]. To this end, we performed strain-driven Rabi flopping between $|-1, 1\rangle$ and $|1, 1\rangle$ for a cantilever amplitude $x_c =$ 120 nm, where we have defined the hyperfine states $|m_s, m_I\rangle$ corresponding to the ^{14}N nuclear spin. The experiment begins by initializing the spin into $|0\rangle$ through optical pumping. The spin is prepared in $|-1, 1\rangle$ with a microwave π pulse. The spin is allowed to free evolve for a time τ under the influence of the mechanical strain field. The spin population in $|-1, 1\rangle$ is then readout by applying a second microwave π pulse to return the spin population to $|0\rangle$ and applying an optical pulse for spin-dependent fluorescence measurements. In fig. 6.1c, we show mechanical Rabi flopping for a Rabi frequency $\Omega_m/2\pi = 1$ MHz.

6.7 Mechanically induced Autler-Townes splitting

To characterize the mechanically dressed spin states, we perform electron spin resonance (ESR) with microwave magnetic fields while driving the cantilever [78, 53]. In the

absence of mechanical driving, the ESR spectrum reveals the triplet hyperfine structure associated with ^{14}N with a hyperfine splitting $A_{\parallel} = 2.16$ MHz for the $|0, m_I\rangle \leftrightarrow |\pm 1, m_I\rangle$ transitions (blue data in fig. 6.1d.). With mechanical driving, we observe an Autler-Townes splitting of the $|\pm 1, 1\rangle$ hyperfine levels that is equal to the mechanical Rabi frequency (maroon data in fig. 6.1d.). The split levels corresponding to the mechanically dressed spin states, $|\pm\rangle$.

6.8 CDD with mechanical driving

Now that we have established our coherent mechanical driving technique, we can perform mechanical CDD and probe the coherence of the mechanical dressed states. To this end, we perform a Ramsey experiment on the $\{|0\rangle, |-\rangle\}$ qubit and compare it to the coherence of the bare spin qubit $\{|0\rangle, |1\rangle\}$. In fig. 6.2a., we show Ramsey data for the bare spin states. We observe a rapid decay of the spin coherence, with $T_2^* = 310 \pm 32$ ns. However, with mechanical CDD, we observing a significant extension in spin coherence. In fig. 6.2b, we show Ramsey data for a mechanical Rabi frequency $\Omega_m/2\pi = 1.5$ MHz. We observe an initial rapid decay associated with off-resonant microwave coupling to the undriven hyperfine state $|1, 0\rangle$ followed by long lived oscillations corresponding to both $|-\rangle$ and $|+\rangle$. From fits to the data, we obtain a $T_2^* = 800 \pm 100$ ns for the undriven hyperfine states and a $T_2^* = 16 \pm 4.9$ μs for the mechanical dressed states, constituting a 50-fold increase in the spin coherence. We note that the increased T_2^* for $|1, 0\rangle$ can be explained by off-resonant mechanical driving of the transition, which partially dresses the $m_I = 0$ hyperfine manifold.

Figure 6.2c. shows a Fourier spectrum of the Ramsey data shown in fig. 6.2b. In the experiment, we tune the microwaves to be symmetrically detuned from $|\pm\rangle$ and hence we expect oscillations of the dressed states to occur at $\Omega_m/4\pi$. Indeed, we observe a strong,

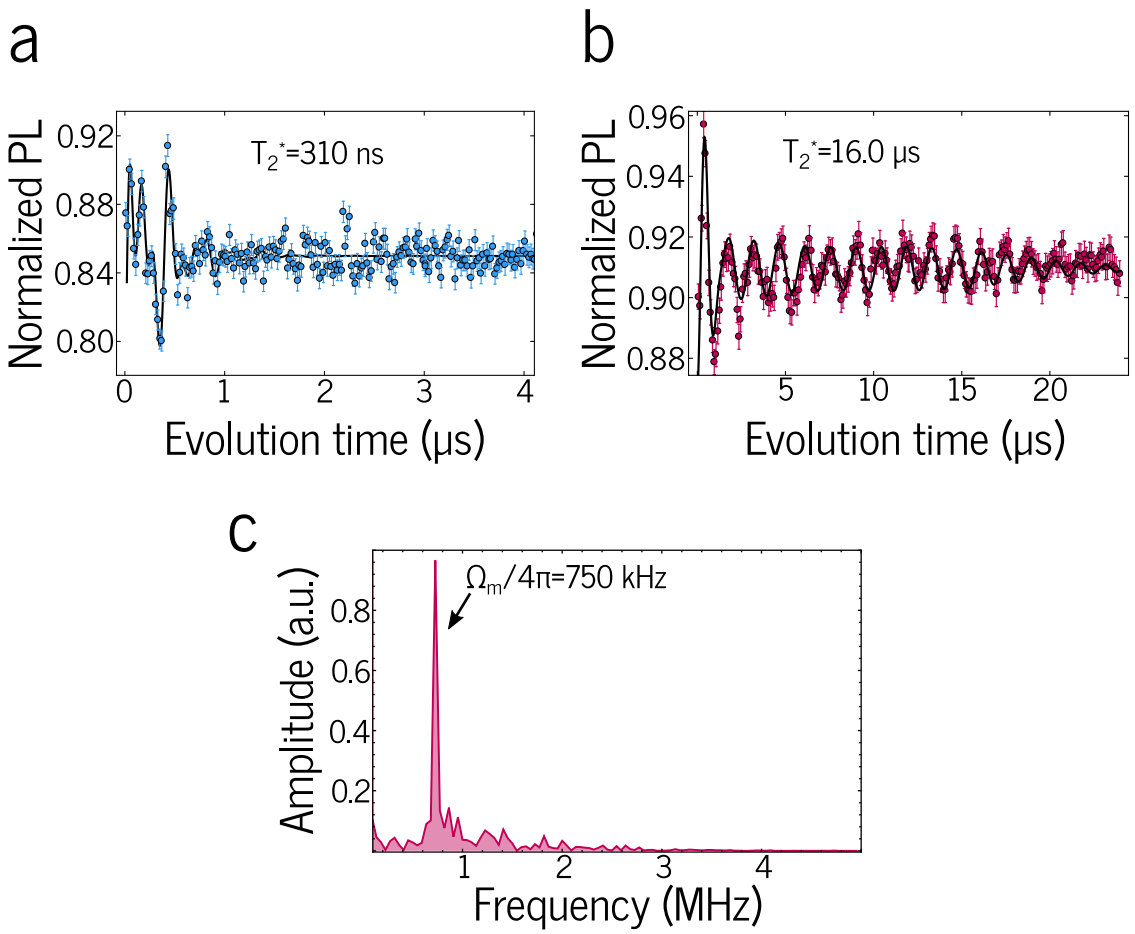

Figure 6.2: **Mechanically driven CDD**. a) Experimental Ramsey data for the undressed spin shows a $T_2^* = 310 \pm 32$ ns. b)Experimental Ramsey data for a mechanically dressed spin with $\Omega_m/2\pi$ =1.5 MHz shows an extended $T_2^* = 16.0 \pm 4.9$ μs c) Fourier spectrum of the Ramsey data in b) shows a strong peak at 750 kHz, consistent with the expected symmetric detuning from each dressed state of $\Omega_m/4\pi$.

narrow peak at 750 kHz, corresponding to half of the mechanical Rabi frequency.

6.9 Hybrid PDD+CDD

Although our CDD protocol offers enhanced spin coherence, the resulting coherence time is significantly shorter than the limit imposed by spin relaxation. Although mechanical CDD renders the spin insensitive to magnetic fields, the spin is still sensitive

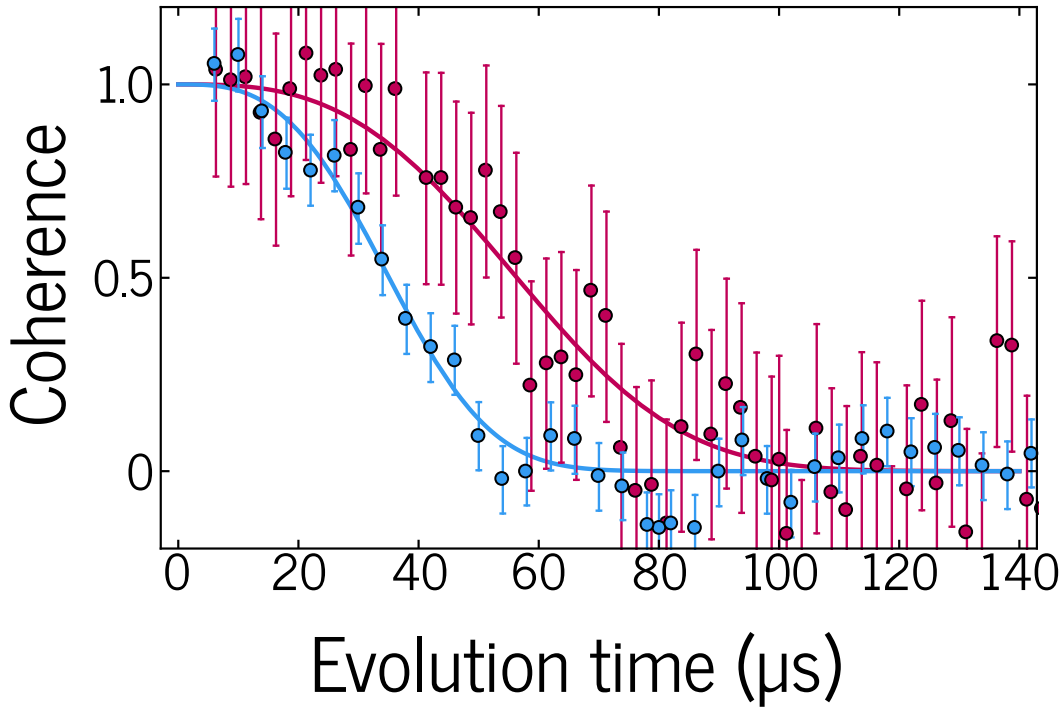

Figure 6.3: **Hybrid CDD+PDD protocol**. Hahn echo spin coherence measurement with (maroon) and without (blue) mechanical CDD. The bare spin states exhibit a $T_2 = 40 \pm 2$ μs. With mechanical CDD and $\Omega_m/2\pi = 1.5$ MHz, the spin exhibits an extended $T_2 = 64 \pm 6$ μs.

to fluctuations in temperature, electric fields, and the mechanical driving field. Recent studies of the NV center indicated that the electric field contribution to decoherence is dominant at low frequencies [139]. Moreover, the mechanical resonator acts as a low-pass filter to noise in the driving field, with a cutoff frequency of approximately 250 Hz (see supporting information). This suggests that the spin may be decoupled from the remaining sources of dephasing through PDD, which excels at decoupling the spin from low frequency noise.

To explore this hypothesis, we performed a Hahn echo experiment with and without mechanical CDD. In the absence of CDD, we observe a spin coherence time $T_2 = 40$ μs. When we use CDD with $\Omega_m/2\pi = 1.45$ MHz, we observe a 50% increase in the spin co-

herence compared to the bare spin states, with $T_2 = 64$ μs. The increase in T_2 shows that the bare NV spin states are still limited by higher frequency magnetic field fluctuations during a Hahn Echo. The modest increase in T_2 suggests two possible sources of decoherence. On the one hand, the spin may be sensitive to higher frequency electric field noise that is unable to be decoupled away in a Hahn echo sequence. On the other hand, high frequency magnetic field noise may be coupling to the qubit in a second order process. Given the decoherence rate measured here, this would correspond to an rms magnetic field of 100 mG at the NV center. This is approximately 50 times higher than the expected rms field produced by the nitrogen spin bath in our sample. Moreover, because our NV centers are approximately 50 nm deep in the diamond, we do not expect any significant magnetic contributions from the surface. Although possible, it seems unlikely that magnetic field noise dominates the residual dephasing. We hypothesize that electric field noise is the dominant dephasing mechanism for our hybrid CDD+PDD scheme.

6.10 Outlook

In this chapter, We have shown for the first time that CDD and PDD can be combined in a synergistic way. We demonstrated a 50-fold enhancement in the spin coherence of single NV centers through continuous mechanical driving. Moreover, when we combined mechanical driving with traditional microwave pulsed dynamical decoupling, we observed a 50% increase in the spin coherence time T_2 compared to the bare NV spin states. Because the spin coherence of the NV center is primarily limited by high frequency magnetic field noise, our protocol can in principle be used to extend the spin coherence time to the energy relaxation limit. In future experiments, we can establish the enhancement in T_2^* and T_2 as a function of mechanical drive strength, which should allow us to quantitatively characterize the residual sources of dephasing. If we observe a saturation effect, then the

residual dephasing is most likely due to electric field noise. Moreover, this hypothesis can be tested through the application of more dynamical decoupling pulses, which should allow for quantitative analysis of the noise spectrum. Furthermore, using magnetic double-quantum microwave pulses, one can probe the decoherence of the $\{|+\rangle, |-\rangle\}$ qubit [78], which is only sensitive to fluctuations in the mechanical driving field. This should allow us to discriminate between electric field noise and residual magnetic field noise.

In a broader context, our protocol should provide enormous benefits to hybrid spin-mechanical devices. The figure of merit for spin-mechanical devices is given by the single phonon cooperativity, $\eta = 2\pi\frac{g^2 T_2}{\bar{n}\omega_m}$, where g is the single phonon coupling strength, and $\bar{n}$ is the equilibrium thermal occupation number of the mechanical resonator. A practical device of the future will typically host many mechanical modes. Therefore, in a future multimode device, one mechanical mode can be used for CDD to improve T_2, leaving other modes to coherently couple to the dressed spin. Furthermore, our protocol can be used in AC electrometry and vibrometry measurements with greater sensitivity, which may assist in future experiments characterizing NV spin decoherence.

6.11 Supporting information

6.11.1 The bare NV spin Hamiltonian

In the main text of this chapter, we condensed the NV spin Hamiltonian into a simple phenomenological form characterized by the parameters D and E. Here, we provide the

full NV spin Hamiltonian for the bare spin states, which is shown below.

$$\begin{aligned} H_{bare} =& (D_0 + \alpha_T + d_\parallel E_z + V_{A_1})S_z^2 + \gamma_{NV}\mathbf{S}\cdot\mathbf{B} \\ & - \left[(d_\perp E_x + V_{E_1})(S_x^2 - S_y^2) - (d_\perp E_y + V_{E_2})(S_x S_y + S_y S_x\right] \end{aligned} \tag{6.6}$$

Here, $D_0 = 2.876$ GHz is the zero-field splitting at 180 K, $\alpha_T = -28$ kHz/K is the temperature shift of the zero-field splitting near 180 K [198], $d_\parallel = 0.35$ Hz $\cdot$ cm/V is the axial electric susceptibility [104], $V_{A_1} = d_{A_1}\epsilon_{zz} + d_{A_1'}(\epsilon_{xx} + \epsilon_{yy})$ is the A_1 symmetric strain interaction [109, 76], $d_\perp = 17$ Hz $\cdot$ cm/V is the transverse electric susceptibility, and $V_{E_1} = d_E(\epsilon_{xx} - \epsilon_{yy}) + 2d_{E'}\epsilon_{xz}$ and $V_{E_2} = 2d_E\epsilon_{xy} + 2d_{E'}\epsilon_{yz}$ are the E symmetric strain interactions. In a typical experiment, an applied magnetic field along the NV axis results in the Zeeman interaction $H_Z = \frac{\Delta_B}{2}S_z$ which does not commute with the transverse electric and E symmetric strain interactions. Therefore, H_Z typically suppresses fluctuations in those terms of the Hamiltonian [139, 76].

6.11.2 Mechanical Rabi frequency

The mechanical Rabi frequency is given by the E symmetric spin-strain interaction. The cantilever employed in this experiment only generates E_1 strain, and hence the interaction Hamiltonian can be written as

$$H_{int} = \frac{1}{2}V_{E_1}(S_+^2 + S_-^2) \tag{6.7}$$

The strain coupling, V_{E_1}, can be quantized in terms of the phonon creation and annihilation operators, $\{a^\dagger, a\}$, resulting in an interaction Hamiltonian

$$H_{int} = \frac{g}{2}(a + a^\dagger)(S_+^2 + S_-^2) \tag{6.8}$$

where g is the strain coupling to the zero-point fluctuations, or alternatively, the single phonon coupling strength. In our experiments, the cantilever is resonantly driven with a piezoelectric transducer, and hence the resonator can be modeled as a large amplitude coherent state, $|\alpha\rangle$, where α is a dimensionless number determining the amplitude of the state. The expectation value of the position operator for a coherent state is simply $X(t) = 2x_0\alpha\cos(\omega_m t)$. Therefore, the mechanical Rabi frequency can be written in terms of the beam displacement, $x_c = 2\alpha x_0$,

$$\Omega_m = g\frac{x_c}{x_0} \tag{6.9}$$

For the device employed here, we observe $g \approx$ 120 mHz, where variations are caused by the different locations and orientations of the NV center with respect to the cantilever.

6.11.3 The dressed NV spin Hamiltonian

For a resonant mechanical strain field, the dressed spin Hamiltonian is reduced to

$$\begin{aligned} H =&(D_0 + d_\parallel E_z + V_{A_1} + \alpha_T)S_z^2 + \frac{1}{2}(\Omega_m + V_E + d_\perp E_\perp)S_z + \gamma_{NV}\delta B_z(S_+^2 + S_-^2) \\ &+ \gamma_{NV}\delta B_\perp\left[\cos(\phi)(|0\rangle\langle +| + |+\rangle\langle 0|) + i\sin(\phi)(|-\rangle\langle 0| - |0\rangle\langle -|)\right] \end{aligned} \tag{6.10}$$

where we have defined $V_E = \sqrt{V_{E_1}^2 + V_{E_2}^2}$ and $E_\perp = \sqrt{E_x^2 + E_y^2}$ and defined the azimuthal orientation of an applied perpendicular magnetic field, $\phi = \arctan\delta B_y/\delta B_x$. Note that because we are working in a rotating frame, the Zeeman terms appear as perturbations in the dressed state Hamiltonian. Importantly, we see that the magnetic field does not affect the dressed state energies to first order.

An important feature of these dressed states is that they are driven by linearly po-

larized microwaves. The magnetic dipole transitions for the bare spin states require circularly polarized microwave fields. Therefore, to perform multi-pulse dynamical decoupling with phase swapping on the mechanical dressed states, circularly polarized microwave fields are required. Since we do not have such control, we are limited to the number of pulses that can be applied by pulse errors.

6.11.4 Experimental details for Ramsey experiments

In our Ramsey measurements of the undressed spin, the microwave field was detuned from the $|1,1\rangle$ transition by 7.5 MHz to make the coherence decay more visible. The microwave Rabi frequency was set to 4.5 MHz in order to drive all three hyperfine states. The Ramsey signal was fit to the following function:

$$\mathcal{S}(t) = e^{-(t/T_2^*)^2} \sum_{m_I} a_{m_I} \cos\left(2\pi\delta_{m_I} t + \varphi_{m_I}\right) + \mathcal{I}_0 \tag{6.11}$$

where a_{m_I}, δ_{m_I}, and φ_{m_I} correspond to the population, microwave detuning, and initial phase for each hyperfine state and $\mathcal{I}_0$ is the steady-state normalized photoluminescence rate for a thermally mixed state.

In our Ramsey measurements of the dressed spin, we tune our microwave field such that it is symmetrically detuned from the dressed states $|\pm\rangle$ by an amount $\Omega_m/2$. This would correspond to a microwave frequency that is resonant with the undressed $|1,1\rangle$ transition. Even though the mechanical resonator is detuned from the other $|\pm 1, m_I\rangle$ transitions, they experience a significant amount of dressing, and hence each hyperfine

transition was fit with their own coherence time.

$$\begin{aligned}\mathcal{S}(t) =& e^{-(t/T^*_{2\pm})^2}\left[a_+\cos\left(2\pi(\Omega_m/4\pi-\delta)t+\varphi_+\right)+a_-\cos\left(2\pi(\Omega_m/4\pi+\delta)t+\varphi_-\right)\right]\\ &+\sum_{m_I=0,1} a_{m_I}e^{-(t/T^*_{2m_I})^2}\cos\left(2\pi\delta_{m_I}t+\varphi_{m_I}\right)+\mathcal{I}_0\end{aligned} \tag{6.12}$$

6.11.5 Experimental details for the Hahn Echo experiment

In our Hahn echo measurements of the dressed state, the microwave field is resonantly tuned to the $|-\rangle$ transition. To reduce pulse errors from residual coupling to the other hyperfine states, we reduce the microwave Rabi frequency to approximately 500 kHz. For both the undressed and dressed state experiments, we fit the data to the following coherence envelope

$$\mathcal{C}(t) = e^{-(t/T_2)^n} \tag{6.13}$$

For the NVs measured in this experiment, we found the spin echo signal to fit to a variety of values of $n \in [2, 3]$. The value of n did not significantly affect the extracted T_2. The fit shown in fig. 6.3 corresponds to $n = 3$.

6.11.6 Amplitude noise filtering with a high-Q oscillator

An attractive aspect of our mechanical driving protocol is the filtering of high frequency fluctuations of the mechanical Rabi frequency by the mechanical oscillator. Standard microwave CDD is typically limited by amplitude fluctuations in the microwave field due to either thermal drifts of the microwave antenna or technical noise in the driving electronics. As a high-Q mechanical oscillator, the cantilever is an excellent filter of am-

plitude noise. To understand this, consider the dynamics of a resonantly driven harmonic oscillator with a noisy drive amplitude

$$\ddot{x} + \gamma\dot{x} + \omega_m^2 x = (F_0 + \delta F(t))\cos(\omega_m t) \tag{6.14}$$

where γ is the cantilever linewidth. The solution this equation is given by the convolution of the driving term with the Green's function for the mechanical oscillator. In frequency space, the solution is the direct product of the cantilever transfer function with the Fourier transform of the mechanical driving field. If we express the noisy force in terms of its Fourier components,

$$\delta F(t) = a_0 + \sum_n \left[a_n \cos(\omega_n t) + b_n \sin(\omega_n t)\right] \tag{6.15}$$

then we can write the frequency domain response to the noisy fluctuations, $\delta x(\omega)$ as

$$\begin{aligned} \delta x(\omega) &= \sum_n \left[\frac{1/2}{\sqrt{(\omega_0^2 - \omega^2)^2 + \gamma^2\omega^2}}(a_n \pm i b_n)\delta(\omega \pm \omega_n t)\right] \\ \delta x(\omega) &= \sum_n \left[\frac{1/2(a_n \pm i b_n)}{\sqrt{(\omega_0^2 - (\omega \pm \omega_n)^2)^2 + \gamma^2(\omega \pm \omega_n)^2}}\right] \end{aligned} \tag{6.16}$$

In the high-Q limit, we obtain the usual Lorentzian mechanical response of a mechanical oscillator and

$$\delta x(\omega) = \sum_n \left[\frac{1/(2\omega_m)(a_n \pm i b_n)}{\sqrt{(\omega - \omega_m \mp \omega_n)^2 + (\gamma/2)^2}}\right] \tag{6.17}$$

We see that the Lorentzian transfer function of the cantilever will effectively suppress amplitude fluctuations for $\omega_n > \gamma/2$. Therefore, the cutoff frequency for the cantilever is given by its linewidth $f_c = \gamma/4\pi = \omega_0/4\pi Q$.

6.11.7 Bright spots

As mentioned in the main text of this chapter, we observe the formation of anomalous bright spots on the diamond surface after long exposure to the 532 nm laser in a vacuum environment. These brights do not correspond to the NV photoluminescence, and as the bright spots grow in size, they dominate the NV fluorescence and no optically detected magnetic resonance can be detected. We have observed that these spots are fluorescent under 532 nm excitation, but are dark under 637 nm excitation. In addition, the bright spot appears to change either the electrostatic or strain environment of near-surface NV centers. To probe this effect, we performed resonant excitation spectroscopy of a single NV center before and after bright spot formation and observed significant changes in the zero-phonon line. The overall PL of the NV center was reduced, which may be due to increased photoionization. Moreover, the polarization dependence and static splitting of the zero-phonon line changed after the formation of the bright spot.

At cryogenic temperatures near 4 K, we observe a formation time of over one month. At room temperature and in high vacuum conditions (10^{-4} torr), bright spots can be formed in minutes depending on the laser power. The growth rate also appears to be exponential in time. It is unclear whether the suppression at cryogenic temperatures is related to the temperature of the sample or the vacuum level, which can reach values of 10^{-9} torr in our chamber. Based on our limited data, we have two hypotheses regarding the origin of these bright spots. One possibility is that the 532 nm laser graphitizes the diamond surface. The second possibility is that contaminants are accumulating at the spot of the laser. This could be due to the laser ionizing material in its path, which can polarize material floating around in the chamber or on the surface. Subsequent Langevin collisions would then cause an accumulation of mass at the surface. In either case, we expect that the primary effect on the NV center would be the introduction of

low frequency electric field noise.

We have found two ways to remove the bright spots from the sample. The first is to irradiate the sample with several mW of 532 nm light in air for several minutes. However, this method appears to be somewhat insufficient. When the sample is returned to vacuum conditions, bright spots appear to form more quickly. The second and more effective method is to clean the sample in a boiling (190° C) 1:1 $H_2SO_4 : HNO_3$ acid mixture for several minutes. Interestingly, sonicating the sample in solvents does not remove the bright spots.

Chapter 7

Theoretical calculations for future NV-phonon interactions

> Fry: How could they even know about a show from 1000 years ago?
>
> Professor: Well, Omicron Persei 8 is about 1000 light years away, so the electromagnetic waves would just recently have gotten there. You see –
>
> Fry: Magic. Got it.
>
> - *Futurama*

NV centers and mechanical oscillators have been developed independently for quantum technologies for several years, but have faced important roadblocks that may be addressed with a hybrid NV-mechanical device. Among these challenges are the generation of multipartite entanglement in an NV center system and preparation of non-classical states of a mechanical oscillator. In this chapter, I will review the theory for several important applications of our hybrid NV-mechanical device, including phonon cooling and spin-spin entanglement. The aim of this discussion is to provide an accessible introduction to the relevant experimental protocols and to provide a realistic scope of the experimental progress that is required to achieve these goals.

7.1 Phonon cooling

The future utility of any hybrid mechanical device hinges on the ability to prepare the mechanical degree of freedom in a non-Gaussian state. For instance, in a device where phonons serve as a flying qubit, quantum information may stored as a superposition of phonon Fock states. An important prerequisite for generating non-Gaussian mechanical states is the preparation of the mechanical oscillator in the ground state of motion. As mentioned in chapter 1, this can be accomplished through passive cooling or through active, optomechanical cooling methods. In general, active cooling of a mechanical oscillator has been accomplished using radiation pressure forces, but has proven to be difficult do the weak nature of radiation pressure [199]. Very recently, the focus has shifted toward the use of single qubits for phonon cooling due to the inherent nonlinear interaction provided by the qubit [54]. A qubit can potentially cool a mechanical oscillator to the ground state and subsequently prepare a non-Gaussian state of motion, such as a Fock state [170, 169]. This would be of fundamental interest as this could not be performed with standard optomechanical devices. More generally, achieving ground state cooling with a qubit would provide a new approach to study the quantum acoustics as an analog to cavity quantum electrodynamics.

Phonon cooling relies on the fact that a qubit prepared in its ground state is effectively at zero temperature. By engineering a coupling between the qubit and mechanical oscillator, the qubit can then be used to remove entropy from the mechanical oscillator. The standard protocol [170] for phonon cooling with a qubit is demonstrated in fig. 7.1 a. A qubit with frequency ω_0 is parametrically coupled to a mechanical oscillator with frequency ω_m. The parametric qubit-phonon coupling produces phonon sidebands on the qubit transition, at frequencies of $\omega = \omega_0 \pm q\omega_m$, where q is an integer. For illustrative purposes, let us encode the qubit in an optical transition that can be coherently driven

with a laser at frequency ω_L. At thermal equilibrium, the qubit population will be entirely in the ground state $|g\rangle$. If the qubit is coherently driven at first red sideband of the qubit transition, $\omega_L = \omega_0 - \omega_m$, a Jaynes-Cummings interaction is created between the qubit and mechanical oscillator, $H_{rsb} \sim (\sigma^+ a + \sigma^- a^\dagger)$ [200, 201]. An excitation of the qubit is accompanied by the removal of a single phonon from the mechanical oscillator, $|g\rangle |n\rangle \rightarrow |e\rangle |n-1\rangle$. Physically, this can be interpreted as the qubit upconverting a photon from the laser to the qubit frequency by absorbing a single phonon. Entropy is carried away from the system through spontaneous emission of a single photon, which returns the qubit to the ground state. This cycle can be repeated until the oscillator is prepared in its quantum ground state.

There are now several proposals for phonon cooling with the NV center [202, 203, 169]. In this section, we will focus on two cooling protocols that utilize the strain-orbit interaction. For a comprehensive review of phonon cooling with an NV center, I refer the reader to refs. [169, 24]. The two cooling protocols are shown in fig. 7.1 b. and c. The protocol shown in fig. 7.1 b. is the standard sideband cooling protocol that we introduced above, which relies on addressing phonon sidebands on the NV optical transitions. The second protocol shown in fig. 7.1 c. is a unique cooling protocol that is enabled by the rich electronic structure of the NV excited state, and relies on a resonant electron-phonon interaction. We will discuss both of these cooling protocols in detail in the following sections.

7.1.1 Sideband cooling

The sideband or "off-resonant" cooling scheme was first proposed in ref. [170] in the context of quantum dots, and was later refined for the NV center in ref. [169]. This protocol relies on a strain-mediated, parametric interaction between the orbital

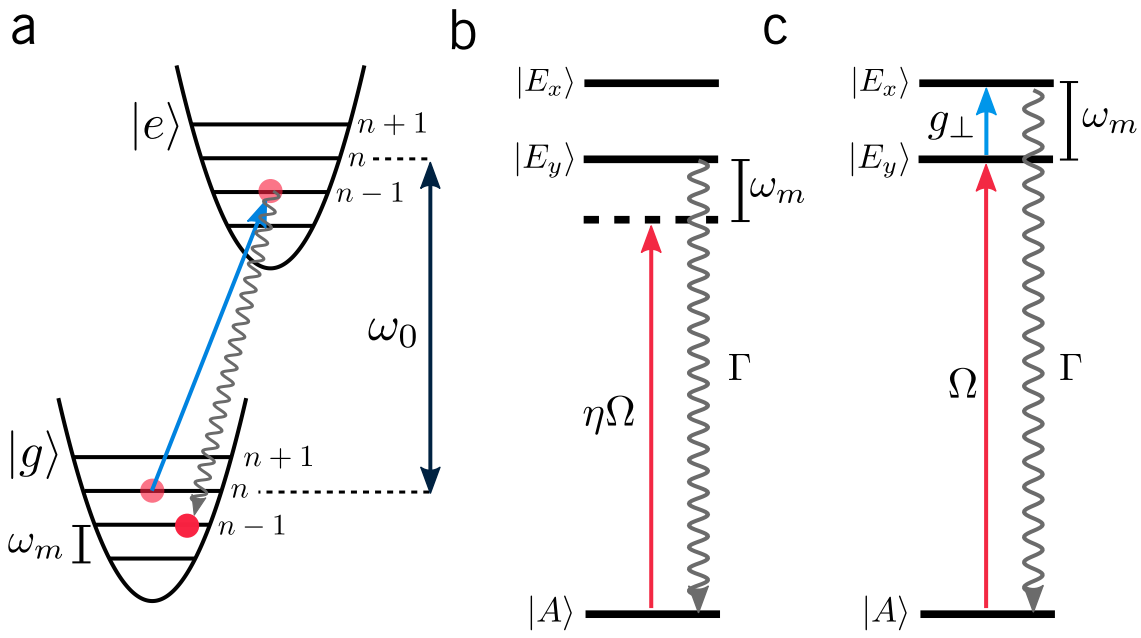

Figure 7.1: **Phonon cooling with a single defect**. a) The standard phonon cooling protocol. An electronic excitation results in a removal of a single phonon from the mechanical oscillator, $|g\rangle|n\rangle \rightarrow |e\rangle|n-1\rangle$. Spontaneous emission of a photon carries away the removed entropy from the harmonic oscillator and the defect returns to the ground state $|g\rangle|n-1\rangle$. After many cycles, the mechanical oscillator can be prepared in the ground state, $|0\rangle$. b) Protocol for sideband cooling or off-resonant cooling with the NV center. The cooling relies on driving the first red sideband of the E_y transition to remove phonons from the mechanical oscillator and spontaneous emission to carry away entropy. c) Protocol for resonant cooling with the NV center. The $|E_x\rangle \leftrightarrow |E_y\rangle$ transition frequency is matched to the phonon frequency. When prepared in $|E_y\rangle$, the NV center absorbs a phonon from the mechanical oscillator and is excited to $|E_x\rangle$, from which the NV center decays back to the ground state through spontaneous emission.

states of the NV center and a mechanical resonator. This parametric interaction results in a modulation of the optical transition frequencies of the NV center, and hence a series of phonon sidebands. If the NV center is coherently driven with a laser on the first red sideband, cooling of the mechanical resonator occurs. As a result, in order for this protocol to be used, the system must be in the resolved-sideband regime where $\omega_m \gg \Gamma$, where Γ is the optical transition linewidth. To describe this process, we introduce the Hamiltonian for a driven two-level system parametrically coupled to a

single-mode harmonic oscillator,

$$H = \frac{\omega_0}{2}\sigma_z + \omega_m a^\dagger a + \frac{g_\parallel}{2}(a + a^\dagger)\sigma_z + \Omega \cos(\omega_L t)\sigma_x \tag{7.1}$$

where ω_0 is the qubit frequency, $\sigma_z = |e\rangle\langle e| - |g\rangle\langle g|$, ω_m is the phonon frequency, a is the annihilation for the mechanical mode, $g_\parallel$ is the parametric coupling, Ω is the optical Rabi frequency and ω_L is the laser frequency.

In the rotating frame of the laser, we have

$$H = -\frac{\delta}{2}\sigma_z + \frac{\Omega}{2}\sigma_x + \omega_m a^\dagger a + \frac{g_\parallel}{2}(a + a^\dagger)\sigma_z \tag{7.2}$$

where $\delta = \omega_L - \omega_0$. As we mentioned, this parametric interaction can be understood as a modulation of the qubit frequency due to the motion of the mechanical oscillator. On the other hand, the the parametric interaction can be understood as a spin-dependent force on the oscillator, which displaces the harmonic oscillator in phase space. Therefore, to better understand the dynamics of the system, we will apply the Polaron transformation to the above Hamiltonian to move into the "displaced-oscillator basis", $\hat{U}H\hat{U}^\dagger$ where $\hat{U} = \exp\left(\frac{g_\parallel}{\omega_m}(a^\dagger - a)\sigma_z\right)$.

In the displaced oscillator basis, we obtain the Hamiltonian

$$\tilde{H} = -\frac{\delta}{2}\sigma_z + \omega_m a^\dagger a + \frac{\Omega}{2}\left(e^{g_\parallel/\omega_m(a^\dagger - a)}\sigma^+ + e^{-g_\parallel/\omega_m(a^\dagger - a)}\sigma^-\right) \tag{7.3}$$

Note that this Hamiltonian is analogous to a trapped ion experiencing a laser-assisted spin dependent momentum kick [200]. In our case, we instead have a laser-assisted, spin-dependent displacement kick of the harmonic oscillator. We are interested in the so-called Lamb-Dicke regime where the recoil energy associated a single spontaneous emission event is much less than phonon energy, $\eta = \frac{g}{\omega_m} \ll 1$. This parameter η is defined as the Lamb-

Dicke parameter. In general, the phonon mode will be in a thermal state, and to account for thermal excitations, we define the thermal Lamb-Dicke parameter $\eta_{th} = \eta\frac{x_{th}}{x_0}$. The amplitude of thermal motion can be calculated via $x_{th} = \sqrt{\langle x^2\rangle} = Tr[x^2\hat{\rho}]$, where ρ is the phonon density matrix.

$$\langle x^2\rangle = \frac{1}{Z}\sum_n e^{-\beta\hbar\omega_m(n+1/2)}\langle n|\, x_0^2(a+a^\dagger)^2\,|n\rangle \tag{7.4}$$

where Z is the partition function for the harmonic oscillator. After some algebra, we find

$$x_{th} = x_0\sqrt{\coth\left(\frac{\hbar\omega_m}{2k_BT}\right)} \tag{7.5}$$

Now, we can write x_{th} in terms of the average thermal population number $\bar{n}$ using the following identity:

$$\bar{n} = \frac{1}{e^{\beta\hbar\omega_m}-1} \tag{7.6}$$

$$= \frac{1}{2}\left[\coth\left(\frac{\hbar\omega_m}{2k_BT}\right)-1\right] \tag{7.7}$$

This implies that $x_{th} = x_0\sqrt{2\bar{n}+1}$, and thus

$$\eta_{th} = \frac{g_\parallel}{\omega_m}\sqrt{2\bar{n}+1} \tag{7.8}$$

Therefore, the Lamb-Dicke limit is defined by $\eta_{th} \ll 1$. Note that the Lamb-Dicke parameters are related to the Huang-Rhys factors [204] by the simple relationships, $S_0 = \eta^2$ and $S = \eta_{th}^2$. To find the dynamics of the system in the Lamb-Dicke regime, we move

into the interaction picture with respect to the qubit,

$$H_I = \frac{\Omega}{2}\left[\sigma^+ e^{-i\delta t} e^{\eta(a^\dagger e^{i\omega_m t} - a e^{-i\omega_m t})} + \sigma^- e^{i\delta t} e^{-\eta(a^\dagger e^{i\omega_m t} - a e^{-i\omega_m t})}\right] \tag{7.9}$$

In the Lamb-Dicke limit, we can Taylor expand the Hamiltonian up to first order in η, and we obtain

$$H_I \approx \frac{\Omega}{2}\left[\sigma^+ e^{-i\delta t}\left(1 + \eta a^\dagger e^{i\omega_m t} - a e^{-i\omega_m t}\right) + \sigma^- e^{i\delta t}\left(1 - (\eta a^\dagger e^{i\omega_m t} - a e^{-i\omega_m t})\right)\right] \tag{7.10}$$

We are interested in the electronic transition $|g\rangle|n\rangle \rightarrow |e\rangle|n'\rangle$. For a particular set of laser detunings, $\delta = (n'-n)\omega_m + \Delta$, the matrix elements $\langle e, n'| H_I |g, n\rangle$ are non-zero. In particular, when the laser is parked on the red sideband, $\delta = -\omega_m$, we can make a rotating wave approximation and we obtain the red sideband Hamiltonian

$$H_{rsb} = \frac{\eta\Omega}{2}(\sigma^+ a + \sigma^- a^\dagger) \tag{7.11}$$

which drives the transition $|g, n\rangle \rightarrow |e, n-1\rangle$ desired for cooling the system. To derive the effective cooling equation, a master equation approach can be used to take into account spontaneous emission, dissipation of the mechanical resonator, and the NV-mechanical coupling. In the Lamb-Dicke limit, the dynamics of the NV center are much faster than the overall cooling rate, and the NV center can be adiabatically eliminated from the master equation [170], resulting in an effective rate equation for the harmonic oscillator

$$\frac{\partial\langle a^\dagger a\rangle}{\partial t} = -\Gamma_c\left(\langle a^\dagger a\rangle - n_f\right) \tag{7.12}$$

where n_f is the steady-state thermal occupation number and we have defined the

cooling rate.

$$\Gamma_c = \frac{g_{\parallel}^2 \Omega^2}{\Gamma \omega_m^2} \tag{7.13}$$

If the cooling rate exceeds the thermalization rate of the mechanical resonator, the final thermal occupation number is given by

$$n_f \approx \frac{\omega_m N_{bath}}{\Gamma_c Q} \tag{7.14}$$

where N_{bath} is the average thermal occupation number of the surrounding bath and Q is the mechanical quality factor. There are a few important aspects of this cooling protocol that should be pointed out. First, the cooling rate scales inversely with the square of the mechanical frequency. This is a direct result of the fact that this protocol is inherently an off-resonant process. As the frequency increases, the Lamb-Dicke parameter effectively goes to zero, which eliminates the NV-mechanical coupling. In addition, the cooling rate increases with the Rabi frequency, and hence the laser power. Unfortunately, there is an upper limit on the optical Rabi frequency. If the transition is driven too strongly, then the cooling becomes less efficient, as the NV center has a finite probability to return to the ground state and adding a phonon to the resonator. As it turns out, the cooling is maximized when $\Omega \approx \omega_m$.

It is important to note that in our analysis, we have not considered any spectral diffusion of the optical transition. Spectral diffusion broadens the transition, but does not increase the spontaneous emission rate, and hence spectral diffusion will lead to lower cooling rate. For a broadened linewidth of Γ_ϕ, the cooling rate is reduced by $\Gamma_c \sim \Gamma/(\Gamma + \Gamma_\phi)$. As we mentioned in chapter 2, the radiative linewidth is approximately $\Gamma = 13.2$ MHz.

7.1.2 Experimental calculations for sideband cooling

The sideband cooling protocol relies on the strain-induced modulation of the optical transition frequencies. Due to the signs and magnitudes of the strain-orbit coupling constants, it is advantageous to use the E_y transition for sideband cooling. In particular, we focus on the A_1 and E_1 symmetric terms of the strain Hamiltonian. In the calculations that follow, we will assume that the NV center is embedded inside of a doubly-clamped nanobeam resonator with dimensions 2 μm $\times$ 100 nm $\times$ 50 nm. The nanobeam contains flexural, compressional, and torsional mechanical modes that can all interact with the NV center. However, the scaling of the Lamb-Dicke parameter is only favorable for flexural vibrations, and hence we will restrict our discussion to the nanobeam flexural modes.

To optimize the single phonon coupling, the nanobeam should be fabricated such that the resonator axis is along the [110] crystal direction, and the NVs used for cooling should be oriented along $[\bar{1}11]$ and $[1\bar{1}1]$. The strain experienced by an NV at a depth d from the surface due to zero-point fluctuations of the n^{th} flexural mode can be written as

$$\epsilon_B = \begin{vmatrix} -\nu\epsilon_n & 0 & 0 \\ 0 & \epsilon_n & 0 \\ 0 & 0 & -\nu\epsilon_n \end{vmatrix} \tag{7.15}$$

where ϵ_n is given by

$$\epsilon_n(z) = \frac{(\beta_n l)^2 x_0}{\sqrt{2} l^2}(t/2 - d)\left[\cos(\beta_n z) + \cosh(\beta_n z) - c_n\left(\sin(\beta_n z) + \sin(\beta_n z)\right)\right] \tag{7.16}$$

where $\beta_n l = (4.73, 7.85, 10.9956, 14.1372, ...)$ are the nanobeam wavenumbers and $c_n = (\frac{1}{1.01781}, \frac{1}{0.99923}, \frac{1}{1.000033551}, \frac{1}{.9999985501}, ...)$ are normalization constants which satisfy

n	$\omega_m/2\pi$	$g_\parallel$	Γ_c	$\bar{n}_i$	$\bar{n}_f$
1	228 MHz	23.4 MHz	928 kHz	367.0	9.0
2	627 MHz	38.8 MHz	337 kHz	133.0	24.8
3	1.23 GHz	54.4 MHz	172 kHz	67.5	48.4
4	2.03 GHz	69.9 MHz	104 kHz	40.6	40.6

Table 7.1: **Experimental estimates for sideband cooling**. Calculated sideband cooling rates for a diamond nanobeam with a bath temperature $T = 4$ K, an optical Rabi frequency Ω=100 MHz, mechanical $Q = 10^4$, and an inhomogeneously broadened transition linewidth $\Gamma_\phi = 100$ MHz.

the boundary conditions for a doubly-clamped beam. Using the derived strain tensor and the definition of H^E, we see that the single phonon coupling for the n^{th} mode can be written as $g_{n\parallel} = -\lambda_{A_1}\nu\epsilon_n + \lambda_{A_1'}(1-\nu)\epsilon_n - \lambda_E(1+\nu)\epsilon_n = (2.31 \text{ PHz})\epsilon_n$, leading to an effective parametric interaction

$$H = g_{n\parallel}(a_n + a_n^\dagger) \left|E_y\right\rangle \left\langle E_y\right| \tag{7.17}$$

From here, we may calculate the cooling rate and final phonon thermal occupation number for some realistic experimental parameters. The first condition is that the NV center is located within 5 nm of the diamond surface and at one of the nanobeam clamping points. The second condition is that the mechanical resonator has a quality factor of $Q = 10^4$. In addition, we assume that the sample is at a temperature of 4 K, which sets the thermalization rate. In table 7.1, we show the cooling rates for an optical Rabi frequency $\Omega = 100$ MHz for an inhomogeneously broadened linewidth $\Gamma_\phi = 100$ MHz.

From these calculations, we observe that sideband cooling can be used to prepare the lowest frequency modes of the nanobeam near their quantum ground state, with the fundamental mode reaching a minimum temperature of $\bar{n} = 9$. The fundamental limit for reaching the ground state is the mechanical quality factor, which we assumed here to be 10^4. However, if we assume that the Q is dominated by clamping losses, we can improve

n	$\omega_m/2\pi$	$g_\parallel$	Γ_c	$\bar{n}_i$	$\bar{n}_f$
1	228 MHz	23.4 MHz	928 kHz	367.0	0.19
2	627 MHz	38.8 MHz	337 kHz	133.0	0.51
3	1.23 GHz	54.4 MHz	172 kHz	67.5	1.00
4	2.03 GHz	69.9 MHz	104 kHz	40.6	1.65

Table 7.2: **Experimental estimates for sideband cooling for a clamping loss limited Q.** Calculated sideband cooling rates for a diamond nanobeam with a bath temperature $T = 4$ K, an optical Rabi frequency Ω=100 MHz, mechanical $Q_{CL} = 480,000$, and an inhomogeneously broadened transition linewidth $\Gamma_\phi = 100$ MHz.

our estimate for the Q [164]. If we assume a clamping-loss limited Q of approximately $Q_{CL} = 480,000$, then we find that the first two modes of the beam can be prepared in the ground state.

7.1.3 Sideband thermometry

The the most direct way to measure the mechanical resonator temperature is through sideband thermometry [201]. In this technique, the amplitude of the red and blue sidebands in the excitation spectrum give a direct measure of the mode temperature. In this section, we will give a full derivation of the excitation spectrum and show how this technique works. To begin, let us return to the interaction picture Hamiltonian in the displaced oscillator basis.

$$H_I = \frac{\Omega}{2}\left[\sigma^+ e^{i\delta t} e^{\eta(a^\dagger e^{i\omega_m t} - a e^{-i\omega_m t})} + \sigma^- e^{-i\delta t} e^{-\eta(a^\dagger e^{i\omega_m t} - a e^{-i\omega_m t})}\right] \tag{7.18}$$

To derive the correct lineshape and get an accurate temperature, it is important to find the exact transition probability. Again, for the set of laser detunings $\delta = (n' - n)\omega_m + \Delta$, the matrix element $\langle e, n'| H_I |g, n\rangle$ can be easily simplified. Only terms with the correct number of creation and annihilation operators in the Taylor expansion of $e^{\eta(a^\dagger - a)}$ will

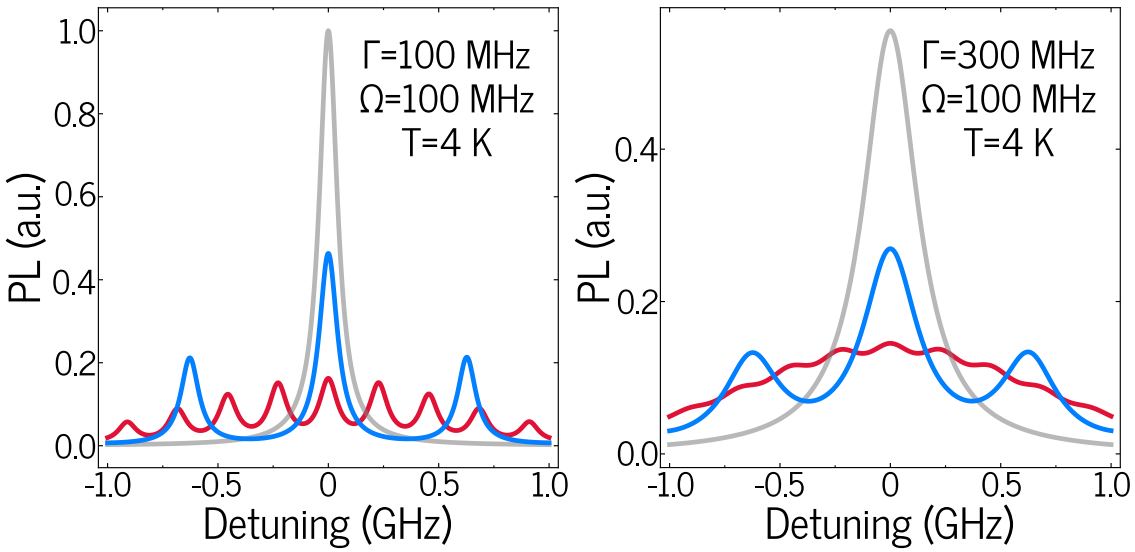

Figure 7.2: **Excitation spectrum for an NV coupled to a thermal mechanical oscillator**. The excitation spectrum for the $|0\rangle \rightarrow |E_y\rangle$ for an NV center embedded in a diamond nanobeam. The vibrational sidebands are induced by thermal fluctuations of the nanobeam. The gray trace corresponds to the $|0\rangle \rightarrow E_y$ transition in the absence of phonons. The red trace corresponds to coupling to the first-order flexural mode of the beam ($\omega_m/2\pi = 238$ MHz). The blue trace corresponds to coupling to the second-order flexural mode ($\omega_m/2\pi = 627$ MHz). The plot on the left (right) corresponds to transition linewidths of $\Gamma = 100(300)$ MHz.

generate non-zero matrix elements.

$$\begin{aligned}
\langle e, n'| H_I |g, n\rangle &= \frac{\Omega}{2} \langle e| \sigma^+ |g\rangle \langle n'| e^{\eta_{th}(a^\dagger - a)} |n\rangle \\
&= \frac{\Omega}{2} e^{i((n'-n)\omega_m + \Delta)t} \sum_{j=0}^{\infty} \frac{\langle n'| \eta(a^\dagger e^{i\omega_m t} - a^{-i\omega_m t})^j |n\rangle}{j!} \\
&= \frac{\Omega}{2} e^{i\Delta t} \langle n'| e^{\eta(a^\dagger - a)} |n\rangle
\end{aligned} \tag{7.19}$$

It can be shown through Taylor expansion that

$$\langle n'| e^{\eta(a^\dagger - a)} |n\rangle = \sqrt{\frac{n_<!}{n_>!}} e^{-\eta^2/2} \eta^{|n'-n|} L_n^{|n-n'|}(\eta^2) \tag{7.20}$$

where $n_{<(>)}$ refers to the smaller (larger) of n' and n and L_n^α is the generalized Laguerre polynomial.

Since the lineshape depends on the transition probability, we must calculate $P_{eg} = |\langle e, n'| H_I |g, n\rangle|^2$.

$$P_{eg} = |\langle e, n'| H_I |g, n\rangle|^2 = \frac{\Omega^2}{4} \left(\frac{n_<!}{n_>!}\right) e^{-\eta^2} \eta^{2|n'-n|} \left(L_n^{|n'-n|}(\eta^2)\right)^2 \tag{7.21}$$

Now, let us define the change in phonon number, $\Delta n = n' - n$. The expression for P_{eg} can be broken up into the case where $\Delta n > 0$ and $\Delta n < 0$. For now, we will focus on the case where $\Delta n < 0$ and note that the analysis for $\Delta n > 0$ follows similarly. We proceed by looking the probability for all transitions involving a change in vibrational quanta of Δn.

$$P_{eg}(\Delta n) = \sum_n P_n |\langle e, n + \Delta n| H_I |g, n\rangle|^2 \tag{7.22}$$

where P_n is the initial probability that the state $|n\rangle$ is occupied. Here, we assume the initial state of the resonator is a thermal state, and $P_n = e^{-n\beta\hbar\omega_m}(1 - e^{-\beta\hbar\omega_m})$.

$$\begin{aligned} P_{eg}(\Delta n) &= (1 - e^{-\beta\hbar\omega_m}) \sum_{m=-\Delta n}^{\infty} e^{-m\beta\hbar\omega_m} |\langle e, m + \Delta n| H_I |g, m\rangle|^2 \\ &= \frac{\Omega^2}{4} e^{-\eta^2} \eta^{2\Delta n} (1 - e^{-\beta\hbar\omega_m}) e^{\Delta n \beta\hbar\omega_m} \\ &\quad \times \sum_{n=0}^{\infty} e^{-n\beta\hbar\omega_m} \frac{n!}{(n - \Delta n)!} \left(L_n^{\Delta n}(\eta^2)\right)^2 \end{aligned} \tag{7.23}$$

In the second step above, we have just made a simple change of variable. To simplify this expression, we use the following identity for the modified Bessel function I_α.

$$\sum_{n=0}^{\infty} \frac{n!}{\Gamma(n+\alpha+1)} L_n^\alpha(x) L_n^\alpha(y) z^n = \frac{1}{1-z} e^{-z\left(\frac{x+y}{1-z}\right)} (xyz)^{-\alpha/2} I_\alpha\left(\frac{2(xyz)^{1/2}}{1-z}\right) \tag{7.24}$$

Clearly, we have $z = e^{-\beta\hbar\omega_m}$, $x = y = \eta^2$, and $\alpha = |\Delta n|$ (noting that $I_\alpha = I_{-\alpha}$). Using this identity, we find

$$P_{eg}(\Delta n) = \frac{\Omega^2}{4} e^{-\eta^2} e^{\Delta n \beta\hbar\omega_m/2} \exp\left[-2\eta^2 \frac{e^{-\beta\hbar\omega_m}}{1-e^{-\beta\hbar\omega_m}}\right] I_{\Delta n}\left(\frac{2\eta^2 e^{-\beta\hbar\omega_m/2}}{1-e^{-\beta\hbar\omega_m}}\right) \tag{7.25}$$

Using hyperbolic functions and noting that again $\bar{n} = (e^{\beta\hbar\omega_m} - 1)^{-1}$, we find

$$\begin{aligned} P_{eg}(\Delta n) &= \frac{\Omega^2}{4} e^{-\eta^2} e^{-\eta^2(\coth(\beta\hbar\omega_m/2)-1)} e^{\Delta n\beta\hbar\omega_m/2} I_{\Delta n}(\eta^2 \csc(\beta\hbar\omega_m/21)) \\ &= \frac{\Omega^2}{4} e^{-\eta^2(2\bar{n}+1)} e^{\Delta n\beta\hbar\omega_m/2} I_{\Delta n}(2\eta^2\sqrt{\bar{n}(\bar{n}+1)}) \end{aligned} \tag{7.26}$$

Finally, noting that $e^{\beta\hbar\omega_m} = \frac{\bar{n}+1}{\bar{n}}$, we find

$$P_{eg}(\Delta n) = \frac{\Omega^2}{4} e^{-\eta^2(2\bar{n}+1)} \left(\frac{\bar{n}+1}{\bar{n}}\right)^{\Delta n/2} I_{\Delta n}(2\eta^2\sqrt{\bar{n}(\bar{n}+1)}) \tag{7.27}$$

Now, we may construct the function describing the excitation spectrum, which we will define as a function of the excitation (laser) frequency, $\sigma(\omega_L)$. The lineshape will be given by a convolution of the phonon transition lineshape $g_{ph}(\omega)$ and the electronic

transition lineshape $g_{el}(\omega)$.

$$\sigma(\omega_L) = \sum_{\Delta n} P_{eg}(\Delta n) g_{ph}(\omega_L - \Delta n\omega_m) \star g_{el}(\omega_L - \omega_0) \tag{7.28}$$

The phonon and electronic transition lineshapes are merely Lorentzians whose widths, γ and Γ are set by the mode Q and excited state lifetime respectively. The convolution of these two Lorentzians is another Lorentzian whose width is $\gamma + \Gamma$. In most cases, $\gamma/\Gamma \approx 10^{-4}$, and it is safe to treat $g_{ph}(\omega)$ as a delta function. Carrying out this convolution and recalling that the laser detuning is $\delta = \omega_L - \omega_0$, we have

$$\sigma(\delta) = \sum_{\Delta n=-\infty}^{\infty} I_{\Delta n}(2\eta^2\sqrt{\bar{n}(\bar{n}+1)}) \left(\frac{\bar{n}+1}{\bar{n}}\right)^{\Delta n/2} e^{-\eta^2(2\bar{n}+1)} \frac{(\Gamma/2)(\Omega/2)^2}{(\Gamma/2)^2 + (\delta - \Delta n\omega_m)^2} \tag{7.29}$$

Some example spectra are shown in fig. 7.2 for a variety of parameters.

Importantly, we see it is possible to probe the phonon temperature by looking at the sideband amplitudes. In particular, comparing the n^{th} red and blue sidebands should give a direct measure of the temperature of the mode. This can be seen via

$$\frac{\sigma(+\Delta n\omega_m)}{\sigma(-\Delta n\omega_m)} = \left(\frac{\bar{n}+1}{\bar{n}}\right)^{|\Delta n|} \tag{7.30}$$

Therefore, if we cool the resonator near its quantum ground state, the red and blue sidebands should appear asymmetric in amplitude. In the ground state, the red sideband should entirely disappear. An example spectrum showing the sideband asymmetry is shown in fig. 7.3, where we have considered the second order mode of the nanobeam described in the previous section at a mode temperature of $\bar{n} = 1$.

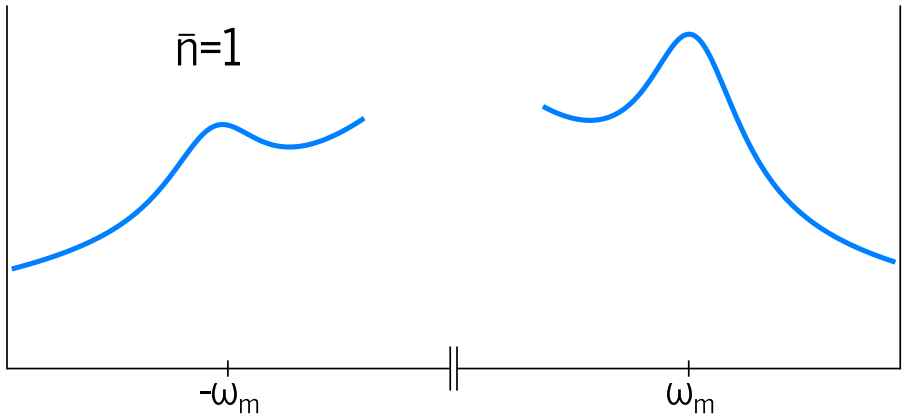

Figure 7.3: **Sideband thermometry**. Excitation spectrum showing the amplitude asymmetry for the first red and blue sidebands of the second order mode of the nanobeam when $\bar{n} = 1$.

7.1.4 Resonant cooling

The second cooling technique relies on a resonant interaction between the NV center and the mechanical resonator [169]. In the case of the NV center, we utilize the transition between $|E_x\rangle$ and $|E_y\rangle$, which can be driven by either E_1 or E_2 symmetric phonons when the energy splitting is equal to the phonon frequency $\Delta_{xy} = \omega_m$. This resonance condition can be achieved by tuning Δ_{xy} with an external, DC electric field. The effective Hamiltonian for this system in the rotating wave approximation can be written as

$$H_{eff} = g_{n\perp} \left(|E_x\rangle \langle E_y| \, a_n + |E_y\rangle \langle E_x| \, a^\dagger \right) \tag{7.31}$$

Notice that an effective Jaynes-Cummings interaction is naturally formed in the NV center, which is a direct result of the orbital doublet nature of the excited state. The single phonon coupling $g_{n\perp}$ depends on the static environment of the NV center. For example, if Δ_{xy} is set by an electric field F_x, which is inherently E_1 symmetric, then $g_{n\perp}$ will be given by the E_2 symmetric strain coupling. Alternatively, if the splitting is set by an electric field F_y, $|E_x\rangle$ and $|E_y\rangle$ mix and form new eigenstates that can be directly

coupled by E_1 symmetric strain.

The cooling process begins by resonantly pumping the $|A\rangle \rightarrow |E_y\rangle$ transition, as shown in fig. 7.1 c. Population in $|E_y\rangle$ will be transferred to $|E_x\rangle$ through the absorption of a single phonon from the mechanical oscillator. Just as the case with sideband cooling, spontaneous emission (this time from $|E_x\rangle$) carries away entropy from the system and returns the NV center to the ground state. Using the same master equation approach, we obtain the same rate equation determining $\langle a^\dagger a\rangle$, with a resonant cooling rate given by

$$\Gamma_c = \frac{4g_{n\perp}^2\Omega^2}{\Gamma^3} \tag{7.32}$$

In contrast with the sideband cooling protocol, the resonant cooling rate does not depend on the phonon frequency. This gives more flexibility in cooling, and opens the door to cooling other mechanical modes, such as compressional modes. We note that the resonant cooling protocol is optimized when the optical transition is saturated, $\Omega = \Gamma$, which would result in a cooling rate $\Gamma_c = \frac{4g_{n\perp}^2}{\Gamma}$. To further optimize the cooling process, the resonant cooling can be combined with the sideband cooling protocol. Instead of resonantly driving the E_y transition, the red sideband can be addressed, potentially removing two phonons from the mechanical oscillator in each optical cycle.

7.1.5 Experimental calculations for resonant cooling

In the calculations that follow, we will consider the same experimental conditions described for the sideband cooling calculations. Due to the magnitudes of the strain coupling parameters, it is advantageous to utilize the E_1 symmetric strain interaction for the resonant cooling protocol. Therefore, the splitting between $|E_x\rangle$ and $|E_y\rangle$ will be set by a DC electric field applied along the y direction of the NV center. Therefore,

n	$\omega_m/2\pi$	$g_\perp$	Γ_c	$\bar{n}_i$	$\bar{n}_f$
1	228 MHz	10.1 MHz	2.8 MHz	367.0	2.99
2	627 MHz	16.8 MHz	7.7 MHz	133.0	1.08
3	1.23 GHz	23.5 MHz	15.1 MHz	67.5	0.55
4	2.03 GHz	30.3 MHz	25.0 MHz	40.6	0.33

Table 7.3: **Experimental estimates for resonant cooling**. Calculated resonant cooling rates for a diamond nanobeam with a bath temperature $T = 4$ K, an optical Rabi frequency Ω=100 MHz, mechanical $Q = 10^4$, and an inhomogeneously broadened transition linewidth $\Gamma_\phi = 100$ MHz.

the single phonon coupling is given by $g_{n\perp} = \lambda_E(1+\nu)\epsilon_n = (950\text{ THz})\epsilon_n$. Calculated resonant cooling rates are shown in table 7.3.

If we again assume a clamping loss limited Q, then every mode of the beam can be prepared in the quantum ground state. From these calculations, it is clear that the resonant cooling protocol is a more efficient and power cooling method.

7.1.6 Fluorescence thermometry

The temperature of the mechanical mode under resonant cooling can be directly probed by measuring the fluorescence level of the NV center. For a mechanical resonator in a thermal state, the probability in time to make a transition from $|E_y\rangle$ to $|E_x\rangle$ is given by an incoherent sum over all Fock states

$$P(t) = \sum_{n=0}^{\infty} \frac{1}{1+\bar{n}} \left(\frac{\bar{n}}{1+\bar{n}}\right)^n \sin^2\left(g_\perp \sqrt{n} t/2\right) \tag{7.33}$$

As the resonator is cooled and $\bar{n}$ decreases, the probability to make a transition to $|E_x\rangle$ also decreases. Therefore, the population in $|E_x\rangle$ gives a direct measure of the resonator temperature. The population in $|E_x\rangle$ will determine the flux of $\hat{y}$-polarized photons emitted from the NV center. The scattering rate of $\hat{y}$ polarized photons can be calculated by solving the master equation, as described in ref. [169]. If the E_y transition

is driven on resonance, the scattering rate is approximately given by

$$\mathcal{I}_y \approx \frac{4g_\perp^2 \Omega^2}{\Gamma^3}\langle a^\dagger a\rangle \tag{7.34}$$

Because the E_y transition is driven by $\hat{x}$ polarized light, this signal should have a high signal to noise ratio, and is only limited by the polarization optics.

7.2 Generating non-Gaussian mechanical states

Generation of non-Gaussian mechanical states can be accomplished through a swapping interaction between the NV center and a mechanical resonator prepared in the quantum ground state [205]. As a simple example, we describe the preparation of a single phonon Fock state. Consider an NV center that is parametrically coupled to a nanomechanical resonator in its ground state through the A_1 strain interaction. The initial wavefunction of the system can be written as $|g\rangle\,|0\rangle$. If we apply a laser pulse resonant with the first blue sideband of the optical transition, we create an anti-Jaynes-Cummings interaction, $H = \frac{\eta\Omega}{2}(\sigma^+ a^\dagger + \sigma^- a)$, and the system evolves into the fully separable state, $|e\rangle\,|1\rangle$, where the mechanical oscillator is in a single phonon Fock state. More complex mechanical states can be generated by through further coherent interactions with the NV center or through dissipative reservoir engineering [206].

7.3 Phonon-mediated spin-spin entanglement

An outstanding challenge in quantum information science is generating controlled interactions between multiple qubits. In the case of the NV center, multipartite entanglement has been accomplished through dipole-dipole interactions [207] and quantum interference of photons [150, 30]. However, there are a few important drawbacks of each

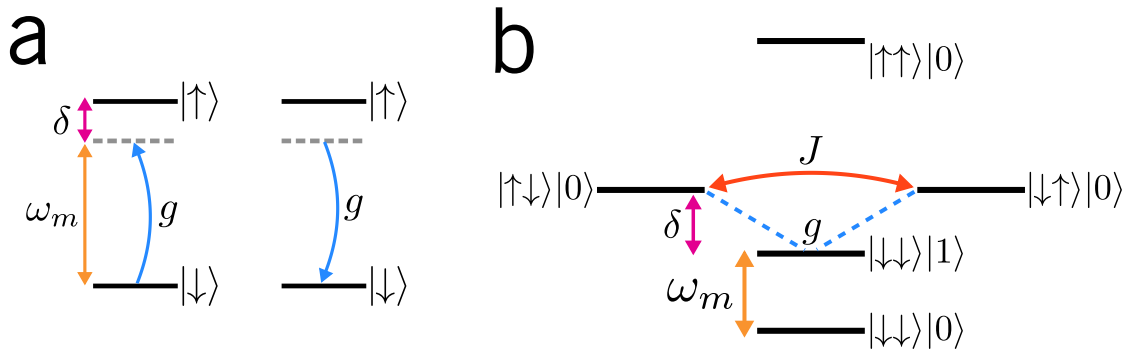

Figure 7.4: **Phonon-mediated spin-spin entanglement**. a) Two NV spins are off-resonantly coupled to the mechanical oscillator, resulting in an effective spin-spin interaction. b) Collective energy diagram of the two spins and mechanical oscillator. An effective coupling J between states of a single electronic excitation, $|\uparrow\downarrow\rangle|0\rangle$ and $|\uparrow\downarrow\rangle|0\rangle$, arises through virtual coupling to the $|\downarrow\downarrow\rangle|1\rangle$ state. Therefore, entanglement arises through a virtual exchange of phonons.

of these techniques. For instance, the dipolar interaction between two NVs separated by a distance d scales as d^{-3}. For NV centers even with long spin coherence times, this limits the maximum NV-NV separation to a few tens of nanometers. With current technologies, it is not feasible to controllably place NV centers within such a small volume. Therefore, this entanglement scheme is poorly suited for scalability. On the other hand, photon-mediated entanglement has been used to entangle NV centers that are separated by over 1 km with high fidelity [30]. However, the entanglement is based on a heralded detection scheme, and the entanglement rate is typically very slow (on the order of mHz). Moreover, photon-mediated entanglement relies on quantum interference of single photons emitted by each NV center, which requires indistinguishable photons [150, 30, 95, 94, 31]. More generally, generating photon-mediated interactions between qubit systems of varying energy scales is exceedingly difficult.

Phonon-mediated interactions offer a promising alternative to these existing schemes by allowing for deterministic, long-range interactions between NV centers. In this section, we will give a brief review of an entanglement protocol based on dispersive, spin-phonon

interactions, as shown in fig. 7.4 a. In the dispersive regime, spin-spin entanglement is achieved through a virtual exchange of phonons [39]. This entanglement protocol is quite general, and can be realized in a variety of ways with the NV center [39, 42, 208, 209, 210, 211, 212, 25]. For illustrative purposes, we consider entanglement between two NV spins that are strain-coupled to a nanomechanical resonator through the E symmetric spin-strain interaction. The Hamiltonian describing the hybrid system in the rotating wave approximation is given by

$$H = \sum_{j=1}^{2} \left[\omega_j \sigma_j^+ \sigma_k^- + g_j(\sigma_j^+ a + \sigma_j^- a^\dagger)\right] + \omega_m a^\dagger a \tag{7.35}$$

where ω_j is the frequency of the j^{th} qubit, $\sigma_l^\pm$ are the qubit raising and lowering operators, g_j is the single phonon coupling, and a is the phonon annihilation operator for a phonon with frequency ω_m. We want to operate in the dispersive regime, where the qubits are far detuned from the mechanical resonator, $\delta_j = \omega_j - \omega_m \gg g_j$. In this regime, we only virtually excite phonons in the mechanical resonator. Furthermore, we can remove the direct spin-phonon interaction and obtain an effective spin-spin interaction by moving into the interaction picture with respect the qubit and resonator and applying a unitary transformation defined by

$$U = \exp\left[\sum_{j=1}^{2} \frac{g_j}{\delta_j}(\sigma_j^+ a - \sigma_j^- a^\dagger)\right] \tag{7.36}$$

The transformed Hamiltonian can be obtained by performing the following expansion

$$e^{\alpha A} B e^{-\alpha A} = B + \alpha[A, B] + \frac{\alpha^2}{2!}[A, [A, B]] + \cdots \tag{7.37}$$

Carrying out the transformation to second order in (g_j/δ_j), we obtain the effective

spin-spin interaction Hamiltonian

$$H_{eff} = \sum_j \left(\frac{\delta_j}{2} + \frac{g_j^2}{\delta_j}(1 + a^\dagger a) \right) \sigma_j^z + \frac{g_1 g_2 (\delta_1 + \delta_2)}{2\delta_1 \delta_2} (\sigma_1^+ \sigma_2^- + \sigma_1^- \sigma_2^+) \tag{7.38}$$

In the first term, we see an effective AC Stark shift of each qubit due to the dispersive interaction. The second term contains the effective spin flip-flop interaction with a rate $J = \frac{g_1 g_2 (\delta_1 + \delta_2)}{2\delta_1 \delta_2}$. By choosing the appropriate gate time, $t_g = \pi/J$, this interaction can generate a two-qubit entangled state. In particular, if both qubits are prepared in an eigenstate of σ_x, then the system will evolve into the two-qubit entangled state, $|\Psi^+\rangle = \frac{1}{\sqrt{2}}(|\uparrow\downarrow\rangle + |\downarrow\uparrow\rangle)$. As mentioned, this entanglement is mediated by a virtual exchange of phonons. To understand this process, consider the dynamics of the total system, shown in fig. 7.4 b. For simplicity, we consider a mechanical oscillator in the ground state of motion, but note that the same reasoning can be applied to an oscillator in a thermal state. In the proposed experiment, the qubits are prepared in a joint state consisting of a single qubit excitation and no phonons, such as $|\uparrow\downarrow\rangle |0\rangle$. The dispersive spin-phonon interaction virtually couples the system to a state where a qubit excitation is exchanged for a single phonon excitation, $|\downarrow\downarrow\rangle |1\rangle$. In essence, by virtually exchanging phonons through the intermediate state $|\downarrow\downarrow\rangle |1\rangle$, the qubits can exchange single electronic excitations. This results in the spin flip-flop interaction shown in the above Hamiltonian.

Although this example was given for a resonator in the ground state, entanglement can still occur even when the resonator is in a thermal state. However, the fidelity is lowered due to the phonon number fluctuations, which enter the Hamiltonian through the effective AC Stark shift. Generating entanglement requires $C = \frac{g^2}{\Gamma_2 \gamma} > 1$, where Γ_2 is the spin dephasing rate and γ is the thermalization rate of the resonator [39]. Therefore, there exists a maximum resonator mode temperature which can accommodate entanglement.

It is important to note that there are a few important drawbacks of this entanglement

scheme. One drawback of the dispersive regime is that the spin-spin coupling J is usually small and hence the gate time t_g can be very long. An obvious solution to speeding up the entanglement rate is to increase the ratio g_j/δ_j. However, as g_j/δ_j increases, the probability to populate the resonator with real phonons becomes significant, and the spins can become entangled with the resonator. Any residual entanglement with the resonator at the end of the gate will result in a reduced fidelity [213, 214]. Nonetheless, it is possible to achieve high fidelity entanglement by keeping track of the resonator in phase space. In particular, the spin and resonator are completely disentangled after the resonator has traversed a closed loop in phase space. The geometric phase acquired is directly imprinted on the two-qubit entangled state [213]. Furthermore, with the use of passive error correction and ground state cooling, the residual entanglement with the resonator can be minimized [25, 215].

Another important drawback of the dispersive coupling scheme is that it requires the ability to turn the coupling off and on at will, which can be difficult to achieve, especially with the E symmetric strain coupling which is intrinsic to the NV center. There are two possible ways to control the dispersive coupling. The first is to generate a large AC Stark shift to bring the qubits out of resonance with each other, which will suppress the spin-spin interaction [214]. In practice, this could be accomplished with individual addressing lasers. The second way is to search for a spin-phonon interaction that is assisted by an external control field. One promising technique that can be used to generate such an interaction is stimulated Raman transitions, which we discuss in detail in the next section.

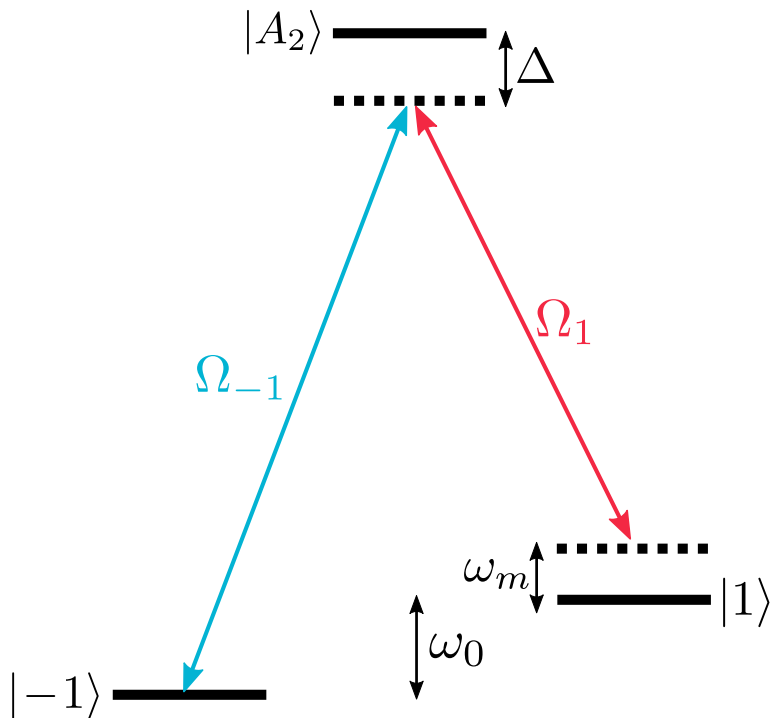

Figure 7.5: **Spin-phonon interactions via stimulated Raman transitions**. Stimulated Raman transitions between $|\pm 1\rangle$ via virtual coupling to the red sideband of the A_2 transition allow for an effective spin-phonon interaction.

7.3.1 Phonon-assisted Raman transitions

In this thesis, we have established that the spin of the NV center is an excellent quantum memory with extended coherence times. However, the spin of the NV center is relatively insensitive to strain, leading to small single phonon couplings. On the other hand, the orbital states of the NV center are highly sensitive to strain, but are poor qubits due to their short coherence times. Ideally, one would be able to combine the coherence of the spin levels with the strain sensitivity of the orbital states. A promising way to achieve this is through stimulated Raman transitions [208, 216]. The use of Raman transitions has the added benefit in that the effective spin-phonon interaction can be turned on and off at will.

A schematic showing the proposed Raman transition can be found in fig. 7.5. We

consider a Λ-system composed of two ground state spin levels, $\{|1\rangle, |-1\rangle\}$ separated by ω_0 and a single excited state level $|A_2\rangle$. The NV is addressed by two laser beams addressing the $|\pm 1\rangle \rightarrow |A_2\rangle$ transitions at frequencies of ω_{-1} and ω_1. The beams are $\sigma^{\pm}$ polarized and generate single-photon Rabi frequencies Ω_{-1} and Ω_1. Moreover, each beam has a controllable phase ϕ_{-1} and ϕ_1.

The NV center is parametrically coupled to a mechanical resonator of frequency ω_m through the A_1-symmetric strain-orbit interaction with a single phonon coupling strength g. Furthermore, we will work in the resolved sideband regime where the phonon frequency greatly exceeds the optical transition linewidths. The reason for this is subtle, but can be explained by the fact that the Lamb-Dicke parameters for the $|\pm 1\rangle \rightarrow |A_2\rangle$ transitions are the same, which means there is no net transfer of quanta between the two-level system and the resonator during a standard Raman transition. However, if we are in the resolved sideband regime, we can perform a Raman transition on a phonon sideband of the excited state. This will allow for an effective spin-phonon coupling.

Consider a Λ system consisting of two ground state levels $\{|-1\rangle, |1\rangle\}$ separated by ω_0 and a single excited state level $|A_2\rangle$. The Hamiltonian for the system including the resonator and the two laser beams can be written as

$$\begin{aligned} H_0 = \omega_0 |1\rangle\langle 1| + \omega_A |A_2\rangle\langle A_2| + \omega_m a^\dagger a + g(a + a^\dagger)|A_2\rangle\langle A_2| \\ - \Omega_{-1}\cos(\omega_{-1}t + \phi_{-1})\left(|A_2\rangle\langle -1| + |-1\rangle\langle A_2|\right) \\ - \Omega_1 \cos\left(\omega_1 t + \phi_1\right)\left(|A_2\rangle\langle 1| + |1\rangle\langle A_2|\right) \end{aligned} \tag{7.39}$$

We move into a rotating frame at the laser frequency ω_{-1} via $U_1 = e^{i\omega_{-1}t|A_2\rangle\langle A_2|}$, and

make a rotating wave approximation (RWA) on the optical frequencies.

$$\begin{aligned} H_1 = &\omega_0 |1\rangle\langle 1| + \Delta |A_2\rangle\langle A_2| + \omega_m a^\dagger a + g(a+a^\dagger)|A_2\rangle\langle A_2| \\ &- \frac{\Omega_{-1}}{2}\left(e^{i\phi_{-1}}|A_2\rangle\langle -1| + e^{-i\phi_{-1}}|-1\rangle\langle A_2|\right) \\ &- \frac{\Omega_1}{2}\left[e^{i(\omega_{-1}-\omega_1)t}e^{i\phi_1}|A_2\rangle\langle 1| + e^{-i(\omega_{-1}-\omega_1)t}e^{-i\phi_1}|1\rangle\langle A_2|\right] \end{aligned} \tag{7.40}$$

We next move into the displaced oscillator basis via the Polaron transformation, $U_2 = e^{\eta(a^\dagger - a)}$, where we have defined the Lamb-Dicke parameter $\eta = g/\omega_m$.

$$\begin{aligned} H_2 = &\omega_0 |1\rangle\langle 1| + \Delta |A_2\rangle\langle A_2| + \omega_m a^\dagger a \\ &- \frac{\Omega_{-1}}{2}\left[e^{\eta(a^\dagger - a)}e^{i\phi_{-1}}|A_2\rangle\langle -1| + e^{-\eta(a^\dagger - a)}e^{-i\phi_{-1}}|-1\rangle\langle A_2|\right] \\ &- \frac{\Omega_1}{2}\left[e^{i(\omega_{-1}-\omega_1)t}e^{\eta(a^\dagger - a)}e^{i\phi_1}|A_2\rangle\langle 1| + e^{-i(\omega_{-1}-\omega_1)t}e^{-\eta(a^\dagger - a)}e^{-i\phi_1}|1\rangle\langle A_2|\right] \end{aligned} \tag{7.41}$$

To simplify the Hamiltonian, we move into the interaction picture with respect to $\omega_0 |1\rangle\langle 1| + \omega_m a^\dagger a$. The Raman resonance condition occurs when the two-photon beatnote, $\omega_{-1} - \omega_1 \sim \omega_0$. Therefore, we assume a near-resonance condition and define the Raman beatnote, $\omega_{-1} - \omega_1 = \delta - \omega_0$.

$$\begin{aligned} H_3 = &\Delta |A_2\rangle\langle A_2| - \frac{\Omega_{-1}}{2}\left[e^{\eta(a^\dagger e^{i\omega_m t} - a e^{-i\omega_m t})}e^{i\phi_{-1}}|A_2\rangle\langle -1| + h.c.\right] \\ &- \frac{\Omega_1}{2}\left[e^{i(\delta t + \phi_1)}e^{\eta(a^\dagger e^{i\omega_m t} - a e^{-i\omega_m t})}|A_2\rangle\langle 1| + h.c.\right] \end{aligned} \tag{7.42}$$

To proceed, we work in the Lamb-Dicke limit and assume that the Raman beams are parked in between the carrier and red sideband such that $\delta = \omega_m + \delta_L$. Keeping terms

to first order in η, we obtain

$$H_4 = \Delta \left|A_2\right\rangle \left\langle A_2\right| - \frac{\Omega_{-1}}{2}\left[\left|A_2\right\rangle \left\langle -1\right| e^{i\phi_{-1}} + h.c.\right] - \frac{\eta\Omega_1}{2}\left[e^{i(\delta_L t+\phi_1)}\left|A_2\right\rangle \left\langle 1\right| \hat{a} + h.c.\right] \quad (7.43)$$

If the overall detuning Δ is large compared to the single photon Rabi frequencies, we can adiabatically eliminate the excited state level and work in the two-level subspace spanned by the ground state spin levels. To this end, we solve the time dependent Schrödinger equation and assume a generic wavefunction $\left|\psi\right\rangle = \alpha\left|-1\right\rangle + \beta\left|1\right\rangle + \gamma\left|A_2\right\rangle$.

$$\begin{aligned} i\dot{\alpha} &= -\frac{\Omega_{-1}}{2}e^{-i\phi_{-1}}\gamma \\ i\dot{\beta} &= -\frac{\eta\Omega_1}{2}e^{-i(\delta_L t+\phi_1)}\hat{a}^\dagger\gamma \\ i\dot{\gamma} &= \Delta\gamma - \frac{\Omega_{-1}}{2}e^{i\phi_{-1}}\alpha - \frac{\eta\Omega_1}{2}e^{i(\delta_l t+\phi_1)}\hat{a}\beta \end{aligned} \quad (7.44)$$

Under adiabatic elimination, $\dot{\gamma} = 0$ and $\gamma = \frac{\Omega_{-1}}{2\Delta}\alpha_n e^{i\phi_{-1}} + \frac{\eta\Omega_1}{2\Delta}e^{i(\delta_L t+\phi_1)}\hat{a}\beta$. Substituting the definition of γ into the Schrödinger equation leads to the following

$$\begin{aligned} i\dot{\alpha} &= -\frac{\Omega_{-1}^2}{4\Delta}\alpha - \frac{\eta\Omega_{-1}\Omega_1}{4\Delta}\hat{a}\beta e^{i(\delta_L t+\Delta\phi)} \\ i\dot{\beta} &= -\frac{\eta\Omega_{-1}\Omega_1}{4\Delta}\hat{a}^\dagger\alpha e^{-i(\delta_L t+\Delta\phi)} - \frac{\eta^2\Omega_1^2}{4\Delta}\hat{a}^\dagger\hat{a}\beta \end{aligned} \quad (7.45)$$

where we have defined $\Delta\phi = \phi_1 - \phi_{-1}$. Assuming a perfect Raman resonance, $\delta_L = 0$, and setting the $\Delta\phi = 0$, we obtain an effective spin-phonon interaction

$$H = \frac{\eta\Omega_1\Omega_{-1}}{4\Delta}\left(\sigma^+ a + \sigma^- a^\dagger\right) \quad (7.46)$$

Note that this interaction is accompanied by a differential AC Stark shift of the qubits given by $\delta f = \frac{\Omega_{-1}^2}{4\Delta} + \frac{\eta^2\Omega_1^2}{4\Delta}a^\dagger a$. In addition, there is an additional decay channel introduced by spontaneous emission, which scrambles the coherence of the spin levels. Although we adiabatically eliminated the excited state, there is still a small probability to populate the level, and hence the spontaneous emission rate is approximately given by $\Gamma_{eff} = \Gamma\frac{\Omega^2}{\Delta^2}$. As expected, the spontaneous emission decreases as the detuning from the excited state increases.

To benchmark the Raman technique, we compare the effective spin-phonon coupling to the spontaneous emission rate, $\mathcal{C} = \frac{g\Delta}{\omega_m\Gamma}$. The spin can coherently exchange quanta with the mechanical resonator in the limit that $\mathcal{C} > 1$. The further the detuning from the excited state, the better the ratio of the coupling to the decoherence rate. In practice, however, there is a fundamental limit to the detuning, since we require the Raman beams to be tuned in between the carrier and red sideband. Therefore, we typically find $\mathcal{C} = \kappa\frac{g}{\Gamma}$ where $0 < \kappa < 1$. In other words, the Raman Rabi frequency will almost always be slow compared to the decoherence rate [216]. However, it may be possible to overcome this limit using shortcut-to-adiabaticity protocols that have been recently developed. In particular, there has been an experimental demonstration such a protocol in which the addition of a single control field dramatically speeds up Raman transitions while maintaining the high fidelity state transfer of adiabatic protocols [217].

7.4 NV centers coupled to a chiral phonon waveguide

In this section, we will show coupling to a chiral phonon waveguide can generate steady-state entanglement between two NV centers [218, 219]. Consider a chiral phonon

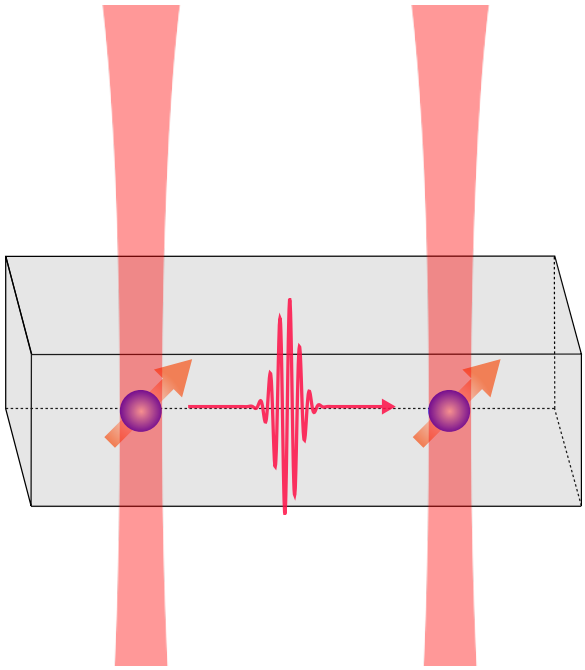

Figure 7.6: **Steady-state entanglement using chiral phonons**. Two NV centers embedded in a chiral phonon waveguide are individually addressed with Raman beams. Emission of a single chiral phonon by an NV center into the waveguide is absorbed by another NV center, producing an two-qubit entangled state.

waveguide that interacts with two embedded NV centers separated by a distance d via the E symmetric spin-phonon interaction. Each spin will be addressed by Raman beams with equal and opposite two-photon detunings δ, equal Rabi frequency Ω, and a relative phase ψ. The spin is resonantly coupled to the phonon waveguide, and hence the phonon emission rate Γ is given by $\Gamma = 2\frac{g^2}{\gamma}$ where γ is the dissipation rate of the phonon mode. If phonons are traveling to the right and NV 1 sits to the left of NV 2, a phonon emitted by NV 1 into the waveguide will be absorbed by NV 2, but a phonon emitted by NV 2 will not interact with NV 1. In this case, NV 1 does not feel the presence of NV 2. The reverse is true for left propagating phonons. The non-unitary Hamiltonian governing this

experiment in the rotating frame of the qubits is

$$H = -\delta\sigma_1^+\sigma_1^- + \delta\sigma_2^+\sigma_-^2 - \frac{\Omega}{2}\left(\sigma_1^+ + e^{-i\psi}\sigma_2^+ + \sigma_1^- + e^{i\psi}\sigma_2^-\right) - i\frac{\gamma}{2}(e^{i\phi}\sigma_1^+\sigma_2^- - e^{-i\phi}\sigma_1^-\sigma_2^+) \tag{7.47}$$

where $\phi = \frac{\omega_m d}{c_s}$ is a path-length dependent phase and c_s is the speed of sound. The first two terms are from the Raman beams driving the two NVs and the second term is an anti-symmetric flip-flop interaction stemming from phonon emission. Because phonon emission is a dissipative process, this term in the Hamiltonian is imaginary. The chirality of the phonons is captured in the antisymmetric nature of the flip-flop interaction. To generate entanglement, we must satisfy commensurability, and hence we set $\psi = \phi$, which can be done easily by adjusting the phase of the Raman beams.

This Hamiltonian produces a dark entangled state that is decoupled from the phonon waveguide [219]. By diagonalization it can be shown that this dark state is

$$|D\rangle = \frac{1}{\sqrt{1+|\alpha|^2}}|\downarrow\downarrow\rangle + \frac{\alpha}{\sqrt{2}}(|\uparrow\downarrow\rangle - |\downarrow\uparrow\rangle) \tag{7.48}$$

where $\alpha = -\sqrt{2}\frac{\Omega}{i\Gamma+2\delta}$

7.5 Nonreciprocal phonon transport with an NV center

Consider an NV embedded in a phonon waveguide that can couple to Lamb waves [220] via the E symmetric spin-phonon interaction. The chirality of the Lamb wave can be defined by a 90° relative phase between the uniaxial and shear strain terms of the strain tensor. For instance, consider the strain imparted by left or right-handed Lamb

waves in the NV coordinate system,

$$\begin{aligned}\epsilon_R &= \begin{pmatrix} \varepsilon_{xx} & i\varepsilon_{xy} & 0 \\ i\varepsilon_{xy} & -\epsilon_{xx} & 0 \\ 0 & 0 & 0 \end{pmatrix}(a + a^\dagger) \\ \epsilon_L &= \begin{pmatrix} \varepsilon_{xx} & -i\varepsilon_{xy} & 0 \\ -i\varepsilon_{xy} & -\epsilon_{xx} & 0 \\ 0 & 0 & 0 \end{pmatrix}(a + a^\dagger)\end{aligned} \tag{7.49}$$

where we have quantized the strain field and ε_{ij} refers to the strain induced by the zero-point motion of the Lamb wave. Recall that the E symmetric spin-strain interaction can be written as

$$H = -\frac{V_{E_1}}{2}(S_+^2 + S_-^2) + \frac{V_{E_2}}{2i}(S_+^2 - S_-^2) \tag{7.50}$$

$$= -\frac{1}{2}\left[(V_{E_1} + iV_{E_2})S_+^2 + (V_{E_1} - iV_{E_2})S_-^2\right] \tag{7.51}$$

where we have defined

$$V_{E_1} = \lambda_E(\epsilon_{yy} - \epsilon_{xx}) + \lambda_{E'}(\epsilon_{xz} + \epsilon_{zx}) \tag{7.52}$$

$$V_{E_2} = \lambda_E(\epsilon_{xy} + \epsilon_{yx}) + \lambda_{E'}\epsilon_{yz} + \epsilon_{zy}) \tag{7.53}$$

The interaction with a right-handed/left-handed Lamb wave in the $|\pm 1\rangle$ basis can be

written as

$$\begin{aligned} H_R &= g_{xx}(a + a^\dagger)(\sigma^+ + \sigma^-) - g_{xy}(a + a^\dagger)(\sigma^+ - \sigma^-) \\ H_L &= g_{xx}(a + a^\dagger)(\sigma^+ + \sigma^-) + g_{xy}(a + a^\dagger)(\sigma^+ - \sigma^-) \end{aligned} \tag{7.54}$$

where $g_{xx} = 2\lambda_E \varepsilon_{xx}$ and $g_{xy} = 2\lambda_E \varepsilon_{xy}$. In the rotating wave approximation, we have the following

$$\begin{aligned} H_R &= (g_{xx} - g_{xy})\sigma^+ a + (g_{xx} + g_{xy})\sigma^- a^\dagger \\ H_L &= (g_{xx} + g_{xy})\sigma^+ a + (g_{xx} - g_{xy})\sigma^- a^\dagger \end{aligned} \tag{7.55}$$

Clearly, we have a nonreciprocal interaction between the NV center and the Lamb waves. For simplicity, we assume that $g_{xx}, g_{xy} > 0$. If an NV center is prepared in $|\downarrow\rangle$, it will preferentially absorb a left-handed Lamb wave. If an NV center is prepared in $|\uparrow\rangle$, it will preferentially emit a right-handed Lamb wave. A perfectly chiral interaction would be achieved if the sum or difference between the two couplings were 0. This could be achieved by placing the NV center in a particular region of the phonon waveguide. Alternatively, a chiral interaction could be achieved utilizing the full three-level nature of the spin ground state by spin locking. If resonant microwaves were used to drive the system into the xy plane of the Bloch sphere, then one could generate an inverted Λ system where each dipole transition is driven by a phonon of a particular chirality.

Chapter 8

Toward spin-phonon interactions in the quantum regime

"The lord giveth and the lord taketh away"

- Anonymous

In this chapter, we will evaluate the prospects and challenges for future hybrid mechanical devices utilizing the NV center. In particular, we will discuss the challenges of reaching the high cooperativity regime and discuss realistic architectures for new devices that can realize quantum coherent interactions between the NV center and a mechanical oscillator. In addition, we will discuss some preliminary data showing optical and mechanical resonances of diamond optomechanical crystals, as well as spectroscopy data characterizing the NV centers inside of these structures.

8.1 Limitations of current devices

To evaluate the limitations of current devices, we will evaluate all of the parameters that can affect the single phonon cooperativity. The single phonon cooperativity pa-

rameter can be written in a more useful way that is explicit in terms of experimentally relevant parameters.

$$C = \frac{2\pi g^2 Q T_2}{\bar{n}\omega_m} \sim \frac{h g^2 Q T_2}{k_B T} \tag{8.1}$$

The recipe for residing in the high cooperativity regime is quite clear: increase the single phonon coupling g, increase the mechanical quality factor Q, reduce the system temperature T, and increase the coherence time of the NV center, T_2. However, given current experimental limitations, it is difficult to achieve all of these tasks simultaneously. In the devices used throughout this thesis, the coupling strengths are limited by the strain induced by the zero point motion of the cantilevers, which scales inversely with the dimensions of the resonator [76, 77, 82]. In addition, strain is maximized at the surface of the cantilever. Therefore, increasing the coupling in these types of architectures will necessarily require bringing the NV center near diamond surfaces. Unfortunately, the spin coherence and optical properties of the NV center are significantly degraded when brought into close proximity of the diamond surface [131, 193, 221, 222, 140]. In the case of the spin coherence, it appears that a combination of magnetic field noise from a a bath of surface electronic spins and electric field noise, possibly from surface dipoles, significantly limit the spin coherence for NV centers within 25 nm of the diamond surface [131, 139, 193]. On other hand, the optical transitions are subject to significant spectral diffusion due to a combination of low frequency electric field noise and NV charge state fluctuations, resulting in optical linewidths of several tens of GHz. In the devices presented throughout this thesis, the NV centers were approximately 50 nm from the surface and had Hahn echo T_2 times of approximately 40 μs and optical linewidths of approximately 1 GHz. Therefore, the high cooperativity regime will require an improvement in both the spin coherence properties.

To date, the longest spin coherence times recorded for NV centers have been for NVs located deep in bulk diamond samples. Under ambient conditions, the longest T_2 time ever recorded is on the order of milliseconds [88]. At liquid nitrogen temperatures, T_2 times on the order of 500 ms were observed [138], and required many refocusing, spin-echo pulses. In addition, narrow optical linewidths of $\Gamma = 17$ MHz were observed in a single spectroscopic measurement on an NV center in a diamond nanocrystal [223]. These linewidths are close to the lifetime limited linewidth, $\Gamma = 13$ MHz, that was observed for NVs in a bulk diamond sample [224]. These results suggest that mitigating surface noise should allow for millisecond spin coherence times and optical linewidths of tens of MHz [145, 146, 225, 223, 113].

Correspondingly, a significant effort in the diamond community is being made to address surface-induced spin decoherence and spectral diffusion through a variety of techniques, including surface passivation [226], downstream etching [227], high temperature annealing[184], and alternative NV formation techniques [228, 97, 229, 230, 231].

NV centers naturally occur in diamond, but can be artificially introduced through nitrogen ion implantation, which is the most common approach taken to introduce NV centers. In general, the spin coherence properties of these implanted NV centers are inferior to naturally occurring NV centers. This degradation in spin coherence is attributed to lattice damage introduced during the implantation process, poor nitrogen to NV center conversion efficiencies, and plasma-induced damage during etching [227]. In 2012, two groups [97, 228] introduced a nitrogen delta-doping technique to form NV centers that is inherently gentler than ion implantation and mitigates lattice damage. In this method, nitrogen gas is introduced during CVD growth of diamond for a short amount of time, introducing a nitrogen-rich layer into the diamond sample. The sample can then be electron irradiated to create vacancies and annealed to create NV centers. This process has been successful in creating shallow NV centers with long coherence times, with an

observed $T_2 > 200$ μs for a 20 nm deep NV center [229] and an observed $T_2 > 100$ μs for a 5 nm deep NV center [97].

Spectral diffusion in the optical transitions has been mostly attributed to lattice damage, in particular, divacancy defects in the diamond. To overcome lattice damage, the diamond sample can be annealed at high temperatures (1200°C). At these temperatures, vacancy clusters can move to the surface and be annealed away, essentially repairing the diamond lattice. This technique was shown to produce narrow optical lines in an implanted diamond sample [184], with the best observed linewidth of $\Gamma = 27$ MHz. Moreover, this technique was used to improve the spin coherence times of implanted NV centers and stabilize the NV charge state [232]. These materials science approaches are promising for engineering shallow NV centers with excellent coherence and optical properties.

In terms of the mechanics, single-crystal diamond should in principle be an excellent substrate material for high quality factor mechanical resonators due to its low intrinsic losses. Indeed, mechanical quality factors exceeding one million have already been demonstrated in SCD cantilevers at cryogenic temperatures [44]. However, as the mechanical frequency increases to improve the single phonon couplings, the quality factor correspondingly decreases while the so called $Q \cdot f$ product remains roughly constant. The reduction in quality factor can be attributed to a number of sources, including two-level defects, surface chemistries, surface roughness,and clamping losses[44, 43, 45]. However, achieving high Q diamond mechanical oscillators with high frequencies is not an impossible task. For instance, the clamped beams that are typically used in our experiments can be designed to avoid clamping losses [164], and with the continual improvements and advancements in diamond processing, these devices could operate in the high cooperativity regime. In addition, a phononic shield placed around the device could also significantly improve the quality factor [61].

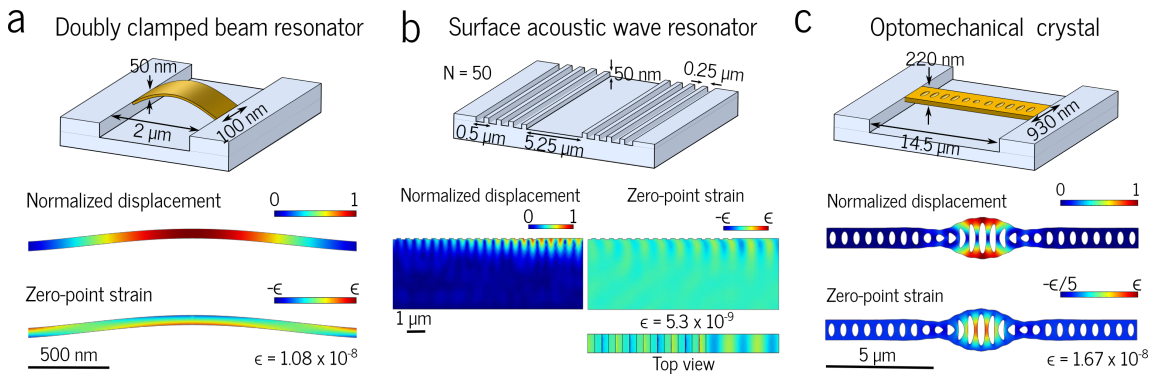

Figure 8.1: **Example devices with potential to operate in the high cooperativity regime**. a) A doubly-clamped nanobeam with dimensions 2 μm×100 nm×50 nm and $\omega_m/2\pi = 230$ MHz. b) SAW cavity with a confined phonon mode $\omega_m \sim 10$ GHz defined by the grating pitch and the speed of sound of diamond. c) Optomechanical crystal with dimensions 14.5 $\mu m \times$ 930 nm× 220 nm and a localized, mechanical breathing mode with $\omega_m/2\pi \sim$6 GHz. For each device, simulations of the mode displacement and zero point strain are displayed underneath the device schematic. These are calculated with finite element simulations.

8.2 Architectures for future devices

The challenge of increasing g while mitigating dissipation and decoherence may be overcome by choosing new types of architectures for hybrid NV-mechanical devices. In particular, diamond optomechanical crystals and surface acoustic wave cavities currently stand out as promising avenues for reaching the high cooperativity regime. SAW cavities have already been used to generate GHz frequency phonon modes in other substrate materials with high quality factors approaching one million at low temperatures [233, 234, 235], and more importantly, they have been demonstrated in the quantum regime [236, 237, 235]. Furthermore, SAW phonons propagate approximately one acoustic wavelength into the surface of the elastic material. Because diamond has a high speed of sound, GHz frequency phonons would propagate several microns into the diamond. This would allow the use of naturally occurring, deep NV centers, which have exhibited the best coherence and optical properties to date. We note that ref. [79] has already utilized this benefit in experiments to use SAWs to perform optomechanical control of naturally

occurring NV centers. However, because there was no cavity element in the device, it cannot be extended to the quantum regime of coupling. SAW cavities in principle should also increase the coupling strength. Finite element simulations performed in COMSOL (see fig.8.1b.) reveal that for a SAW cavity device supporting a 10 GHz phonon mode, $g_{A_1} = 10$ MHz can be achieved. Assuming a reasonable $Q = 10^5$ and optical linewidth $\Gamma = 100$ MHz, it should be possible to enter the high cooperativity regime with the orbital states of the NV center.

Optomechanical crystal devices provide a promising platform for NV-mechanical experiments due to their potential to generate high single phonon couplings, isolate the NV center from surface noise, and mitigate clamping losses. Optomechanical crystals (OMCs) are structures that support both optical and mechanical resonances. Importantly, the optical and mechanical modes can be localized to a small volume through bandgap engineering. The optomechanical crystal supports a quasi-phononic and quasi-photonic bandgap wherein lie the optical and mechanical modes of the crystal. In addition, the optical and mechanical modes are localized to the same volume, known as the defect region of the OMC, which allows for a mutual coupling between phonons and photons. For instance, a mechanical vibration will deform the crystal, and hence modifies the effective optical cavity length [238]. This "optomechanical" coupling allows for radiation pressure forces to actuate the mechanical mode. The partial phononic bandgap of the OMC prevents phonons of the mode of interest from tunneling out of the mechanical structure, improving the Q [61].

In general, this bandgap can be designed to increase the Q of a high frequency mechanical mode whose strain profile is constant through the cross section of the structure. For instance, consider the 1-D diamond optomechanical crystal shown in fig. 8.1c., which has dimensions 14.5 $\mu m \times$ 930 nm $\times$ 220 nm. This crystal supports a localized, mechanical breathing mode, with an eigenfrequency of $\sim$ 6 GHz. The strain induced by the motion

of this mode is highest at the center of the length of the beam. However, the strain is also constant through out the thickness of the beam. This means that a target NV center could be located at the volumetric center of this beam, with the nearest diamond surface being approximately 100 nm away. Since the NV would not be in close proximity to a surface, its coherence and optical properties should in principle resemble those in bulk diamond samples [131]. If the NVs are introduced using nitrogen delta-doping, then these coherence properties should not be significantly affected [97, 228]. Therefore, a ground state spin coherence time $T_2^s = 10$ ms and orbital coherence time $T_2^o = 10$ ns should be reasonably attainable in this device [97, 184]. Moreover, a quality factor of $Q = 10^4$ should also be attainable for this mechanical mode, which is consistent with recent measurements of diamond optomechanical crystals [48].

Diamond optomechanical crystals can not only offer improvements to both the mechanical and NV decoherence, but also offer improved NV-phonon couplings. For the mechanical mode depicted in fig. 8.1c., the orbital single phonon couplings would be $g^o \sim 20$ MHz, with the spin single phonon coupling being $g^s \sim 1$ kHz. With these improved couplings, and assuming the reasonable parameters of $Q = 10^4$, $T_2^s = 10$ ms, $T_2^o = 10$ ns, the single phonon cooperativities should be $C^o \sim 3$ for an operation temperature of 4 K and $C^s \sim 0.4$ for an operation temperature of 100 mK.

In addition to the NV center, the mechanical mode of the optomechanical crystal can directly couple to the photonic modes of the crystal via radiation pressure [61]. Therefore, this device could achieve mechanical cooling that combines radiation pressure back action cooling with single defect cooling. This paves the way for studies of the interplay between the two interactions and cavity quantum electrodynamics (cQED) experiments in diamond optomechanical crystals [239, 240].

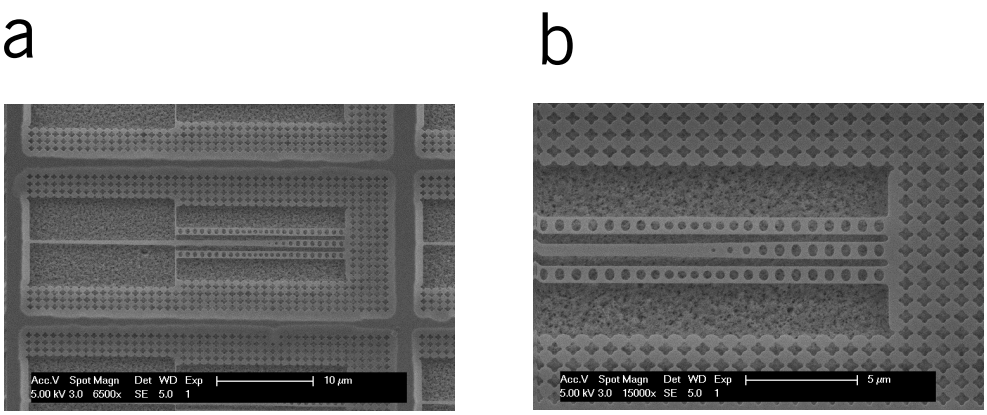

Figure 8.2: **SEM micrograph of diamond optomechanical crystals**. a) Image of a single device containing two optomechanical crystals on either side of a tapered optical waveguide. The device is surrounded by a two-dimensional phononic crystal with an expected 1 GHz bandgap at a frequency of 6 GHz. b) Zoomed in image of the OMCs and waveguide.

8.3 Diamond optomechanical crystals hosting NV centers

Very recently, we have been able to fabricate 1-D diamond optomechanical crystals (OMCs) hosting NV centers. A scanning electron micrograph image of one of the devices is shown in fig. 8.2. The device contains two optomechanical crystals that sit on either side of tapered optical waveguide. Light coupled into the waveguide evanescently couples to the optomechanical crystals. The device is designed to host an optical mode near 1550 nm and a mechanical breathing mode at approximately 6 GHz. There are several reasons why these parameters were chosen. From a practical standpoint, the use of 1550 nm light allows us to take advantage of the mature technologies developed in the telecommunications industry, such as tunable lasers and fiber-optics. From a theoretical standpoint, an optomechanical crystal operating in this wavelength range could provide an infrared band photonic interface to the NV center, providing an alternate route to quantum photonics with the NV electron spin. In terms of the mechanical mode, the

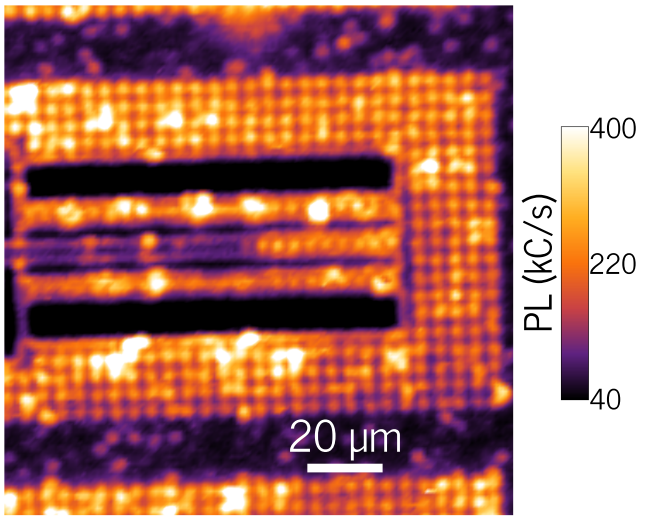

Figure 8.3: **Confocal micrograph of diamond optomechanical crystals**. The device is surrounded in a two-dimensional phononic shield. Most of the bright spots correspond to NV centers.

device was optimized for the mechanical quality factor and the strength of the strain coupling, which requires a balance between the feature sizes on the device, such as the holes.

8.3.1 Optical modes

To probe the optical and mechanical resonances of the device, we constructed a new experimental setup which integrates a tapered fiber spectrometer with a standard laser scanning confocal microscope. A confocal image of the optomechanical crystals shown in fig. 8.2 is shown in fig. 8.3. A simple experimental schematic is shown in fig. 8.4. Light from a tunable, 1550 nm laser is fiber coupled and sent through a circulator to the device. Light reflected from the device is then sent to a fast photodiode for analysis. To mode match the optical fiber to the device waveguide, we taper the optical fiber so that the index of refraction adiabatically evolves from the usual fiber index to the index of the optical fiber. To couple light into the device, we place the tapered fiber in

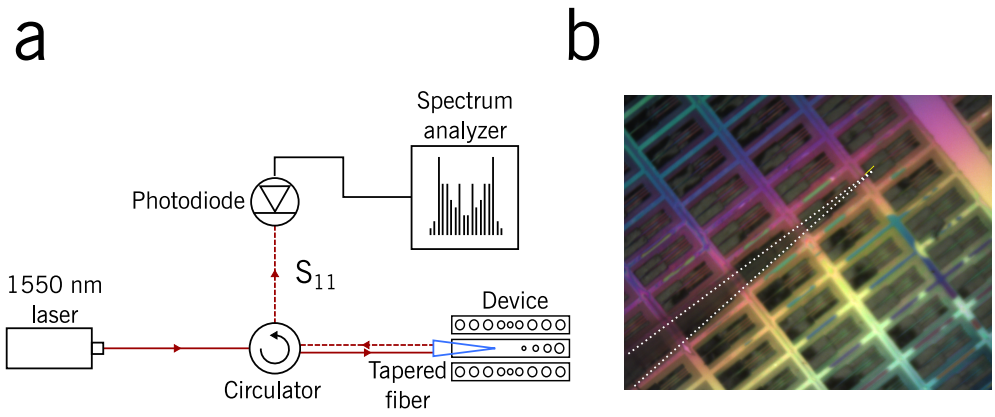

Figure 8.4: **Tapered fiber setup for measuring OMCs**. a) Simplified schematic showing the tapered fiber measurement of the OMCs. Light from a fiber-coupled, tunable 1550 nm laser is sent through a circulator to the device. A tapered fiber (blue) allows the laser light to couple into the device. Light reflected from the device is sent to a photodiode for analysis. b) Photograph of our diamond OMCs from above. A tapered fiber (shadow roughly outlined in white dashed line) is in contact with one of the device waveguides.

contact with the waveguide, as shown in the photograph in fig. 8.4. To optimize the coupling into the waveguide, we move the sample with respect to the tapered fiber with nanopositioning stages and monitor the reflected power coming back into the circulator, S_{11}. We typically observe fiber-waveguide couplings between $10 - 15\%$, and note that this is not a limiting factor in our current experiments. To probe the optical resonances of the OMCs, we scan the wavelength of the input laser and monitor changes in S_11. When the laser is resonant with one of the optical modes of the OMCs, we see a dip in S_{11}, corresponding to the transmission of light from the waveguide to the OMC. In fig. 8.5, we show experimental measurements of the optical modes of one of our devices. In fig. 8.5a., we show the measured S_{11} over the full scanning range of the laser. Notably, we observe two sharp dips in the reflected signal at approximately 1547 nm and 1556 nm, corresponding to the fundamental optical modes of the two OMCs around the waveguide. Figs. 8.5b-c. show a zoomed in view of both optical modes. Fits of both modes to Fano resonances indicate a quality factor of 11,200 for one mode and 12,400 for the other mode.

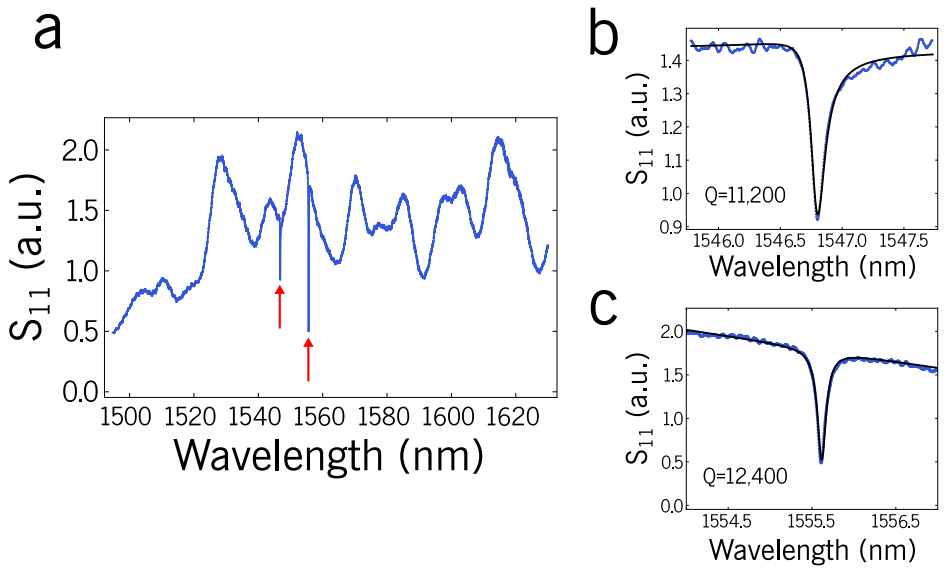

Figure 8.5: **Optical modes of a diamond optomechanical crystal**. a) Reflected power from the device as a function of laser wavelength. Two sharp dips in the reflectance (red arrows) correspond to the fundamental optical modes of the two OMCs. b) and c) show zoomed in spectra of the optical modes with their measured quality factors of 11,200 and 12,400. Black lines correspond to fits to a Fano resonance.

These values are approximately an order of magnitude lower than other demonstrations of diamond photonic crystals in this frequency range [48], indicating that there is room for improvement. As we discuss in our measurement of the mechanical modes, this may be limited by residual oxide on the back side of the device that has was not etched away during the release process.

8.3.2 Mechanical modes

To measure the mechanical modes of the OMCs, we park the laser near resonance with the optical mode, and measure the phase of the reflected light from the device in a measurement that is very similar to the Fabry-Perot interferometry technique used to measure the cantilevers. To describe this effect, we make use of the linearized optome-

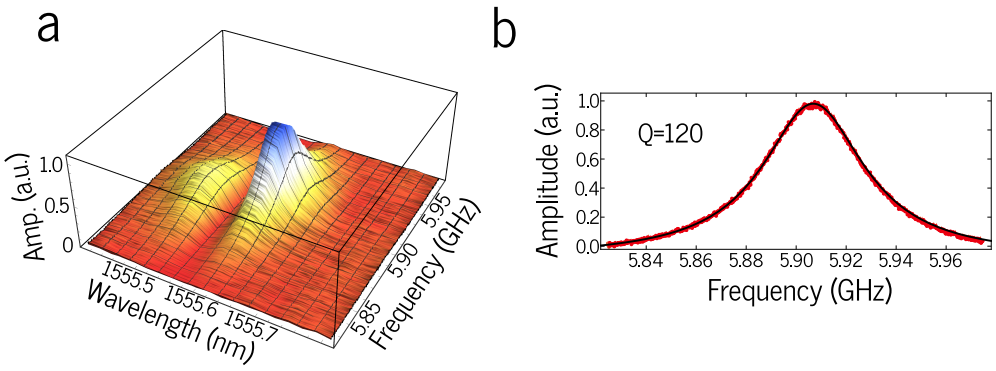

Figure 8.6: **Mechanical mode of a diamond optomechanical crystal**. a) Measured mechanical spectrum as a function of laser wavelength. When the laser is on resonance with the cavity, we observe a large mechanical signal at approximately 5.9 GHz. Surprisingly, when we tune blue of the cavity, we observe damping and softening of the mechanical resonance, which may suggest drifts in the system or optomechanical self-oscillations. b) Spectroscopy of the mechanical mode when the laser is resonant with the cavity shows a mode at 5.9 GHz with $Q = 120$.

chanical interaction [199], which can be described by

$$H_{OM} = g\sqrt{\bar{n}_{cav}}(d + d^{\dagger})(b + b^{\dagger}) \tag{8.2}$$

where g is the single photon optomechanical coupling, $\bar{n}_{cav}$ is the average number of photons in the cavity, d is the annihilation mode for the displaced cavity field, and b is the annihilation operator of the mechanical mode. If we park the laser directly on resonance with the optical mode, we see the cavity mode is displaced by an amount proportional to the mechanical displacement, which amounts to an effective phase shift of the light that has traveled through the cavity. Obviously, the phase acquired will be directly proportional to the optomechanical coupling. Moreover, the modulation depth will be increased as the intracavity photon number increases. To measure the mechanical mode, we send the output of the photodiode directly to a spectrum analyzer. In fig. 8.6b., we show the mechanical spectrum for the OMC hosting an optical mode near 1556 nm when the laser is resonant with the cavity mode. We observe a mechanical mode at

approximately 5.90 GHz with a quality factor of approximately 120. In fig. 8.6a., we show the mechanical spectrum for a variety of difference laser wavelengths. When the laser is resonant with the cavity, we observe the largest mechanical response. Interestingly, when we are blue detuned from the cavity, we see a damped mechanical response, which is the opposite of what one would expect. When we are red detuned, we observe no mechanical response. In the bad cavity limit, blue detuning from the cavity resonance will generate an optical spring effect, resulting a positive shift of the mechanical frequency and a narrowing of the mechanical linewidth. Conversely, red detuning from the cavity resonance will damp the mechanical motion. Our measurement is more consistent with optical damping, which suggests the cavity may have drifted with respect to the laser during the measurement. On the other hand, for a large input laser power, it is possible to generate an instability in the mechanical oscillator displacement due to self-induced oscillations, which will bring the cavity out of resonance with the laser and reduce the signal. In the future, we can test this hypothesis by repeating the experiment for various input powers. Additionally, a measurement of g should allow us to numerically integrate the equations of motion to determine the threshold for optomechanical self-oscillations. To combat any possible laser drifts, we can lock the laser to a stable reference cavity with a Pound-Drever-Hall locking scheme.

There are several possible sources of dissipation that may be affecting the quality factor. The first and perhaps most obvious limitation is from an apparent layer of oxide that is on the backside of the device. In optical microscopy, we see a strong interference pattern that is not consistent with the wedge thickness of the diamond sample. Any contaminants on the surface will significantly degrade the Q. This effect was also observed in our cantilever samples at cryogenic temperatures. As the sample cryopumped more and more materials, the quality factor slowly degraded. The next source of error may be from the outer phononic shield, which suffered from some fabrication errors. In particular,

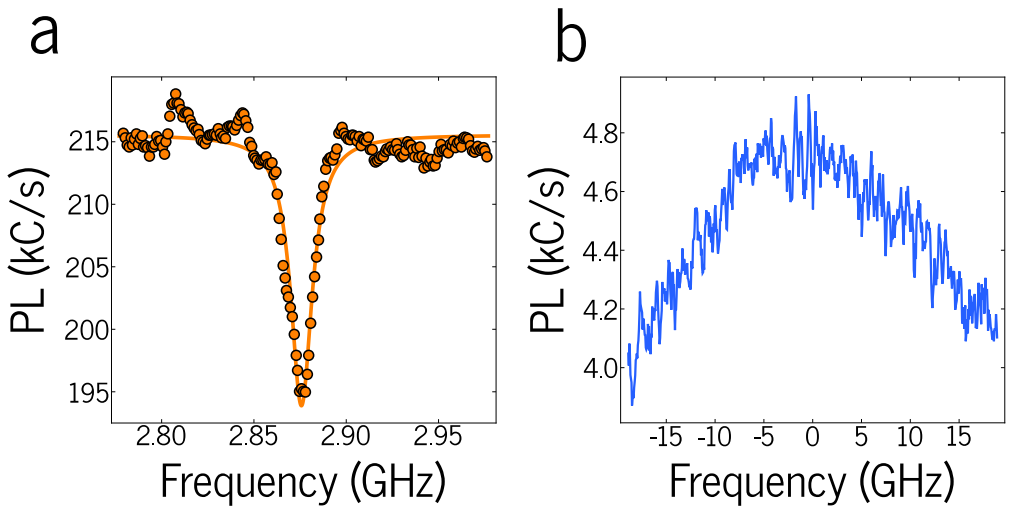

Figure 8.7: **Spectroscopy of NV centers in an OMC**. a) ESR spectrum with no applied magnetic field for likely several NV centers located in the defect region of the OMC. b) RES data taken at 4 K for possibly several NV centers showing broad optical lines with linewidths exceeding 20 GHz.

the cross-shaped holes are smaller and slightly rounded compared to the optimized shape. This may reduce the phononic bandgap enough that phonon tunneling is limiting the Q.

8.3.3 ESR and RES

The diamond optomechanical crystals that we have fabricated currently contain large ensembles of NV centers. As a first step toward characterizing our devices, we performed cw ESR and resonant excitation spectroscopy on NV centers located inside of the OMCs. In fig. 8.7a., we show an ESR spectrum for what is likely multiple NV centers located inside the defect region of an optomechanical crystal. We see a fluorescence contrast of approximately 10%, which is likely limited by the large background. The background may be caused from waveguiding or may just be stray fluorescence from the HSQ bonding layer which is still underneath the sample. In fig. 8.7b., we show a representative resonant excitation spectroscopy measurement for what is likely multiple NV centers in the OMC.

The line is at a very minimum 20 GHz wide, as we could not see the tails of the Lorentzian due to the finite scanning range of the laser. The RES spectrum is not stable from scan to scan, suggesting that spectal diffusion plays a major role in the broadening of these lines. However, it is unclear whether the broad linewidth is due purely to spectral diffusion or contributions from several NV centers. If we look at any point of the sample, we can measure an ESR signal, which suggests that the NV density is high in this sample. In the future, we can tune the nitrogen incorporation into the sample to reduce the NV density and hopefully identify and characterize the coherence and optical properties of single NV centers.

8.4 Summary

In this thesis, we have carefully the coherent dynamics of a hybrid spin-mechanical oscillator quantum system. We first established that such a system was possible, by studying how the parametric coupling between the mechanical motion and the electron spin of the NV center can be used to coherently drive the spin evolution on the Bloch sphere. Using quantum control protocols and the mechanical properties of a diamond cantilever, we quantitatively characterized the spin-strain interaction. Our analysis allowed us to quantitatively image the strain profile of our diamond cantilever and more broadly, establishes the NV center as a nanoscale strain sensor. We next demonstrated a strong, strain-mediated coupling between the orbital states of the NV center and a diamond cantilever. Careful control of the mechanical motion through optical interferometry and feedback allowed us to deterministically shift the optical resonances of the NV center by several GHz, with potential shifts up to several THz. Furthermore, we showed that strain can be used to deterministically control the frequency and polarization dependence of the optical transitions of single NV centers. In the future, this tuning

modality could be crucial for chips hosting many optical emitters, and will be critical for optical tuning of defect centers with inversion symmetry. We concluded our characterization of these cantilever devices by examining a resonant interaction between the NV spin and cantilever motion. With continuous mechanical driving, we engineering a series of dressed spin states that are insensitive to magnetic field fluctuations, and demonstrated a significant enhancement in the spin coherence time. Importantly, these engineered spins states are still sensitive to strain, and hence can be used for future quantum devices without significant experimental overhead. More generally, the techniques and results established in this thesis can be applied very generally to any solid-state defect system, and may be used to identify other promising strain-sensitive defects.

Looking ahead toward the future, we hypothesize that diamond optomechanical crystals will provide the necessary environment to achieve strong coupling between the NV center and coherent phonons. Our simulations suggest that these devices will be well suited to perform many of the desirable applications discussed in this thesis, including phonon cooling, generation of non-classical mechanical states, and multi-partite entanglement. More broadly, an optomechanical crystal platform can be used to interface dark spins with infrared photons through phonons, which should bolster the use of solid-state spins of hybrid quantum networks. Strain-coupled devices are still very much in the early stages of development, and have enormous room for growth. As nanofabrication techniques and our understanding of the noise environment of solid-state defects mature, these devices will be poised to make a significant impact in quantum technologies.

Appendix A

Group Theory and C_{3v} symmetry

This appendix is intended to give a brief introduction to C_{3v} symmetry and group theory to allow the reader to perform the theoretical calculations in chapter 2 of this thesis. I would not describe the following as mathematically rigorous, but more of a general guide to understanding how group theory and quantum mechanics are related. For a comprehensive and accessible overview of group theory and its application to quantum mechanics, I highly recommend the online notes of Dr. Mildred Dresselhaus.

A.1 Group theory and quantum mechanics

The energy structure of a quantum system is intrinsically linked to its inherent symmetries. If we consider a general Hamiltonian H with eigenstates defined by

$$H\left|\psi_n\right\rangle = E\left|\psi_n\right\rangle \tag{A.1}$$

then we can find some symmetry operators, P_Γ under which the Hamiltonian is invariant, $P_\Gamma H P_\Gamma^\dagger$. These symmetry operators can refer to a number of physical operations, such as rotations, reflections or inversion. Applying these operators to the Hamiltonian

will not alter the Hamiltonian or its energy eigenvalues. Therefore, the wavefunction $P|\psi_n\rangle$ is also an eigenstate of H with energy E_n. The set of these operators $\{P_\Gamma\}$ are referred to as the symmetry group of the Hamiltonian.

This is an extraordinarily powerful statement. It follows that we can generate all eigenstates of energy E_n by applying the symmetry operators to $|\psi_n\rangle$. Suppose that the Hamiltonian contains an m-fold degenerate manifold with energy E_n and eigenstates $\{|\psi_{nm}\rangle\}$. Then, we see

$$P_\Gamma|\psi_{nm}\rangle = \sum_p D_{pm}(\Gamma)|\psi_{np}\rangle \tag{A.2}$$

where $D_{pm}(\Gamma)$ is an irreducible representation describing the symmetry operator. The distinct energy eigenstates of the system are related to each other by these irreducible matrices.

These symmetry operators can similarly be thought of as projection operators, which project any set of eigenstates onto the irreducible representations of the symmetry group. In the following section, we will show how to construct the projection operators for the C_{3v} symmetry group, which describes the physical symmetry of the NV center. Moreover, we will show how these projection operators can be used to construct the wavefunctions of the NV center and their response to external perturbations.

A.2 C_{3v} symmetry

The NV center is a trigonal center in diamond with C_{3v} point group symmetry. The NV symmetry axis (the z axis or NV axis) lies along the bond connecting the nitrogen and the vacancy. The x axis is in the plane perpendicular to the symmetry axis, and lies along the projection of one of the carbon bonds onto this plane. The C_{3v} symmetry

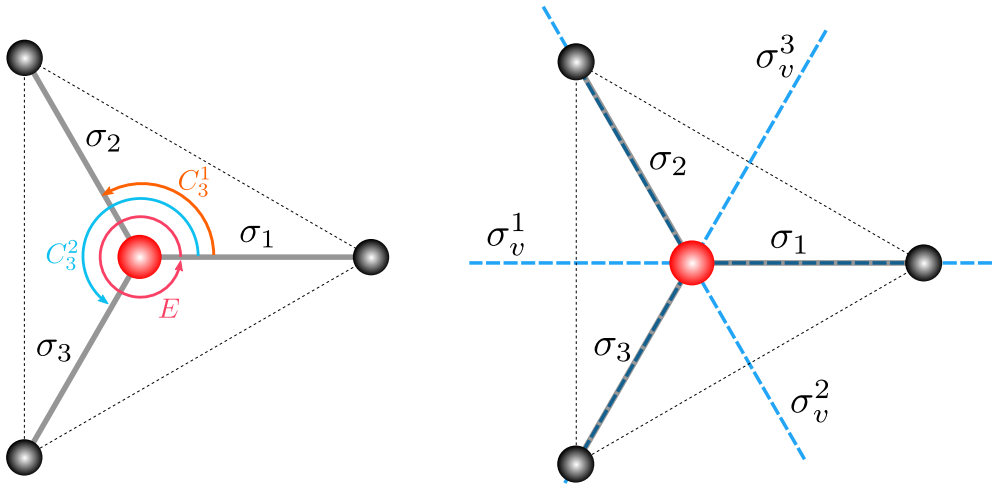

Figure A.1: C_{3v} **symmetry operations**. Left: C_3 rotations. Right: σ_v reflections

group has 6 elements, which are operations under which the NV symmetry is preserved: $\{E, C_3, C_3^2, \sigma_v^1, \sigma_v^2, \sigma_v^3\}$. The element E is the identity, the elements C_3 and C_3^2 refer to rotations about the z axis by $2\pi/3$ and $4\pi/3$ respectively, and the elements σ_v refer to reflections in the vertical plane containing the z axis and a single carbon atom. These operations are shown schematically in fig.

To understand the NV electronic structure, we need to construct the irreducible representations of the C_{3v} group. Let us first construct a simple matrix representation of the C_{3v} symmetry group. We will work in a 4 dimensional basis spanned by the 4 dangling bonds associated with the NV center: $\{\sigma_1, \sigma_2, \sigma_3, \sigma_N\}$.

The matrix representation of E is obviously

$$E = \begin{pmatrix} 1 & 0 & 0 & 0 \\ 0 & 1 & 0 & 0 \\ 0 & 0 & 1 & 0 \\ 0 & 0 & 0 & 1 \end{pmatrix} \tag{A.3}$$

The action of C_3 has $(\sigma_3 \to \sigma_1, \sigma_1 \to \sigma_2, \sigma_2 \to \sigma_3)$ and the action of C_3^2 has $(\sigma_2 \to \sigma_1, \sigma_3 \to \sigma_2, \sigma_1 \to \sigma_3)$, thus we have

$$C_3 = \begin{pmatrix} 0 & 0 & 1 & 0 \\ 1 & 0 & 0 & 0 \\ 0 & 1 & 0 & 0 \\ 0 & 0 & 0 & 1 \end{pmatrix} \tag{A.4}$$

$$C_3^2 = \begin{pmatrix} 0 & 1 & 0 & 0 \\ 0 & 0 & 1 & 0 \\ 1 & 0 & 0 & 0 \\ 0 & 0 & 0 & 1 \end{pmatrix} \tag{A.5}$$

The reflection operators σ_v merely swap two of the carbon bonds, depending on which carbon atom is contained in the reflection plane. We see that

$$\sigma_v^1 = \begin{pmatrix} 1 & 0 & 0 & 0 \\ 0 & 0 & 1 & 0 \\ 0 & 1 & 0 & 0 \\ 0 & 0 & 0 & 1 \end{pmatrix} \tag{A.6}$$

$$\sigma_v^2 = \begin{pmatrix} 0 & 0 & 1 & 0 \\ 0 & 1 & 0 & 0 \\ 1 & 0 & 0 & 0 \\ 0 & 0 & 0 & 1 \end{pmatrix} \tag{A.7}$$

$$\sigma_v^3 = \begin{pmatrix} 0 & 1 & 0 & 0 \\ 1 & 0 & 0 & 0 \\ 0 & 0 & 1 & 0 \\ 0 & 0 & 0 & 1 \end{pmatrix} \tag{A.8}$$

An important property of representations is the *character*of the representation. Mathematically, it is defined as the trace of the matrix representation. The reason the character is important is because it is invariant under similarity transformations – this allows a representation to be identified even if it is not defined in a diagonal basis. As it turns out, the character will be helpful in finding all of the irreducible representations in addition to showing how different physical quantities transform under the irreducible representations.

If we look at the characters of the 6 representations, we see that operations of the same type all have the same characters: $tr(E) = 4$, $tr(C_3) = tr(C_3^2) = 1$, $tr(\sigma_v^i) = 2$. We say that operations of the same form belong to the same class. In the C_{3v} group we have 3 classes: the identity E, rotations C_3, and reflections σ_v. Group theory tells us that the number of irreducible representations of a group is equal to the number of classes in a group. Moreover, the sum of the squares of the dimensionalities of the irreducible representations must equal the total number of elements in the group (known as the order), which is 6. So we have 3 irreducible representations $\Gamma_1, \Gamma_2, \Gamma_3$ and $Dim(\Gamma_1)^2 + Dim(\Gamma_2)^2 + Dim(\Gamma_3)^2 = 6$. It's easy to see that the upper bound on the dimension of any of the irreducible representation is 2, and moreover, only one may have a dimension of 2. Therefore, we are looking for two one dimensional representations and one two dimensional representation. Looking at the 4×4 representations above, we see that they can be written in block diagonal form with one 3×3 and one 1×1. The 1×1 matrix which is just the constant (1), is an irreducible representation, which we label A_1. The character of each operation in this representation is simply 1. The 3×3 representation can

	E	C_3	σ_v
A_1	1	1	1
E	2	-1	0

Table A.1: Character table for the first two irreducible representations.

be reduced by applying a similarity transformation, which again allows it to be written in block diagonal form with one 1×1 representation and one 2×2 representation. It turns out the 1×1 representation is A_1 again, so we can ignore it. The 2×2 representation, however, turns out to be the 2 dimensional irreducible representation, which we denote as the E irreducible representation. The character table for these two irreducible representations can be found below:

The last one dimensional irreducible representation can be found using the character orthogonality theorem from group theory. If we define the character of an element R in an IR, Γ_i, to be $\chi^{\Gamma_i}(R)$, then we have the following orthogonality condition:

$$\sum_R \chi^{\Gamma_i}(R)\chi^{\Gamma_j}(R) = h\delta_{i,j} \tag{A.9}$$

where h is the order of the group (for C_{3v}, $h = 6$).

Using this relation, we can finally construct the final one dimensional IR, A_2.

	E	C_3	σ_v
A_1	1	1	1
A_2	1	1	-1
E	2	-1	0

Table 2: Full character table for the C_{3v} group.

The names of the irreducible representations are consistent with what is called Mulliken notation. A refers to the fact that the IR is one dimensional and that it is fully symmetric under C_3 operations (as defined by the character). The subscripts of A_1 and A_2 refer to whether a wavefunction picks up a negative sign under rotations R_z. Under

reflections σ_v, rotations R_z are reversed, which corresponds to the -1 character of σ_v operations in A_2. E refers to the fact that the representation is two dimensional.

To understand the NV Hamiltonian construct the total NV wavefunctions, it is important to know the so called basis functions of the irreducible representations. Basis functions can be used to generate the matrices for the elements of a particular irreducible representation. Moreover, the basis functions dictate the form of each term in the NV Hamiltonian. In particular, we would like to see which IR the linear basis functions $\{x, y, z, R_x, R_y, R_z\}$ and quadratic basis functions $\{z^2, x^2+y^2, x^2-y^2, xy, yx, xz, zx, yz, zy\}$ belong to. Let's start with the easiest example: z. Under all symmetry operations of the group, z remains invariant, which corresponds to the IR A_1. The quantities x and y are slightly more complicated. If we apply the symmetry operations to x and y, we see that they form a linearly independent basis in a two-dimensional subspace which can be described by simple 2×2 matrices. If we compare these 2×2 matrices to the 2 dimensional IR found above, we see that they are equivalent! Therefore, we see that x and y transform as the E irreducible representation. The rest of these basis functions can be found in the table below.

	linear basis functions	quadratic basis functions
A_1	z	z^2,x^2+y^2, R_z^2, $R_x^2+R_y^2$
A_2	R_z	
E	(x,y),(R_x,R_y)	(x^2-y^2, xy), (xz, yz)

Table 3: Linear and quadratic basis functions for the C_{3v} irreducible representations.

A.2.1 Constructing the projection operators

Now that we have found all the irreducible representations and their characters, we can now return to the NV structure. As mentioned before, there are 4 dangling bonds associated with the NV center: $\{\sigma_1, \sigma_2, \sigma_3, \sigma_N\}$, shown in fig. A.2. The relevant molecular orbitals of the NV center are constructed by linear combinations of these dangling bonds.

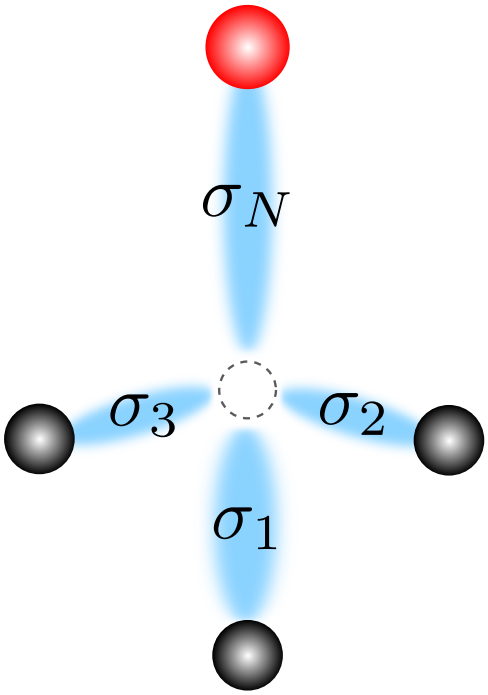

Figure A.2: **Dangling bonds associated with the NV center.**

In other words, we are just making a change of basis, which means we can use Clebsch-Gordan coefficients to describe these transformations. Recall that in quantum mechanics, a wave function $|\Psi\rangle$ can be expressed in any complete basis that spans the Hilbert space, $\{\phi_i\}$ by

$$\sum_i \langle\Psi|\phi_i\rangle\,|\phi_i\rangle$$

. The same applies here, except we define our projection operators $|\phi\rangle\langle\phi|$ in terms of the group symmetry operators and their character in each irreducible representation. Specifically, the projection operator for a particular IR Γ_i is defined by

$$P_{\Gamma_i} = \frac{1}{h}\sum_R \chi^{\Gamma_i}(R)R \tag{A.10}$$

where again $\chi^{\Gamma_i}(R)$ is the character for a symmetry element R. Just to be super

pedantic and give an example, the projection operator for the IR A_2 would be

$$P_{A_2} = \frac{1}{6}(E + C_3 + C_3^2 - \sigma_v^1 - \sigma_v^2 - \sigma_v^3) \tag{A.11}$$

To find the molecular orbitals of the NV center, we can apply the projection operators $\{P_{A_1}, P_{A_2}, P_E\}$ to the 4 dangling bonds. The result will be a linear combination of the dangling bonds which transforms as that respective IR. Let's start with the two easiest examples: First, let's apply P_{A_1} to $|\sigma_N\rangle$. Clearly, all the symmetry operations will leave σ_N unchanged, thus we see $P_{A_1}|\sigma_N\rangle = \sigma_N \equiv a_N$. Now let's apply it to one of the carbon bonds, σ_1. From symmetry, it is easy to see that $P_{A_1}|\sigma_1\rangle = P_{A_1}|\sigma_2\rangle = P_{A_1}|\sigma_3\rangle = \frac{1}{3}(\sigma_1 + \sigma_2 + \sigma_3) \equiv a_C$. We now have two of the four molecular orbitals. If we apply the projection operator for A_2, we see that we get 0 for all 4 dangling bonds, which means there are no molecular orbitals that transform as A_2. This means the remaining two orbitals transform as E. $P_E|\sigma_N\rangle = 0$, thus we only need to focus on the carbon bonds. If we apply the projection operator to each, we find

$$P_E|\sigma_1\rangle = \frac{1}{6}(2\sigma_1 - \sigma_2 - \sigma_3) \equiv e_1 \tag{A.12}$$

$$P_E|\sigma_2\rangle = \frac{1}{6}(2\sigma_2 - \sigma_3 - \sigma_1) \equiv e_2 \tag{A.13}$$

$$P_E|\sigma_3\rangle = \frac{1}{6}(2\sigma_3 - \sigma_1 - \sigma_2) \equiv e_3 \tag{A.14}$$

At first glance, it appears that we have 3 orbitals that transform as E, but we can easily see that only two of these orbitals are linearly independent. We can see this by the fact that $e_3 = -(e_1 + e_2)$. If I choose e_1 to be one of our orbitals, e_x, this means that I can generate another orbital e_y, that is orthogonal to e_x and is a linear combination of e_2 and e_3, $e_y = \alpha e_2 + \beta e_3$. It follows that $\alpha = -\beta$ and $e_y = \frac{1}{2}(\sigma_2 - \sigma_3)$.

We have now recovered all 4 orbitals associated with the NV center. It is important to note that the use of the dangling bonds is an approximation, so the orbitals are not exactly correct. However, they do have the correct symmetry. The final molecular orbitals can be obtain by applying the Coulomb interaction to the system, which sets the energy ordering of the orbitals. The Coulomb interaction is a fully symmetric interaction and thus transforms as A_1. Therefore, it will mix the a_N and a_C orbitals since they are also of the same symmetry (see below discussion). Including the Coulomb interaction we are left with our final molecular orbitals (normalized):

$$a_1 = \alpha a_C + \beta a_N \tag{A.15}$$

$$a_2 = \alpha a_N + \beta a_C \tag{A.16}$$

$$e_x = \frac{1}{\sqrt{6}}(2\sigma_1 - \sigma_2 - \sigma_3) \tag{A.17}$$

$$e_y = \frac{1}{\sqrt{2}}(\sigma_2 - \sigma_3) \tag{A.18}$$

In general, this technique can be applied to calculate the many-body NV wavefunction and calculate the symmetry components of some external perturbation on the NV center, such as the strain-orbit interaction.

A.2.2 Calculating matrix elements

To calculate the matrix elements for a physical observable, one must consider the group multiplication table for the symmetry group. In particular, a matrix element $\langle\phi|\,\mathcal{O}\,|\psi\rangle$ is non-zero when $\mathcal{O}\,|\psi\rangle$ has the same symmetry as $|\phi\rangle$. In general, the element $\mathcal{O}\,|\psi\rangle$ will have symmetry $\Gamma_{\mathcal{O}} \otimes \Gamma_{\psi}$, which can be calculated using the product table shown below.

	A_1	A_2	E
A_1	A_1	A_2	E
A_2	A_2	A_1	E
E	E	E	A_1+A_2+E

Table A.2: Product table for the C_{3v} group.

This leads to the following results. An A_1 symmetric interaction may only couple states of the same symmetry. An A_2 symmetric interaction can couple a state of A_1 symmetry to a state of A_2 symmetry, and can also couple states of E symmetry. Finally, an E symmetric interaction can couple states of all symmetries.

A.2.3 Direct products of degenerate irreducible representations

Throughout this thesis, I break down components that transform as the doubly degenerate E irreducible representation into terms of E_1 and E_2 symmetry, which correspond to the first and second rows of the E irreducible representation. The direct product of $E \otimes E$ was shown to be $A1 + A2 + E$ in table A.2. However, we can break down this direct product in terms of E_1 and E_2, and determine which products correspond to the each symmetry component of $E \otimes E$. This is important in determining matrix elements such as the electric dipole operator between $^3A_2$ and ^3E. Suppose we have two E symmetric quantities with basis functions $\{\alpha_x, \alpha_y\}$ and $\{\beta_x, \beta_y\}$ which transform as $\{E_1, E_2\}$, and we want to know the symmetry of the direct product of these two quantities $\alpha \otimes \beta = \{\alpha_x\beta_x, \alpha_x\beta_y, \alpha_y\beta_x, \alpha_y\beta_y\}$. We can construct symmetric and anti-symmetric combinations of these quantities which transform as a particular irreducible representation.

Specifically, we see that

$$\begin{aligned} \alpha_x\beta_x + \alpha_y\beta_y &\rightarrow A_1 \\ \alpha_x\beta_y - \alpha_y\beta_x &\rightarrow A_2 \\ \alpha_x\beta_x - \alpha_y\beta_y &\rightarrow E_1 \\ \alpha_x\beta_y + \alpha_y\beta_x &\rightarrow E_2 \end{aligned} \tag{A.19}$$

From here, we can immediately understand the symmetry argument for the matrix elements of the strain and electric dipole operators. In particular, we see why d_x couples $|0\rangle$ to $|E_y\rangle$ and why d_y couples $|0\rangle$ to $|E_x\rangle$. If the electronic ground state were, for instance, A_1 symmetric, then $\hat{x}$ polarized light would drive the E_x transition instead of $\hat{y}$ polarized light.

This product rule can also be applied to D_{3d} defects. However, because of inversion symmetry, there is an additional product rule which states that $g \otimes g = u \otimes u = g$ and $g \otimes u = u$. This is a fairly intuitive result, as these labels correspond to even and odd parity.

Appendix B

Hybrid mechanical devices based on D_{3d} defects in diamond

In this appendix, we will study the electronic structure of negatively charged defect centers in diamond incorporating a group IV atom. In particular, we focus on defect centers with D_{3d} symmetry, such the silicon-vacancy center (SiV), germanium-vacancy center (GeV), and the tin-vacancy (SnV). These defects are promising for photonic interactions due to their exceptional optical properties, in particular their large Debye-Waller factors. Defects with D_{3d} symmetry are inversion symmetric, and hence lack a permanent electric dipole moment. This mitigates the spectral diffusion induced by electric field noise that is typically observed in the NV center. However, the optical transitions of these defects are still highly susceptible to crystal strain, and thus it may be advantageous to pursue hybrid mechanical devices incorporating D_{3d} defect centers. We demonstrate that electric fields cannot be used to effectively tune the optical transitions of these defects and that strain provides a promising platform for tuning the frequency and polarization selection rules.

B.1 Structure and D_{3d} symmetry

The D_{3d} color centers of interest consist of two vacancies in a "split-vacancy" configuration along the [111] crystal axis, with an interstitial atom in between them, as shown in fig. B.1. The electronic structure of these defects are determined by the dangling bonds associated with the 6 nearest neighbor carbon atoms as well as the interstitial atom.

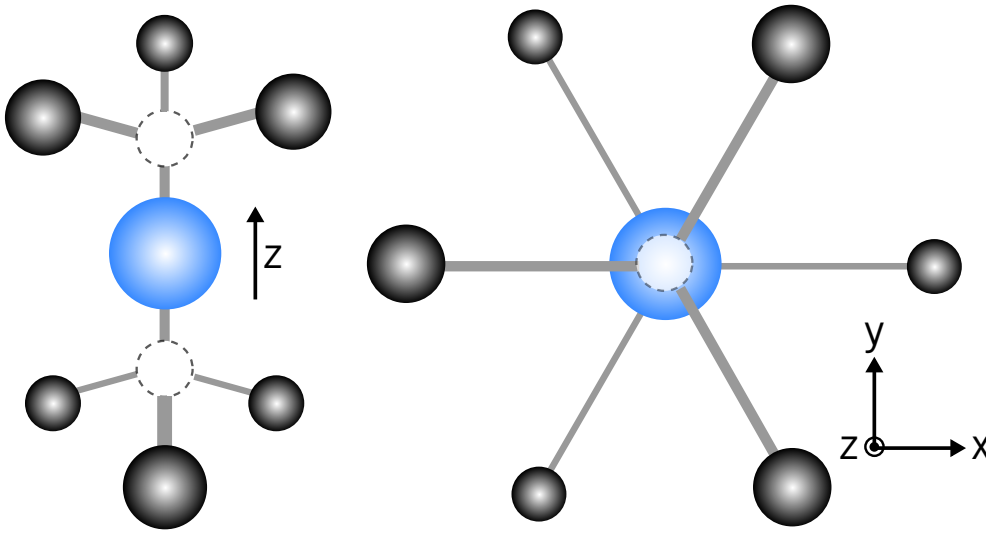

Figure B.1: **Physical structure**. On the left is a schematic of the D_{3d} defect structure where the white atoms represent vacancies, the yellow atom is the interstitial group IV atom, and the blue atoms are the nearest-neighbor carbon atoms. On the right we are looking down the z axis of the defect center, which is along the [111] direction.

The D_{3d} symmetry group has 12 elements, and for these defects, the symmetry point is the interstitial atom. The group elements are $\{E, C_3^1, C_3^2, C_2^1, C_2^2, C_2^3, i, S_6^1, S_6^2, \sigma_d^1, \sigma_d^2, \sigma_d^3\}$. The element E refers to the identity operation. The elements C_3^1 and C_3^2 refer to rotations about the z axis by $2\pi/3$ and $4\pi/3$ respectively. The elements C_2^1, C_2^2, and C_2^3 refer to

	E	C_3	C_2	i	S_6	σ_d
A_{1g}	1	1	1	1	1	1
A_{2g}	1	1	-1	1	1	-1
E_g	2	-1	0	2	-1	0
A_{1u}	1	1	1	-1	-1	-1
A_{2u}	1	1	-1	-1	-1	1
E_u	2	-1	0	2	1	0

Table B.1: **Full character table for the D_{3d} group.**

rotations of π around axes in the transverse plane, where the rotation axis is 30 degrees away from any carbon atom. The element i refers to the inversion operation, where $\{x, y, z\} \rightarrow \{-x, -y, -z\}$. The elements σ_d^1,σ_d^2 and σ_d^3 refer to reflections about the so called dihedral mirror planes. These dihedral mirror planes are vertical and intersect the carbon bonds. Finally, the elements S_6^1 and S_6^2 refer to improper rotations. In this case, this operation refers to a rotation about the z axis by 60 degrees followed by a reflection over the $x-y$ plane. In principal, there should be 6 of these operations, but it turns out that some improper rotations lead to symmetry operations that we've already established, and only 2 of these improper rotations are new symmetries.

There are six irreducible representations of the D_{3d} group: $\{A_{1g}, A_{2g}, E_g, A_{1u}, A_{2u}, E_u\}$. The character table for the group is shown in B.1. As we recall, an irreducible representation A is a one-dimensional representation that is symmetric about the C_3 rotations. The subscript 1 and 2 refer to the character of the IR under the C_2 operations, where A_1 has a $+1$ character and A_2 has a -1 character. An irreducible representation E is simply a two-dimensional representation. The subscripts g and u refer to the parity under the inversion operation. The letters g and u specifically are abbreviations of the german words "gerade" and "ungerade" which mean even and odd respectively, thus g refers to a character of $+1$ for i and u refers to a character -1 for i.

Using the character tables, we can generate the basis functions for each irreducible

representation, which will be key to understanding the electronic structure of these defects. For example, the position operator z is unaffected by the identity operator and C_3 rotations and obviously by reflections about vertical planes. However, we see the rotation C_2 inverts z, inversion inverts z, and the improper rotations invert z through the reflections in the transverse plane. Therefore, we see that z transforms as the A_{2u} irreducible representation. The position pair $\{x, y\}$ transform into each other via two-dimensional matrices, and thus transform as an E irreducible representation. Moreover, since they are negative under inversion, we see that they must transform as E_u. The rest of the basis functions can be found in the table below

	linear basis functions	quadratic basis functions
A_{1g}		z^2, $x^2 + y^2$
A_{2g}	R_z	
E_g	(R_x, R_y)	$(x^2 - y^2, xy)$, (xz, yz)
A_{1u}		
A_{2u}	z	
E_u	(x, y)	

Table 2: Linear and quadratic basis functions for the D_{3d} irreducible representations.

B.1.1 Molecular model of D_{3d} defects

Next, we must find the symmetry-adapted molecular orbitals of these negatively charged D_{3d} color centers, which are linear combinations of the atomic dangling bonds. To do this, we use the same projection operator method that we used to find the NV molecular orbitals. For now, we only consider the 6 dangling bonds associated with the center's carbon atoms. We find that there is one orbital that transforms as A_{1g} which we denote a_{1g}. There is one orbital that transforms as A_{2u} which we denote a_{2u}. There are two orbitals that transform as E_g, which we denote e_{gx} and e_{gy}. Finally, there are two orbitals that transform as E_u, which we denote e_{ux} and e_{uy}. Their explicit definitions can be found below:

$$a_{1g} = \frac{1}{\sqrt{6}}(\sigma_1 + \sigma_2 + \sigma_3 + \sigma_1' + \sigma_2' + \sigma_3') \tag{B.1}$$

$$a_{2u} = \frac{1}{\sqrt{6}}(\sigma_1 + \sigma_2 + \sigma_3 - \sigma_1' - \sigma_2' - \sigma_3') \tag{B.2}$$

$$e_{gx} = \frac{1}{2\sqrt{3}}(2\sigma_1 - \sigma_2 - \sigma_3 + 2\sigma_1' - \sigma_2' - \sigma_3') \tag{B.3}$$

$$e_{gy} = \frac{1}{2}(\sigma_2 - \sigma_3 + \sigma_2' - \sigma_3') \tag{B.4}$$

$$e_{ux} = \frac{1}{2\sqrt{3}}(2\sigma_1 - \sigma_2 - \sigma_3 - 2\sigma_1' + \sigma_2' + \sigma_3') \tag{B.5}$$

$$e_{uy} = \frac{1}{2}(\sigma_2 - \sigma_3 - \sigma_2' + \sigma_3') \tag{B.6}$$

Now, we must take into account the electronic orbitals of the interstital atom. As an example, consider the SiV center. The electron configuration of the silicon atom is $[\mathrm{Ne}]3s^2 3p^2$. Therefore, the electrons may occupy a $3s$ orbital or any of the 3 possible $3p$ orbitals which are labeled $3p_x$, $3p_y$, and $3p_z$. The orbital $3p_z$ corresponds to the $m_l = 0$ orbital and the $3p_x$ and $3p_y$ orbitals are linear combinations of the $m_l = \pm 1$ orbitals. The orbitals of the Si atom can mix with the above molecular orbitals through the Coulomb interaction, which is an A_{1g} symmetric interaction. Therefore, the symmetry adapted molecular orbitals can only mix with Silicon orbitals of the same symmetry.

Since the $3s$ orbital is spherically symmetric, it clearly will transform as A_{1g}. The orbitals $3p_x$ and $3p_y$ transform as x and y and thus transform as E_u. Finally the $3p_z$ orbital transforms as z and hence transforms as A_{2u}. Therefore, a_{1g} couples to the $3s$ orbital, a_{2u} couples to the $3p_z$ orbital and the e_u orbitals couples to the $3p_{x,y}$ orbitals. This procedure can be used to determine the mixing of the heavier interstitial atoms.

B.1.2 Constructing the ground and excited states

Through density functional theory, it is possible to predict the energy ordering of these electronic states. It was found that the energy ordering (from lowest to highest) is a_{1g} a_{2u} e_u e_g. As group theory tells us, the orbitals e_{gx} and e_{gy} are degenerate and the orbitals e_{ux} and e_{uy} are degenerate. There are 11 total electrons associated with negatively charged D_{3d} defec centers: 4 electrons are provided by the group IV interstitial atom, 6 electrons are provided by the dangling bonds, and a single electron is trapped from a nearby donor in the crystal (thus providing the negative charge). The ground state electronic configuration is $a_{1g}^2 a_{2u}^2 e_u^4 e_g^3$, where one electron hole occupies either the e_{gx} or e_{gy} orbital. In the excited state, the hole is promoted to an e_u orbital, and the electronic configuration is $a_{1g}^2 a_{2u}^2 e_u^3 e_g^4$. We will henceforth assume the hole representation.

Note that the dynamics of the color center are dictated by a single hole, which has spin $s = 1/2$. We will denote the electronic spin-doublet orbital-doublet ground state by ${}^2E_g$ and the spin-doublet orbital-doublet excited state by ${}^2E_u$. Although the ${}^2E_u$ excited state orbitals should mix with the orbitals of the interstitial atom, it has been shown with *abinitio* calculations that this mixing is quite small and can be neglected. We can now write out the 4 possible ground and excited states explicitly:

$$2_g^E \rightarrow \{|e_{gx},\uparrow\rangle, |e_{gx},\downarrow\rangle, |e_{gy},\uparrow\rangle, |e_{gy},\downarrow\rangle\} \tag{B.7}$$

$$2_u^E \rightarrow \{|e_{ux},\uparrow\rangle, |e_{ux},\downarrow\rangle, |e_{uy},\uparrow\rangle, |e_{uy},\downarrow\rangle\} \tag{B.8}$$

At this stage, all 4 levels in both manifolds are degenerate. As we will see, these degeneracies are partially lifted by the spin-orbit interaction and can be completely lifted with external fields.

	A_{1g}	A_{2g}	E_g	A_{1u}	A_{2u}	E_u
A_{1g}	A_{1g}	A_{2g}	E_g	A_{1u}	A_{2u}	E_u
A_{2g}	A_{2g}	A_{1g}	E_g	A_{2u}	A_{1u}	E_u
E_g	E_g	E_g	$A_{1g} + A_{2g} + E_g$	E_u	E_u	$A_{1u} + A_{2u} + E_u$
A_{1u}	A_{1u}	A_{2u}	E_u	A_{1g}	A_{2g}	E_g
A_{2u}	A_{2u}	A_{1u}	E_u	A_{2g}	A_{1g}	E_g
E_u	E_u	E_u	$A_{1u} + A_{2u} + E_u$	E_g	E_g	$A_{1g} + A_{2g} + E_g$

Table B.2: **Product table for the D_{3d} group.**

B.2 Interactions

Now that we have established the relevant energy levels,, we can determine how other interactions affect the electronic structure. To do this, it will be necessary to know the group multiplication table, which is shown in table B.2. The following calculations are similar to those shown in chapter 2 of this thesis.

B.2.1 Spin-orbit coupling

Let us now calculate the effect of spin-orbit coupling on both the ground and excited states. The spin-orbit interaction takes the form $H_{SO} \sim \mathbf{L} \cdot \mathbf{S}$, and for D_{3d} symmetry can be simplified to

$$H_{SO} = \lambda_z L_z S_z + \lambda_{xy}(L_x S_x + L_y S_y) \tag{B.9}$$

Recall that (L_x, L_y, L_z) transform as (E_{g2}, E_{g1}, A_{2g}) respectively.

It will be useful to consider a new set of electronic orbitals, $e_{g\pm}$ and $e_{u\pm}$, where $e_+ = -\frac{1}{\sqrt{2}}(e_x + ie_y)$ and $e_- = \frac{1}{\sqrt{2}}(e_x - ie_y)$. The L_z operator preserves the symmetry of the e orbitals, and because the e orbitals are mutually orthogonal, we see that the L_z

operator can be written as

$$L_z = \ell \left(|e_+\rangle \langle e_+| - |e_-\rangle \langle e_-| \right) \tag{B.10}$$

In addition to L_z we can define the raising and lowering operators $L_\pm = L_x \pm iL_y$, where $L_+ |e_+\rangle = 0$ and $L_- |e_-\rangle = 0$. Recall from the previous section that the e orbitals are similar to p atomic orbitals. Therefore, the orbitals $e_\pm$ correspond to orbitals with $m_l = \pm 1$. If we recall, the orbital with $m_l = 0$ is an A_{2u} symmetric orbital, and hence we see that $L_+ |e_-\rangle = L_- |e_+\rangle \ \ |a_{2u}\rangle$. It is clear that these raising and lowering operators do not directly couple the $e_\pm$ orbitals, and are thus equal to 0 in the $e_\pm$ subspace. As a result, the operators L_x and L_y are equal to 0 in the e_x and e_y basis. If we rewrite the angular momentum operators in the $e_{x,y}$ basis, we see

$$L_x = 0 \tag{B.11}$$

$$L_y = 0 \tag{B.12}$$

$$L_z = i\ell \left(|e_x\rangle \langle e_y| - |e_y\rangle \langle e_x| \right) \tag{B.13}$$

The spin-orbit Hamiltonian can now be written explicity in terms of the orbital and spin eigenstates

$$H_{SO} = -\frac{\lambda_\parallel}{2} L_z S_z \tag{B.14}$$

$$= \lambda \left(|e_+\rangle \langle e_+| - |e_-\rangle \langle e_-| \right) \left(|\uparrow\rangle \langle \uparrow| - |\downarrow\rangle \langle \downarrow| \right) \tag{B.15}$$

In both the ground and excited states, the four-fold degeneracy is lifted and two

branches emerge, as shown in the figure below.

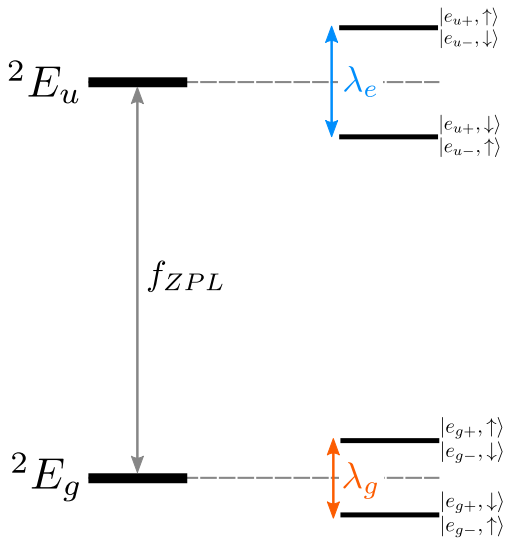

Figure B.2: **Electronic structure with spin-orbit coupling**. The crystal-field for D_{3d} defects is set by the spin-orbit interaction. The values of the splittings for the SiV are $\lambda_g = 48$ GHz and $\lambda_e = 259$ GHz [1]. For GeV, we have λ_g=190 GHz and λ_e=981 GHz [2]. For SnV, we have λ_g=850 GHz and λ_e=3 THz. [3]

B.2.2 Magnetic fields

External magnetic fields couple to both the orbital and spin degree of freedom through the Zeeman interaction. The Zeeman Hamiltonian is given by the following

$$H_B = \gamma_\ell \mathbf{L} \cdot \mathbf{B} + \gamma_s \mathbf{S} \cdot \mathbf{B} \tag{B.16}$$

where $\gamma_\ell = \mu_B/\hbar = 1.4$ MHz/G and $\gamma_s = 2\mu_B/\hbar = 2.8$ MHz/G are the orbital and spin gyromagnetic ratios respectively. Recall that the transverse angular momentum operators are precisely zero, and thus the Hamiltonian simplifies to

$$H_B = \gamma_\ell L_z B_z + \gamma_s \mathbf{S} \cdot \mathbf{B} \tag{B.17}$$

Let's work in the spin-orbit basis once more. Also, let's define a generic perpendicular magnetic field, $B_\perp = \sqrt{B_x^2 + B_y^2}$ and a corresponding azimuthal angle $\theta_B = \arctan(B_y/B_x)$ such that $B_x = B_\perp \cos(\theta_B)$ and $B_y = B_\perp \sin(\theta_B)$.

We can express this Hamiltonian in terms of the spin-orbit basis states in either manifold, given by $\{|e_+,\uparrow\rangle, |e_+,\downarrow\rangle, |e_-,\uparrow\rangle, |e_-,\downarrow\rangle\}$.

$$H_B = \begin{pmatrix} (\gamma_\ell + \gamma_s)B_z & \gamma_s B_\perp e^{-i\theta_B} & 0 & 0 \\ \gamma_s B_\perp e^{i\theta_B} & (\gamma_\ell - \gamma_s)B_z & 0 & 0 \\ 0 & 0 & -(\gamma_\ell - \gamma_s)B_z & \gamma_s B_\perp e^{-i\theta_B} \\ 0 & 0 & \gamma_s B_\perp e^{i\theta_B} & -(\gamma_\ell + \gamma_s)B_z \end{pmatrix} \tag{B.18}$$

B.2.3 Strain-orbit coupling

The interaction of the D_{3d} defects with crystal strain arises from a change in the ion-electron Coulomb interaction, similarly to the NV center. The Hamiltonian can be written as

$$H_{strain} = \sum_{j,k} H_{jk} = \sum_{j,k} V_{jk}\epsilon_{jk} \tag{B.19}$$

where $V_{jk} = \sum_l \frac{\partial U_{el-ion}}{\partial(\delta R_j^l)}\delta R_k^l$. Note that $\mathbf{V}$ and $\boldsymbol{\epsilon}$ are both second rank symmetric tensors, and so their components transform as the quadratic forms of the D_{3d} group. Therefore, it will be useful to express H_{strain} in terms of quantities that transform as specific irreducible representations. Using table B.2, we see that the strain Hamiltonian can be written as

$$H_{strain} = V_A\epsilon_{zz} + V_{A'}(\epsilon_{xx}+\epsilon_{yy}) + V_x(\epsilon_{xx}-\epsilon_{yy}) + V_y(\epsilon_{xy}+\epsilon_{yx}) + V_{x'}(\epsilon_{xz}+\epsilon_{zx}) + V_{y'}(\epsilon_{yz}+\epsilon_{zy}) \tag{B.20}$$

where $V_{A,A'}$ are orbital operators of A_{1g} symmetry, $V_{x,x'}$ are orbital operators transforming as the first row of the E_g irreducible representation and $V_{y,y'}$ are orbital operators transforming as the second row of the E_g irreducible representation.

Let us work in a 4-dimensional basis spanned by the orbital eigenstates $\{|e_{gx,y}\rangle, |e_{ux,y}\rangle\}$. We note that strain may couple both the excited state and ground state orbitals to the A symmetric orbitals, but we neglect that interaction here as the large energy gap between the orbitals will suppress it. Moreover, we will temporarily neglect the spin-orbit interaction. The total strain Hamiltonian can thus be written as

$$\begin{aligned} H_{strain} &= (\lambda_1\epsilon_{zz} + \lambda_2(\epsilon_{xx}+\epsilon_{yy}))(|e_{gx}\rangle\langle e_{gx}| + |e_{gy}\rangle\langle e_{gy}|) \\ &+ (\lambda_3\epsilon_{zz} + \lambda_4(\epsilon_{xx}+\epsilon_{yy}))(|e_{ux}\rangle\langle e_{ux}| + |e_{uy}\rangle\langle e_{uy}|) \\ &- (\lambda_5(\epsilon_{xx}-\epsilon_{yy})) - \lambda_6(\epsilon_{xz}+\epsilon_{zx}))(|e_{gx}\rangle\langle e_{gx}| - |e_{gy}\rangle\langle e_{gy}|) \\ &- (\lambda_7(\epsilon_{xx}-\epsilon_{yy})) - \lambda_8(\epsilon_{xz}+\epsilon_{zx}))(|e_{ux}\rangle\langle e_{ux}| - |e_{uy}\rangle\langle e_{uy}|) \\ &+ (\lambda_9(\epsilon_{xy}+\epsilon_{yx})) + \lambda_{10}(\epsilon_{yz}+\epsilon_{zy}))(|e_{gx}\rangle\langle e_{gy}| + |e_{gy}\rangle\langle e_{gx}|) \\ &+ (\lambda_{11}(\epsilon_{xy}+\epsilon_{yx})) + \lambda_{12}(\epsilon_{yz}+\epsilon_{zy}))(|e_{ux}\rangle\langle e_{uy}| + |e_{uy}\rangle\langle e_{ux}|) \end{aligned} \quad \text{(B.21)}$$

Since the strain interaction is much more likely to be small compared to the spin-orbit coupling, it will be wise to rewrite the strain Hamiltonian in terms of the spin-orbit basis states. For simplicity, let's work within either the ground or excited state manifold (it doesn't matter which one we choose). The simplified Hamiltonian can be written as

$$H = V_A(|e_x\rangle\langle e_x| + |e_y\rangle\langle e_y|) + V_{E_1}(|e_x\rangle\langle e_x| - |e_y\rangle\langle e_y|) + V_{E_2}(|e_x\rangle\langle e_y| + |e_y\rangle\langle e_x|) \quad \text{(B.22)}$$

If we include the spin, the transformation to the spin-orbit basis takes the form

$\mathbf{Q} = T \otimes I$, where T is defined by

$$\begin{pmatrix} e_+ \\ e_- \end{pmatrix} = T \begin{pmatrix} e_x \\ e_y \end{pmatrix} \tag{B.23}$$

which means that $T = \frac{1}{\sqrt{2}} \begin{pmatrix} -1 & -i \\ 1 & -i \end{pmatrix}$. The strain Hamiltonian in the spin-orbit basis is given by $\tilde{H} = QHQ^\dagger$, and we see

$$\begin{aligned} \tilde{H} &= V_A \Big[|e_+,\uparrow\rangle\langle e_+,\uparrow| + |e_+,\downarrow\rangle\langle e_+,\downarrow| + |e_-,\uparrow\rangle\langle e_-,\uparrow| + |e_-,\downarrow\rangle\langle e_-,\downarrow| \Big] \\ &- (V_{E_1} + iV_{E_2}) \Big[|e_+,\uparrow\rangle\langle e_-,\uparrow| + |e_+,\downarrow\rangle\langle e_-,\downarrow| \Big] \\ &- (V_{E_1} - iV_{E_2}) \Big[|e_-,\uparrow\rangle\langle e_+,\uparrow| + |e_-,\downarrow\rangle\langle e_+,\downarrow| \Big] \end{aligned} \tag{B.24}$$

defining the total E type strain coupling as $V_E = \sqrt{V_{E_1}^2 + V_{E_2}^2}$ and $\tan(\phi) = V_{E_2}/V_{E_1}$, we see the Hamiltonian can be written as

$$\begin{aligned} \tilde{H} &= V_A \Big[|e_+,\uparrow\rangle\langle e_+,\uparrow| + |e_+,\downarrow\rangle\langle e_+,\downarrow| + |e_-,\uparrow\rangle\langle e_-,\uparrow| + |e_-,\downarrow\rangle\langle e_-,\downarrow| \Big] \\ &- V_E \Big[e^{i\phi} \Big[|e_+,\uparrow\rangle\langle e_-,\uparrow| + |e_+,\downarrow\rangle\langle e_-,\downarrow| \Big] + e^{-i\phi} \Big[|e_-,\uparrow\rangle\langle e_+,\uparrow| + |e_-,\downarrow\rangle\langle e_+,\downarrow| \Big] \Big] \end{aligned} \tag{B.25}$$

B.2.4 Spin-strain coupling

There is now considerable interest in the spin of the D_{3d} defects center for applications in quantum information processing. In this section, we demonstrate that the spin of such defects is insensitive to crystal strain, and hence should be immune to decoherence due to direct (single) phonon processes, unlike the spinorbit states.

Spin-strain interaction typically requires the presence of fine structure. In the case

of the NV center, spin-strain interaction arises due to the presence of transverse spin-orbit coupling as well as direct modification of the spin-spin interactiob due to distortion of the unpaired spin density. As these defects lacks spin-spin interaction, spin-orbit coupling is the only possible mechanism for spin-strain coupling. However, as we showed in the previous section, the tranverse spin-orbit interaction is precisely zero within the ground and excited state manifolds. Additionally, the transverse spin-orbit interaction transforms as E_g and hence cannot couple states of opposite parity, which means there is no coupling between the ground and excited states either. Therefore, strain does not affect the spin degree of freedom. We note, however, that D_{3d} defects with spin $S > 1/2$, such as SiV^0, may exhibit spin-strain coupling.

B.2.5 The Stark effect

Let us now consider the electric field interaction with the ground and excited state manifolds. The electric field Hamiltonian in the dipole approximation is given by

$$H_E = -\vec{d} \cdot \vec{E} \tag{B.26}$$

where $\vec{d} = q\vec{r}$ is the electric dipole operator. Again, let us neglect the spin-orbit coupling and consider the effect of the electric field on the unperturbed orbital eigenstates. Because the dipole operator is a vector quantity, its components will transform as the linear elements of the D_{3d} group. Therefore, we see that (d_x, d_y, d_z) will transform as (E_{u1}, E_{u2}, A_{2u}). Interestingly, we immediately see that strain and electric field are NOT equivalent for D_{3d} since they are of different symmetry. This is a direct result of the inversion symmetry. Indeed the Stark effect is quite different from the effect of crystal strain. Using the group multiplication table, the dipole operators can be written in the $\{|e_{gx}\rangle, |e_{gy}\rangle, |e_{ux}\rangle, |e_{uy}\rangle\}$.

$$d_z = \begin{pmatrix} 0 & 0 & d_\parallel & 0 \\ 0 & 0 & 0 & d_\parallel \\ d_\parallel^* & 0 & 0 & 0 \\ 0 & d_\parallel^* & 0 & 0 \end{pmatrix} \tag{B.27}$$

$$d_x = \begin{pmatrix} 0 & 0 & d_\perp & 0 \\ 0 & 0 & 0 & d_\perp \\ d_\perp^* & 0 & 0 & 0 \\ 0 & -d_\perp^* & 0 & 0 \end{pmatrix} \tag{B.28}$$

$$d_y = \begin{pmatrix} 0 & 0 & 0 & d_\perp \\ 0 & 0 & d_\perp & 0 \\ 0 & d_\perp^* & 0 & 0 \\ d_\perp^* & 0 & 0 & 0 \end{pmatrix} \tag{B.29}$$

As we can see, the electric field has no effect within the ground or excited state manifolds, but only acts to connect the two manifolds. In contrast with the NV center, the z component of the dipole operator can drive optical transitions in D_{3d} defects. To get the final matrix elements, we rewrite the dipole operators in the spin-orbit basis. This can be done via $Qd_iQ^\dagger$, where $Q = \begin{pmatrix} T & 0 \\ 0 & T \end{pmatrix}$.

The dipole operators written in the basis $\{|e_{g+}, m_s\rangle, |e_{g-}, m_s\rangle, |e_{u+}, m_s\rangle, |e_{u-}, m_s\rangle\}$ are

$$d_z = \begin{pmatrix} 0 & 0 & d_\parallel & 0 \\ 0 & 0 & 0 & d_\parallel \\ d_\parallel^* & 0 & 0 & 0 \\ 0 & d_\parallel^* & 0 & 0 \end{pmatrix} \tag{B.30}$$

$$d_x = \begin{pmatrix} 0 & 0 & 0 & -d_\perp \\ 0 & 0 & -d_\perp & 0 \\ 0 & -d_\perp^* & 0 & 0 \\ -d_\perp^* & 0 & 0 & 0 \end{pmatrix} \tag{B.31}$$

$$d_y = \begin{pmatrix} 0 & 0 & 0 & -id_\perp \\ 0 & 0 & id_\perp & 0 \\ 0 & -id_\perp^* & 0 & 0 \\ id_\perp^* & 0 & 0 & 0 \end{pmatrix} \tag{B.32}$$

From here, we see the $|e_{g\pm}, m_s\rangle \to |e_{u\pm}, m_s\rangle$ transitions are driven by linearly polarized light along the z direction. Moreover, the $|e_{g+}, m_s\rangle \to |e_{u-}, m_s\rangle$ and $|e_{g-}, m_s\rangle \to |e_{u+}, m_s\rangle$ transitions are driven by circularly polarized light. Specifically, the $|e_{g+}, m_s\rangle \to |e_{u-}, m_s\rangle$ transition is mediated by $\sigma^+ = \hat{x} + i\hat{y}$ polarized light and the $|e_{g-}, m_s\rangle \to |e_{u+}, m_s\rangle$ transition is mediated by $\sigma^- = \hat{x} - i\hat{y}$ polarized light. A diagram showing the relevant selection rules is shown in fig. B.3.

Selection rules under crystal strain

The polarization selection rules for these will be modified by the presence of E_g symmetric crystal strain. Let us work within either the ground or excited state manifold.

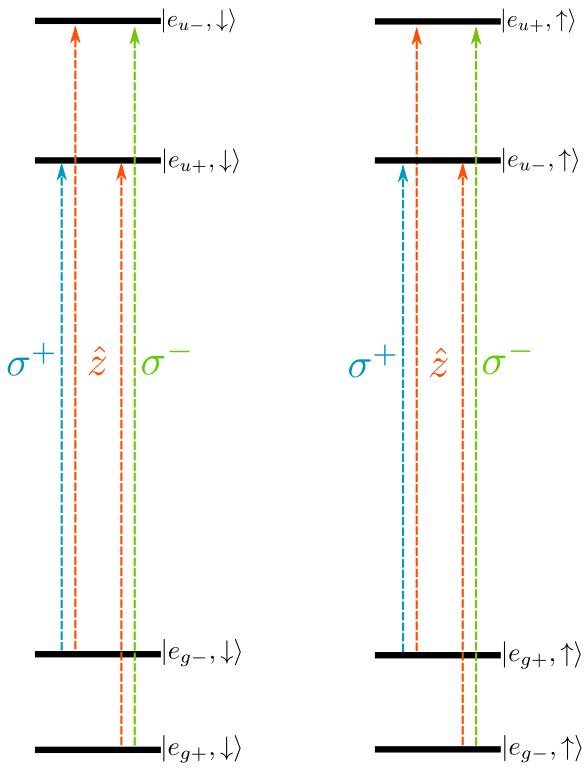

Figure B.3: **Polarization selection rules**. Here, we show the polarization selection rules with no external perturbations

The total Hamiltonian defined in the $\{|e_+,\uparrow\rangle, |e_+,\downarrow\rangle, |e_-,\uparrow\rangle, |e_-,\downarrow\rangle\}$ basis is given by

$$H = \begin{pmatrix} V_A + \frac{\lambda}{2} & 0 & -V_E e^{i\phi} & 0 \\ 0 & V_A - \frac{\lambda}{2} & 0 & -V_E e^{i\phi} \\ -V_E e^{-i\phi} & 0 & V_A - \frac{\lambda}{2} & 0 \\ 0 & -V_E e^{-i\phi} & 0 & V_A + \frac{\lambda}{2} \end{pmatrix} \tag{B.33}$$

The spin-orbit coupling and the E_g symmetric strain interaction do not commute, and will lead to the following new eigenstates

$$|+,\uparrow\rangle = \sin(\theta)\,|e_+,\uparrow\rangle + e^{-i\phi}\cos(\theta)\,|e_-,\uparrow\rangle \tag{B.34}$$

$$|-,\uparrow\rangle = -\cos(\theta)\,|e_+,\uparrow\rangle + e^{-i\phi}\sin(\theta)\,|e_-,\uparrow\rangle \tag{B.35}$$

$$|-,\downarrow\rangle = \sin(\theta)\,|e_+,\downarrow\rangle - e^{-i\phi}\cos(\theta)\,|e_-,\downarrow\rangle \tag{B.36}$$

$$|+,\downarrow\rangle = \cos(\theta)\,|e_+,\downarrow\rangle + e^{-i\phi}\sin(\theta)\,|e_-,\downarrow\rangle \tag{B.37}$$

where we have defined $\tan(2\theta) = 2V_E/\lambda$. These corresponding energies are

$$E_{+\uparrow} = V_A - \sqrt{\lambda^2/4 + V_E^2} \tag{B.38}$$

$$E_{-\uparrow} = V_A + \sqrt{\lambda^2/4 + V_E^2} \tag{B.39}$$

$$E_{-\downarrow} = V_A + \sqrt{\lambda^2/4 + V_E^2} \tag{B.40}$$

$$E_{+\downarrow} = V_A - \sqrt{\lambda^2/4 + V_E^2} \tag{B.41}$$

Note that we still have two two-fold degenerate branches within each manifold. Now we can re-express the dipole operators in terms of these new eigenstates. We will work in the following basis $\{|+_g\rangle, |-_g\rangle, |+_u\rangle, |-_u\rangle\}$ and treat spin up and spin down separately. We will explicitly show the spin up calculation and leave the spin down calculation as an exercise for you. Expressing the dipole operators in the eigenstates of the strain Hamiltonian requires the transformation $Ud_iU^\dagger$, where $U = \begin{pmatrix} Q & 0 \\ 0 & Q \end{pmatrix}$.

$$\mathbf{Q} = \begin{pmatrix} \sin(\theta) & e^{-i\phi}\cos(\theta) \\ -\cos(\theta) & e^{-i\phi}\sin(\theta) \end{pmatrix} \tag{B.42}$$

The resulting dipole operators are

$$d_z = \begin{pmatrix} 0 & 0 & d_\parallel & 0 \\ 0 & 0 & 0 & d_\parallel \\ d_\parallel^* & 0 & 0 & 0 \\ 0 & d_\parallel^* & 0 & 0 \end{pmatrix} \tag{B.43}$$

$$d_x = \begin{pmatrix} 0 & X \\ X & 0 \end{pmatrix} \tag{B.44}$$

$$X = \begin{pmatrix} -d_\perp \cos(\phi)\sin(2\theta) & d_\perp(\cos(2\theta)\cos(\phi) - i\sin(\phi)) \\ d_\perp(\cos(2\theta)\cos(\phi) + i\sin(\phi)) & d_\perp \cos(\phi)\sin(2\theta) \end{pmatrix} \tag{B.45}$$

$$d_y = \begin{pmatrix} 0 & Y \\ Y & 0 \end{pmatrix} \tag{B.46}$$

$$Y = \begin{pmatrix} d_\perp \sin(\phi)\sin(2\theta) & -d_\perp(\cos(2\theta)\sin(\phi) + i\cos(\phi)) \\ id_\perp(\cos(2\theta)\sin(\phi) + \cos(\phi)) & -d_\perp \sin(\phi)\sin(2\theta) \end{pmatrix} \tag{B.47}$$

B.3 Conclusion

In this chapter, we have calculated the electronic structure of negatively charged D_{3d} defect centers incorporating group IV atoms. We explicitly showed that electric fields do not affect the optical transitions to first order, and are thus inefficient for tuning the optical properties. Furthermore, we demonstrated that the A_1 symmetric strain interaction can be used to shift the zero-phonon line of these defects, and moreover, that E symmetric strain can be used to modify the dipole selection rules.

Appendix C

Spin phonon coupling with Si:Bi

C.1 Strain coupling to Si:Bi

Bismuth donors in silicon (Si:Bi) are a promising platform for a quantum memory due to their exceptional spin coherence properties [241]. The Si:Bi system contains a single electron spin with $S = 1/2$ coupled to a nuclear spin $I = 9/2$. The rich energy structure and unusually large hyperfine constant of $A = 1.475169$ GHz give rise to several unique properties that are ideal for quantum memories. For instance, hyperfine clock transitions have been isolated with coherence times exceeding 1 s at cryogenic temperatures. Very recently, experiments have shown that the Si:Bi system is extremely senstive to crystal strain [242], opening up the door to possible spin-phonon experiments. In this appendix, we investigate a system of large ensembles of Si:Bi coupled to a mechanical oscillator through crystal strain. In particular, we assess the possibility of measuring strong coupling between the spin ensemble and the mechanical resonator through measurements of the mechanical resonance.

C.1.1 Si:Bi strain coupling

There are two possible mechanisms that may explain the strain coupling to the Si:Bi system. The first is through a strain-induced quadrupolar interaction and the second is a direct modification of the hyperfine interaction. Let us first consider the quadrupole interaction.

The orbital ground state of the Si:Bi system has A_1 symmetry which is spherically symmetric, and hence does exhibit and nuclear quadrupolar coupling. However, E symmetric strain can mix the A_1 ground state with the E symmetric excited state, generating an effective electric field gradient which couples to the nuclear quadrupole moment. This could also be explained by a strain-induced mixing between the T_2 orbitals due to shear strain, which transforms as the T_2 irreducible representation. Without going into too many details, we can write the quadrupolar strain coupling Hamiltonian as

$$H_{strain} = \sum_{ij} Q_{ij}\epsilon_{ij} \tag{C.1}$$

where ϵ is the elastic strain tensor and Q is the quadrupole tensor. As it turns out, strain of E symmetry directly couples nuclear spin states with $|\Delta m_I| = 2$, similar to the NV center, whereas A symmetric strain shifts the nuclear spin sublevels relative to each other.

Now, let us consider the effect of strain on the hyperfine interaction. As we discussed in chapter 2 of this thesis, the hyperfine interaction consists of an isotropic contact interaction plus an anisotropic spin-spin interaction. A positive hydrostatic pressure, corresponding to an A_1 strain, could increase the electron density at the site of the Bismuth atom, thereby increasing the contact interaction and increasing the spin-spin interaction. The effect of E and T_2 strain would be negligible, because the A_1 ground state is unaffected by those strains to first order. The modification of the hyperfine

interaction would also be large due to the large intrinsic hyperfine coupling. Recent unpublished studies have shown that the large strain coupling in the Si:Bi system is to A_1 strain, and hence the hyperfine modification may be the primary effect at work (Private communication with John Morton)

To keep things simple, let us consider two hyperfine levels that can be connected via strain, and label them $|\uparrow\rangle$ and $|\downarrow\rangle$. Moreover, let us consider a strain field produced by a resonant mode of a mechanical oscillator with phonon annihilation (creation) operator a ($a^\dagger$) and frequency ω_m.

Let us first consider the interaction of a single donor with the resonator, and deal with ensemble dynamics later. For both possible strain mechanisms, we may describe the interaction of a single donor with the mecahnical resonator with the Jaynes-Cummings Hamiltonian

$$H = \frac{\omega_0}{2}\sigma_z + \omega_m a^\dagger a + g(\sigma^+ a + \sigma^- a^\dagger) \tag{C.2}$$

where g represents the the strain coupling to the zero point motion of the resonator. Moving into the interaction picture, and assuming resonance ($\omega_0 = \omega_m$), we have

$$H_I = g(\sigma^+ a + \sigma^- a^\dagger) \tag{C.3}$$

Clearly we can drive transitions between the two spin levels by adding or removing vibrational quanta with a Rabi frequency that is proportional to g and dependent on the vibrational level state. The eigenstates of the Hamiltonian are the so-called dressed states: $|\pm, n\rangle = (|\uparrow, n\rangle \pm |\downarrow, n+1\rangle)/\sqrt{2}$. These two states are separated by $2g\sqrt{n+1}$. If the resonator is initially in its ground state, then the separation is merely $2g$. Therefore, $2g$ is sometimes referred to as the vacuum Rabi splitting. When doing spectroscopy of the resonator or the spin, an avoided crossing with a gap of $2g$ would appear.

Let us now consider a measurement of the mechanical resonance as a way to probe the spin-phonon coupling. Our experiments will be carried out at temperatures around 4 K, and we will be unable to further cool the mechanical mode. Therefore, any mode less than 50 GHz will not be in the ground state, but some thermal state with average occupation number $\bar{n}$. In a thermal state, the probability to be in a vibrational state $|n\rangle$ is given by

$$P_n = \frac{1}{1+\bar{n}}\left(\frac{\bar{n}}{1+\bar{n}}\right)^n \tag{C.4}$$

Therefore, the total wavefunction for the system can be written as

$$|\psi\rangle = (\alpha\,|\uparrow\rangle + \beta\,|\downarrow\rangle) \otimes \sum_n P_n\,|n\rangle \tag{C.5}$$

Populating several vibrational states in an incoherent manner induces dephasing and hence washes out the Rabi splitting. As $\bar{n}$ increases, the oscillator damping term begins to dominate the spin-phonon interaction. This is because the damping scales linearly with n while the spin-phonon interaction scales as $\sqrt{n}$. As a result, the spectrum of the resonator will just appear as the usual Lorentzian spectrum describing a damped harmonic oscillator. Therefore, we need to look in the limit that $g\sqrt{n} > n\Gamma$, where $\Gamma = \omega_m/Q$ is the damping rate. This implies that we need $\bar{n} < (g/\Gamma)^2 = (gQ/\omega_m)^2$. In other words, we need to be in the high cooperativity regime.

To demonstrate this, I have simulated some spectra assuming some lofty parameters, shown in fig. C.1. In these simulations, I assume that $Q = 10^5$ and $g = .001\omega_m$ and vary the thermal occupation number of the resonator. As the temperature of the resonator increases, the Rabi splitting decreases and the peaks overlap. The spectrum of the

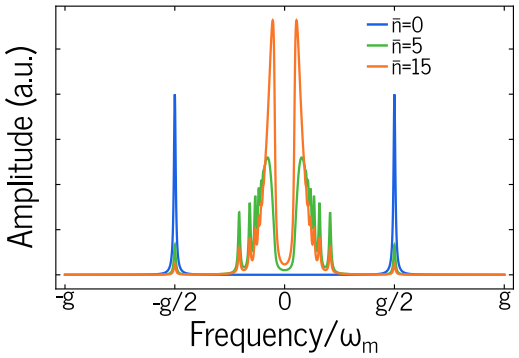

Figure C.1: **Vacuum Rabi splitting of a mechanical oscillator coupled to a single SiBi**. As the thermal occupation of the resonator increases, the Rabi splitting is washed out.

mechanical oscillator is defined by

$$S_{xx}(\omega) = \int_{-\infty}^{\infty} dt e^{i\omega t} \langle x(0)x(t) \rangle \tag{C.6}$$

where $x = a + a^\dagger$. The power spectrum of the oscillator position depends on the transition rates between the dressed states in the following way

$$S_{xx}(\omega) = \sum_{i,f} P_i |\langle f| a + a^\dagger |i\rangle|^2 \left(\frac{\Gamma/2}{(\Gamma/2)^2 + (\omega - \omega_{fi})^2} + \frac{\Gamma/2}{(\Gamma/2)^2 + (\omega + \omega_{fi})^2} \right) \tag{C.7}$$

where $|i(f)\rangle$ refer to the dressed states and ω_{fi} refers to the frequency difference between the states. Note that we have assumed the high Q limit which allows us to write the power spectrum as a series of Lorentzians. The position operator leads to non-zero matrix elements between states whose phonon numbers differ by one. More specifically, the allowed transitions can be broken up into two subclasses: The first couple $|\pm, n-1\rangle$ to $|\pm, n\rangle$ and the second couple $|\pm, n-1\rangle$ to $|\mp, n\rangle$. It can be shown that the second class listed will have a negligible affect on the mechanical spectrum, as they are highly

suppressed by temperature. The first class, however, contributes significantly to the spectrum. By doing some algebra, one can show

$$|\langle f|\, a + a^\dagger\, |i\rangle\,| = \frac{1}{2}(\sqrt{n} + \sqrt{n+1}) \tag{C.8}$$

$$\omega_{fi} = g(\sqrt{n+1} - \sqrt{n}) \tag{C.9}$$

C.1.2 Ensemble dynamics and the Tavis-Cummings model

As shown in the previous section, for a single spin coupled to a thermal oscillator with $\bar{n} > 1$, the mechanical spectrum is highly non-linear and the Rabi splitting is suppressed with increasing temperature. Overcoming this non-linear behavior can be accomplished by cooling the mechanical mode or by adding more spins into the system. The addition of spins suppresses the Jaynes-Cummings nonlinearity because the collective spin can hold onto more phonon excitations than a single spin. Indeed, if the number of spins N exceeds the number of phonon excitations n, the energy spectrum is approximately linear and the Rabi splitting is maintained.

To show this, let us introduce the Tavis-Cummings model, which deals with N spins coupled to a single phonon mode.

$$H = \frac{\omega_0}{2} J_z + \omega_m a^\dagger a + \bar{g}(J_+ a + J_- a^\dagger) \tag{C.10}$$

Here $\mathbf{J}$ is the collective spin operator, with $J_z = \sum_{i=1}^{N} \sigma_z^i$ and $J_\pm = \sum_{i=1}^{N} \sigma_\pm^i$. In this model, we have assumed the single-spin coupling g_i is different for each spin, and have

replaced it with the effective coupling $\bar{g}$.

$$\bar{g} = \sqrt{\frac{\sum_{i=1}^{N} g_i^2}{N}} \tag{C.11}$$

We can define the system in terms of the total number of excitations $M = J_+ J_- + a^\dagger a$ and note that $[H, M] = 0$. The total excitation number then counts the number of up spins in the system and the phonon number. The ground state of the Tavis-Cummings model is a state with zero total excitations, that is

$$|M = 0\rangle = |\downarrow\downarrow \cdots \downarrow_i \cdots \downarrow_N\rangle \, |n = 0\rangle \tag{C.12}$$

For now, let us consider the resonant case where $\omega_0 = \omega_m$. The first excited state of course contains one single excitation, either from the spin or the phonon field and can be written as

$$|\pm\rangle = \frac{1}{\sqrt{2N}} \sum_{i=1}^{N} |\downarrow\downarrow \cdots \uparrow_i \cdots \downarrow_N\rangle \, |n = 0\rangle \pm \frac{1}{\sqrt{2}} \, |\downarrow\downarrow \cdots \downarrow_i \cdots \downarrow_N\rangle \, |n = 1\rangle \tag{C.13}$$

The energy gap between these two states is simply $\Delta E = 2\bar{g}\sqrt{N}$. The $M = 2$ manifold contains three states, and as we ascend the Tavis-Cummings ladder, the number of levels in each manifold M increases until $n > N$. For $n < N$, there are $n + 1$ levels in each manifold. For $n > N$ there are $N + 1$ levels in each manifold. Hence, for $n > N$ the number of states in each manifold is constant and the energy-level spacing changes, introducing strong non-linearity.

Let's assume for now that we are working in the large N limit where n controls the number of states in each manifold. The approximate energies of the system are written

as

$$E(n,j) \approx (n - N/2)\omega_0 + 2j\bar{g}\sqrt{N} \tag{C.14}$$

where of course $0 \leq n \leq N$ and $-n/2 \leq j \leq n/2$. You can think of j as the effective m number for a given multiplet. In the $n = 1$ manifold for instance there are two dressed states and correspondingly, we have $j \in \{-1/2, 1/2\}$. The energy splitting between those two states would then be $E(1, 1/2) - E(1, -1/2) = 2\bar{g}\sqrt{N}$ as we would expect.

As discussed in the previous section, our measurements probe the position operator of the resonator $x = a + a^\dagger$ which couples states of different manifolds and hence probes their difference frequencies. In the limit of large N, the power spectral density of the position (offset by ω_0 in frequency) can be written as

$$\begin{aligned} S_{xx}(\omega) = &\sum_{n,j,j'} P_n \left|\langle n+1, j| \, a + a^\dagger \, |n, j'\rangle\right|^2 \\ &\times \left(\frac{\Gamma/2}{(\Gamma/2)^2 + (\omega - (j-j')2\bar{G}\sqrt{N})^2} + \frac{\Gamma/2}{(\Gamma/2)^2 + (\omega + (j-j')2\bar{G}\sqrt{N})^2} \right) \end{aligned} \tag{C.15}$$

For large numbers of spins, we expect the $\Delta j = \pm 1/2$ terms to dominate the spectrum, as the other terms are suppressed by temperature.

C.1.3 Thermally Polarized Spins

In our experiments, we will be working with a relatively large ensemble of spins. Since we have no way of polarizing the spins, they will be in a thermal state and hence described by Boltzmann statistics. To calculate the thermal population, we must consider the full nuclear spin Hamiltonian, which includes hyperfine interaction. The total Hamiltonian

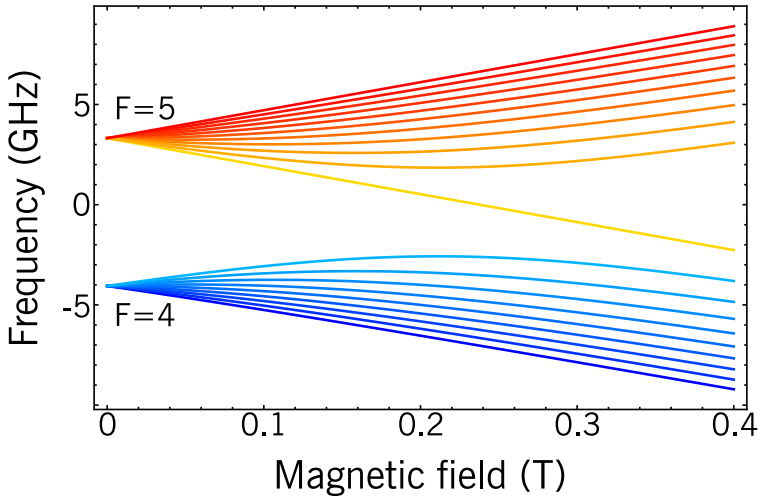

Figure C.2: **Energy of the Si:Bi system with magnetic fields**.

is

$$H = A(\mathbf{S} \cdot \mathbf{I}) - (\gamma_e \mathbf{S} + \gamma_n \mathbf{I}) \cdot \mathbf{B} \tag{C.16}$$

In the low magnetic field regime, the eigenstates of the Hamiltonian correspond to eigenstates of the total angular momentum operator, $\mathbf{F} = \mathbf{I} + \mathbf{S}$ and can be labeled $|F, m_F\rangle$. In the high magnetic field regime, $\mathbf{I}$ and $\mathbf{S}$ are good quantum numbers and the states can be written as $|m_s, m_I\rangle$. We will most likely be working in regimes where $\mathbf{F}$ is a good quantum number, but we will solve for the exact eigenstates and eigenvalues anyway. Luckily, we have $S = 1/2$ and the solution to the system can be solved for analytically. The solution is the famous Breit-Rabi formula, and an energy plot of the eigenstates as a function of magnetic field is shown in fig. C.2.

The full spin Hamiltonian can be recast in terms of the spin operators

$$H = AS_zI_z + \frac{A}{2}(S_+I_- + S_-I_+) - (\gamma_e S_z + \gamma_n I_z)B \tag{C.17}$$

In all regimes, the quantity $m_F = m_I + m_S$ is conserved. It is useful to define the

eigenstates of the system in terms of m_F:

$$|\pm\rangle = |m_S = \pm 1/2, m_I = m_F \mp 1/2\rangle \tag{C.18}$$

As we can see, the Hamiltonian can be diagonalized within a series of 2-D matrices spanned by $|\pm\rangle$, where + refers to the $F = 5$ manifold and − refers to the $F = 4$ manifold. The eigenvalues of this Hamiltonian are

$$E(\pm, m_F) = A\left(-\frac{1}{4} + \frac{\gamma_n B}{A} m_F \pm \sqrt{(I+1/2)^2 + 2m_F x + x^2}\right) \tag{C.19}$$

where $x = \frac{(\gamma_e - \gamma_n)B}{A}$ gives the relative strength of the magnetic field with respect to the hyperfine coupling. It is important to note that these eigenvalues are not valid for the $|F = 5, m_F = \pm 5\rangle$ states since they do not have any direct coupling to states in the $F = 4$ manifold. This is evident by their linear behavior. The eigenvalues for these two states are $E(5, \pm 5) = \frac{9A}{4} \pm 5\gamma_n B \pm (\gamma_e - \gamma_n)B$. The spectrum showing all 20 eigenstates is shown above.

The dipole selection rules in the regime where F is a good quantum number obey $(\Delta F = 0, \Delta m_F = \pm 1)$ and $(\Delta F = \pm 1, \Delta m_F = 0, \pm 1)$.

Now that we know the energies, we can calculate the density matrix for the system when its thermally populated. The system temperature will be set to 4 K. We must also choose the magnetic field strength. To choose the proper strength, we must identify where a target transition has a resonance frequency near 5 GHz, which will be near the mechanical frequency. The quadrupole-strain interaction can be written as

$$H_Q = g_{A_1} I_z^2 + g_E (I_+^2 + I_-^2) \tag{C.20}$$

Because of the strong hyperfine interaction, the transverse strain or E symmetric

strain will be able to induce transitions with $\Delta m_F = \pm 2$. Looking back at our spectrum, it makes sense to set the field strength to be near 200 mT, where the $|4, -3\rangle \leftrightarrow |5, -5\rangle$ transition is near 5 GHz.

Now that we have all of our parameters, we can solve for the populations, given by

$$\rho_i = \frac{e^{-E_i/k_B T}}{\sum_j e^{-E_j/k_B T}} \tag{C.21}$$

where i and j index all 20 eigenstates. At a temperature of 4 K, the population difference between the $|4, -3\rangle$ and $|5, -5\rangle$ states is about $\Delta\rho = 0.7\%$.

C.1.4 Calculation of the strain coupling

The measured strain coupling for Si:Bi (unpublished) is approximately 150 GHz. To see if measuring a Rabi splitting is possible, we assume optimistic parameters that purposefully overestimate the strength of the coupling. Let us consider a SAW cavity described in chapter 8, but in silicon instead of diamond. This device would generate the approximate 5 GHz frequency calculated from the previous section. The peak zero-point strain in the device is roughly 8×10^{-10}. In this calculation, we assume a uniform density of Si:Bi spins through the SAW cavity volume of (5.25 μm, 200 μm, 200 nm). The maximum bismuth donor implantation density is 10^{23} spins/m^3. If we assume a constant strain profile throughout the device with a value of the peak strain, and a generous 5% spin polarization, the ensemble coupling would be $g = 30$ kHz. At 4 K, the average thermal occupation of the SAW is approximately $\bar{n} = 16$ which is much less than the number of spins. Therefore, it is safe to treat this system as a single spin with an effective $S = N/2$ interacting with the phonon field, and we would expect a vacuum Rabi splitting of 30 kHz. However, if the SAW cavity has a quality factor $Q = 10^5$, then the mechanical linewidth would be 50 kHz, and we would be unable to resolve the

vacuum Rabi splitting, which is likely overestimated by an order of magnitude, if not more. Unless the spin polarization is dramatically improved, this system is unlikely to reach the strong coupling regime.

Appendix D

Spectrum under a coherent mechanical drive

In our first experiments with high frequency resonators, we will look at the mechanical sidebands of the ZPL for a coherently driven mechanical mode. To model the spectral response of the NV center, we introduce the Hamiltonian

$$H = -\frac{\omega_0}{2}\sigma_z + \omega_m a^\dagger a + g_\parallel(a + a^\dagger)\sigma_z + \Omega\cos(\omega_L t)\sigma_x \tag{D.1}$$

where $\sigma_z = |g\rangle\langle g| - |e\rangle\langle e|$. Under a coherent mechanical drive, the resonator's motion can be described by a large amplitude coherent state,

$$|\alpha\rangle = e^{-\alpha^2/2}\sum_{n=0}^{\infty}\frac{\alpha^n}{\sqrt{n!}}|n\rangle \tag{D.2}$$

where $|n\rangle$ represent the Fock states of the resonator mode and α is a dimensionless number giving the amplitude of the coherent state. If we define $g = 2g_\parallel\alpha$, then the above

Hamiltonian can be written as

$$H = -\frac{\omega_0}{2}\sigma_z + g\cos\omega_m t\sigma_z + \Omega\cos\omega_L t\sigma_x \tag{D.3}$$

Here, the qubit frequency is oscillating at the resonator frequency, and thus moves in and out of resonance with the probe laser. In the stationary frame of the qubit, it appears as though the laser frequency is thus being modulated at the resonator frequency. Equivalently, this frequency modulation can expressed as a phase modulation of the laser light, producing sidebands on the laser. In this picture, the Hamiltonian obeys

$$H = -\frac{\omega_0}{2}\sigma_z + \Omega\cos\left(\omega_L t + \frac{g}{\omega_m}\cos\omega_m t\right)\sigma_x \tag{D.4}$$

In the interaction picture with respect to $-\frac{\omega_0}{2}\sigma_z$, we have

$$H_I = \frac{\Omega}{2}\left(e^{-i(\omega_L t + g/\omega_m\cos(\omega_m t))} + \left(e^{i(\omega_L t + g/\omega_m\cos(\omega_m t))}\right)\left(e^{i\omega_0 t}\sigma^+ + e^{-i\omega_0 t}\sigma^-\right)\right. \tag{D.5}$$

Defining the laser detuning $\delta = \omega_L - \omega_0$ and making the RWA, we find

$$H_I = \frac{\Omega}{2}\left(e^{-i(\delta t + g/\omega_m\cos(\omega_m t))}\sigma^+ + e^{i(\delta t + g/\omega_m\cos(\omega_m t))}\sigma^-\right) \tag{D.6}$$

Using the Jacobi-Anger expansion, this is simplified to

$$H_I = \frac{\Omega}{2}\left(\sum_{n=-\infty}^{\infty} J_n\left(\frac{g}{\omega_m}\right)e^{-i(\delta+n\omega_m)t}\sigma^+ + \sum_{n=-\infty}^{\infty} J_n\left(\frac{g}{\omega_m}\right)e^{i(\delta+n\omega_m)t}\sigma^-\right) \tag{D.7}$$

Now we can solve the time-dependent Schrodinger equation in the interaction picture.

$$i\dot{c}_g = \frac{\Omega}{2}\sum_{n=-\infty}^{\infty} J_n\left(\frac{g}{\omega_m}\right) e^{-i(\delta+n\omega_m)t} c_e \tag{D.8}$$

$$i\dot{c}_e = \frac{\Omega}{2}\sum_{n=-\infty}^{\infty} J_n\left(\frac{g}{\omega_m}\right) e^{i(\delta+n\omega_m)t} c_g \tag{D.9}$$

Let the laser detuning be written in terms of a detuning Δ from a sideband: $\delta = -n'\omega_m + \Delta$.

$$i\dot{c}_g = \frac{\Omega}{2}\sum_{n=-\infty}^{\infty} J_n\left(\frac{g}{\omega_m}\right) e^{-i((n-n')\omega_m+\Delta)t} c_e \tag{D.10}$$

$$i\dot{c}_e = \frac{\Omega}{2}\sum_{n=-\infty}^{\infty} J_n\left(\frac{g}{\omega_m}\right) e^{i((n-n')\omega_m+\Delta)t} c_g \tag{D.11}$$

Assuming that we are in the resolved sideband regime and under weak excitation power (small Ω), then we can consider transitions to the n^{th} sideband individually.

$$i\dot{c}_g = \frac{\Omega}{2} J_n\left(\frac{g}{\omega_m}\right) e^{-i\Delta t} c_e \tag{D.12}$$

$$i\dot{c}_e = \frac{\Omega}{2} J_n\left(\frac{g}{\omega_m}\right) e^{i\Delta t} c_g \tag{D.13}$$

Taking the time derivative of the above equations allows us to decouple the two states and we find

$$\ddot{c}_g + i\Delta\dot{c}_g + \frac{\Omega^2}{4} J_n^2\left(\frac{g}{\omega_m}\right) c_g = 0 \tag{D.14}$$

which has solutions $c_g(t) = e^{i\Delta t}\left(a_1\cos\left(\frac{\Omega_R t}{2}\right) + a_2\sin\left(\frac{\Omega_R t}{2}\right)\right)$, where the Rabi fre-

quency is $\Omega_R = \sqrt{\Omega^2 J_n^2\left(\frac{g}{\omega_m}\right) + \Delta^2}$

The probability to be in the excited state is given by $|c_e|^2$. Assuming that the qubit is initialized into the ground state, we find that the probability of being in the NV excited state is given by

$$P_e(t) = \frac{\Omega J_n\left(\frac{g}{\omega_m}\right)}{\sqrt{\Omega^2 J_n^2\left(\frac{g}{\omega_m}\right) + \Delta^2}} \sin^2\left(\frac{\Omega_R t}{2f}\right) \tag{D.15}$$

Bibliography

[1] Christian Hepp, Tina Müller, Victor Waselowski, Jonas N Becker, Benjamin Pingault, Hadwig Sternschulte, Doris Steinmüller-Nethl, Adam Gali, Jeronimo R Maze, Mete Atatüre, et al. Electronic structure of the silicon vacancy color center in diamond. *Physical Review Letters*, 112(3):036405, 2014.

[2] Mihir K Bhaskar, Denis D Sukachev, Alp Sipahigil, Ruffin E Evans, Michael J Burek, Christian T Nguyen, Lachlan J Rogers, Petr Siyushev, Mathias H Metsch, Hongkun Park, et al. Quantum nonlinear optics with a germanium-vacancy color center in a nanoscale diamond waveguide. *Physical Review Letters*, 118(22):223603, 2017.

[3] T. Iwasaki et al. Tin-vacancy quantum emitters in diamond. *arXiv preprint arXiv:1708.03576*, 2017.

[4] S Debnath, NM Linke, C Figgatt, KA Landsman, K Wright, and C Monroe. Demonstration of a small programmable quantum computer with atomic qubits. *Nature*, 536(7614):63–66, 2016.

[5] R Barends, J Kelly, A Megrant, A Veitia, D Sank, E Jeffrey, TC White, J Mutus, AG Fowler, B Campbell, et al. Superconducting quantum circuits at the surface code threshold for fault tolerance. *Nature*, 508(7497):500–503, 2014.

[6] NM Linke, M Gutierrez, KA Landsman, C Figgatt, S Debnath, KR Brown, and C Monroe. Experimental demonstration of quantum fault tolerance. *arXiv preprint arXiv:1611.06946*, 2016.

[7] Hannes Bernien, Sylvain Schwartz, Alexander Keesling, Harry Levine, Ahmed Omran, Hannes Pichler, Soonwon Choi, Alexander S Zibrov, Manuel Endres, Markus Greiner, et al. Probing many-body dynamics on a 51-atom quantum simulator. *arXiv preprint arXiv:1707.04344*, 2017.

[8] J Zhang, G Pagano, PW Hess, A Kyprianidis, P Becker, H Kaplan, AV Gorshkov, Z-X Gong, and C Monroe. Observation of a many-body dynamical phase transition with a 53-qubit quantum simulator. *arXiv preprint arXiv:1708.01044*, 2017.

[9] John Preskill. Quantum computing and the entanglement frontier. *arXiv preprint arXiv:1203.5813*, 2012.

[10] Peter W Shor. Polynomial-time algorithms for prime factorization and discrete logarithms on a quantum computer. *SIAM review*, 41(2):303–332, 1999.

[11] Charles H Bennett, Gilles Brassard, Claude Crépeau, Richard Jozsa, Asher Peres, and William K Wootters. Teleporting an unknown quantum state via dual classical and einstein-podolsky-rosen channels. *Physical review letters*, 70(13):1895, 1993.

[12] IM Georgescu, S Ashhab, and Franco Nori. Quantum simulation. *Reviews of Modern Physics*, 86(1):153, 2014.

[13] Kihwan Kim, Ming-Shien Chang, Simcha Korenblit, Rajibul Islam, Emily E Edwards, James K Freericks, Guin-Dar Lin, Lu-Ming Duan, and Christopher Monroe. Quantum simulation of frustrated ising spins with trapped ions. *Nature*, 465(7298):590, 2010.

[14] Soonwon Choi, Joonhee Choi, Renate Landig, Georg Kucsko, Hengyun Zhou, Junichi Isoya, Fedor Jelezko, Shinobu Onoda, Hitoshi Sumiya, Vedika Khemani, et al. Observation of discrete time-crystalline order in a disordered dipolar many-body system. *Nature*, 543(7644):221–225, 2017.

[15] Jae-yoon Choi, Sebastian Hild, Johannes Zeiher, Peter Schauß, Antonio Rubio-Abadal, Tarik Yefsah, Vedika Khemani, David A Huse, Immanuel Bloch, and Christian Gross. Exploring the many-body localization transition in two dimensions. *Science*, 352(6293):1547–1552, 2016.

[16] Michael Schreiber, Sean S Hodgman, Pranjal Bordia, Henrik P Lüschen, Mark H Fischer, Ronen Vosk, Ehud Altman, Ulrich Schneider, and Immanuel Bloch. Observation of many-body localization of interacting fermions in a quasirandom optical lattice. *Science*, 349(6250):842–845, 2015.

[17] J Smith, A Lee, P Richerme, B Neyenhuis, PW Hess, P Hauke, M Heyl, DA Huse, and C Monroe. Many-body localization in a quantum simulator with programmable random disorder. *Nature Physics*, 12(10):907–911, 2016.

[18] Philip Richerme, Zhe-Xuan Gong, Aaron Lee, Crystal Senko, Jacob Smith, Michael Foss-Feig, Spyridon Michalakis, Alexey V Gorshkov, and Christopher Monroe. Nonlocal propagation of correlations in quantum systems with long-range interactions. *Nature*, 511(7508):198–201, 2014.

[19] D. P. DiVincenzo. The physical implementation of quantum computation. *Fortschritte der Physik*, 48:771–783, 2000.

[20] Mark Saffman, Thad G Walker, and Klaus Mølmer. Quantum information with rydberg atoms. *Reviews of Modern Physics*, 82(3):2313, 2010.

[21] Jason R Petta, Alexander Comstock Johnson, Jacob M Taylor, Edward A Laird, Amir Yacoby, Mikhail D Lukin, Charles M Marcus, Micah P Hanson, and Arthur C Gossard. Coherent manipulation of coupled electron spins in semiconductor quantum dots. *Science*, 309(5744):2180–2184, 2005.

[22] David D Awschalom, Lee C Bassett, Andrew S Dzurak, Evelyn L Hu, and Jason R Petta. Quantum spintronics: engineering and manipulating atom-like spins in semiconductors. *Science*, 339(6124):1174–1179, 2013.

[23] Gershon Kurizki, Patrice Bertet, Yuimaru Kubo, Klaus Mølmer, David Petrosyan, Peter Rabl, and Jörg Schmiedmayer. Quantum technologies with hybrid systems. *Proceedings of the National Academy of Sciences*, 112(13):3866–3873, 2015.

[24] Donghun Lee, Kenneth W Lee, Jeffrey V Cady, Preeti Ovartchaiyapong, and Ania C Bleszynski Jayich. Topical review: Spins and mechanics in diamond. *Journal of Optics*, 19(3):033001, 2017.

[25] P Rabl, SJ Kolkowitz, FHL Koppens, JGE Harris, P Zoller, and MD Lukin. A quantum spin transducer based on nanoelectromechanical resonator arrays. *Nature Physics*, 6(8):602, 2010.

[26] Xiu Gu, Anton Frisk Kockum, Adam Miranowicz, Yu-xi Liu, and Franco Nori. Microwave photonics with superconducting quantum circuits. *arXiv preprint arXiv:1707.02046*, 2017.

[27] Thomas Aref, Per Delsing, Maria K Ekström, Anton Frisk Kockum, Martin V Gustafsson, Göran Johansson, Peter J Leek, Einar Magnusson, and Riccardo Manenti. Quantum acoustics with surface acoustic waves. In *Superconducting Devices in Quantum Optics*, pages 217–244. Springer, 2016.

[28] Xiao Mi, JV Cady, DM Zajac, PW Deelman, and JR Petta. Strong coupling of a single electron in silicon to a microwave photon. *Science*, page aal2469, 2016.

[29] T. E. Northrup and R. Blatt. Quantum information transfer using photons. *Nature Photonics*, 8:356–363, 2014.

[30] Bas Hensen, H Bernien, AE Dréau, A Reiserer, N Kalb, MS Blok, J Ruitenberg, RFL Vermeulen, RN Schouten, C Abellán, et al. Experimental loophole-free violation of a bell inequality using entangled electron spins separated by 1.3 km. *arXiv preprint arXiv:1508.05949*, 2015.

[31] Wolfgang Pfaff, BJ Hensen, Hannes Bernien, Suzanne B van Dam, Machiel S Blok, Tim H Taminiau, Marijn J Tiggelman, Raymond N Schouten, Matthew Markham, Daniel J Twitchen, et al. Unconditional quantum teleportation between distant solid-state quantum bits. *Science*, 345(6196):532–535, 2014.

[32] S Olmschenk, DN Matsukevich, P Maunz, D Hayes, L-M Duan, and C Monroe. Quantum teleportation between distant matter qubits. *Science*, 323(5913):486–489, 2009.

[33] Sheng-Kai Liao, Wen-Qi Cai, Wei-Yue Liu, Liang Zhang, Yang Li, Ji-Gang Ren, Juan Yin, Qi Shen, Yuan Cao, Zheng-Ping Li, et al. Satellite-to-ground quantum key distribution. *arXiv preprint arXiv:1707.00542*, 2017.

[34] P. Treutlein, C. Genes, K. Hammerer, M. Poggio, and P. Rabl. *Hybrid Mechanical Systems*. Springer, 2014.

[35] Sophia R Sklan. Splash, pop, sizzle: Information processing with phononic computing. *AIP Advances*, 5(5):053302, 2015.

[36] Menno Poot and Herre SJ van der Zant. Mechanical systems in the quantum regime. *Physics Reports*, 511(5):273–335, 2012.

[37] Benjamin P Abbott, Richard Abbott, TD Abbott, MR Abernathy, Fausto Acernese, Kendall Ackley, Carl Adams, Thomas Adams, Paolo Addesso, RX Adhikari, et al. Observation of gravitational waves from a binary black hole merger. *Physical review letters*, 116(6):061102, 2016.

[38] D Rugar, R Budakian, HJ Mamin, and BW Chui. Single spin detection by magnetic resonance force microscopy. *Nature*, 430(6997):329, 2004.

[39] SD Bennett, Norman Ying Yao, Johannes Otterbach, Peter Zoller, Peter Rabl, and Mikhail D Lukin. Phonon-induced spin-spin interactions in diamond nanostructures: application to spin squeezing. *Physical review letters*, 110(15):156402, 2013.

[40] SJM Habraken, K Stannigel, Mikhail D Lukin, P Zoller, and P Rabl. Continuous mode cooling and phonon routers for phononic quantum networks. *New Journal of Physics*, 14(11):115004, 2012.

[41] MJA Schuetz, EM Kessler, G Giedke, LMK Vandersypen, MD Lukin, and JI Cirac. Universal quantum transducers based on surface acoustic waves. *Physical Review X*, 5(3):031031, 2015.

[42] Yan-Lei Zhang, Chang-Ling Zou, Xu-Bo Zou, Liang Jiang, and Guang-Can Guo. Phonon-induced spin squeezing based on geometric phase. *Physical Review A*, 92(1):013825, 2015.

[43] P Ovartchaiyapong, LMA Pascal, BA Myers, P Lauria, and AC Bleszynski Jayich. High quality factor single-crystal diamond mechanical resonators. *Applied Physics Letters*, 101(16):163505, 2012.

[44] Y Tao, JM Boss, BA Moores, and CL Degen. Single-crystal diamond nanomechanical resonators with quality factors exceeding one million. *Nature communications*, 5:3638–3638, 2014.

[45] Michael J Burek, Daniel Ramos, Parth Patel, Ian W Frank, and Marko Lončar. Nanomechanical resonant structures in single-crystal diamond. *Applied Physics Letters*, 103(13):131904, 2013.

[46] Behzad Khanaliloo, Harishankar Jayakumar, Aaron C Hryciw, David P Lake, Hamidreza Kaviani, and Paul E Barclay. Single-crystal diamond nanobeam waveguide optomechanics. *Physical Review X*, 5(4):041051, 2015.

[47] Matthew Mitchell, Behzad Khanaliloo, David P Lake, Tamiko Masuda, JP Hadden, and Paul E Barclay. Single-crystal diamond low-dissipation cavity optomechanics. *Optica*, 3(9):963–970, 2016.

[48] Michael J Burek, Justin D Cohen, Seán M Meenehan, Nayera El-Sawah, Cleaven Chia, Thibaud Ruelle, Srujan Meesala, Jake Rochman, Haig A Atikian, Matthew Markham, et al. Diamond optomechanical crystals. *Optica*, 3(12):1404–1411, 2016.

[49] Y. Tsaturyan, A. Barg, E. S. Polzik, and A Schliesser. Ultracoherent nanomechanical resonators via soft clamping and dissipation dilution. *Nature Nanotechnology*, 12:776–783, 2017.

[50] Fedor Jelezko, T Gaebel, I Popa, A Gruber, and Jorg Wrachtrup. Observation of coherent oscillations in a single electron spin. *Physical review letters*, 92(7):076401, 2004.

[51] ER MacQuarrie, TA Gosavi, NR Jungwirth, SA Bhave, and GD Fuchs. Mechanical spin control of nitrogen-vacancy centers in diamond. *Physical review letters*, 111(22):227602, 2013.

[52] ER MacQuarrie, TA Gosavi, AM Moehle, NR Jungwirth, SA Bhave, and GD Fuchs. Coherent control of a nitrogen-vacancy center spin ensemble with a diamond mechanical resonator. *Optica*, 2(3):233–238, 2015.

[53] Arne Barfuss, Jean Teissier, Elke Neu, Andreas Nunnenkamp, and Patrick Maletinsky. Strong mechanical driving of a single electron spin. *Nature Physics*, 11(10):820–824, 2015.

[54] Tomás Ramos, Vivishek Sudhir, Kai Stannigel, Peter Zoller, and Tobias J Kippenberg. Nonlinear quantum optomechanics via individual intrinsic two-level defects. *Physical review letters*, 110(19):193602, 2013.

[55] AP Reed, KH Mayer, JD Teufel, LD Burkhart, W Pfaff, M Reagor, L Sletten, X Ma, RJ Schoelkopf, E Knill, et al. Faithful conversion of propagating quantum information to mechanical motion. *arXiv preprint arXiv:1703.02548*, 2017.

[56] Aaron D OConnell, Max Hofheinz, Markus Ansmann, Radoslaw C Bialczak, Mike Lenander, Erik Lucero, Matthew Neeley, Daniel Sank, H Wang, M Weides, et al. Quantum ground state and single-phonon control of a mechanical resonator. *Nature*, 464(7289):697–703, 2010.

[57] Hybrid discrete- and continuous-variable quantum information.

[58] AP Lund, TC Ralph, and HL Haselgrove. Fault-tolerant linear optical quantum computing with small-amplitude coherent states. *Physical review letters*, 100(3):030503, 2008.

[59] Shuntaro Takeda, Hugo Benichi, Takahiro Mizuta, Noriyuki Lee, Jun-ichi Yoshikawa, and Akira Furusawa. Quantum mode filtering of non-gaussian states for teleportation-based quantum information processing. *Physical Review A*, 85(5):053824, 2012.

[60] JD Teufel, T Donner, Dale Li, JW Harlow, MS Allman, K Cicak, AJ Sirois, JD Whittaker, KW Lehnert, and RW Simmonds. Sideband cooling of micromechanical motion to the quantum ground state. *Nature*, 475(7356):359–364, 2011.

[61] Jasper Chan, TP Mayer Alegre, Amir H Safavi-Naeini, Jeff T Hill, Alex Krause, Simon Gröblacher, Markus Aspelmeyer, and Oskar Painter. Laser cooling of a nanomechanical oscillator into its quantum ground state. *Nature*, 478(7367):89, 2011.

[62] M Underwood, D Mason, D Lee, H Xu, L Jiang, AB Shkarin, Kjetil Børkje, SM Girvin, and JGE Harris. Measurement of the motional sidebands of a nanogram-scale oscillator in the quantum regime. *Physical Review A*, 92(6):061801, 2015.

[63] RW Peterson, TP Purdy, NS Kampel, RW Andrews, P-L Yu, KW Lehnert, and CA Regal. Laser cooling of a micromechanical membrane to the quantum backaction limit. *Physical review letters*, 116(6):063601, 2016.

[64] MD LaHaye, J Suh, PM Echternach, Keith C Schwab, and Michael L Roukes. Nanomechanical measurements of a superconducting qubit. *Nature*, 459(7249):960, 2009.

[65] JM Pirkkalainen, SU Cho, J Li, GS Paraoanu, PJ Hakonen, MA Sillanpaa, et al. Hybrid circuit cavity quantum electrodynamics with a micromechanical resonator. *Nature*, 494(7436):211–215, 2013.

[66] S. Etaki, M. Poot, I. Mahboob, K. Onomitsu, H. Yamaguchi, and H. S. J. van der Zant. Motion detection of a micromechanical resonator embedded in a d.c. squid. *Nature Physics*, 4:785–788, 2008.

[67] Yiwen Chu, Prashanta Kharel, William H Renninger, Luke D Burkhart, Luigi Frunzio, Peter T Rakich, and Robert J Schoelkopf. Quantum acoustics with superconducting qubits. *arXiv preprint arXiv:1703.00342*, 2017.

[68] Andreas Jöckel, Aline Faber, Tobias Kampschulte, Maria Korppi, Matthew T Rakher, and Philipp Treutlein. Sympathetic cooling of a membrane oscillator in a hybrid mechanical–atomic system. *Nature nanotechnology*, 10(1):55–59, 2015.

[69] Stephan Camerer, Maria Korppi, Andreas Jöckel, David Hunger, Theodor W Hänsch, and Philipp Treutlein. Realization of an optomechanical interface between ultracold atoms and a membrane. *Physical review letters*, 107(22):223001, 2011.

[70] David Hunger, Stephan Camerer, Theodor W Hänsch, Daniel König, Jörg P Kotthaus, Jakob Reichel, and Philipp Treutlein. Resonant coupling of a bose-einstein condensate to a micromechanical oscillator. *Physical review letters*, 104(14):143002, 2010.

[71] Michael Metcalfe, Stephen M Carr, Andreas Muller, Glenn S Solomon, and John Lawall. Resolved sideband emission of inas/gaas quantum dots strained by surface acoustic waves. *Physical review letters*, 105(3):037401, 2010.

[72] Inah Yeo, Pierre-Louis De Assis, Arnaud Gloppe, Eva Dupont-Ferrier, Pierre Verlot, Nitin S Malik, Emmanuel Dupuy, Julien Claudon, Jean-Michel Gérard, Alexia Auffèves, et al. Strain-mediated coupling in a quantum dot-mechanical oscillator hybrid system. *Nature nanotechnology*, 9(2):106–110, 2014.

[73] Michele Montinaro, Gunter Wust, Mathieu Munsch, Yannik Fontana, Eleonora Russo-Averchi, Martin Heiss, Anna Fontcuberta i Morral, Richard J Warburton, and Martino Poggio. Quantum dot opto-mechanics in a fully self-assembled nanowire. *Nano letters*, 14(8):4454–4460, 2014.

[74] O Arcizet, V Jacques, A Siria, P Poncharal, P Vincent, and S Seidelin. A single nitrogen-vacancy defect coupled to a nanomechanical oscillator. *Nature Physics*, 7(11):879, 2011.

[75] Shimon Kolkowitz, Ania C Bleszynski Jayich, Quirin P Unterreithmeier, Steven D Bennett, Peter Rabl, JGE Harris, and Mikhail D Lukin. Coherent sensing of a mechanical resonator with a single-spin qubit. *Science*, 335(6076):1603–1606, 2012.

[76] Preeti Ovartchaiyapong, Kenneth W Lee, Bryan A Myers, and Ania C Bleszynski Jayich. Dynamic strain-mediated coupling of a single diamond spin to a mechanical resonator. *Nature Communications*, 5:4429, 2014.

[77] J Teissier, A Barfuss, P Appel, E Neu, and P Maletinsky. Strain coupling of a nitrogen-vacancy center spin to a diamond mechanical oscillator. *Physical review letters*, 113(2):020503, 2014.

[78] ER MacQuarrie, TA Gosavi, SA Bhave, and GD Fuchs. Continuous dynamical decoupling of a single diamond nitrogen-vacancy center spin with a mechanical resonator. *Physical Review B*, 92(22):224419, 2015.

[79] D Andrew Golter, Thein Oo, Mayra Amezcua, Kevin A Stewart, and Hailin Wang. Optomechanical quantum control of a nitrogen-vacancy center in diamond. *Physical review letters*, 116(14):143602, 2016.

[80] Kenneth W Lee, Donghun Lee, Preeti Ovartchaiyapong, Joaquin Minguzzi, Jero R Maze, and Ania C Bleszynski Jayich. Strain coupling of a mechanical resonator to a single quantum emitter in diamond. *Physical Review Applied*, 6(3):034005, 2016.

[81] Sungkun Hong, Michael S Grinolds, Patrick Maletinsky, Ronald L Walsworth, Mikhail D Lukin, and Amir Yacoby. Coherent, mechanical control of a single electronic spin. *Nano letters*, 12(8):3920–3924, 2012.

[82] Srujan Meesala, Young-Ik Sohn, Haig A Atikian, Samuel Kim, Michael J Burek, Jennifer T Choy, and Marko Lončar. Enhanced strain coupling of nitrogen-vacancy spins to nanoscale diamond cantilevers. *Physical Review Applied*, 5(3):034010, 2016.

[83] F Jelezko and J Wrachtrup. Single defect centres in diamond: A review. *physica status solidi (a)*, 203(13):3207–3225, 2006.

[84] Ronald Hanson and David D Awschalom. Coherent manipulation of single spins in semiconductors. *Nature*, 453(7198):1043, 2008.

[85] Romana Schirhagl, Kevin Chang, Michael Loretz, and Christian L Degen. Nitrogen-vacancy centers in diamond: nanoscale sensors for physics and biology. *Annual review of physical chemistry*, 65:83–105, 2014.

[86] L. Childress, R. Walsworth, and M. Lukin. *Physics Today*, 67:38–43, 2014.

[87] L Rondin, JP Tetienne, T Hingant, JF Roch, P Maletinsky, and V Jacques. Magnetometry with nitrogen-vacancy defects in diamond. *Reports on progress in physics*, 77(5):056503, 2014.

[88] Gopalakrishnan Balasubramanian, Philipp Neumann, Daniel Twitchen, Matthew Markham, Roman Kolesov, Norikazu Mizuochi, Junichi Isoya, Jocelyn Achard, Johannes Beck, Julia Tissler, et al. Ultralong spin coherence time in isotopically engineered diamond. *Nature materials*, 8(5):383, 2009.

[89] Peter Christian Maurer, Georg Kucsko, Christian Latta, Liang Jiang, Norman Ying Yao, Steven D Bennett, Fernando Pastawski, David Hunger, Nicholas Chisholm, Matthew Markham, et al. Room-temperature quantum bit memory exceeding one second. *Science*, 336(6086):1283–1286, 2012.

[90] Andreas Reiserer, Norbert Kalb, Machiel S Blok, Koen JM van Bemmelen, Tim H Taminiau, Ronald Hanson, Daniel J Twitchen, and Matthew Markham. Robust quantum-network memory using decoherence-protected subspaces of nuclear spins. *Physical Review X*, 6(2):021040, 2016.

[91] L Childress, MV Gurudev Dutt, JM Taylor, AS Zibrov, F Jelezko, J Wrachtrup, PR Hemmer, and MD Lukin. Coherent dynamics of coupled electron and nuclear spin qubits in diamond. *Science*, 314(5797):281–285, 2006.

[92] E Togan, Y Chu, AS Trifonov, L Jiang, J Maze, L Childress, MVG Dutt, AS Sørensen, PR Hemmer, AS Zibrov, et al. Quantum entanglement between an optical photon and a solid-state spin qubit. *Nature*, 466(7307):730, 2010.

[93] BB Buckley, GD Fuchs, LC Bassett, and DD Awschalom. Spin-light coherence for single-spin measurement and control in diamond. *Science*, 330(6008):1212–1215, 2010.

[94] Hannes Bernien, Lilian Childress, Lucio Robledo, Matthew Markham, Daniel Twitchen, and Ronald Hanson. Two-photon quantum interference from separate nitrogen vacancy centers in diamond. *Physical Review Letters*, 108(4):043604, 2012.

[95] Alp Sipahigil, Michael Lurie Goldman, Emre Togan, Yiwen Chu, Matthew Markham, Daniel J Twitchen, Alexander S Zibrov, Alexander Kubanek, and Mikhail D Lukin. Quantum interference of single photons from remote nitrogen-vacancy centers in diamond. *Physical review letters*, 108(14):143601, 2012.

[96] JR Weber, WF Koehl, JB Varley, A Janotti, BB Buckley, CG Van de Walle, and David D Awschalom. Quantum computing with defects. *Proceedings of the National Academy of Sciences*, 107(19):8513–8518, 2010.

[97] Kenichi Ohno, F Joseph Heremans, Lee C Bassett, Bryan A Myers, David M Toyli, Ania C Bleszynski Jayich, Christopher J Palmstrøm, and David D Awschalom. Engineering shallow spins in diamond with nitrogen delta-doping. *Applied Physics Letters*, 101(8):082413, 2012.

[98] Matthias Pfender *et al.*. Protecting a diamond quantum memory by charge state control. *arXiv preprint arXiv:1702.01590*, 2017.

[99] JR Maze, Adam Gali, Emre Togan, Yiwen Chu, Alexei Trifonov, Efthimios Kaxiras, and MD Lukin. Properties of nitrogen-vacancy centers in diamond: the group theoretic approach. *New Journal of Physics*, 13(2):025025, 2011.

[100] Marcus W Doherty, Neil B Manson, Paul Delaney, Fedor Jelezko, Jörg Wrachtrup, and Lloyd CL Hollenberg. The nitrogen-vacancy colour centre in diamond. *Physics Reports*, 528(1):1–45, 2013.

[101] JM Taylor, P Cappellaro, L Childress, L Jiang, D Budker, PR Hemmer, A Yacoby, R Walsworth, and MD Lukin. High-sensitivity diamond magnetometer with nanoscale resolution. *Nature Physics*, 7(3):270–270, 2011.

[102] JR Maze, PL Stanwix, JS Hodges, S Hong, JM Taylor, P Cappellaro, L Jiang, MV Gurudev Dutt, E Togan, AS Zibrov, et al. Nanoscale magnetic sensing with an individual electronic spin in diamond. *Nature*, 455(7213):644, 2008.

[103] Thomas Wolf, Philipp Neumann, Kazuo Nakamura, Hitoshi Sumiya, Takeshi Ohshima, Junichi Isoya, and Jörg Wrachtrup. Subpicotesla diamond magnetometry. *Physical Review X*, 5(4):041001, 2015.

[104] F Dolde, H Fedder, MW Doherty, T Nöbauer, F Rempp, G Balasubramanian, T Wolf, F Reinhard, LCL Hollenberg, F Jelezko, et al. Electric-field sensing using single diamond spins. *Nature Physics*, 7(6):459, 2011.

[105] Florian Dolde, Marcus W Doherty, Julia Michl, Ingmar Jakobi, Boris Naydenov, Sebastien Pezzagna, Jan Meijer, Philipp Neumann, Fedor Jelezko, Neil B Manson, et al. Nanoscale detection of a single fundamental charge in ambient conditions using the nv- center in diamond. *Physical review letters*, 112(9):097603, 2014.

[106] David M Toyli, F Charles, David J Christle, Viatcheslav V Dobrovitski, and David D Awschalom. Fluorescence thermometry enhanced by the quantum coherence of single spins in diamond. *Proceedings of the National Academy of Sciences*, 110(21):8417–8421, 2013.

[107] VM Acosta, E Bauch, MP Ledbetter, A Waxman, L-S Bouchard, and D Budker. Temperature dependence of the nitrogen-vacancy magnetic resonance in diamond. *Physical review letters*, 104(7):070801, 2010.

[108] Philipp Neumann, Ingmar Jakobi, Florian Dolde, Christian Burk, Rolf Reuter, Gerald Waldherr, Jan Honert, Thomas Wolf, Andreas Brunner, Jeong Hyun Shim, et al. High-precision nanoscale temperature sensing using single defects in diamond. *Nano letters*, 13(6):2738–2742, 2013.

[109] Michael S J Barson *et al.*. Nanomechanical sensing using spins in diamond. *Nano Letters*, 17(3):1496–1503, 2017.

[110] Michael Lurie Goldman, Alp Sipahigil, MW Doherty, Norman Ying Yao, SD Bennett, M Markham, DJ Twitchen, NB Manson, Alexander Kubanek, and Mikhail D Lukin. Phonon-induced population dynamics and intersystem crossing in nitrogen-vacancy centers. *Physical review letters*, 114(14):145502, 2015.

[111] Jarryd J Pla, Kuan Y Tan, Juan P Dehollain, Wee H Lim, John JL Morton, David N Jamieson, Andrew S Dzurak, and Andrea Morello. A single-atom electron spin qubit in silicon. *Nature*, 489(7417):541–545, 2012.

[112] Paul Delaney, James C Greer, and J Andreas Larsson. Spin-polarization mechanisms of the nitrogen-vacancy center in diamond. *Nano letters*, 10(2):610–614, 2010.

[113] N Aslam, G Waldherr, P Neumann, F Jelezko, and J Wrachtrup. Photo-induced ionization dynamics of the nitrogen vacancy defect in diamond investigated by single-shot charge state detection. *New Journal of Physics*, 15(1):013064, 2013.

[114] Lucio Robledo, Lilian Childress, Hannes Bernien, Bas Hensen, Paul FA Alkemade, and Ronald Hanson. High-fidelity projective read-out of a solid-state spin quantum register. *Nature*, 477:574–578, 2011.

[115] Brendan John Shields, QP Unterreithmeier, NP De Leon, H Park, and Mikhail D Lukin. Efficient readout of a single spin state in diamond via spin-to-charge conversion. *Physical review letters*, 114(13):136402, 2015.

[116] David A Hopper, Richard R Grote, Annemarie L Exarhos, and Lee C Bassett. Near-infrared-assisted charge control and spin readout of the nitrogen-vacancy center in diamond. *Physical Review B*, 94(24):241201, 2016.

[117] Florian M Hrubesch, Georg Braunbeck, Martin Stutzmann, Friedemann Reinhard, and Martin S Brandt. Efficient electrical spin readout of nv- centers in diamond. *Physical Review Letters*, 118(3):037601, 2017.

[118] Kasper Jensen, Nathan Leefer, Andrey Jarmola, Yannick Dumeige, Victor M Acosta, Pauli Kehayias, Brian Patton, and Dmitry Budker. Cavity-enhanced room-temperature magnetometry using absorption by nitrogen-vacancy centers in diamond. *Physical review letters*, 112(16):160802, 2014.

[119] A Gruber, A Dräbenstedt, C Tietz, L Fleury, J Wrachtrup, and C Von Borczyskowski. Scanning confocal optical microscopy and magnetic resonance on single defect centers. *Science*, 276(5321):2012–2014, 1997.

[120] HJ Mamin, M Kim, MH Sherwood, CT Rettner, K Ohno, DD Awschalom, and D Rugar. Nanoscale nuclear magnetic resonance with a nitrogen-vacancy spin sensor. *Science*, 339(6119):557–560, 2013.

[121] M Pelliccione, A Jenkins, P Ovartchaiyapong, C Reetz, E Emmanouilidou, N Ni, and Jayich AC Bleszynski. Scanned probe imaging of nanoscale magnetism at cryogenic temperatures with a single-spin quantum sensor. *Nature nanotechnology*, 11(8):700–705, 2016.

[122] Thomas Unden, Priya Balasubramanian, Daniel Louzon, Yuval Vinkler, Martin B Plenio, Matthew Markham, Daniel Twitchen, Alastair Stacey, Igor Lovchinsky, Alexander O Sushkov, et al. Quantum metrology enhanced by repetitive quantum error correction. *Physical review letters*, 116(23):230502, 2016.

[123] Sebastian Zaiser, Torsten Rendler, Ingmar Jakobi, Thomas Wolf, Sang-Yun Lee, Samuel Wagner, Ville Bergholm, Thomas Schulte-Herbrüggen, Philipp Neumann, and Jörg Wrachtrup. Enhancing quantum sensing sensitivity by a quantum memory. *Nature communications*, 7, 2016.

[124] G Waldherr *et al.*. Quantum error correction in a solid-state hybrid spin register. *Nature*, 506(7487):204, 2014.

[125] Lilian Isabel Childress. *Coherent manipulation of single quantum systems in the solid state*. Harvard University, 2007.

[126] S Felton, AM Edmonds, ME Newton, PM Martineau, D Fisher, DJ Twitchen, and JM Baker. Hyperfine interaction in the ground state of the negatively charged nitrogen vacancy center in diamond. *Physical Review B*, 79(7):075203, 2009.

[127] Mo Chen, Masashi Hirose, Paola Cappellaro, et al. Measurement of transverse hyperfine interaction by forbidden transitions. *Physical Review B*, 92(2):020101, 2015.

[128] MW Doherty, F Dolde, H Fedder, F Jelezko, J Wrachtrup, NB Manson, and LCL Hollenberg. Theory of the ground-state spin of the nv- center in diamond. *Physical Review B*, 85(20):205203, 2012.

[129] GD Fuchs, VV Dobrovitski, R Hanson, A Batra, CD Weis, T Schenkel, and DD Awschalom. Excited-state spectroscopy using single spin manipulation in diamond. *Physical review letters*, 101(11):117601, 2008.

[130] A Dréau, M Lesik, L Rondin, P Spinicelli, O Arcizet, J-F Roch, and V Jacques. Avoiding power broadening in optically detected magnetic resonance of single nv defects for enhanced dc magnetic field sensitivity. *Physical Review B*, 84(19):195204, 2011.

[131] Bryan A Myers, A Das, MC Dartiailh, K Ohno, David D Awschalom, and AC Bleszynski Jayich. Probing surface noise with depth-calibrated spins in diamond. *Physical review letters*, 113(2):027602, 2014.

[132] R Hanson, VV Dobrovitski, AE Feiguin, O Gywat, and DD Awschalom. Coherent dynamics of a single spin interacting with an adjustable spin bath. *Science*, 320(5874):352–355, 2008.

[133] Vittorio Giovannetti, Seth Lloyd, and Lorenzo Maccone. Advances in quantum metrology. *Nature photonics*, 5(4):222–229, 2011.

[134] Herman Y Carr and Edward M Purcell. Effects of diffusion on free precession in nuclear magnetic resonance experiments. *Physical review*, 94(3):630, 1954.

[135] G De Lange, D Ristè, VV Dobrovitski, and R Hanson. Single-spin magnetometry with multipulse sensing sequences. *Physical review letters*, 106(8):080802, 2011.

[136] G De Lange, ZH Wang, D Riste, VV Dobrovitski, and R Hanson. Universal dynamical decoupling of a single solid-state spin from a spin bath. *Science*, 330(6000):60–63, 2010.

[137] K Khodjasteh and DA Lidar. Fault-tolerant quantum dynamical decoupling. *Physical review letters*, 95(18):180501, 2005.

[138] N Bar-Gill, LM Pham, A Jarmola, D Budker, and RL Walsworth. Solid-state electronic spin coherence time approaching one second. *Nature communications*, 4:1743–1743, 2013.

[139] Bryan A Myers, Amila Ariyaratne, and AC Bleszynski Jayich. Double-quantum spin-relaxation limits to coherence of near-surface nitrogen-vacancy centers. *Physical Review Letters*, 118(19):197201, 2017.

[140] Y Romach, C Müller, T Unden, LJ Rogers, T Isoda, KM Itoh, M Markham, A Stacey, J Meijer, S Pezzagna, et al. Spectroscopy of surface-induced noise using shallow spins in diamond. *Physical review letters*, 114(1):017601, 2015.

[141] Lee C Bassett, F Joseph Heremans, David J Christle, Christopher G Yale, Guido Burkard, Bob B Buckley, and David D Awschalom. Ultrafast optical control of orbital and spin dynamics in a solid-state defect. *Science*, 345(6202):1333–1337, 2014.

[142] Christopher G Yale, Bob B Buckley, David J Christle, Guido Burkard, F Joseph Heremans, Lee C Bassett, and David D Awschalom. All-optical control of a solid-state spin using coherent dark states. *Proceedings of the National Academy of Sciences*, 110(19):7595–7600, 2013.

[143] AE Hughes and WA Runciman. Uniaxial stress splitting of doubly degenerate states of tetragonal and trigonal centres in cubic crystals. *Proceedings of the Physical Society*, 90(3):827, 1967.

[144] Gordon Davies and MF Hamer. Optical studies of the 1.945 ev vibronic band in diamond. In *Proceedings of the Royal Society of London A: Mathematical, Physical and Engineering Sciences*, volume 348, pages 285–298. The Royal Society, 1976.

[145] LC Bassett, FJ Heremans, CG Yale, BB Buckley, and DD Awschalom. Electrical tuning of single nitrogen-vacancy center optical transitions enhanced by photoinduced fields. *Physical Review Letters*, 107(26):266403, 2011.

[146] VM Acosta, C Santori, A Faraon, Z Huang, K-MC Fu, A Stacey, DA Simpson, K Ganesan, S Tomljenovic-Hanic, AD Greentree, et al. Dynamic stabilization of the optical resonances of single nitrogen-vacancy centers in diamond. *Physical review letters*, 108(20):206401, 2012.

[147] Marcus W Doherty, Julia Michl, Florian Dolde, Ingmar Jakobi, Philipp Neumann, Neil B Manson, and Jörg Wrachtrup. Measuring the defect structure orientation of a single nv- centre in diamond. *New Journal of Physics*, 16(6):063067, 2014.

[148] W.B. Mims. *The Linear Electric Field Effect In Paramagnetic Resonance*. Oxford University Press, 1976.

[149] Eric Van Oort and Max Glasbeek. Electric-field-induced modulation of spin echoes of nv centers in diamond. *Chemical Physics Letters*, 168(6):529–532, 1990.

[150] H Bernien, B Hensen, W Pfaff, G Koolstra, MS Blok, L Robledo, TH Taminiau, M Markham, DJ Twitchen, L Childress, et al. Heralded entanglement between solid-state qubits separated by three metres. *Nature*, 497(7447):86, 2013.

[151] Michael Lurie Goldman, MW Doherty, Alp Sipahigil, Norman Ying Yao, SD Bennett, NB Manson, Alexander Kubanek, and Mikhail D Lukin. State-selective intersystem crossing in nitrogen-vacancy centers. *Physical Review B*, 91(16):165201, 2015.

[152] Lucio Robledo, Hannes Bernien, Toeno van der Sar, and Ronald Hanson. Spin dynamics in the optical cycle of single nitrogen-vacancy centres in diamond. *New Journal of Physics*, 13(2):025013, 2011.

[153] JP Tetienne, L Rondin, P Spinicelli, M Chipaux, T Debuisschert, JF Roch, and V Jacques. Magnetic-field-dependent photodynamics of single nv defects in diamond: an application to qualitative all-optical magnetic imaging. *New Journal of Physics*, 14(10):103033, 2012.

[154] GD Fuchs, VV Dobrovitski, DM Toyli, FJ Heremans, CD Weis, Thomas Schenkel, and DD Awschalom. Excited-state spin coherence of a single nitrogen-vacancy centre in diamond. *Nature Physics*, 6(9):668, 2010.

[155] Patrik Rath, Sandeep Ummethala, Christoph Nebel, and Wolfram HP Pernice. Diamond as a material for monolithically integrated optical and optomechanical devices. *physica status solidi (a)*, 212(11):2385–2399, 2015.

[156] Claude A Klein and Gregory F Cardinale. Young's modulus and poisson's ratio of cvd diamond. *Diamond and Related Materials*, 2(5-7):918–923, 1993.

[157] Michael J Burek, Nathalie P de Leon, Brendan J Shields, Birgit JM Hausmann, Yiwen Chu, Qimin Quan, Alexander S Zibrov, Hongkun Park, Mikhail D Lukin, and Marko Loncar. Free-standing mechanical and photonic nanostructures in single-crystal diamond. *Nano letters*, 12(12):6084–6089, 2012.

[158] Igor Aharonovich, Jonathan C Lee, Andrew P Magyar, Bob B Buckley, Christopher G Yale, David D Awschalom, and Evelyn L Hu. Homoepitaxial growth of single crystal diamond membranes for quantum information processing. *Advanced materials*, 24(10), 2012.

[159] Jonathan C Lee, Andrew P Magyar, David O Bracher, Igor Aharonovich, and Evelyn L Hu. Fabrication of thin diamond membranes for photonic applications. *Diamond and Related Materials*, 33:45–48, 2013.

[160] A.N. Cleland. *Foundations of Nanomechanics: From Solid-State Theory to Device Applications*. Advanced Texts in Physics. Springer Berlin Heidelberg, 2002.

[161] Preeti Ovartchaiyapong. *Strain-coupled hybrid devices based on single-crystal diamond mechanical resonators and nitrogen-vacancy center qubits*. PhD thesis, University of California, Santa Barbara, 2016.

[162] D Rugar, HJ Mamin, and Peter Guethner. Improved fiber-optic interferometer for atomic force microscopy. *Applied Physics Letters*, 55(25):2588–2590, 1989.

[163] T Ikehara, J Lu, M Konno, R Maeda, and T Mihara. A high quality-factor silicon cantilever for a low detection-limit resonant mass sensor operated in air. *Journal of Micromechanics and Microengineering*, 17(12):2491, 2007.

[164] G. D. Cole, I. Wilson-Rae, K. Werbach, M. R. Vanner, and M. Aspelmeyer. Phonon-tunnelling dissipation in mechanical resonators. *Nature Communications*, 2:231, 2011.

[165] Robert H Webb. Confocal optical microscopy. *Reports on Progress in Physics*, 59(3):427, 1996.

[166] Colin JR Sheppard and David M Shotton. *Confocal laser scanning microscopy*. BIOS Scientific Publishers, 1997.

[167] Kai-Mei C Fu, Charles Santori, Paul E Barclay, Lachlan J Rogers, Neil B Manson, and Raymond G Beausoleil. Observation of the dynamic jahn-teller effect in the excited states of nitrogen-vacancy centers in diamond. *Physical Review Letters*, 103(25):256404, 2009.

[168] Bryan Andrew Myers. *Quantum decoherence of near-surface nitrogen-vacancy centers in diamond and implications for nanoscale imaging*. PhD thesis, University of California, Santa Barbara, 2016.

[169] KV Kepesidis, SD Bennett, S Portolan, Mikhail D Lukin, and P Rabl. Phonon cooling and lasing with nitrogen-vacancy centers in diamond. *Physical Review B*, 88(6):064105, 2013.

[170] I Wilson-Rae, P Zoller, and A Imamolu. Laser cooling of a nanomechanical resonator mode to its quantum ground state. *Physical Review Letters*, 92(7):075507, 2004.

[171] Lilian Childress and Ronald Hanson. Diamond nv centers for quantum computing and quantum networks. *MRS bulletin*, 38(2):134–138, 2013.

[172] Paolo Andrich, Charles F Casas, Xiaoying Liu, Hope L Bretscher, Jonson R Berman, F Joseph Heremans, Paul F Nealey, and David D Awschalom. Hybrid nanodiamond-yig systems for efficient quantum information processing and nanoscale sensing. *arXiv preprint arXiv:1701.07401*, 2017.

[173] SD Bennett, S Kolkowitz, QP Unterreithmeier, P Rabl, AC Bleszynski Jayich, JGE Harris, and Mikhail D Lukin. Measuring mechanical motion with a single spin. *New Journal of Physics*, 14(12):125004, 2012.

[174] CL Degen, F Reinhard, and P Cappellaro. Quantum sensing. *Reviews of Modern Physics*, 89(3):035002, 2017.

[175] Marcus W Doherty, Viktor V Struzhkin, David A Simpson, Liam P McGuinness, Yufei Meng, Alastair Stacey, Timothy J Karle, Russell J Hemley, Neil B Manson, Lloyd CL Hollenberg, et al. Electronic properties and metrology applications of the diamond nv- center under pressure. *Physical review letters*, 112(4):047601, 2014.

[176] Abram L Falk, Paul V Klimov, Bob B Buckley, Viktor Ivády, Igor A Abrikosov, Greg Calusine, William F Koehl, Ádám Gali, and David D Awschalom. Electrically and mechanically tunable electron spins in silicon carbide color centers. *Physical review letters*, 112(18):187601, 2014.

[177] William F Koehl, Bob B Buckley, F Joseph Heremans, Greg Calusine, and David D Awschalom. Room temperature coherent control of defect spin qubits in silicon carbide. *Nature*, 479(7371):84, 2011.

[178] P-L Yu, TP Purdy, and CA Regal. Control of material damping in high-q membrane microresonators. *Physical review letters*, 108(8):083603, 2012.

[179] Kai Stannigel, Peter Rabl, Anders S Sørensen, Peter Zoller, and Mikhail D Lukin. Optomechanical transducers for long-distance quantum communication. *Physical review letters*, 105(22):220501, 2010.

[180] RW Andrews, RW Peterson, TP Purdy, K Cicak, RW Simmonds, CA Regal, and KW Lehnert. Bidirectional and efficient conversion between microwave and optical light. *Nature Physics*, 10:321–326, 2014.

[181] Joerg Bochmann, Amit Vainsencher, David D Awschalom, and Andrew N Cleland. Nanomechanical coupling between microwave and optical photons. *Nature Physics*, 9(11):712, 2013.

[182] K-MC Fu, C Santori, PE Barclay, and RG Beausoleil. Conversion of neutral nitrogen-vacancy centers to negatively charged nitrogen-vacancy centers through selective oxidation. *Applied Physics Letters*, 96(12):121907, 2010.

[183] Vadym N Mochalin, Olga Shenderova, Dean Ho, and Yury Gogotsi. The properties and applications of nanodiamonds. *Nature nanotechnology*, 7(1):11–23, 2012.

[184] Y Chu, Nathalie Pulmones de Leon, BJ Shields, B Hausmann, R Evans, E Togan, Michael John Burek, M Markham, A Stacey, Alexander S Zibrov, et al. Coherent optical transitions in implanted nitrogen vacancy centers. *Nano letters*, 14(4):1982–1986, 2014.

[185] HJ McSkimin and WL Bond. Elastic moduli of diamond. *Physical Review*, 105(1):116, 1957.

[186] Anil Ghimire, Eyal Shafran, and Jordan M Gerton. Using a sharp metal tip to control the polarization and direction of emission from a quantum dot. *Scientific reports*, 4, 2014.

[187] Dirk Heinze, Dominik Breddermann, Artur Zrenner, and Stefan Schumacher. A quantum dot single-photon source with on-the-fly all-optical polarization control and timed emission. *Nature communications*, 6, 2015.

[188] M Artoni and A Zavatta. Large phase-by-phase modulations in atomic interfaces. *Physical review letters*, 115(11):113005, 2015.

[189] David P Franke, Florian M Hrubesch, Markus Künzl, Hans-Werner Becker, Kohei M Itoh, Martin Stutzmann, Felix Hoehne, Lukas Dreher, and Martin S Brandt. Interaction of strain and nuclear spins in silicon: quadrupolar effects on ionized donors. *Physical review letters*, 115(5):057601, 2015.

[190] Lucio Robledo, Hannes Bernien, Ilse van Weperen, and Ronald Hanson. Control and coherence of the optical transition of single nitrogen vacancy centers in diamond. *Physical review letters*, 105(17):177403, 2010.

[191] MS Grinolds, M Warner, Kristiaan De Greve, Yuliya Dovzhenko, L Thiel, Ronald Lee Walsworth, S Hong, P Maletinsky, and Amir Yacoby. Subnanometre resolution in three-dimensional magnetic resonance imaging of individual dark spins. *Nature nanotechnology*, 9(4):279–284, 2014.

[192] I Lovchinsky, AO Sushkov, E Urbach, NP de Leon, S Choi, K De Greve, R Evans, R Gertner, E Bersin, C Müller, et al. Nuclear magnetic resonance detection and spectroscopy of single proteins using quantum logic. *Science*, 351(6275):836–841, 2016.

[193] M Kim, HJ Mamin, MH Sherwood, K Ohno, DD Awschalom, and Dan Rugar. Decoherence of near-surface nitrogen-vacancy centers due to electric field noise. *Physical review letters*, 115(8):087602, 2015.

[194] Lorenza Viola, Emanuel Knill, and Seth Lloyd. Dynamical decoupling of open quantum systems. *Physical Review Letters*, 82(12):2417, 1999.

[195] Jean Teissier, Arne Barfuss, and Patrick Maletinsky. Hybrid continuous dynamical decoupling: a photon-phonon doubly dressed spin. *Journal of Optics*, 19(4):044003, 2017.

[196] Xiangkun Xu, Zixiang Wang, Changkui Duan, Pu Huang, Pengfei Wang, Ya Wang, Nanyang Xu, Xi Kong, Fazhan Shi, Xing Rong, et al. Coherence-protected quantum gate by continuous dynamical decoupling in diamond. *Physical review letters*, 109(7):070502, 2012.

[197] D Andrew Golter, Thomas K Baldwin, and Hailin Wang. Protecting a solid-state spin from decoherence using dressed spin states. *Physical review letters*, 113(23):237601, 2014.

[198] Marcus W Doherty, Victor M Acosta, Andrey Jarmola, Michael SJ Barson, Neil B Manson, Dmitry Budker, and Lloyd CL Hollenberg. Temperature shifts of the resonances of the nv- center in diamond. *Physical Review B*, 90(4):041201, 2014.

[199] Markus Aspelmeyer, Tobias J Kippenberg, and Florian Marquardt. Cavity optomechanics. *Reviews of Modern Physics*, 86(4):1391, 2014.

[200] Dietrich Leibfried, Rainer Blatt, Christopher Monroe, and David Wineland. Quantum dynamics of single trapped ions. *Reviews of Modern Physics*, 75(1):281, 2003.

[201] Ch Monroe, DM Meekhof, BE King, Steven R Jefferts, Wayne M Itano, David J Wineland, and P Gould. Resolved-sideband raman cooling of a bound atom to the 3d zero-point energy. *Physical Review Letters*, 75(22):4011, 1995.

[202] Peter Rabl, P Cappellaro, MV Gurudev Dutt, Liang Jiang, JR Maze, and Mikhail D Lukin. Strong magnetic coupling between an electronic spin qubit and a mechanical resonator. *Physical Review B*, 79(4):041302, 2009.

[203] P Rabl. Cooling of mechanical motion with a two-level system: The high-temperature regime. *Physical Review B*, 82(16):165320, 2010.

[204] Kun Huang and Avril Rhys. Theory of light absorption and non-radiative transitions in f-centres. In *Proceedings of the Royal Society of London A: Mathematical, Physical and Engineering Sciences*, volume 204, pages 406–423. The Royal Society, 1950.

[205] DM Meekhof, C Monroe, BE King, Wayne M Itano, and David J Wineland. Generation of nonclassical motional states of a trapped atom. *Physical Review Letters*, 76(11):1796, 1996.

[206] JF Poyatos, JI Cirac, and P Zoller. Quantum reservoir engineering with laser cooled trapped ions. *Physical review letters*, 77(23):4728, 1996.

[207] F Dolde, I Jakobi, B Naydenov, N Zhao, S Pezzagna, C Trautmann, J Meijer, P Neumann, F Jelezko, and J Wrachtrup. Room-temperature entanglement between single defect spins in diamond. *Nature Physics*, 9(3):139, 2013.

[208] Andreas Albrecht, Alex Retzker, Fedor Jelezko, and Martin B Plenio. Coupling of nitrogen vacancy centres in nanodiamonds by means of phonons. *New Journal of Physics*, 15(8):083014, 2013.

[209] ZY Xu, YM Hu, WL Yang, M Feng, and JF Du. Deterministically entangling distant nitrogen-vacancy centers by a nanomechanical cantilever. *Physical Review A*, 80(2):022335, 2009.

[210] Li-gong Zhou, LF Wei, Ming Gao, and Xiang-bin Wang. Strong coupling between two distant electronic spins via a nanomechanical resonator. *Physical Review A*, 81(4):042323, 2010.

[211] Zhang-qi Yin, Tongcang Li, Xiang Zhang, and LM Duan. Large quantum superpositions of a levitated nanodiamond through spin-optomechanical coupling. *Physical Review A*, 88(3):033614, 2013.

[212] L Chotorlishvili, D Sander, A Sukhov, V Dugaev, VR Vieira, A Komnik, and J Berakdar. Entanglement between nitrogen vacancy spins in diamond controlled by a nanomechanical resonator. *Physical Review B*, 88(8):085201, 2013.

[213] PC Haljan, K-A Brickman, L Deslauriers, PJ Lee, and C Monroe. Spin-dependent forces on trapped ions for phase-stable quantum gates and entangled states of spin and motion. *Physical review letters*, 94(15):153602, 2005.

[214] J Majer, JM Chow, JM Gambetta, J Koch, BR Johnson, JA Schreier, L Frunzio, DI Schuster, AA Houck, A Wallraff, et al. Coupling superconducting qubits via a cavity bus. *Nature*, 449(7161):443–447, 2007.

[215] D Hayes, SM Clark, S Debnath, D Hucul, IV Inlek, KW Lee, Q Quraishi, and C Monroe. Coherent error suppression in multiqubit entangling gates. *Physical review letters*, 109(2):020503, 2012.

[216] D Andrew Golter, Thein Oo, Mayra Amezcua, Ignas Lekavicius, Kevin A Stewart, and Hailin Wang. Coupling a surface acoustic wave to an electron spin in diamond via a dark state. *Physical Review X*, 6(4):041060, 2016.

[217] Brian B Zhou, Alexandre Baksic, Hugo Ribeiro, Christopher G Yale, F Joseph Heremans, Paul C Jerger, Adrian Auer, Guido Burkard, Aashish A Clerk, and David D Awschalom. Accelerated quantum control using superadiabatic dynamics in a solid-state lambda system. *Nature Physics*, 2016.

[218] Tomás Ramos, Hannes Pichler, Andrew J Daley, and Peter Zoller. Quantum spin dimers from chiral dissipation in cold-atom chains. *Physical review letters*, 113(23):237203, 2014.

[219] Pierre-Olivier Guimond, Hannes Pichler, Arno Rauschenbeutel, and Peter Zoller. Chiral quantum optics with v-level atoms and coherent quantum feedback. *Physical Review A*, 94(3):033829, 2016.

[220] Christopher J Sarabalis, Jeff T Hill, and Amir H Safavi-Naeini. Guided acoustic and optical waves in silicon-on-insulator for brillouin scattering and optomechanics. *APL Photonics*, 1(7):071301, 2016.

[221] T Rosskopf, A Dussaux, K Ohashi, M Loretz, Romana Schirhagl, H Watanabe, S Shikata, KM Itoh, and CL Degen. Investigation of surface magnetic noise by shallow spins in diamond. *Physical review letters*, 112(14):147602, 2014.

[222] BK Ofori-Okai, S Pezzagna, K Chang, M Loretz, R Schirhagl, Y Tao, BA Moores, K Groot-Berning, J Meijer, and CL Degen. Spin properties of very shallow nitrogen vacancy defects in diamond. *Physical Review B*, 86(8):081406, 2012.

[223] Yumin Shen, Timothy M Sweeney, and Hailin Wang. Zero-phonon linewidth of single nitrogen vacancy centers in diamond nanocrystals. *Physical Review B*, 77(3):033201, 2008.

[224] Ph Tamarat, T Gaebel, JR Rabeau, M Khan, AD Greentree, H Wilson, LCL Hollenberg, S Prawer, P Hemmer, F Jelezko, et al. Stark shift control of single optical centers in diamond. *Physical review letters*, 97(8):083002, 2006.

[225] P. Siyushev, H. Pinto, M. Vörös, A. Gali, F. Jelezko, and J. Wrachtrup. Low temperature studies of charge dynamics of nitrogen-vacancy defect in diamond. *Phys. Rev. Lett.*, 110:167402, 2013.

[226] Shanying Cui and Evelyn L Hu. Increased negatively charged nitrogen-vacancy centers in fluorinated diamond. *Applied Physics Letters*, 103(5):051603, 2013.

[227] Shanying Cui, Andrew S Greenspon, Kenichi Ohno, Bryan A Myers, Ania C Bleszynski Jayich, David D Awschalom, and Evelyn L Hu. Reduced plasma-induced damage to near-surface nitrogen-vacancy centers in diamond. *Nano letters*, 15(5):2887–2891, 2015.

[228] Toyofumi Ishikawa, Kai-Mei C Fu, Charles Santori, Victor M Acosta, Raymond G Beausoleil, Hideyuki Watanabe, Shinichi Shikata, and Kohei M Itoh. Optical and spin coherence properties of nitrogen-vacancy centers placed in a 100 nm thick isotopically purified diamond layer. *Nano letters*, 12(4):2083–2087, 2012.

[229] Claire A McLellan, Bryan A Myers, Stephan Kraemer, Kenichi Ohno, David D Awschalom, and Ania C Bleszynski Jayich. Patterned formation of highly coherent nitrogen-vacancy centers using a focused electron irradiation technique. *Nano letters*, 16(4):2450–2454, 2016.

[230] Kenichi Ohno, F Joseph Heremans, Charles F de las Casas, Bryan A Myers, Benjamín J Alemán, Ania C Bleszynski Jayich, and David D Awschalom. Three-dimensional localization of spins in diamond using 12c implantation. *Applied Physics Letters*, 105(5):052406, 2014.

[231] Z Huang, W-D Li, C Santori, VM Acosta, A Faraon, T Ishikawa, W Wu, D Winston, RS Williams, and RG Beausoleil. Diamond nitrogen-vacancy centers created by scanning focused helium ion beam and annealing. *Applied Physics Letters*, 103(8):081906, 2013.

[232] Boris Naydenov, Friedemann Reinhard, Anke Lämmle, V Richter, Rafi Kalish, Ulrika FS DHaenens-Johansson, Mark Newton, Fedor Jelezko, and Jörg Wrachtrup. Increasing the coherence time of single electron spins in diamond by high temperature annealing. *Applied Physics Letters*, 97(24):242511, 2010.

[233] A. El Habti, F. Bastien, E. Bigler, and T. Thorvaldsson. High frequency surface acoustic wave devices at very low temperature. *J. Acoust. Soc. Am.*, 100:272–277, 1996.

[234] K. Yamanouchi, H. Nakagawa, and H. Odagawa. Ghz-range surface acoustic wave low loss filter at super low temperature. *Proc. Meet. Eur. Freq. Time Forum/IEEE Int. Freq. Cont. Symp.*, 2:911–914, 1999.

[235] Riccardo Manenti, MJ Peterer, Ani Nersisyan, EB Magnusson, Andrew Patterson, and PJ Leek. Surface acoustic wave resonators in the quantum regime. *Physical Review B*, 93(4):041411, 2016.

[236] Martin V Gustafsson, Thomas Aref, Anton Frisk Kockum, Maria K Ekström, Göran Johansson, and Per Delsing. Propagating phonons coupled to an artificial atom. *Science*, 346(6206):207–211, 2014.

[237] Martin V Gustafsson, Paulo V Santos, Göran Johansson, and Per Delsing. Local probing of propagating acoustic waves in a gigahertz echo chamber. *Nature Physics*, 8(4), 2012.

[238] M. Eichenfield, J. Chan, R. M. Camacho, K. J. Vahala, and O. Painter. Optomechanical crystals. *Nature*, 462:78–82, 2009.

[239] H Jeff Kimble. Strong interactions of single atoms and photons in cavity qed. *Physica Scripta*, 1998(T76):127, 1998.

[240] Juan Restrepo, Cristiano Ciuti, and Ivan Favero. Single-polariton optomechanics. *Physical review letters*, 112(1):013601, 2014.

[241] Gary Wolfowicz, Alexei M Tyryshkin, Richard E George, Helge Riemann, Nikolai V Abrosimov, Peter Becker, Hans-joachim Pohl, Mike LW Thewalt, Stephen A Lyon, and John JL Morton. Atomic clock transitions in silicon-based spin qubits. *Nature Nanotechnology*, 8(8):561, 2013.

[242] JJ Pla, A Bienfait, G Pica, J Mansir, FA Mohiyaddin, A Morello, T Schenkel, BW Lovett, JJL Morton, and P Bertet. Strain-induced nuclear quadrupole splittings in silicon devices. *arXiv preprint arXiv:1608.07346*, 2016.